



OTTO VON GUERICKE
UNIVERSITÄT
MAGDEBURG

VST

FACULTY OF PROCESS
AND SYSTEMS ENGINEERING

Processing and characterization of tailor-made superparamagnetic iron oxide nanoparticles (SPIO-NPs) for pharmaceutical applications

Dissertation

zur Erlangung des akademischen Grades

**Doktoringenieur
(Dr.-Ing.)**

von M.Sc. Muhammad Kamran Khalid
geb. am 10.08.1977 in Lahore, Pakistan

genehmigt durch die Fakultät für Verfahrens- und Systemtechnik
der Otto-von-Guericke-Universität Magdeburg

Promotionskommission:	Prof. Dr.-Ing. Eckehard Specht	(Vorsitz)
	Prof. Dr. Ir. Berend van Wachem	(Gutachter)
	Prof. Dr. rer. nat. Franziska Scheffler	(Gutachter)
	Prof. Dr.-Ing. Sergiy Antonyuk	(Gutachter)

eingereicht am: 02.05.2018
Promotionskolloquium am: 05.12.2018

Acknowledgements

First I thank **GOD** who gave me the courage to complete this work and also for HIS countless blessings on every step of my life.

This work would be incomplete without acknowledging and appreciating many friends and colleagues who helped me directly or indirectly in many ways.

I would like to recall the memories of my first supervisor **Prof. Dr.- Ing. habil. Jürgen Tomas** who accepted me in his esteemed chair for my PhD work under his kind supervision. Unfortunately, he left us too early. He was a tremendous scientist and a very kind personality. His praiseworthy services and immaculate contributions to the scientific community will always be remembered and he will always live on in our hearts. Then, I would like to thank and acknowledge my second supervisor and chair **Prof. Dr. Ir. Berend van Wachem** for accepting me as a PhD researcher under his erudite supervision after the loss of Prof. Tomas. His impeccable encouragement and commendable supervision are highly appreciated. He always supported and guided me towards a perfect goal.

Afterwards, it is time to thank and appreciate my co-supervisor **Dr. rer. nat. Werner Hintz**. I have no hesitation to claim that this research work could not be possible without his scholastic and preeminent guidance, meritorious support, and encouragement. He helped me not only in project related matters but also in different issues related to the administration from my admission to the final form of this work. He introduced me deep into the topic. He always welcomed me into his office with a *smile*; I found him ready for the critical discussions all the time. His every word was valued for me and I was very lucky that I worked with such a nice, kind and belletristic personality. The word 'thanks' is not justified with his lots of support and help. But I have no other words to say: Thank you very much Dr. Hintz!

I would also like to thank Prof. Dr.-Ing. Eckehard Specht (head of commission) and my review committee Prof. Dr. rer. nat. Franziska Scheffler (Institute of chemistry, Otto-von-Guericke-University Magdeburg) and Prof. Dr.-Ing. Sergiy Antonyuk (Chair of mechanical process engineering, Technical University Kaiserslautern) for their precious time and valuable suggestions.

My gratitude goes to my dearest office colleagues and friends Abbas Kamranian Marnani and Eduard Lukas for creating such a nice research and pleasant atmosphere in the office. We had lots of conscientious discussions on different international issues and also related to our works of course. We exchanged plenty of information, ideas and scientific tools with each other which were highly helpful for my work. Here I would say; wherever I live, I will miss you guys always.

I would also like to thank my other colleagues who made my time pleasant and memorable at the chair, especially: Dr.-Ing. habil. Müller, Dr.-Ing. Schlinkert, Dr. rer. nat. Aman, Dr.-Ing. Mader-Arndt, Dr.-Ing. Todorova, Farhad, Zhang Xiwei, Talea, Michael, Zheni, Nicolle, and Peter Siebert. Thanks are due to PD Dr. Petra Henrich-Noack and Ms. Lisa Grigartzik from Institute of Medical Psychology (IMP) for their support for the biological tests (*in vitro* and *in vivo* toxicity studies) of many samples and also for their expert suggestions and discussions on the results always. Dr. Henrich-Noack took a keen interest in my project and made it successful. Thanks are due to Dr. Peter Veit for support in TEM investigations of many samples and also of his very generous welcoming smile always.

I am also thankful to my master students who wrote their master thesis on the topic: namely, Mohsin, Hammad, Saad, Ninand, Somnath, Zeeshan, and Asad.

I am thankful to my best friends, cousins, and colleagues in Pakistan who helped me indirectly and also prayed for my success. My sincere gratitude goes to Khalid Masood, Fayyaz, Asif, Mehmood, Imran, Manan, Junaid, Sarfraz Akram, Talat Rasheed, Hammad Hassan, Asghar Farooq, and Ubaid-Ullah.

I would like to express my heartfelt gratitude and indebtedness to my loving parents for the immense support throughout my life. Without their unconditional love, encouragement, and help, I could never have come so far. Whatever I am today and will be in tomorrow is because of their prayers, care, and love. I am also thankful to my caring and friendly brothers Muhammad Irfan Khalid, Muhammad Naveed Khalid and bhabis Ms. Ammara Irfan and Ms. Zunera Naveed for their love and also for bearing my family responsibilities during my long absence abroad. They always encouraged me and asked for be focused on my PhD work. I must say here that if I could pick the best brothers, I would pick both of you. I and my wife are also emotional by remembering my lost father-in-law and mother-in-law Mr. & Mrs. Muhammad Aslam. They were a piece of gems in their character. I am grateful my entire family in Pakistan for their endless love and especially, here I would like to recall the memories of my cousin and great mathematician Dr. Hayat Muhammad Khalid (late) that inspired me many years ago to go ahead for a PhD. At that time, it seemed to be too early and now this dream came true.

At the last but not least, I express my cordial thanks to my caring wife Mehwish Kamran whose forbearance, motivation, and support have been exquisite. She always compromised and cooperated with the changing situations. We are also blessed with our first son 'Muhammad Bilal Hassan' just after submitting my dissertation and it was a great moment for me. Dear Mehwish! You are the best thing that happened to me. You are the best thing that is still happening to me and you are going to be the best thing to happen to me, ever.

*I dedicated this work to my beloved parents **Mr. & Mrs. Bashir Ahmad Khalid** and to the memories of my grandfathers and grandmothers.*

Muhammad Kamran Khalid

November 2018

Magdeburg, Germany

Kurzfassung

Das Forschungsgebiet der Eisenoxid-Nanopartikel, auch bekannt als Magnetit, wächst sehr schnell. Diese Nanopartikel sind Kernbestandteil der Nanotechnologie, die heute eine Multimilliarden-Dollar-Industrie darstellt. Das weltweit zunehmende Interesse der verschiedenen Forscher an Nanopartikeln beruht auf ihren einzigartigen und vielseitigen physikalischen und chemischen Eigenschaften, insbesondere auf sogenannten „quantum size effects“. Eine einzigartige Klasse von speziell hergestellten Eisenoxid-Nanopartikeln sind superparamagnetische Eisenoxid-Nanopartikel (SPIO-NP). Dieser Superparamagnetismus tritt in magnetischen Materialien auf, wenn die Partikelgröße 30 nm unterschreitet. Er bietet die Möglichkeit, die Partikel nach Applikation in einem Prozess durch magnetische Felder zu beeinflussen. Verschiedene industrielle und biomedizinische Anwendungen hängen von der Stabilität der SPIO-NP unter verschiedenen Bedingungen ab. Es ist interessant, dass unter allen anderen magnetischen Nanopartikeln nur Eisenoxid-Nanopartikel in biomedizinischen Anwendungen wie Hyperthermie, Magnetresonanztomographie (MRT) und zielgerichteter Wirkstofffreisetzung aufgrund ihrer hervorragenden magnetischen Eigenschaften verwendet werden und bei der Entfernung des angelegten Magnetfeldes komplett ihre Magnetisierung verlieren.

Ziel der vorliegenden Doktorarbeit ist es, theoretisch fundierte Beschreibungen für den Einsatz in biomedizinischen Anwendungen (insbesondere in der Wirkstofffreisetzung) mit Methoden aus der mechanischen Verfahrenstechnik zu entwickeln: Analyse und Optimierung des Herstellungsprozesses von biokompatiblen SPIO-NP, gekennzeichnet durch die Merkmale (a) die Partikelgröße der SPIO-NP zwischen 10-125 nm, die durch Co-Präzipitationsverfahren synthetisiert wurden, (b) die Modifikationen und Funktionalisierung der Partikeloberflächen und -kerne, für die Überwindung der Blut-Hirn-Schranke (BHS) und den Transport relevanter pharmazeutischer Wirkstoffe sowie (c) Optimierung der Kern- und Oberflächenmodifizierung und -funktionalisierung mit erstens: Chemischen Substanzen zur Maskierung der SPIO-NP zur Überwindung der BHS (Tween 80, Dextran 70.000 und DEAE-Dextran) und zweitens: Fluoreszenzmarker - Rhodamin 123 (Partikel im Blutstrom, während der Durchquerung der BHS) und Propidiumiodid (PI) (zum Nachweis der Nanopartikel im Zellgewebe).

Eine weiteres Ziel des Projekts bestand darin, detaillierte Kenntnisse über die konzentrationsabhängige *in vitro*- und *in vivo*-Toxizität der synthetisierten beschichteten SPIO-NP zu erlangen, insbesondere wenn sie nach ihrer Interaktion mit Gehirnzellen (C6-Zellen), die aus Ratten-Glia-Tumoren extrahiert wurden, mit Fluoreszenzfarbstoffen markiert wurden. SPIO-NP wurden bisher nicht als Modell für BHS in den retinalen Ganglienzellen untersucht, indem konfokale Neuroimaging *in vivo* verwendet wurde.

Die SPIO-NP wurden mittels Co-Präzipitationsmethode aus Eisen- und Eisensalzlösung mit einem Molverhältnis von 2:1 in deionisiertem Wasser (Deionat) in einem Dreihals-Rundboden-Glasreaktor unter kräftigem Rühren synthetisiert. Die Tenside (Dextran 70.000, DEAE-Dextran und Tween 80) wurden im Deionat separat in einem Glasbecher gelöst und anschließend in den Dreihals-Reaktionskolben gegeben. Die Reaktionstemperatur wurde auf 40-100 °C eingestellt, bei der NaOH oder 25%ige NH₃-Lösung schnell in den Glasreaktor gespritzt wurde, um den pH-

Wert der Lösung zu erhöhen. Die so entstandene schwarze Suspension, wies auf die Magnetitbildung hin. Die Reaktion wurde bei einer Rührerdrehzahl von 400 U/min bis 1000 U/min (Umfangsgeschwindigkeit von 1,21 m/s bis 3,03 m/s) bei gleicher Temperatur für eine Stunde durchgeführt. Die Nanopartikelsynthese wurden dann 10 Minuten lang mithilfe von Ultraschall untersucht. Für die Markierung mit Fluoreszenzmarker wurde der Fluoreszenzfarbstoff in Deionat gelöst und anschließend mit der stöchiometrischen Menge an Eisenoxid-Nanopartikeln und anschließendem Magnetrührer eingebracht. Die Nanopartikel wurden hinsichtlich Größe, Größenverteilung, Zetapotenzial und Morphologie charakterisiert. Die *in vitro* Zytotoxizität und relative Zellebensfähigkeit wurde mit Hilfe des MTT kolorimetrischen Assays gemessen, wenn SPIO-NP den C6-Gliomzellen mit unterschiedlichen Inkubationszeiten ausgesetzt wurden. Für die *in vivo* zytotoxische Studie wurde die zelluläre Aufnahme durch Injektion verschiedener Variationen von fluoreszierenden SPIO-NP in Tiergruppen (Ratten) durchgeführt: retrograde Markierung von retinalen Ganglienzellen, intravitreale SPIO-NP Injektion, *in vivo* konfokale Neuroimaging und *ex vivo* konfokale Bildgebung.

Die Ergebnisse zeigen, dass die synthetisierten SPIO-NP, die mit Tween 80, Dextran 70.000 und DEAE-Dextran beschichtet sind, im Größenbereich von 10~100 nm liegen und sowohl mit positivem als auch negativem Zetapotential vorkommen. Die Verwendung von Tween 80 als Oberflächenbeschichtung führt zu einer schmaleren Größenverteilung und einem höheren Zetapotenzial. Die Überlebenswahrscheinlichkeit der Zellen bei SPIO-NP-Exposition war bei einer DEAE-Dextran-Beschichtung mit 16 Stunden Inkubationszeit größer. Wenn die Inkubationszeit auf 24 Stunden erhöht wurde, war die Überlebenswahrscheinlichkeit signifikant reduziert. Die niedrigste Überlebenswahrscheinlichkeit wurde für Tween 80 beschichtete SPIO-NP gemessen. Für den Fall von beschichteten SPIO-NP, die gleichzeitig mit Fluoreszenzfarbstoffen markiert sind, wurde die maximale Überlebenswahrscheinlichkeit mit Propidiumiodid für die Dextran-70.000-Beschichtung ermittelt.

Die Akkumulation von fluoreszierenden SPIO-NP in Somazellen wurde durch die konfokale Bildgebung bestätigt. In-Vivo-Untersuchungen ergaben, dass wir für höhere Dosierung von SPIO-NP hellere Fluoreszenzsignale erhielten, verglichen mit jenen Kontrolltieren, die nur Träger-NP erhielten. Bei niedrig dosierten Injektionen waren die SPIO-NP gleichmäßig über die Netzhaut verteilt.

Keywords: Superparamagnetische Eisenoxid-Nanopartikel (SPIO-NP), biomedizinische Anwendungen, Ko-Präzipitation (Fällung), Blut-Hirn-Schranke (BHS), *in vitro* und *in vivo* Toxizität, C6- Gliomzellen, retinale Ganglienzellen

Abstract

The field of iron oxide nanoparticles also known as magnetite is growing very rapidly and these nanoparticles are core component of nanotechnology which is a multi-billion dollars industry today. This globally increasing interest of various researchers in 'nano'-objects is due to their unique and versatile physical and chemical properties, so-called quantum size effects. A unique class of iron oxide nanoparticles is superparamagnetic iron oxide nanoparticles (SPIO-NPs) and this superparamagnetism phenomenon occurs in magnetic materials when they comprised of the extremely small size below than 30 nm. SPIO-NPs are a very special class of engineered nanoparticle that can be influenced by an external magnetic field when applied. Various industrial and biomedical applications depend on the stability of SPIO-NPs under a number of different conditions. It is an interesting fact that among all other magnetic nanoparticles, only iron oxide nanoparticles are under use in biomedical applications such as hyperthermia, magnetic resonance imaging (MRI), and targeted drug delivery due to their excellent magnetic properties and have zero magnetization on the removal of the applied magnetic field.

The objectives of the present doctoral work were to develop theoretically based descriptions for use in biomedical applications (especially in drug delivery) with simplified assumptions used in mechanical process engineering. Analysis and optimization of the production process of biocompatible SPIO-NPs which characterized by the features (a) the particle size of the SPIO-NPs between 10-125 nm synthesized by a co-precipitation method (b) the modifications and functionalization in particles core and surface aiming SPIO-NPs passing the blood-brain barrier (BBB) and transporting relevant pharmaceutical compounds (c) systematic studies to optimize the process of core and surface modification and functionalization (particle core, surface coatings, and loadings) with (1) chemical compounds for masking the SPIO-NPs to overcome the BBB-Tween 80, Dextran 70,000, and DEAE-Dextran (2) fluorescence markers – rhodamine 123 (particles in blood stream, during crossing the BBB), and propidium iodide (PI) (to prove the NPs in the cell tissue). Another challenge of the project was to obtain the detailed knowledge about the concentration-dependent *in vitro* and *in vivo* toxicity of the synthesized coated SPIO-NPs and especially when labelled with fluorescent dyes after their interaction with the brain cells (C6 cells) extracted from rat glial tumor. SPIO-NPs were not studied before as a model of BBB in the retinal ganglion cells by using *in vivo* confocal neuroimaging.

SPIO-NPs were synthesized via a co-precipitation method of ferric and ferrous salts solution with 2:1 molar ratio in deionized (DI) water in a three-neck round bottom glass reactor under vigorous stirring. Surfactants (Dextran 70,000, DEAE-Dextran, and Tween 80) were solubilized in DI water separately in a glass beaker and then added into the three-neck reaction flask. The reaction temperature was adjusted to 40-100 °C at which NaOH or 25% NH₃ solution was quickly syringed into the glass reactor to increase the solution pH. A black color suspension was thus formed indicating the magnetite formation. The reaction was carried out for nucleation and growth of nanoparticles at 400 rpm to 1000 rpm (stirrer tip speed from 1.21 m/s to 3.03 m/s) under the same temperature for one hour. Nanoparticles syntheses were then probed to sonication for 10 minutes. For labelling with fluorescence marker, fluorescence dye was dissolved in DI water and then introduced with the

stoichiometric amount of iron oxide nanoparticles followed by a magnetic shaker. Afterward, the nanoparticles were separated from the unlabeled solution by centrifugation and re-dispersed in DI water. The nanoparticles were characterized for size, size distribution, zeta potential, and morphology. The *in vitro* cytotoxicity and relative cell viability was measured using MTT colorimetric assay when SPIO-NPs were exposed to C6 glioma cells at different incubation times. For *in vivo* cytotoxic study, cellular uptake was performed by injecting different variations of fluorescent SPIO-NPs in animal (rat) groups for retrograde labelling of retinal ganglion cells, intravitreal SPIO-NPs injection, *in vivo* confocal neuroimaging, and *ex vivo* confocal imaging.

The results show that synthesized SPIO-NPs coated with Tween 80, Dextran 70,000, and DEAE-Dextran were in the size range of 10~100 nm with positive or negative zeta potentials. But the size distribution using Tween 80 as the surface coating material is narrower and also has higher zeta potentials. The cell viability of SPIO-NPs was greater in the case of DEAE-Dextran coated SPIO-NPs with 16 hours' incubation. When incubation time was increased to 24 hours, then the cell viability was decreased. The least cell viability was measured for the case when SPIO-NPs were coated with Tween 80. For the case of coated SPIO-NPs simultaneously labelled with fluorescent dyes, maximum cell viability was recorded with propidium iodide for Dextran 70,000 coated SPIO-NPs. The accumulation of fluorescent SPIO-NPs in cell soma was confirmed by the confocal photographs. *In vivo* investigations revealed that for higher dosage of SPIO-NPs, we obtained brighter fluorescence signals as compared to those control animals which only received vehicle injections. SPIO-NPs were evenly distributed over the retina when animals were injected low dosage injections.

Keywords: Superparamagnetic iron oxide nanoparticles (SPIO-NPs), biomedical applications, co-precipitation, blood-brain barrier (BBB), *in vitro* and *in vivo* toxicity, C6 glioma cells, retinal ganglion cells

Table of contents

Kurzfassung	iv
Abstract	vi
List of figures	xii
List of tables	xviii
1 Introduction.....	1
1.1 Superparamagnetic iron oxide nanoparticles	2
1.2 Coating of nano-scaled magnetic particles	3
1.3 Iron oxide nanoparticles.....	3
1.3.1 Hematite (α -Fe ₂ O ₃)	4
1.3.2 Magnetite (Fe ₃ O ₄).....	4
1.3.3 Maghemite (γ -Fe ₂ O ₃)	5
1.4 Potential applications of magnetic iron oxide nanoparticles.....	6
1.4.1 Industrial applications	6
1.4.2 Biomedical applications.....	6
1.5 Challenges in the field of magnetic nanoparticles	7
1.6 Objectives of the present work.....	8
1.7 Outline of the contents	9
2 Magnetic properties and biomedical applications.....	10
2.1 Nanomagnetism	10
2.1.1 Types of nanomagnetic materials	10
2.1.2 Diamagnetic materials.....	10
2.1.3 Paramagnetic materials.....	11
2.1.4 Ferromagnetic materials	11
2.1.5 Ferrimagnetic materials	11
2.1.6 Antiferromagnetic materials	11
2.2 Superparamagnetism	12
2.3 Magnetic hysteresis.....	13
2.4 Biomedical applications of superparamagnetic iron oxide nanoparticles	17
2.4.1 Targeted drug delivery	19
2.4.1.1 Physicochemical characteristics essential for drug delivery	22
2.4.1.1.1 Shape of the nanoparticles.....	23
2.4.1.1.2 Size of the nanoparticles	23
2.4.1.1.3 Surface properties of the nanoparticles.....	24

2.4.1.2	Blood-brain barrier and targeted drug delivery	25
2.4.1.3	Blood-brain barrier (BBB)	25
2.4.1.4	<i>In vivo</i> confocal neuroimaging (ICON) and BBB	27
2.4.2	Magnetic hyperthermia (MHT).....	28
2.4.3	Magnetic resonance imaging (MRI)	30
3	Synthesis and stabilization of SPIO-NPs	33
3.1	Synthesis of superparamagnetic iron oxide nanoparticles	34
3.2	Liquid phase synthesis of Fe ₃ O ₄ nanoparticles.....	36
3.2.1	Co-precipitation method	36
3.2.2	Sol-gel method	41
3.2.3	Hydrothermal method.....	42
3.2.4	Microemulsion method.....	43
3.3	Surface coating of SPIO-NPs.....	44
3.3.1	Polymeric superparamagnetic iron oxide nanoparticles.....	48
3.3.2	Synthesis methods of polymer coated NPs.....	50
3.3.3	Fluorescent magnetic nanoparticles	51
3.4	Liquid-liquid phase transfer of magnetic nanoparticles.....	53
3.4.1	Theoretical background of liquid-liquid phase transfer process.....	54
3.4.2	Preliminary work of liquid-liquid phase transfer of magnetic nanoparticles.....	55
3.5	Toxicity of magnetic nanoparticles	59
3.5.1	Mechanism of toxicity	60
3.5.2	<i>In vitro</i> toxicity of magnetic iron oxide nanoparticles.....	61
3.5.3	<i>In vivo</i> toxicity of magnetic iron oxide nanoparticles.....	61
3.5.4	Factors affecting the SPIO-NPs toxicity	63
3.5.4.1	Effect of size	63
3.5.4.2	Effect of dose.....	63
3.5.4.3	Effect of shape.....	64
3.5.4.4	Effect of surface chemistry.....	64
3.6	Nucleation and growth of nanoparticles.....	65
3.7	Inter-particles forces	67
3.7.1	van der Waals attractive forces.....	67
3.7.2	Electrostatic repulsive forces	67
3.7.3	DLVO theory	68
3.7.4	Stabilization of magnetic nanoparticles	69
4	Material properties and characterizations of iron oxide nanoparticles.....	72

4.1	Experimental equipment.....	72
4.2	Reactor set-up	73
4.3	Synthesis of SPIO-NPs.....	73
4.3.1	Cell culture of C6 glioma cells.....	74
4.3.2	MTT assay with iron oxide nanoparticles and C6 glioma cells	75
4.3.3	Animal models.....	77
4.3.4	Effect of pH on the particle size of SPIO-NPs	78
4.3.5	Effect of temperature on the particle size of SPIO-NPs	78
4.3.6	Effect of stirring velocity on the particle size of SPIO-NPs	79
4.3.7	Effect of precursors concentration on the particles size of SPIO-NPs	79
4.3.8	Effect of surfactants on the particles size of SPIO-NPs	79
4.3.9	Effect of sonication on the particle size of SPIO-NPs	80
4.4	Physicochemical characterizations of magnetite nanoparticles.....	80
4.4.1	Dynamic light scattering (DLS).....	80
4.4.2	Scanning electron microscopy (SEM)	82
4.4.3	Transmission electron microscopy (TEM)	82
4.4.4	Vibrating sample magnetometer (VSM).....	83
4.4.5	Spectrophotometry	84
5	Influence of process parameters on the properties of SPIO-NPs	86
5.1	Experiments with Tween 80 as a surface coating material.....	86
5.1.1	Effect of temperature on the synthesis of Tween 80-SPIO-NPs	86
5.1.2	Effect of stirring velocity on the synthesis of Tween 80-SPIO-NPs	88
5.1.3	Effect of pH variation on the synthesis of Tween 80-SPIO-NPs	90
5.1.4	Effect of Fe^{3+}/Fe^{2+} molar ratio on the synthesis of Tween 80-SPIO-NPs.....	92
5.2	Experiments with Dextran 70,000 as a surface coating material.....	94
5.2.1	Effect of temperature on the synthesis of Dextran 70,000-SPIO-NPs	94
5.2.2	Effect of stirring velocity on the synthesis of Dextran 70,000-SPIO-NPs	96
5.2.3	Effect of pH variation on the synthesis of Dextran 70,000-SPIO-NPs	97
5.2.4	Effect of Fe^{3+}/Fe^{2+} molar ratio on the synthesis of Dextran 70,000-SPIO-NPs.....	99
5.3	Experiments with DEAE-Dextran as a surface coating material.....	101
5.3.1	Effect of temperature on the synthesis of DEAE-Dextran-SPIO-NPs.....	101
5.3.2	Effect of stirring velocity on the synthesis of DEAE-Dextran-SPIO-NPs	103
5.3.3	Effect of pH variation on the synthesis of DEAE-Dextran-SPIO-NPs	104
5.3.4	Effect of Fe^{3+}/Fe^{2+} molar ratio on the synthesis of DEAE-Dextran-SPIO-NPs.....	106
6	Cytotoxicity and uptake studies of coated fluorescent SPIO-NPs.....	110

6.1	<i>In vitro</i> toxicity experiments.....	110
6.1.1	Cytotoxicity of fluorescent Tween 80 coated SPIO-NPs.....	110
6.1.2	Cytotoxicity of fluorescent Dextran 70,000 coated SPIO-NPs.....	113
6.1.3	Cytotoxicity of fluorescent DEAE-Dextran coated SPIO-NPs.....	117
6.1.4	Cytotoxicity of fluorescent dyes: rhodamine 123 and propidium iodide	122
6.2	<i>In vivo</i> and <i>ex vivo</i> uptake experiments	123
7	Conclusions and future outlook	128
7.1	Conclusions.....	128
7.2	Future outlook.....	130
	Bibliography.....	131
	Appendix.....	154

List of figures

Figure 1: View of crystal structure and crystallographic data of the hematite, magnetite, and maghemite (the black ball is denoting for Fe^{2+} , the green ball is dedicating for Fe^{3+} and the red ball is representing O^{2-}) [15]	4
Figure 2: Potential applications of magnetic nanoparticles in multidisciplinary fields.....	7
Figure 3: Summary of magnetic dipole alignment of all types of magnetic materials with their magnetic slope behaviours [55]	12
Figure 4: Magnetic behavior of magnetic NPs when the magnetic field is applied. The X-axis is the applied field (Oe), and the Y-axis is the magnetization of the sample as a function of field exposure (emu/g) [50].....	13
Figure 5: A graphical illustration explaining the blocking temperature of magnetic nanoparticles [50].....	15
Figure 6: A schematic illustration of the change in the surface-to-volume ratio between microsphere (left) and when the same microsphere composed of nanoparticles (right) [63].....	16
Figure 7: Effect of decreasing particles size on the hysteresis curve of ferromagnetic materials [10].....	16
Figure 8: Plethora of possible biomedical applications of magnetic nanoparticles [56].....	18
Figure 9: A schematic explanation for the different therapeutic and diagnosis strategies using magnetic (iron oxide) nanoparticles (MNPs). Accumulation of MNPs in the targeted tumor tissues using magnetic drug delivery systems, diagnosis by magnetic resonance imaging (MRI), and magnetic hyperthermia (MHT) for cancer treatment under the application of an alternating magnetic field [72].....	18
Figure 10: Two different drug loading options in the nanoparticles during the targeted drug delivery [77].....	21
Figure 11: Schematic representation of the magnetically driven targeted drug delivery mechanism to a particular region. Insertion of a catheter is shown into an arterial feed to the tumor under the magnetic stand which is positioned just over the specific target region (left). A holistic view of the targeted drug delivery system (right) [68].....	21
Figure 12: Different physiochemical considerations of superparamagnetic iron oxide nanoparticles for targeted drug delivery system [11].....	23
Figure 13: View of the blood-brain barrier; above, a cross-section through the brain; center, a schematic representation of the BBB; below, cellular structure [98]	26
Figure 14: Interruption of NPs in the blood-brain barrier (BBB), which tends to accumulate at the tumor site. Receptor-mediated endocytosis of the functionalized NPs by cells overexpressing a receptor can retain NPs inside the tumor [99]	27
Figure 15: Phenomena of magnetization heat generation when an alternating magnetic field is applied (H_0 , f), (left). A representation of the hysteresis loss mechanism of heat generation [12]	30
Figure 16: Control of MR contrast effect of magnetic nanoparticles. MNPs can be equally used as T_1 contrast agents or as T_2 contrast agents and this selection of their use depends on their various properties. In addition, the MR contrast effect can be adjusted by changing their core size, surface states including surface atoms and coating, composition, and assembly of multiple nanoparticles [127].....	32

Figure 17: Two basic approaches to nanomaterials fabrication: top-down and bottom-up	33
Figure 18: Various other chemical, physicochemical, and physical syntheses methods of magnetic nanoparticles.....	35
Figure 19: Biomedically applicable nanoparticles are only synthesis in the liquid phase, the dotted line is the indication for that material which synthesized in solid state and non-water soluble, therefore, they may have no suitability for the biomedical applications [125].....	35
Figure 20: Co-precipitation method using Fe^{2+} and Fe^{3+} aqueous solutions of salts with the addition of a base	37
Figure 21: A representation of formation pathways of magnetite nanoparticles by a co-precipitation method. Yellow areas indicate the main intermediate phases [186].....	41
Figure 22: Typical microemulsion process: a) oil in water microemulsion b) water in oil microemulsion [191]	43
Figure 23: Morphologies of magnetic nanocomposite materials are depicted. Blue spheres representing magnetic NPs. Grey color is for the non-magnetic entities and matrix materials. The nonmagnetic entity may provide the composite material with further functionalities and properties, providing multifunctional hybrid system [197].....	46
Figure 24: Comparison of <i>in-situ</i> and <i>ex-situ</i> surface coating strategies of SPIO-NPs [63].....	47
Figure 25: A plethora of different compounds which are used for the coating and stabilization of magnetic nanoparticles [198]	48
Figure 26: Schematic representation of the stabilization of MNPs by surface coating with inorganic (a) or organic materials (b) or by encapsulation into nanospheres (c) or nanocapsules (d) [199]	49
Figure 27: Various techniques used for the preparation of different polymer nanoparticles. SCF: supercritical fluid technology, C/LR: controlled/living radical [206].....	51
Figure 28: Schematic representation of targeted magnetic fluorescent nanoparticles. Covalent bonding (top) and electrostatic interaction (bottom) with conjugation of targeted ligands [212].....	52
Figure 29: Fluorescent magnetic nanoparticles synthesis by encapsulation. The magnetic core is encapsulated with silica or polymers to form a new composite in which targeted ligands are conjugated onto the surface of magnetic-fluorescent nanoparticles [212]	52
Figure 30: Preparation of fluorescent magnetic nanoparticles with the relation and focusing to their fields of applications [215]	53
Figure 31: Phase transfer mechanism and deagglomeration in the presence of surfactant molecules present at the interface [225].....	55
Figure 32: Fundamental steps which are used in the mechanism process during the phase transfer [222].....	55
Figure 33: Experimental setups for the phase transfer in the gravitational field (1) and centrifuge field (2) [229].....	56
Figure 34: A view of the phase behavior at 10 mass % (a, b) comparison with 0.01 mass % (c) ammonia in the aqueous phase [229]	57

Figure 35: Chemical structure of (a) oleic acid, (b) α -cyclodextrin (CD), and (c) organic to aqueous phase transfer process of oleic acid modified nanoparticles when using α -CD as surface modifying agent [232].....	58
Figure 36: Photographs of a two-phase mixture of iron oxide nanoparticles (a) before and (b) after phase transfer, and (c) aqueous suspension after centrifuge. The top layers were hexane and bottom layers were α -CD aqueous solutions [232]	59
Figure 37: Possible exposure pathways of NPs to the human body, different affected organs, and associated diseases from epidemiological, <i>in vivo</i> and <i>in vitro</i> studies are shown [237].....	60
Figure 38: Potential toxic effects of superparamagnetic iron oxide nanoparticles due to the ROS generation [239].....	61
Figure 39: Step-to-step NPs-based bench-to-bedside approval procedure in humans. Important deliberations of each approval rout are highlighted [244].....	62
Figure 40: A diagram illustrating the LaMer nucleation and growth model [262]	65
Figure 41: Dependence of the cluster free energy, ΔG , on the cluster radius, r . The curve has a maximum free energy ΔG at a critical cluster size, r^* , which defines the first stable particles – the nuclei	67
Figure 42: Graphical demonstration of interaction energies in the approach of the particles.....	68
Figure 43: The role of two paramount stabilization types of nanoparticles: most important properties and the relevant forms, influencing factors, and applications are illustrated [268]	69
Figure 44: Electrical double layer representation: ionic concentration and potential differences as a function of distance from the charged surface	70
Figure 45: Zeta potential measurement [270]	71
Figure 46: Experimental set-up (1- three-necked round bottom glass reactor, 2- overhead mechanical stirrer, 3- thermostatic water bath).....	73
Figure 47: Schematic representation of one well: the portion of each solution over C6 glioma cells is shown.....	76
Figure 48: Working principle of the dynamic light scattering	81
Figure 49: Schematic illustrations of both TEM and SEM components [279]	83
Figure 50: Vibrating sample magnetometer setup [281].....	84
Figure 51: Working principle of the spectrophotometer [282].....	85
Figure 52: Cumulative particle size distribution $Q_0(d)$ of Tween 80-SPIO-NPs for the reaction temperatures between 40 °C to 100 °C at a Fe^{3+}/Fe^{2+} molar ratio of 2:1 and 400 rpm	86
Figure 53: Effect of temperature on the median ($d_{50, 0}$) particle size of Tween 80-SPIO-NPs.....	87
Figure 54: Change of zeta potential with the solution pH of Tween 80-SPIO-NPs	87
Figure 55: Cumulative particle size distribution $Q_0(d)$ of Tween 80-SPIO-NPs at stirring velocities between 400 rpm to 1000 rpm (1.21 m/s to 3.03 m/s stirrer tip speed) with a Fe^{3+}/Fe^{2+} molar ratio of 2:1 and at 40 °C.....	88
Figure 56: Effect of stirring velocity on the median ($d_{50, 0}$) particle size of Tween 80-SPIO-NPs.....	89
Figure 57: Variation of zeta potential with the solution pH of Tween 80-SPIO-NPs.....	89

Figure 58: Cumulative particle size distribution $Q_0(d)$ of Tween 80-SPIO-NPs for the solution pH 11.0 to 12.30 with a Fe^{3+}/Fe^{2+} molar ratio of 2:1, 400 rpm, and at 40 °C	90
Figure 59: Variation of zeta potential with the solution pH of Tween 80-SPIO-NPs.....	91
Figure 60: Effect of the solution pH on the median ($d_{50,0}$) particle size of Tween 80-SPIO-NPs.....	91
Figure 61: Cumulative particle size distribution $Q_0(d)$ of Tween 80-SPIO-NPs for Fe^{3+}/Fe^{2+} molar ratios 1.25:1 to 2:1 at 40 °C and 400 rpm	92
Figure 62: Change of zeta potential with the solution pH for different Fe^{3+}/Fe^{2+} molar ratios	93
Figure 63: Effect of Fe^{3+}/Fe^{2+} molar ratios on the median ($d_{50,0}$) particle size of Tween 80-SPIO-NPs.....	93
Figure 64: TEM images of Tween 80 coated SPIO-NPs (a) SPIO-NPs at 40 °C (b) SPIO-NPs at 1000 rpm (3.03 m/s stirrer tip speed) (c) SPIO-NPs at pH 11 (d) SPIO-NPs at Fe^{3+}/Fe^{2+} molar ratio = 2:1.....	94
Figure 65: Cumulative particle size distribution $Q_0(d)$ of Dextran 70,000-SPIO-NPs for the reaction temperatures between 40 °C to 100 °C at a Fe^{3+}/Fe^{2+} molar ratio of 2:1 and 400 rpm	94
Figure 66: Effect of temperature on the median ($d_{50,0}$) particle size of Dextran 70,000-SPIO-NPs.....	95
Figure 67: Cumulative particle size distribution $Q_0(d)$ at stirring velocities between 400 rpm to 1000 rpm (1.21 m/s to 3.03 m/s stirrer tip speed) with a Fe^{3+}/Fe^{2+} molar ratio of 2:1 and at 40 °C.....	96
Figure 68: Effect of stirring velocity on the median ($d_{50,0}$) particle size of Dextran 70,000-SPIO-NPs.....	97
Figure 69: Cumulative particle size distribution $Q_0(d)$ of Dextran 70,000-SPIO-NPs for the solution pH 8.45 to 9.56 with a Fe^{3+}/Fe^{2+} molar ratio of 2:1, 400 rpm, and at 40 °C	97
Figure 70: Effect of the solution pH on the median ($d_{50,0}$) particle size of Dextran 70,000-SPIO-NPs.....	98
Figure 71: Cumulative particle size distribution $Q_0(d)$ of Dextran 70,000-SPIO-NPs for Fe^{3+}/Fe^{2+} molar ratios 1.25:1 to 2:1 at 40 °C and 400 rpm	99
Figure 72: Effect of Fe^{3+}/Fe^{2+} molar ratios on the median ($d_{50,0}$) particle size of Dextran 70,000-SPIO-NPs	100
Figure 73: TEM micrographs of Dextran 70,000 coated SPIO-NPs (a) SPIO-NPs at 40 °C (b) SPIO-NPs at 1000 rpm (3.03 m/s stirrer tip speed) (c) SPIO-NPs at pH 9.56 (d) SPIO-NPs at Fe^{3+}/Fe^{2+} molar ratio = 2:1	100
Figure 74: Cumulative particle size distribution $Q_0(d)$ of DEAE-Dextran-SPIO-NPs for the reaction temperatures between 40 °C to 100 °C at a Fe^{3+}/Fe^{2+} molar ratio of 2:1 and 400 rpm	101
Figure 75: Effect of temperature on the median ($d_{50,0}$) particle size for DEAE-Dextran coated SPIO-NPs.....	102
Figure 76: Change of zeta potential with the solution pH for DEAE-Dextran coated SPIO-NPs.....	102
Figure 77: Cumulative particle size distribution $Q_0(d)$ of DEAE-Dextran-SPIO-NPs at stirring velocities between 400 rpm to 1000 rpm (1.21 m/s to 3.03 m/s stirrer tip speed) with a Fe^{3+}/Fe^{2+} molar ratio of 2:1 and at 40 °C.....	103

Figure 78: Effect of stirring velocity on the median ($d_{50, 0}$) particle size for DEAE-Dextran-SPIO-NPs	104
Figure 79: Effect of the solution pH on zeta potential for DEAE-Dextran-SPIO-NPs	104
Figure 80: Cumulative particle size distribution $Q_0(d)$ of DEAE-Dextran-SPIO-NPs for the solution pH 8.49 to 9.45 with a Fe^{3+}/Fe^{2+} molar ratio of 2:1, 400 rpm, and at 40 °C	104
Figure 81: Effect of the solution pH on the median ($d_{50, 0}$) particle size for DEAE-Dextran coated SPIO-NPs	105
Figure 82: Effect of the solution pH on zeta potential for DEAE-Dextran coated SPIO-NPs	105
Figure 83: Cumulative particle size distribution $Q_0(d)$ of DEAE-Dextran-SPIO-NPs for Fe^{3+}/Fe^{2+} molar ratios 1.25:1 to 2:1 at 40 °C and 400 rpm	106
Figure 84: Effect of different Fe^{3+}/Fe^{2+} molar ratios on the median ($d_{50, 0}$) particle size for DEAE-Dextran coated SPIO-NPs	107
Figure 85: Effect of the solution pH on zeta potential for DEAE-Dextran coated SPIO-NPs	107
Figure 86: TEM micrographs of DEAE-Dextran coated SPIO-NPs (a) SPIO-NPs at 40 °C (b) SPIO-NPs at 1000 rpm (3.03 m/s stirrer tip speed) (c) SPIO-NPs at pH 8.49 (d) SPIO-NPs at Fe^{3+}/Fe^{2+} molar ratio = 2:1	108
Figure 87: The effects of Tween 80-SPIO-NPs on the cell viability of C6 glioma cells determined by MTT assay	110
Figure 88: The effects of Tween 80-SPIO-NPs labelled with rhodamine 123 on the cell viability of C6 glioma cells determined by MTT assay	111
Figure 89: The effects of Tween 80-SPIO-NPs labelled with propidium iodide on the cell viability of C6 glioma cells determined by MTT assay	111
Figure 90: Intracellular localization of Tween 80 coated SPIO-NPs in C6 glioma cells is shown by confocal microscopic images after 24 hours of incubation (a) when SPIO-NPs were labelled with rhodamine 123, (c) when SPIO-NPs were labelled with propidium iodide, (b) and (d) zoom into cell labelled with an asterisk in (a) and (c) to illustrate the dotted labelling (yellow arrows) and gap (white arrows) for both rhodamine 123 and propidium iodide respectively	112
Figure 91: The effects of Dextran 70,000-SPIO-NPs on the cell viability of C6 glioma cells determined by MTT assay	113
Figure 92: The effects of Dextran 70,000-SPIO-NPs labelled with rhodamine 123 on the cell viability of C6 glioma cells determined by MTT assay	114
Figure 93: The effects of Dextran 70,000-SPIO-NPs labelled with propidium iodide on the cell viability of C6 glioma cells determined by MTT assay	114
Figure 94: Intracellular localization of Dextran 70,000 coated SPIO-NPs in C6 glioma cells is shown by confocal microscopic images after 24 hours of incubation (a) when SPIO-NPs were labelled with rhodamine 123, (c) when SPIO-NPs were labelled with propidium iodide, (b) and (d) zoom into cell labelled with an asterisk in (a) and (c) to illustrate the dotted labelling (yellow arrows) and gap (white arrows) for both rhodamine 123 and propidium iodide respectively	116
Figure 95: The effects of DEAE-Dextran-SPIO-NPs on the cell viability of C6 glioma cells determined by MTT assay	117

Figure 96: The effects of DEAE-Dextran-SPIO-NPs labelled with rhodamine 123 on the cell viability of C6 glioma cells determined by MTT assay.....	118
Figure 97: The effects of DEAE-Dextran-SPIO-NPs labelled with propidium iodide on the cell viability of C6 glioma cells determined by MTT assay.....	118
Figure 98: Intracellular localization of DEAE-Dextran coated SPIO-NPs in C6 glioma cells is shown by confocal microscopic images after 24 hours of incubation (a) when SPIO-NPs were labelled with rhodamine 123, (c) when SPIO-NPs were labelled with propidium iodide, (b) and (d) zoom into cell labelled with an asterisk in (a) and (c) to illustrate the dotted labelling (yellow arrows) and gap (white arrows) for both rhodamine 123 and propidium iodide respectively	120
Figure 99: The effect of rhodamine 123 on the cell viability of C6 glioma cells determined by MTT assay	122
Figure 100: The effect of propidium iodide on the cell viability of C6 glioma cells determined by MTT assay	123
Figure 101: Retrograde labelling of retinal ganglion cells by injection of fluorescently labelled SPIO-NPs into the superior colliculus. The focused shows the position of a contact lens which is directly placed on the rat's eye (left). Internal structure of retina is shown (right) [106], [294]	124
Figure 102: Photographs of control animal experiments where animals received the only phosphate buffered saline intravitreally: (a) it can be clearly seen that no fluorescence visibly <i>in vivo</i> cellular images appeared of the retina of animals, (b) no any signal in the <i>ex vivo</i> retina (whole mount), (c) the whole mount is imaged after incubation with Hoechst 33342, which is selective maker of nuclei.....	124
Figure 103: Repeated clear and bright imaging of the same fluorescent labelled ganglion cells when animals received 500 µg/ml concentration dose intravitreally of Dextran coated SPIO-NPs labelled with rhodamine 123: (a) left eye image of animal, (b) right eye image of animal, (c) no any signal in the <i>ex vivo</i> retina (whole mount), (d) the whole mount is imaged after incubation with Hoechst 33342, which is selective maker of nuclei.....	125
Figure 104: Repeated clear and bright imaging of the same fluorescent labelled ganglion cells when animals received 31 µg/ml concentration dose intravitreally of Dextran coated SPIO-NPs labelled with rhodamine 123: (a) left eye image of animal, (b) right eye image of animal, (c) no any signal in the <i>ex vivo</i> retina (whole mount), (d) the whole mount is imaged after incubation with Hoechst 33342, which is selective maker of nuclei.....	126

List of tables

Table 1: Physical and magnetic properties of iron oxide [7]	5
Table 2: Tunable magnetic properties important for biomedical applications	14
Table 3: Continuous developments of targeted drug delivery systems since 1950 [75]	19
Table 4: The barriers to overcome in the 3G drug delivery systems [75].....	20
Table 5: Comparison of different characteristic features of the iron oxide nanoparticles fabricated through different methods.....	44
Table 6: Polymers used for polymeric nanoparticles.....	50
Table 7: Chemicals used.....	72
Table 8: Reaction characteristics at temperatures 40 °C to 100 °C	87
Table 9: Reaction characteristics at stirring velocities from 400 rpm to 1000 rpm (1.21 m/s to 3.03 m/s stirrer tip speed).....	89
Table 10: Reaction characteristics at various solution pH.....	90
Table 11: Reaction characteristics at different Fe ³⁺ /Fe ²⁺ molar ratios	93
Table 12: Reaction characteristics at temperatures between 40 °C and 100 °C	95
Table 13: Reaction characteristics at stirring velocities between 400 rpm to 1000 rpm (1.21 m/s to 3.03 m/s stirrer tip speed).....	96
Table 14: Reaction characteristics at pH 8.45 to 9.56.....	98
Table 15: Reaction characteristics at different Fe ³⁺ /Fe ²⁺ molar ratios	99
Table 16: Reaction characteristics at different temperatures in case of coating with DEAE-Dextran	101
Table 17: Reaction characteristics at different stirring velocities between 400 rpm to 1000 rpm (1.21 m/s to 3.03 m/s stirrer tip speed) for DEAE-Dextran- SPIO-NPs.....	103
Table 18: Reaction characteristics at pH from 8.49 to 9.45 for DEAE-Dextran coated SPIO-NPs	105
Table 19: Reaction characteristics at different Fe ³⁺ /Fe ²⁺ molar ratios for DEAE- Dextran coated SPIO-NPs	107
*Table 20: Variations of the experiments (using kinematic viscosity $\nu = 6.10^{-7}$ m ² /s)	108

Acronyms

AAS	Atomic Absorption Spectroscopy
ATCC	American Type Culture Collection
BBB	Blood-Brain Barrier
BHAB	Benzyltrimethylhexadecylammonium Bromide
BSC	Biological Safety Cabinet
CCD	Charged Coupled Device
CD	α -Cyclodextrin
CNS	Central Nervous System
CTAB	Cetyltrimethylammonium Bromide
DCM	Dichloromethane
DDAB	Didodecyldimethylammonium Bromide
DDSs	Drug Delivery Systems
DI	Deionized
DLS	Dynamic Light Scattering
DMSA	Dimercaptosuccinic Acid
DMSO	Dimethyl Sulfoxide
DNA	Deoxyribonucleic Acid
EDTA	Ethylene Diamine Tetraacetic Acid
FC	Field-Cooled
FCC	Face Centered Cubic
FDA	Federal Drug Administration
FITC	Fluorescein Isothiocyanate
FTIR	Fourier Transmission Infrared
GMP	Good Manufacturing Practice
ICON	<i>In vivo</i> Confocal Neuroimaging
IEP	Isoelectric Point
IONPs	Iron Oxide Nanoparticles
LCD	Liquid Crystal Display
LDH	Lactate Dehydrogenase
LR	Living Radical
MEA	Monoethanolamine
MHT	Magnetic Hyperthermia
MNPs	Magnetic Nanoparticles
MPI	Magnetic Particle Imaging
MPS	Magnetic Particle Spectroscopy
MRI	Magnetic Resonance Imaging
NMR	Nuclear Magnetic Resonance
NPs	Nanoparticles
OA	Oleic Acid
OD	Optical Density
OTAB	Octadecyltrimethylammonium Bromide
PAA	Poly(Acrylic Acid)
PBCA	Poly (butylcyanoacrylate)

PBS	Phosphate Buffered Saline
PCS	Photon Correlation Spectroscopy
PDI	Polydispersity Index
PECL	Poly (ϵ -caprolactone)
PEG	Polyethylene Glycol
PHCA	Polyhexalcyanoacrylate
PI	Propidium Iodide
PICA	Poly (Isobutylcyanoacrylates)
PLA	Poly (Lactic Acid)
PLGA	Poly (Lactide-co-Glycolide Acid)
PMA	Polymethylacrylate
PMMA	Polymethylmethacrylate
PSD	Particle Size Distribution
PTFE	Polytetrafluoroethylene
PVA	Poly Vinyl Alcohol
PVP	Poly(Vinyl Pyrrolidone)
QDs	Quantum Dots
RES	Reticuloendothelial System
RESS	Rapid Expansion of Supercritical Solution
RF	Radio Frequency
RGCs	Retinal Ganglion Cells
ROS	Reactive Oxygen Species
RPM	Revolutions Per Minute
SC	Superior Colliculi
SCF	Super Critical Fluid
SDS	Sodium Dodecyl Sulfate
SEM	Scanning Electron Microscopy
SPIO-NPs	Superparamagnetic Iron Oxide Nanoparticles
TEM	Transmission Electron Microscopy
USPIO-NPs	Ultra-small Superparamagnetic Iron Oxide Nanoparticles
UV	Ultraviolet
UVS	Ultraviolet Spectroscopy
VSM	Vibrating Sample Magnetometer
XRD	X-Ray Diffraction
ZFC	Zero-Field Coolant
ZP	Zeta Potential

1 Introduction

During the last more than two decades, terms with prefix “nano” have been increasingly appeared in the scientific vocabulary, as, for example, nanoparticles, nanostructure, nanotechnology, nanomaterials, nanocluster, nanochemistry, nanocolloids, nanoreactors, and many more. New series of journals came into being particularly to address these areas. Further, “nano-specified” institutes, chairs and laboratories were found along with numerous conferences are held during this period. This development is associated with the globally increasing interest of researchers in nano-objects and is due to the nano-systems’ unique and versatile physical and chemical properties, so-called quantum size effects. The prefix comes from the ancient Greek ‘νᾶνος’ through the Latin ‘nanus’ meaning literally dwarf and by extension, very small. The growing field of nanotechnology allows the scientists, engineers, chemists, as well as physicists to work at a molecular and cellular level for their important and significant uses in drug delivery approaches, imaging techniques, and sensor technology, where nanoparticles need to be injected inside the body [1]–[4]. Especially particles of 1-100 nm in size with defined characteristics are used in biomedical engineering [4], [5] and according to some reports, nanoscale materials, like metallic gold was serving humans for different medical purposes already since 2500 B.C. [4]. Cobalt, nickel, iron, and iron oxides such as maghemite ($\gamma\text{-Fe}_2\text{O}_3$) and magnetite (Fe_3O_4) nanoparticles have been widely considered as the most suitable materials for medical applications due to their superparamagnetic property. Among these, iron oxide (along with its different types) is considered as one of the most important metal oxide for technological applications and it has the advantage of being widespread in nature because oxygen, hydrogen, and iron are abundantly present in the earths’ crust. Sixteen pure phases of iron oxides, i.e., oxides, hydroxides or oxyhydroxides are known to date [6]–[8]. These are:

Oxides:

- Iron(II) oxide, wüstite (FeO)
- Iron(II, III) oxide, magnetite (Fe_3O_4)
- Iron(III) oxide (Fe_2O_3)
 - Alpha phase, hematite ($\alpha\text{-Fe}_2\text{O}_3$)
 - Beta phase ($\beta\text{-Fe}_2\text{O}_3$)
 - Gamma phase, maghemite ($\gamma\text{-Fe}_2\text{O}_3$)
 - Epsilon phase ($\varepsilon\text{-Fe}_2\text{O}_3$)

Hydroxides:

- Iron (II) hydroxide ($\text{Fe}(\text{OH})_2$)
- Iron (III) hydroxide ($\text{Fe}(\text{OH})_3$), (bernalite)

Oxides/hydroxide:

- Goethite ($\alpha\text{-FeOOH}$)
- Akaganéite ($\beta\text{-FeOOH}$)
- Lepidocrocite ($\gamma\text{-FeOOH}$)
- Feroxyhyte ($\delta\text{-FeOOH}$)

- Ferrihydrite ($\text{Fe}_5\text{HO}_8 \cdot 4\text{H}_2\text{O}$ approx.), or $5\text{Fe}_2\text{O}_3 \cdot 9\text{H}_2\text{O}$, better recast as $\text{FeOOH} \cdot 0.4\text{H}_2\text{O}$
- High-pressure FeOOH
- Schwertmannite (ideally $\text{Fe}_8\text{O}_8(\text{OH})_6(\text{SO}) \cdot n\text{H}_2\text{O}$ or $\text{Fe}^{3+}_{16}\text{O}_{16}(\text{OH}, \text{SO}_4)_{12-13} \cdot 10-12\text{H}_2\text{O}$)

Iron (III) oxide (Fe_2O_3) is an inorganic compound and among the three core oxides of iron with two other iron (II) oxides (FeO), which is rare, and Iron (II, III) oxide, (Fe_3O_4) which is a naturally occurring substance as a mineral magnetite.

1.1 Superparamagnetic iron oxide nanoparticles

Superparamagnetic iron oxide nanoparticles (SPIO-NPs), such as magnetite Fe_3O_4 , are among the most frequently used biocompatible particles system in pharmacy and biomedicine. Based on their physical properties (such as particle size), these nanoparticles (NPs) have numerous advantages in diagnostics and therapeutical applications (selective release of drugs, a better and enhanced pharmaceutical kinetics and dynamics, local medication). Superparamagnetic nanoparticles are a very special class of engineered nanoparticles that can be influenced by an external magnetic field when applied. Various industrial and biomedical applications depend on the stability of SPIO-NPs under a number of different conditions. SPIO-NPs are the magnetic nanoparticles having a size around 10-20 nm show a better performance in various applications. Above the temperature so-called blocking temperature, each of nanoparticles behaves as a single magnetic domain and thus shows superparamagnetic behavior. Finite-size effects and surface effects are considered as two vital issues in the magnetic properties of nanoparticles for their different special features [5]. Some studies show that magnetic nanoparticles (MNPs) with size 10-100 nm have a significant use in different biomedical applications due to their effective surface areas, high stability in suspension, and infiltration by the reticuloendothelial system (RES). Especially, SPIO-NPs size in a superparamagnetic regime has an influence in various biomedical applications. Different challenges which are associated with the MNPs are core and coating. Chemical composition, synthesis method, and size are affecting the magnetic properties of SPIO-NPs [9]. Magnetic nanoparticles are categorized into three major groups namely; diamagnetic, paramagnetic, and ferromagnetic. A detailed description of these magnetic categories is presented in chapter 2.

Magnetic nanoparticles consist on cations, e.g., Fe, Ni, Co, Cr, Gd, and their oxides, such as magnetite (Fe_3O_4), maghemite ($\gamma\text{-Fe}_2\text{O}_3$), hematite ($\alpha\text{-Fe}_2\text{O}_3$), cobalt ferrite (Fe_2CoO_4), chromium dioxide (CrO_2), and gadolinium oxide (Gd_2O_3) [10]. The present doctoral dissertation is limited only to the magnetite (Fe_3O_4) due to its excellent magnetic properties especially in drug delivery to the blood-brain barrier (BBB).

1.2 Coating of nano-scaled magnetic particles

Coating of fabricated SPIO-NPs by different organic or inorganic materials is a very next step. Coating with some suitable polymers produces useful impacts for transport of SPIO-NPs to the blood-brain barrier (BBB). Coating of SPIO-NPs is very crucial because of:

- Aggregation of naked particles must be avoided;
- Improving the colloidal and dispensability of SPIO-NPs;
- Protection of SPIO-NPs from oxidation;
- Increases the blood circulation time by avoiding the clearance by the reticuloendothelial system of our body;
- Makes the SPIO-NPs biocompatible and minimize the nano-specified interactions which lead to toxicity reduction.

Uniform coating of SPIO-NPs can be achieved either during their synthesis process or after the synthesis. In both cases, the successful uniform coating has been reported [11]. In the present research, a coating of SPIO-NPs was done by (a) chemical compounds for “masking” the magnetite NPs to overcome the BBB-Tween 80, Dextran 70,000, DEAE-Dextran (b) fluorescence markers-rhodamine 123, and propidium iodide were used to label the synthesized SPIO-NPs.

1.3 Iron oxide nanoparticles

Iron oxide has a superior biocompatibility as compared to other magnetic materials, based on oxides or on pure metals and therefore; the most investigated material for biomedical uses. Among its several types, hematite ($\alpha\text{-Fe}_2\text{O}_3$), maghemite ($\gamma\text{-Fe}_2\text{O}_3$) and magnetite (Fe_3O_4) are most common and fulfill the requirements for various biomedical applications which need a sufficiently high magnetic moment, chemical stability in physiological conditions and most importantly low toxicity, facile and cheap synthetic techniques for the synthesis of these important materials. For different biomedical applications, iron oxide performance is affected by various factors such as their degree of atomic orders, or in simple words their degree of crystallinity and their dispersity in terms of size and shape of the nanoparticles. From their physical and chemical properties point of view, iron oxide nanoparticles (IONPs) differ with their atoms and bulk counterparts [12], [13]. Mainly, biomedical applications depend on the size and composition of the magnetic nanoparticles which further subdivided into ultra-small superparamagnetic iron oxide nanoparticles (USPIO-NPs) having size below 10 nm and superparamagnetic iron oxide nanoparticles (SPIO-NPs) with a size range from 10-30 nm which exhibit superparamagnetism [14].

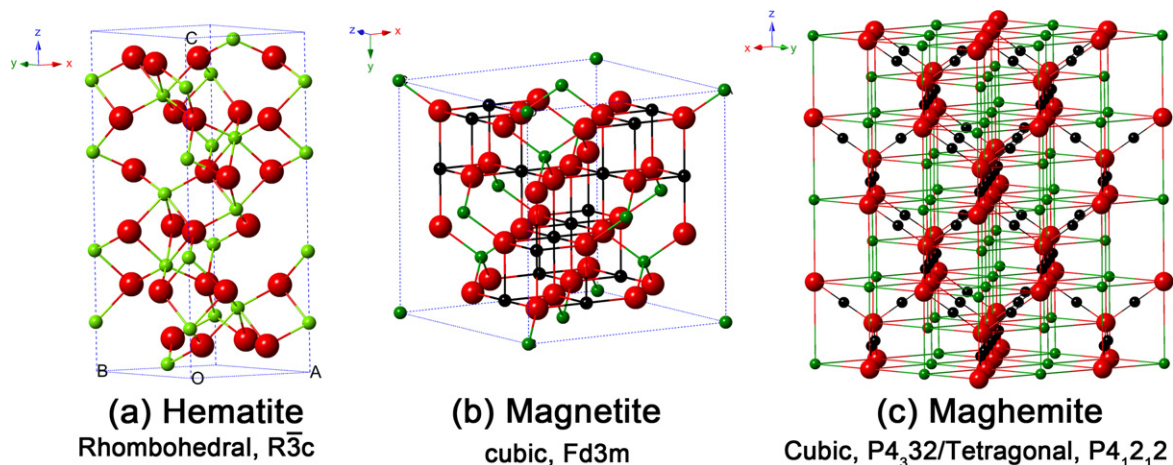


Figure 1: View of crystal structure and crystallographic data of the hematite, magnetite, and maghemite (the black ball is denoting for Fe^{2+} , the green ball is dedicating for Fe^{3+} and the red ball is representing O^{2-}) [15]

1.3.1 Hematite ($\alpha\text{-Fe}_2\text{O}_3$)

Hematite ($\alpha\text{-Fe}_2\text{O}_3$) is an *n*-type semiconductor and weakly ferromagnetic under ambient conditions and considered as a most stable oxide of iron. It has high resistance to corrosion, biodegradability, high stability, environmentally friendly, low toxicity, and also of low cost; therefore, is widely used in catalysts, pigments, solar cells, hydrocarbons and carbon monoxide gas sensors, water treatment, and biomedicines. A thorough research has been conducted for its use as starting material in the synthesis of maghemite ($\gamma\text{-Fe}_2\text{O}_3$) and magnetite (Fe_3O_4) [15]–[19]. Special attention already has been paid to explore the high-pressure behavior of hematite mainly due to their geophysical interest and also unclear role of Fe^{3+} ions (in their crystal structure) in nature and dynamics of the earth's lowest mantle [20]. As shown in figure 1(a), Fe^{3+} ions occupy two-thirds of the octahedral sites that are confined by nearly ideal hexagonal close-packed 'O' lattice.

1.3.2 Magnetite (Fe_3O_4)

Magnetite is composed of Fe (II) and Fe (III) oxides and denoted by Fe_3O_4 . It is a part of "spinel" structure minerals which have general formulation AB_2X_4 , A, B can be divalent, trivalent, or quadrivalent cations [21]. Diverse applications and unusual properties make the magnetite a remarkable material. A million tons per year magnetite iron ore are used for the production of steel. Highly pure magnetite is used as feedstock to produce various iron-based chemicals and a famous use of it's as a catalyst in the ammonia synthesis. Adoption in a number of new applications as speciality filler in plastics, rubber, and coatings is increased during over last two decades [22]. As shown in figure 1(b), magnetite (Fe_3O_4) has a spinel structure which is face-centered cubic (FCC). The unit cell of (Fe_3O_4) consists of 32 O^{2-} ions that are close-packed along the direction of length $a = 0.839$. A cubic close-packed array of O^{2-} ions are found in the inverse spinel structure. However, half of the octahedral sites are occupied by Fe^{2+} ions and the remaining octahedral and the

tetrahedral sites are evenly split by Fe³⁺ ions. In the stoichiometric equation, the molar ratio of Fe³⁺ and Fe²⁺ is 0.5 and its divalent ions can mutually replace by other divalent ions such as Co, Zn, and Mn etc. So, Fe₃O₄ can be both an *n*-type and a *p*-type semiconductor [15].

1.3.3 Maghemite (γ -Fe₂O₃)

Among different magnetic material, maghemite (γ -Fe₂O₃) is a promising class of magnetic iron oxide material and due to its excellent transparent properties, it is considered as an ideal element for luminescent fabrication and magnetic dual functional nano-composites [23]. The name of maghemite was first proposed in 1927. Maghemite is very similar to the magnetite in their spinal structure and composition and also shows high magnetization and biocompatibility characteristics [24]. Figure 1(c) shows the cubic structure of maghemite (γ -Fe₂O₃) with each unit of maghemite contains 32 O²⁻ ions, 21 $\frac{1}{3}$ Fe³⁺ ions and 2 $\frac{1}{3}$ vacancies [15]. Maghemite is a ferromagnetic material in nature [25]. It transforms into hematite (α -Fe₂O₃) and also losses its magnetization with the rise in temperature at about 300 °C in a poorly oxidized sample and in a better-oxidized sample, it may rise higher than 400 °C [26].

Physical and magnetic properties of these iron oxides are summarized in the following table 1.

Table 1: Physical and magnetic properties of iron oxide [7]

Property	Oxide		
	Hematite	Magnetite	Maghemite
Molecular formula	α -Fe ₂ O ₃	Fe ₃ O ₄	γ -Fe ₂ O ₃
Density (g/cm ³)	5.26	5.18	4.87
Melting point (°C)	1350	1583-1597	-
Hardness	6.5	5.5	5
Type of magnetism	Weakly ferromagnetic or antiferromagnetic	Ferromagnetic	Ferrimagnetic
Curie temperature (K)	956	850	820-986
M _s at 300 K (A·m ² /kg)	0.3	92-100	60-80
Standard free energy of formation ΔG_f° (kJ/mol)	-742.7	-1012.6	-711.1
Crystallographic system	Rhombohedral, hexagonal	Cubic	Cubic or tetrahedral
Structural type	Corundum	Inverse spinel	Defect spinel
Space group	R3c (hexagonal)	Fd3m	P4 ₃ 32 (cubic); P4 ₁ 2 ₁ 2 (tetragonal)
Lattice parameter (mm)	$\alpha = 0.5034$, $c = 1.375$ (hexagonal) $\alpha_{Rh} = 0.5427$ $\alpha = 55.3^\circ$ (rhombohedral)	$\alpha = 0.8396$	$\alpha = 0.83474$ (cubic); $\alpha = 0.8347$, $c = 2.501$ (tetragonal)

1.4 Potential applications of magnetic iron oxide nanoparticles

1.4.1 Industrial applications

Magnetite (Fe_3O_4) is the most prominent among other magnetic oxides and has been attracting intensive interest in recent years because of its unique magnetic and electric properties and is widely used for industrial applications, such as ceramics, catalysts, energy storage, and magnetic data storage [27], recording media, pigments, magnetic fluids [28], dyes, in cosmetic industry for ultraviolet (UV) protection (organic and inorganic sub-micron UV filters), organic color filters for liquid crystal display (LCD) technology, as solar cell constituents [29], bioengineering, biosensors and magnetic refrigeration, color imaging, bioprocessing and high grade magnetic separation [30], photocatalysis [31], in Lithium-ion batteries, and in metal chemo-sensors [32]. Due to extensively use of magnetic nanoparticles in various types of industrial processes, environmental challenges are also increasing with this boom in nanotechnology. Their use in pollutant removal or toxicity mitigation is very promising. For instance, different researchers show the use of maghemite ($\gamma\text{-Fe}_2\text{O}_3$) and magnetite (Fe_3O_4) nanoparticles for heavy metals removal from the contaminated water. Contaminants desorption by reusing the magnetic nanoparticles and regaining the removal capacity has already proven a successive treatment. This may lead towards to sustainable treatment process. These environmental applications of magnetic nanoparticles are simply not due to their large removal capacity, fast kinetics, and high reactivity for contaminant removal because of their intensively small size but strongly depend upon their magnetic properties and these magnetic properties make the magnetic separation process a cost-effective [33], [34]. For purification of wastewater that does not needs the generation of secondary waste, recycling of material is highly recommended and magnetic nanoparticles offer this solution [35]. Although, a comprehensive research has been done still more research is needed in this area because water and wastewater have intensive impacts on human health and also related to environmental issues. Nanoparticles technology being a low-cost production and their easy availability is the most prominent among other techniques to solve the problems associated with the wastewater pollution by using nanoparticles as adsorbent materials [36].

1.4.2 Biomedical applications

The potential applications of magnetic nanoparticles (MNPs) for biomedical or pharmaceutical purposes rely on the synthesis of high-quality materials, mainly regarding crystallinity and magnetic response. In this perspective, it is essential to minimize the polydispersity and heterogeneity of the particles and to maximize their magnetic response. For instance, MNPs for drug delivery [37]–[39] and contrast agents for magnetic resonance imaging must exhibit a high magnetic response to the external fields and should have functionalized biocompatible surface [40]. Following recent advances in nanotechnology, the composition, size, morphology, and the surface chemistry of particles can be tailored, which in combination with their

nanoscale magnetic properties make them highly attractive for biomedicine. Magnetic (Fe_3O_4) nanoparticles are particularly being used in various biomedical applications such as cell separation and cellular therapy involving cell labelling and targeting, tumor hyperthermia, tissue repair, targeted drug delivery, magnetic resonance imaging (MRI) [41], [42] and hyperthermia for cancer treatment [43]–[45]. However, due to the highest saturation magnetization, pure metals are highly toxic and extremely sensitive to oxidation; therefore, without a suitable surface treatment, such magnetic nanoparticles from pure metals are not suitable for biomedical applications. In contrast, iron oxides are less sensitive to oxidation and therefore, can give a stable magnetic response [44]. A short hierarchy of these industrial and biomedical applications of magnetic nanoparticles is shown in figure 2. A complete description with a physical background of these biomedical/pharmaceutical applications is given in a proceeding chapter 2.

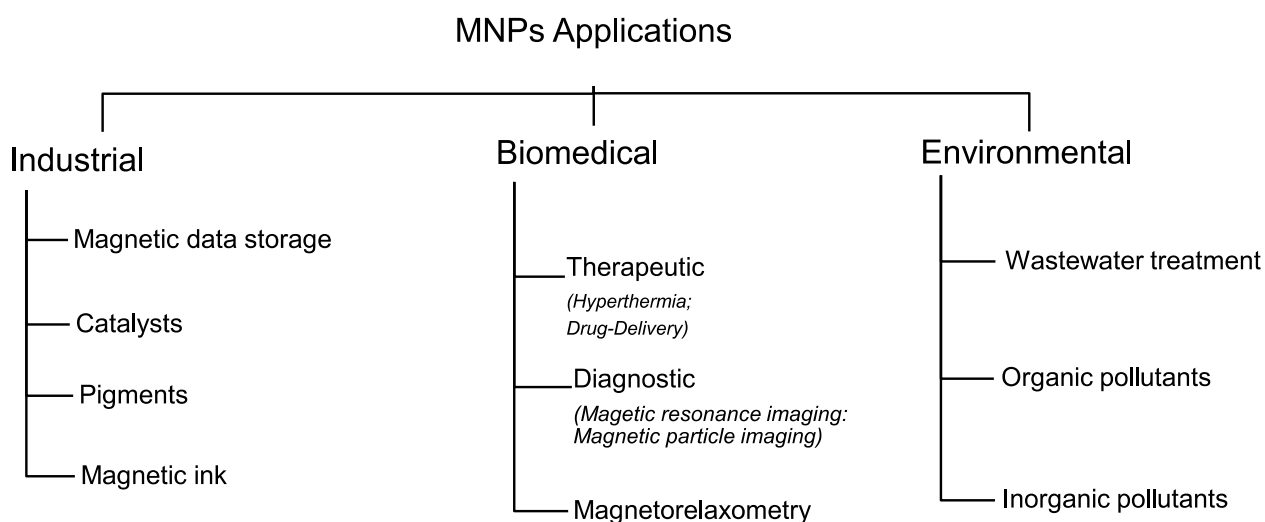


Figure 2: Potential applications of magnetic nanoparticles in multidisciplinary fields

1.5 Challenges in the field of magnetic nanoparticles

Recent advancement in the nanoparticle technology opens a door for various applications of a large number of fabricated nanoparticles. Biocompatible superparamagnetic iron oxide nanoparticles have size-dependent magnetic characteristics. Typically, single domain particles have a primary particles size between 3 to 15 nm. Multi-domain agglomerates have particles size up to several hundred of nanometers. In fact, these particles have a high magnetizability (the integral magnetizability can be calculated by multiplication of each primary particle of the aggregate). In contrast, larger single domain particles (< 126 nm) have the attraction that the magnetizability scales with d^3 (volume proportional magnetizability), but they still keep the switchable superparamagnetic properties as well as the stability of the suspension. These not comprehensively explored processes are built up by complexly connected micro-processes. A key element to using superparamagnetic iron oxide nanoparticles in biomedical applications is their magnetic response, and also requires a complete characterization of their magnetic

behavior. Over 500 consumer products containing nanoparticles related materials are in use today. Further, the United States federal drug administration (FDA) has already approved 12 nanomedicines containing magnetic iron oxide nanoparticles mainly for *in vivo* administration and a series of new “nano-systems” are in pipeline for their approval; therefore, the design of such magnetic nanoparticles will be of significantly crucial [46]–[48]. Clearly, the toxicity of magnetic nanoparticles is one of the most debatable issues that should be properly investigated. Importantly, nanoparticle toxicity depends on a number of factors like dose, chemical composition, a method of administration, particle size, biodegradability, surface chemistry, and shape, just to name a few [44]. These factors need to be assessed for the development of SPIO-NPs with optimum properties for the BBB drug delivery.

1.6 Objectives of the present work

The objectives of the present doctoral work were to develop theoretically based descriptions of the migration process for use in biomedical applications (especially in drug delivery) with simplified assumptions used in mechanical process engineering (diffusion, convection, and carrier controlled migration). Analysis and optimization of the production process of biocompatible SPIO-NPs which characterized by the features: (a) the particle size of the SPIO-NPs between 10-125 nm (adjustable through suitable choice of process and apparatus parameters in the synthesis) in a liquid phase, (b) approaching monodispersity (narrow size distribution), biocompatibility of coating binding of pharmaceutical agents and their physiological parameters in a liquid phase, SPIO-NPs should have a positive and a negative zeta potential; anionic, non-ionic, or cationic surfactants with controlled particles size distribution, composition, and morphology, (c) the modifications and functionalization of particles core and surface aiming SPIO-NPs passing the blood-brain barrier (BBB) and transporting relevant pharmaceutical compounds, and (d) systematic studies to optimize the process of core and surface modifications and functionalization (particle core, surface coatings, and loadings) with (1) chemical compounds for “masking” the SPIO-NPs to overcome the BBB-Tween 80, Dextran 70,000, and DEAE-Dextran, and (2) fluorescence markers – rhodamine 123 (particles in blood stream, during crossing the BBB), and propidium iodide (to prove the NPs in the cell tissue).

Since iron oxide nanoparticles are under an intensive research for more than decades, but their successful pharmaceutical developments are very rare, especially their toxicity concerns are not properly addressed. Therefore, another challenge of the project was to obtain the detailed knowledge about the concentration-dependence *in vitro* (using a MTT colorimetric assay for relative toxicity quantification or cell viability) and *in vivo* toxicity of the synthesized SPIO-NPs after coating with Tween 80, Dextran 70,000, and DEAE-Dextran when they expose with the brain cells (C6 glioma cells) extracted from rat glial tumor. Since cytotoxic studies of these coated SPIO-NPs when they simultaneously labelled with rhodamine 123 and propidium iodide fluorescent dyes were not yet performed; therefore, it was particularly important to perform such studies. SPIO-NPs were not studied before as

a model of BBB in the retina, therefore, *in vivo* cytotoxic study was equally demanding in the cellular uptake by injecting the different variations of fluorescent iron oxide nanoparticles in animal (rat) groups for: retrograde labelling of retinal ganglion cells (RGCs), intravitreal SPIO-NPs injection, *in vivo* confocal neuroimaging, and *ex vivo* (whole mount) confocal imaging of retina.

1.7 Outline of the contents

This dissertation is divided into seven chapters. The proceeding *chapter 2* is about the magnetic studies and biomedical applications of SPIO-NPs. It is comprised of two sections: the first section presents an overview of magnetic properties and their use in iron oxides and the second section is devoted to the various biomedical applications associated with the SPIO-NPs.

Chapter 3 discusses the different synthesis methods of SPIO-NPs. It is comprised of seven sections. First two sections present the various synthesis methods of SPIO-NPs. The third section is about the different surface coatings and polymeric SPIO-NPs. An introduction to fluorescent magnetic nanoparticles is also a part of this section. Phase transfer of synthesized iron oxide nanoparticles from an aqueous phase to the organic (oil) phase is explained in section four. Toxicity of magnetic nanoparticles is presented in section five. Nucleation and an overview of inert-particles forces are also explained in the remaining sections of this chapter.

Chapter 4 deals with various chemicals, apparatus, the method used for synthesis experiments, experimental setup, and C6 cell culture. A short description of various characterization techniques like DLS, SEM, TEM, VSM, and spectrophotometry are also discussed here.

Chapter 5 focuses on the first part of the results and discussions. In this chapter, synthesis results of SPIO-NPs coated with Tween 80, DEAE-Dextran, and Dextran 70,000 regarding their particle size, particle size distribution, and the zeta potential are discussed.

Chapter 6 is dedicated to a second part of the results which are the applications of fluorescence labelled SPIO-NPs for relative *in vitro* toxicity (cell viability) of the synthesized iron oxide nanoparticles using a MTT colorimetric assay when they exposed with the C6 glioma cells. The *in vivo* and *ex vivo* studies in the cellular uptake and by injecting different variations of fluorescent SPIO-NPs in animal groups are also given in this second last chapter.

The terminal *chapter 7* describes a short summary of the main findings in this dissertation and presents an outlook for the future research.

2 Magnetic properties and biomedical applications

2.1 Nanomagnetism

Generally, the nanomaterials which are influenced by an applied external field are classified as nanomagnetic materials and study of these nanomaterials is known as nanomagnetism. The term “magnetic dipole” is analogous to an electric dipole in the magnetic nanoparticles. Nanomaterials experience a torque along the applied magnetic field due to the alignment of magnetic moment and quantity of magnetic moment is actually the torque experienced by that material under the influence of a magnetic field. Scientifically, in an atom, each electron shows magnetic moment because of (i) electrons orbital movement around the nucleus, and (ii) spinning of an electron around its own axis. In magnetism, *magnetization* (M) is an average magnetic field strength due to the magnetic dipole at a particular point. *Magnetic susceptibility* (χ_m) is the degree of net magnetization for a particular material under an applied magnetic field and it is a ratio of magnetization (M) to the applied field (H); $\chi_m = M/H$ [10]. For various applications, it is very important to have an accurate knowledge regarding the nanoparticles size and particle size distribution (PSD) to work with their numerous applications. Particle size distribution is possible to measure with the help of a magnetization curve and this method is based on the superparamagnetism behavior of nanoparticles [49].

2.1.1 Types of nanomagnetic materials

Magnetic nanomaterials are classified into five types which are based on their intrinsic magnetic dipole and their response in the presence and absence of applied magnetic field [10], [50].

- Diamagnetic materials
- Paramagnetic materials
- Ferromagnetic materials
- Ferrimagnetic materials
- Antiferromagnetic materials

Among the above magnetic materials, diamagnetic and paramagnetic materials are the most important as they exhibit magnetic behavior at room temperature. Most of the elements from the periodic table are non-magnetic and where it is cited as magnetic, then it is referred to as ferromagnetic materials. From an industrial point of view, ferromagnetic materials have an utmost interest [51].

2.1.2 Diamagnetic materials

Diamagnetic materials do not show any moment in the absence of a magnetic field because there are no any unpaired electrons in their outermost shells and have a negative value of susceptibility ($\chi_m < 0$). When a magnetic field is applied to such

materials, the produced magnetic dipole is oriented opposite to that of the applied field. These are the temperature independent materials [10], [50].

2.1.3 Paramagnetic materials

Paramagnetic materials have unpaired electrons in their outermost shell so; they have a net value of the magnetic moment. Induced dipoles are aligned only when an external magnetic field will be applied. The value of χ_m will be small and positive. Paramagnetic materials are temperature dependent and obey Curie law which describes that susceptibility (χ_m) is inversely proportional to the temperature [10], [50], [52]. Magnetic properties of nanoparticles are classified and based on their susceptibility [53]. If 'C' is Curie constant and 'T' is temperature, then by a mathematical expression 2.1;

$$\text{Susceptibility } (\chi_m) = \frac{C}{T} \quad (2.1)$$

2.1.4 Ferromagnetic materials

Ferromagnetic materials have a net magnetization even in the absence of an applied external magnetic field which is called spontaneous magnetization. This is due to their net aligned dipole magnetic moment [50], [52]. Below the Curie temperature, nanomagnetic materials show the ferromagnetic behavior because of the spontaneous magnetization and above this Curie temperature, materials exhibit phase transfer to paramagnetic materials [10]. Initially, with strengthening the external magnetic field the magnetization intensity of ferromagnetic materials also increases. Upon the further increase in the external magnetic field to such a value, there will be no increase in their magnetization intensity which is referred to a saturation phenomenon [54].

2.1.5 Ferrimagnetic materials

Ferrimagnetic materials have an atomic dipole moment same as of ferromagnetic materials and thus show net spontaneous magnetization because of the unequal magnetic alignment moment. Such materials have a positive susceptibility as well as the magnetization but little weaker when compared to the ferromagnetic materials [10], [50].

2.1.6 Antiferromagnetic materials

Antiferromagnetic materials have antiparallel magnetic dipole alignment, therefore, exhibit zero net magnetization [10], [50]. Normally, antiferromagnetic phenomena exist at a sufficiently low temperature.

A summary of the magnetic dipole alignments of all the above types of magnetic materials based on their electronic structure is given in the following figure 3.

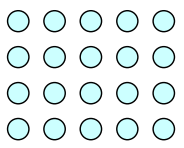
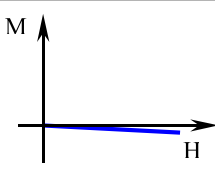
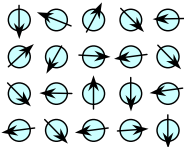
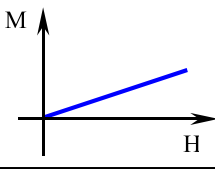
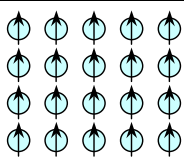
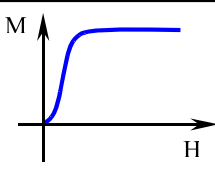
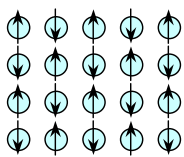
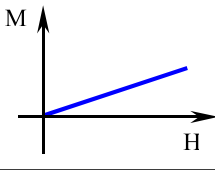
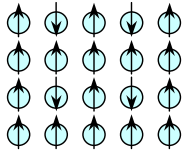
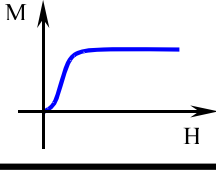
Type	Atomic / Magnetic Behaviour	
Dia-magnetism	 <p>Atoms have no magnetic moment</p>	
Para-magnetism	 <p>Atoms have randomly oriented magnetic moments</p>	
Ferro-magnetism	 <p>Atoms have parallel aligned magnetic moments</p>	
Antiferro-magnetism	 <p>Atoms have anti-parallel aligned magnetic moments</p>	
Ferri-magnetism	 <p>Atoms have mixed parallel and anti-parallel aligned magnetic moments</p>	

Figure 3: Summary of magnetic dipole alignment of all types of magnetic materials with their magnetic slope behaviours [55]

2.2 Superparamagnetism

Superparamagnetism phenomena occur in magnetic materials which composed of extremely small size. That small size normally depends on the nature of the materials. Iron oxide (Fe_3O_4) nanoparticles become superparamagnetic at a size less than 25 nm [56]. Superparamagnetic materials have zero magnetization on the removal of the applied magnetic field which makes them suitable for drug delivery, magnetic resonance imaging (MRI), and other applications based on their magnetic properties because importantly superparamagnetic nanoparticles strongly influenced by an applied external field. Neel was the first who proposed the idea of superparamagnetism to explain the thermal fluctuation in the ferromagnetic materials. The term magnetic anisotropy is associated with the superparamagnetic nanomaterials and is dependence of the internal energy in the direction of spontaneous magnetization, responsible for easy and hard directions of the magnetization. Magnetic anisotropy phenomenon is also due to the shape of nanoparticle samples. Generally speaking, magnetic anisotropy energy is directly correlated with the volume. For nanoparticles of volume V , the magnetic anisotropy can be written with the help of an equation 2.2.

$$E_A = KV \sin^2 \theta \quad (2.2)$$

In the above relation, K represents the anisotropy energy constant; θ is the angle between magnetization and the easy axis of the nanoparticles. This means that for a small volume, the magnetic anisotropy energy will approach to its thermal energy level. The superparamagnetism phenomenon is due to the large magnetic moment at a larger volume for a single atom. For a uniform magnetized single domain spherical nanoparticles, there are no any demagnetization factors so, does not exhibit shape anisotropy. Conversely, magnetization along a long axis than along a short direction is much easier for non-spherical nanoparticles, therefore, shape anisotropy exist in the non-spherical nanomaterials [57], [58].

2.3 Magnetic hysteresis

When ferromagnetic or ferrimagnetic nanoparticles are placed in an applied magnetic field, they observe a typical sigmoidal shaped curve, called hysteresis as shown in figure 4 where the relationship between magnetization (M) and strength of magnetic field (H) is plotted.

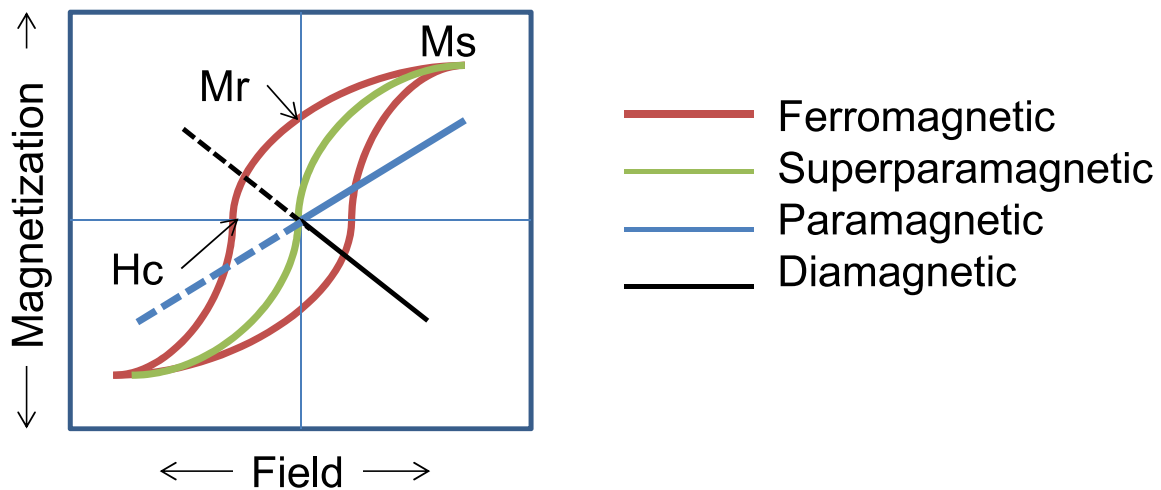


Figure 4: Magnetic behavior of magnetic NPs when the magnetic field is applied. The X-axis is the applied field (Oe), and the Y-axis is the magnetization of the sample as a function of field exposure (emu/g) [50]

Typical characteristics of this hysteresis loops are magnetic saturation (M_s , maximum induced magnetization), a remanent magnetization (M_r , induced magnetization remaining after removal of applied magnetic field), and coercivity (H_c , the magnitude of the applied magnetic field in the negative direction to make magnetization zero). Superparamagnetic nanoparticles follow the green line, shows no hysteresis. Curve rapidly increases initially and reaches its maximum value M_s . On monotonical reduction in the value of H_c ; curves follow a different path in an opposite direction (red line). On its moment in the negative direction, curve passes through an origin (M_r) where the applied magnetic field (H) is zero. At this level of magnetism in the nanoparticles, sigmoidal curve tends to a point where magnetization is zero which is

a point of coercivity on the curve. On further increase in H_c , the nanoparticles will be magnetically saturated again in a negative direction. The curve returns to a saturated magnetization again in a positive direction after passing through a point (where $H_c=0$), where the hysteresis curve is completed. This curve is shown in figure 4 by a red line and ferromagnetic nanoparticles follow this red line curve. The behavior of paramagnetic (blue line) and diamagnetic (black line) are also significant in figure 4. Magnetic saturation (M_s) is a temperature dependent property and is at a maximum value at 0 K [50], [59]. On the basis of coercivity of hysteresis loop, ferromagnetic materials are further classified as soft and hard magnetic materials; soft magnetic materials have low coercive value and remanence, therefore, can be magnetized easily. Area of the hysteresis loop is directly related to the energy loss per unit volume and resulting in heat generation which is of a great importance in hyperthermia treatment. Soft magnetic materials have this type of hysteresis loop. Hard magnetic materials have high values of coercivity and remanence so, cannot magnetize easily. Heat loss per unit volume is high with the thick hysteresis loop in such materials [51]. In table 2 different tunable magnetic properties are given which are vital for various biomedical applications.

Table 2: Tunable magnetic properties important for biomedical applications

Tunable property	Applications
Saturation magnetization (M_s)	Biosensing, drug delivery, magnetic resonance imaging (MRI)
Coercivity (H_c)	Biosensing, magnetic hyperthermia (MHT)
Blocking temperature (T_B)	Biosensing, drug delivery, MHT
Neel and Brownian relaxation time of nanoparticles (t_N and t_B)	Biosensing, magnetic hyperthermia

The transition temperature is termed as Curie temperature (T_C) for ferromagnetic and ferrimagnetic materials and Neel temperature (T_N) for antiferrimagnetic materials. Superparamagnetic materials are normally termed as blocking temperature (T_B) [52], [60]. Blocking temperature (T_B) is a temperature above which ferromagnetic and ferrimagnetic nanoparticles exhibit superparamagnetic characteristics. The value of T_B is associated with the energy barrier and it is dependent on the characteristics measuring time. Difference between measuring time and the relaxation time leads to measure the nanoparticles magnetic behavior. Nanoparticles will be in the superparamagnetic regime when measuring time will be greater than the relaxation time but when measuring time will be less, then nanoparticles will be in “blocked” (ferromagnetic) regime [50]. Blocking temperature value is also strongly dependent on composition, particles size, morphology, and also on the type of coating or surfactant that covered the nanoparticles surface to avoid their agglomeration and magnetic attraction [61].

Blocking temperature (T_B) is a merging point of two magnetization curves: zero-field cooled (ZFC) and field-cooled (FC) magnetization curves. For ZFC measurements, nanomaterials samples cool first at a sufficiently low temperature from 300K to 10K without applying any magnetic field. After reaching a particularly low-temperature point, a magnetic field is applied and magnetic moment is observed as a function of temperature increase. Conversely, for FC measurement, nanomaterials samples cool under an applied magnetic field and the magnetic moment is recorded as a function of temperature increase. The merging point of two curves is referred to irreversible temperature (T_{irr}) and the maximum point of ZFC curve gives the blocking temperature (T_B) value [15], [50] as shown in figure 5.

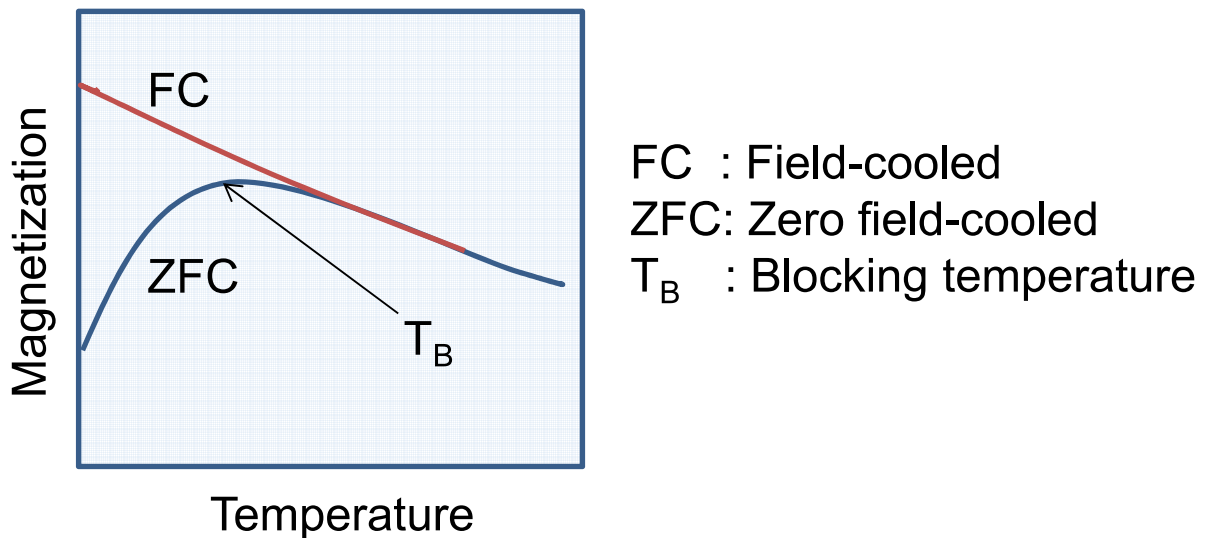


Figure 5: A graphical illustration explaining the blocking temperature of magnetic nanoparticles [50]

Finite-size effects (single-domain or multi-domain structures) and surface effects are two key factors of magnetic nanoparticles and are responsible for main features of considerable different magnetic characteristics associated with the iron oxide nanoparticles as compared to the corresponding bulk materials [60], [62]. With the decrease in nanoparticle size, number of residual atoms (or fraction of the entities) also increases significantly on the particle surface as compared to the particle increasing the surface-to-volume ratio and this increase in surface-to-volume ratio is an important factor for various industrial and biomedical applications when compared to their corresponding bulk materials [10], [63]. In simple words, the total surface area increases with the increase in the surface-to-volume ratio of nanoparticles [63] as shown in figure 6.

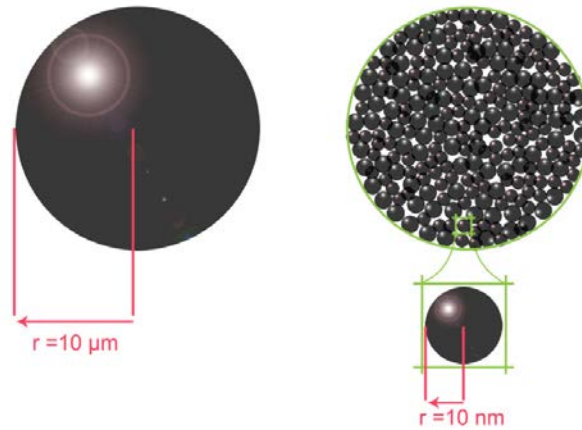


Figure 6: A schematic illustration of the change in the surface-to-volume ratio between microsphere (left) and when the same microsphere composed of nanoparticles (right) [63]

The 'domain' is a term which is associated with the ferromagnetic materials and is an association of magnetons in groups. When all magnetons are aligned in the same direction by exchanging forces in a particular volume of ferromagnetic materials, is known as magnetic domain [59]. A bulk ferromagnetic is further subdivided into a multi-domain structure in order to balance magneto-crystalline anisotropy and to reduce the magnetostatic energy associated with a large stray field. In a single domain, all particles are uniformly aligned in the same direction. When the size of nanoparticles is gone on decreasing until just below the critical limit, nanoparticles will behave as a single domain and thus will show superparamagnetic behavior and will have no hysteresis with zero or negligible remanence and coercivity [10]. For the IONPs with a size range 30 to 80 nm (above the superparamagnetic regime), single domain ferrimagnetism with an intrinsic remanence phenomenon is observed and for the nanoparticle size from 80 to 100 nm, the IONPs are divided into multi-domain with their lowering the magnetostatic energy [64] as illustrated in figure 7.

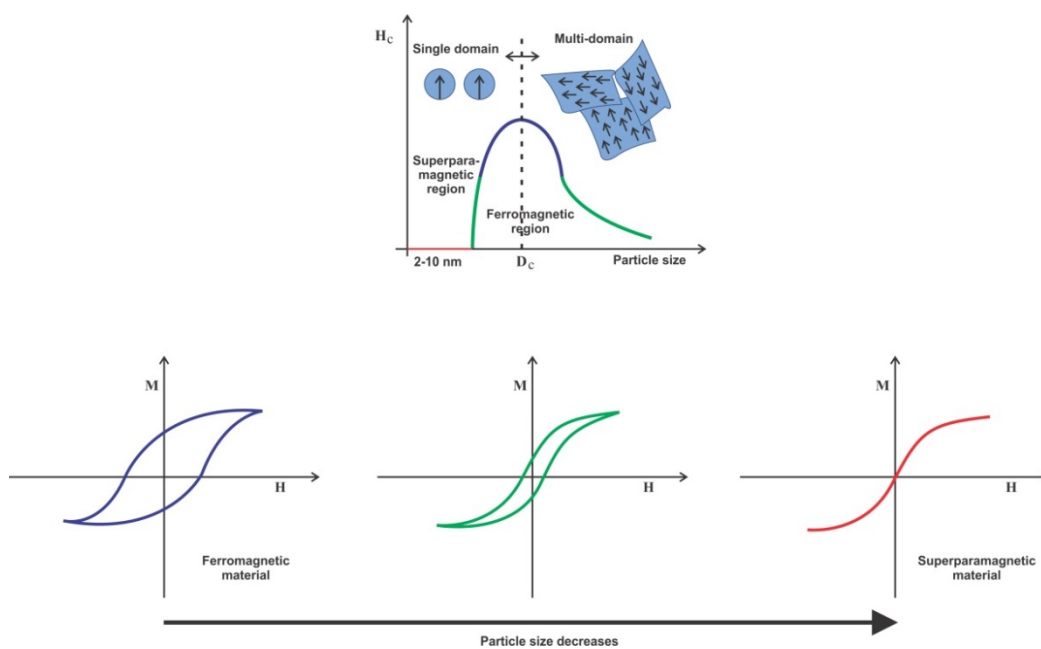


Figure 7: Effect of decreasing particles size on the hysteresis curve of ferromagnetic materials [10]

2.4 Biomedical applications of superparamagnetic iron oxide nanoparticles

There are many magnetic NPs which are candidates for their use in biomedical purposes, but iron oxide NPs are preferred due to a profound reason that our human body has organs and metabolic system which only can transfer iron into safe storage for later use. The obtained iron oxide nanoparticles after synthesis are not directly employed for biomedical applications because they are not bio-tolerable. Several post synthesis steps like the removal of any toxicity materials during their synthesis are required [65]. It is worth noted that iron oxide NPs are very much compatible with the human body cells (10-100 μm), viruses (20-450 nm), proteins (5-50 nm), and genes (2 nm wide by 10-100 nm long). Due to their small enough size, they are liable to move inside the body without disturbing any normal body functions and are easily accessible to all those places that are inaccessible to other materials [66], [67]. For biomedical applications, the use of nanoparticles that present superparamagnetic behavior at room temperature with no remanence and having a single domain are preferred due to their unique particle size. The size distribution of the synthesized iron oxide nanoparticles is very crucial for their biomedical uses including diagnostics. Biocompatibility and toxicity are the two important factors for use in biomedical treatments and are the functions of nature for the magnetic materials, particle size, surface structure, surface charge, their core, and coatings.

Biomedical applications of magnetic nanoparticles can be categorized according to their application inside (*in vivo*) or outside (*in vitro*) [6], [67]–[69]. *In vivo* applications require that the magnetic nanoparticles must be coated with a biocompatible polymer during or after the synthesis process in order to prevent the formation of larger aggregates, changes from the original structure and biodegradation when exposed to the biological system. Regarding the size of the MNPs, it must be small enough to evade uptake by the reticuloendothelial system (RES) of our body and to avoid renal clearance, it should be large enough. Elimination of small-sized MNPs from our body stream is faster than the larger MNPs have already reported. A biomedical nanoparticle is the combination of an inorganic nanoparticle core and a biocompatible (an organic) coating which promotes the stability under the physiological conditions [70]. Polymer coating not only provides them from the danger of aggregation but also allow binding of drugs by a covalent attachment and adsorption on the particle surface. *In vivo* applications are further classified as therapeutic (hyperthermia and drug-targeting) and diagnostic applications (nuclear magnetic resonance (NMR imaging)). *In vitro* applications lie in diagnostic (separation/selection, and magnetorelaxometry) [68]. Various therapeutic and diagnostic applications are summarized in the following figure 8.

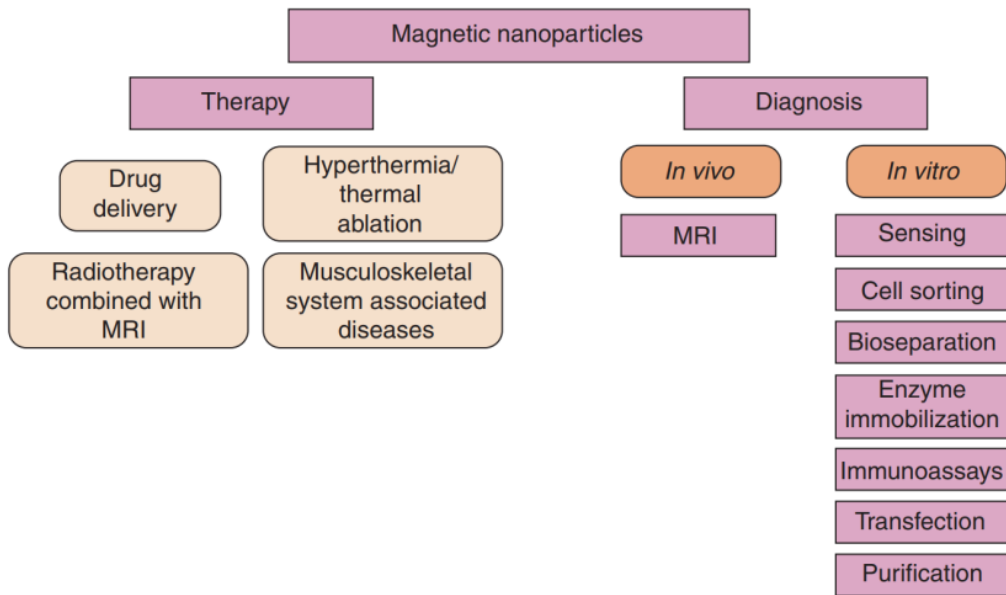


Figure 8: Plethora of possible biomedical applications of magnetic nanoparticles [56]

For an effective use in drug delivery, magnetic hyperthermia, and in magnetic resonance imaging (MRI) applications, the main criteria involve that iron oxide nanoparticles must be water-dispersible, high crystallinity, and also have monodisperse with a narrow particle size distribution [71]. For our present study, we are concerned with Fe_3O_4 superparamagnetic nanoparticles to use in the BBB drug delivery applications. A physical illustration of the therapeutic applications of iron oxide nanoparticles under the influence of an applied alternating magnetic field in the human body is shown in the following figure 9.

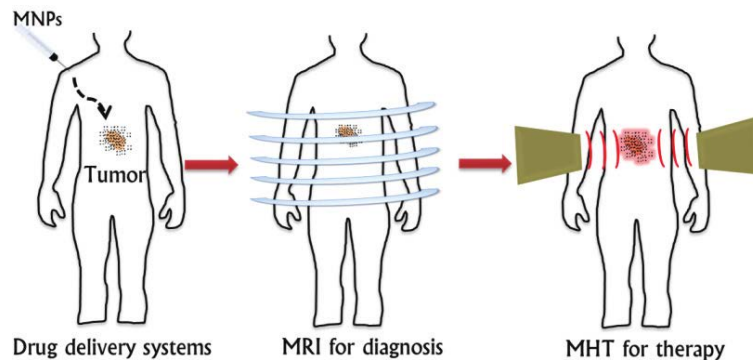


Figure 9: A schematic explanation for the different therapeutic and diagnosis strategies using magnetic (iron oxide) nanoparticles (MNPs). Accumulation of MNPs in the targeted tumor tissues using magnetic drug delivery systems, diagnosis by magnetic resonance imaging (MRI), and magnetic hyperthermia (MHT) for cancer treatment under the application of an alternating magnetic field [72]

A complete description of therapeutic (targeted drug delivery and magnetic hyperthermia) and magnetic resonance imaging (MRI) applications is presented in the proceeding sections of the present chapter.

2.4.1 Targeted drug delivery

The idea of iron oxide nanoparticles transportation through our vascular system and the concentration in particular part of our body with the help of a magnet was developed in the early 1950s and since then magnetic nanoparticles for the delivery of drugs, targeting ligands like antibodies, small molecules or peptides to diseases infected body part is a focus of scientific interest as the next generation of targeted drug delivery [68], [73], [74]. Magnetic nanoparticles in combination with magnetizable implants targeted to the area under focus and then fix the local site for releasing the medicine.

In table 3, the drug delivery development during the last 60 years is categorized into two generations: the first generation (1G) and the second generation (2G). The main focus of drug delivery during 1G was to develop oral and transdermal formulations. Four main controlled release technologies dissolution, diffusion, osmosis, and ion-exchange were established during 1G. Development of more advanced drug delivery systems was under consideration in the 2G, such as zero-order drug release systems and environment-sensitive delivery systems using smart polymers and hydrogels. The last 10 years of the 2G were devoted to the development of nanotechnology-based formulations [75].

Table 3: Continuous developments of targeted drug delivery systems since 1950 [75]

1 st Generation (1G)			2 nd Generation (2G)			3 rd Generation (3G)		
1950s	1960s	1970s	1980s	1990s	2000s	2010s	2020s	2030s
<u>Basics of Controlled Release</u>			<u>Smart delivery systems</u>			<u>Modulated delivery systems</u>		
Oral delivery: Twice-a-day, once-a-day			Zero-order release: Zero- vs. first-order release Smart polymers and			On-off insulin release: Glucose-sensitive release		
Transdermal delivery: Once-a-day, once-a-week			hydrogels: Environment-sensitive, Self-regulated release			Targeted delivery: Anticancer drugs, siRNA		
Drug delivery mechanisms: Dissolution, diffusion, osmosis, and ion-exchange			Peptide and protein delivery: Biodegradable depot nanoparticles: Tumor-targeted delivery, gene delivery			Long-term delivery systems: 6-12 months delivery with minimal initial burst effect <i>In vitro-in vivo</i> correlation: Prediction of PK profiles from <i>in vitro</i> release study		

Table 4 lists some of the technologies to be developed during the 3G. The drug delivery systems listed in table 3 can be further divided into two categories depending on the barriers to overcome, i.e., formulation or biological barriers. Two formulation barriers that preferably need to be overcome: formulation of poorly soluble drugs and elimination of initial burst release. The former barrier is still a major issue since began [75] and therefore, need to be further investigated.

Table 4: The barriers to overcome in the 3G drug delivery systems [75]

Formulation barriers	Biological barriers
<ol style="list-style-type: none"> 1. Oral delivery of poorly soluble drugs; 2. Injectable depot formulations with no initial burst release. 	<ol style="list-style-type: none"> 1. Gastric retention in the fast condition; 2. Self-regulated drug delivery systems; 3. Injectable depot formulations for peptides and proteins; 4. Targeted drug delivery (systemic and intracellular targeting).

Estimations that about 70%–90% of the new drug candidates are poorly water-soluble and new, innovative formulations are urgently needed so that the poorly soluble drugs can be administered without using.

Drug delivery systems (DDSs) based on the SPIO-NPs are commonly composed of magnetite and maghemite NPs with an organic or inorganic coating. These magnetic drug-bearing nanostructures are only effective when an external magnetic field is applied and then guided to the target tissue. Magnetic vehicles (magnetoliposomes) not only reduce the clearance of drugs but also increase their blood circulation time. The reduction in total required dosage and related side effects took place by SPIO-NPs is due to the fact that SPIO-NPs have increased drug internalization efficiency within the target cells and minimize the nonspecific cellular interactions. Under an applied external magnetic field, SPIO-NPs are fully saturated magnetized and thus high magnetic susceptibility. There is no any magnetic interaction is observed in the absence of an applied magnetic field. This makes possible the SPIO-NPs to capable to drag the drug (encapsulated/attached) to the target site in the body under the externally applied magnetic field and is inactivated on the removal of that magnetic field [76].

Despite the fact that naked SPIO-NPs are stable in high- and low- pH suspensions and not in the neutral pH, they must be coated for their *in vivo* applications. Coatings largely influence the functionality and biological fate of DDSs. For example, a coating of the NPs with hydrophilic polymers, including polyethylene glycol (PEG), poloxamers, polysorbate 20 and 80, tocopheryl PEG succinate, and dextran can inhibit the formation of a protein layer at the particle's surface by providing a hydrophilic cloud and neutral chains. Although PEGylation improves the pharmacokinetic profile of DDSs and enhances the accumulation of nanoscale DDS in the tumor, coating with Tween 80 has been shown to improve the blood-brain barrier (BBB) transport of NPs [76]. The advantage of using a polymer coating is not only the creation of more hydrophilic nanostructures, but a various surface functional groups are also provided in order to bind drug molecules, inhibit aggregation, and increase stability [66]. A complete description of the coating of SPIO-NPs is

described in proceeding chapter 3 (section 3.3). Once the suitable coating accomplished, the drug can be attached either by the conjugation to the nanoparticles surface or by an encapsulation in the nanoparticles [77] and this process is explained in figure 10.

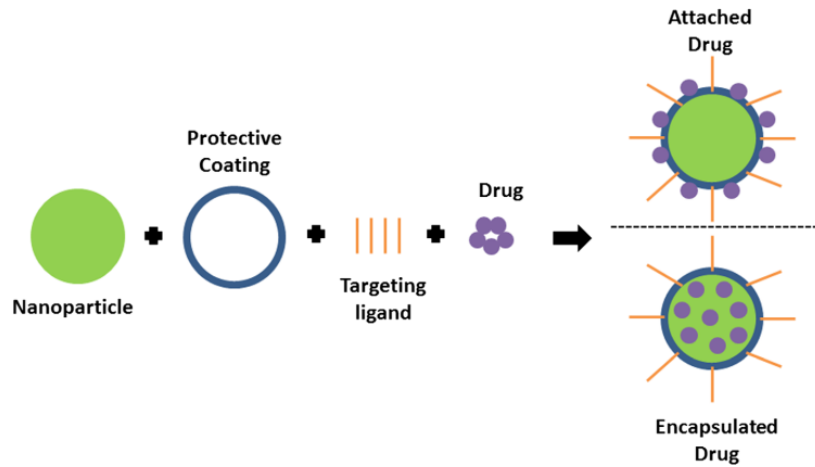


Figure 10: Two different drug loading options in the nanoparticles during the targeted drug delivery [77]

By using SPIO-NPs as a drug carrier for a specific targeted site, side effects to healthy tissues can be eliminated and may also protect drugs from early biodegradation. For a medically safe targeted drug delivery, the system is designed to specifically targeting the body tissue and controlling the drug release for a prolonged time [2], [78]. Figure 11 is a simple mechanism of the drug delivery process with a magnetic aid. On a desired targeted site, the drug is released through an enzymatic activity or by changing the pH or temperature or osmolality [77], [79].

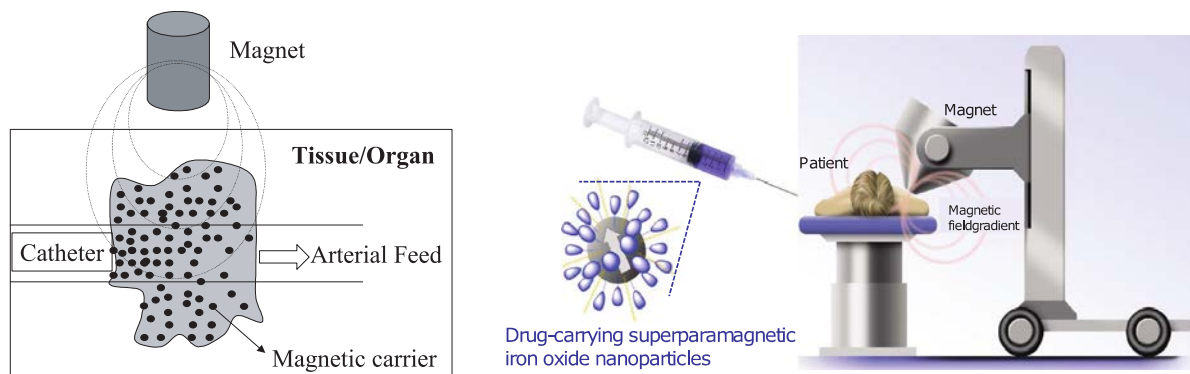


Figure 11: Schematic representation of the magnetically driven targeted drug delivery mechanism to a particular region. Insertion of a catheter is shown into an arterial feed to the tumor under the magnetic stand which is positioned just over the specific target region (left). A holistic view of the targeted drug delivery system (right) [68].

Some other advantages associated with the SPIO-NPs drug targeting are [3], [80], [81]:

- Passive and active drug targeting is possible due to the SPIO-NPs size and their surface characteristics;
- Drug releasing at a controlled and sustainable rate during the transportation and at the site of localization;
- Choice of suitable matrix constituents, controlled drug release, and particles degradation could be possible;
- Drug loading is high and the drug can be incorporated into the system without any chemical reaction;
- No any study has reported the wastage of drug so; it enhanced bioavailability of drugs at a targeted site in the desired proportion.

Some limitations of using SPIO-NPs in drug delivery are [81]:

- Particle-particle aggregation is observed due to the small size and large surface area which makes the particles physically difficult in liquid and dry form;
- Small particle size and large surface area limits in drug loading and burst release. These problems should be overcome before their clinical utilization and commercial availability of the SPIO-NPs.

Adsorption of hydrophobic drugs, where other problems involve site-specific drug targeting to a particular diseased site is a limitation of drug delivery. Because of the SPIO-NPs significance for improved efficacy and biocompatibility of drugs, hence to release drugs at the targeted site and adsorption sufficient adsorption of drugs by the specific cell will be a critical improvement. SPIO-NPs are colloiddally stable due to their lack of permanent magnetization. For biomedical applications, a certain level of magnetization is usually required [82].

When drug delivery by iron oxide nanoparticles is carried out, the competition of two forces takes place: (1) force exerted by blood compartment on the nanoparticles and (2) magnetic force by applying a magnetic field on the particles. Magnetic particles retain at a particular targeted site when the magnetic force exceeds the linear blood flow rate. Some problems associated with the drug delivery may be uniform pharmaceutical distribution throughout the body, large dose necessity to have a high local concentration, importantly non-specific toxicity associated with a high drug dose. Targeting of drugs to a particular cell could be a possibility with the direct coatings but retaining the drug in this particular cell for a longer length of time would not be possible. Retaining drugs for a long time usually depends on the blood flow rate and the intensity of the applied magnetic field [70].

2.4.1.1 Physicochemical characteristics essential for drug delivery

For a successful targeted drug delivery system designing, monodispersity (particles with same shape and size), their superparamagnetic behavior, low toxicity, water-

dispersibility, surface property, and the most importantly their stability are among the main requirements from their biomedical utilization point of view. Nanoparticles stability can be achieved by a core-shell structure which consists of a metallic core with an inorganic or organic (polymeric) coatings to engineer their outer surface [11], [79], [83], [84] as shown in figure 12. These are the properties usually govern the blood distribution profile of the iron oxide nanoparticles [11].

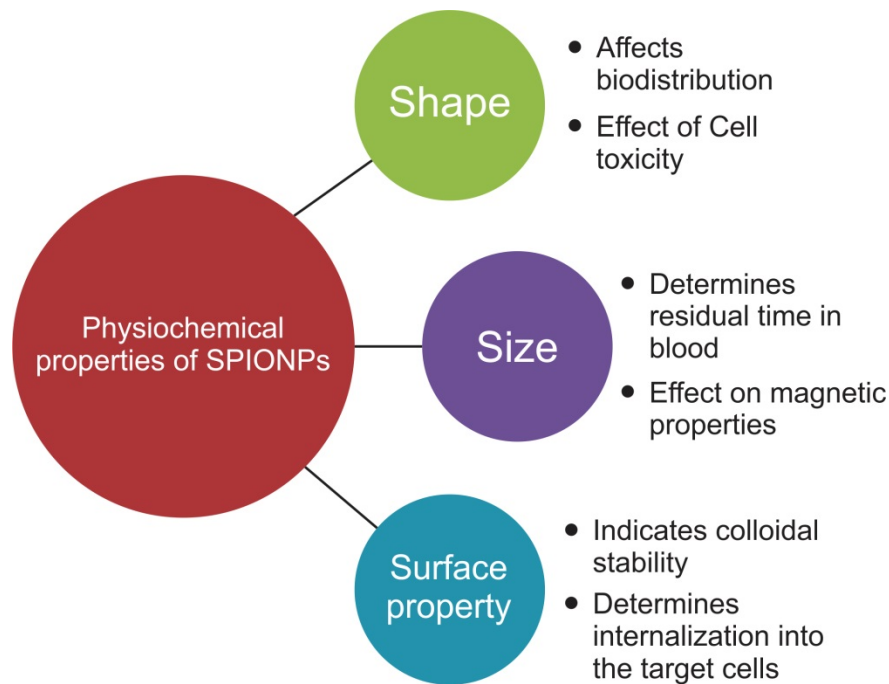


Figure 12: Different physiochemical considerations of superparamagnetic iron oxide nanoparticles for targeted drug delivery system [11]

2.4.1.1.1 Shape of the nanoparticles

The shape of superparamagnetic iron oxide nanoparticles is not studied well yet. Synthesis conditions and different substances involved in their synthesis effects the final morphology of such nanoparticles. Presence of heavy hydrocarbons as surfactants has a pronounced effect on their growing crystal shape. It already has been reported that the shape of iron oxide nanoparticles directly influences the cell toxicity [11]. Also, it has been suggested in the literature that anisotropically shaped NPs can avoid bio-elimination better than spherical NPs. For *in vivo* study, evaluation of high aspect ratio shaped MNPs also has been studied and resulted that to have similarly enhanced blood circulation times over the spherical counterparts. These types of studies are found to be promising but more detailed research is still required to exactly what aspect ratios yield the most dramatic influence on the MNPs pharmacokinetics [85].

2.4.1.1.2 Size of the nanoparticles

Particle size and size distribution are the most important characteristics of nanoparticle systems. Size of MNPs significantly helps for: (1) helps govern the NPs

concentration profile in the blood vessel and (2) affects the mechanism of NPs clearance both the clearance and the biodistribution of nanoparticles, but this parameter is not always perfectly controlled and often poorly described in the literature. The mean MNPs size may also be able to increase due to the presence of some aggregates. Size of MNPs can be control through many parameters: viscosity or pH of the suspension medium, temperature, concentration, and a particle sedimentation are among some of them [85], [86].

To determine the *in vivo* distribution, biological fate, toxicity and the targeting ability of nanoparticle systems, it is important to find the particle size and particle size distribution. Very small sized nanoparticles less than 10 nm are subjected to remove by renal clearance and nanoparticles larger than 200 nm are liable to concentrate in the spleen or are taken up by phagocytic cells of the body. Optimum size range in between 10-100 nm is considered for biomedical uses because these NPs can penetrate through very small capillaries [11]. It has been established that using these types of NPs will lead to the longest blood circulation time. The volume of these 10-100 nm sized NPs is quite small enough to escape the phagocytosis of the reticuloendothelial system and penetrate into capillary vessels in the body tissues, which ensures an effective distribution in specific tissues [66]. Further, the drug loading, drug release, and stability of nanoparticles can also depend on the NPs size. Drug release is also affected by the particle size. Smaller particles have the larger surface area; therefore, most of the drug associated would be at or near the particle surface, leading to a fast drug release. Whereas, larger particles have large cores which allow more drug to be encapsulated and slowly diffuse out. Smaller particles have a tendency to agglomerate during their storage and transportation of nanoparticle dispersion. It is always a challenge to formulate nanoparticles with the smallest size possible with the maximum stability [87].

2.4.1.1.3 Surface properties of the nanoparticles

High positive and negative zeta potential leads to dispersion stability of nanoparticles and therefore, they do not agglomerate on storage. Nanoparticles body distribution also based on surface charge and it affects the internalization of such nanoparticles in their target cells [11]. Apart from the size of nanoparticles, their surface hydrophobicity determines the amount of adsorbed blood components. This in turn, influences the *in vivo* fate of nanoparticles. The surface charge property of nanoparticles is characterized by a zeta potential of a nanoparticle. Zeta potential is strongly influenced by the composition of the particle and the medium in which it is dispersed. Generally speaking, nanoparticles with a zeta potential above (+/-) 30 mV are considered to be stable in suspension, as the surface charge also prevents aggregation of the particles. Positively charged NPs can also bind to non-targeted cells (typically negatively charged) leading to non-specific internalization. To determine whether a charged active material is encapsulated within the center of the nanocapsule or adsorbed onto the surface, a zeta potential is also helpful for this purpose [85], [87].

2.4.1.2 Blood-brain barrier and targeted drug delivery

Delivering the drug to the brain is the ultimate goal and challenge for drug delivery. Drug delivery to the brain is always very challenging to the scientists. This challenge is due to the existence of the blood-brain barrier (BBB) which is considered as the best gatekeeper to the brain. Degenerative diseases of the brain are liable to increase with aging peoples; so, it became a big challenge for drug delivery to the brain [88]. It is a general debate that pharmaceuticals and most of the small molecules do not cross this BBB under various conditions.

2.4.1.3 Blood-brain barrier (BBB)

Nanotechnology has significant application to the central nervous system (CNS) and is the development of technologies for delivery of drugs and many other small molecules like genes, oligonucleotides, and many contrast agent across the blood-brain barriers (BBB) [89]. The blood-brain barrier is a complex system and a physical barrier made up of structurally distinct tight junctions of endothelial cells and their powerful ejection transport systems that protect the brain from toxic substances, separates the blood from the extracellular fluid of the brain and helps to maintain the brain homeostasis. It also prevents the entrance of many drugs like antibiotics, antineoplastic agents [90]–[92] and blood-borne substances into the central nervous system (CNS). There are two challenges faced by the CNS drug delivery system to deliver non-penetrating drugs: (i) specifically across the BBB and (ii) achieving the required pharmacokinetic of sufficient drug amount within the CNS tissue. It already has been reported that about 98% of compounds used for crossing the BBB are failed to do so [91].

At the beginning of the 20th century, the existence of BBB was first proposed and confirmed later on. The BBB consists of endothelial cells connected by complex tight junctions, and a pool of enzymes, receptors, transporters, and efflux pumps of multidrug resistance pathways [93], [94]. These tight junctions of BBB control the paracellular diffusion of hydrophilic substances and prevent only small and lipophilic molecules having a molecular weight less than 500 Da through space between cells and their passage occurs only by entering the cells. Tight junctions also promote the integral membrane proteins movements between the apical and basolateral membranes of the cells [95]–[97]. Brain cells have tight junctions resisting the passage of different carriers including pharmaceuticals. This passage can, however, be compromised with different types of transport systems like passive and active transports as well as carrier-mediated transport. Several studies have evolved stating the various types of nanoparticles crossing this barrier and thus can be used as a carrier transport system to deliver the drug into the brain [88]. Nanoparticle size is a dominant factor to enter the BBB and nanoparticles of 12 nm size have a tendency to cross the BBB [97]. Figure 13 is a typical representation of the BBB and its different functions.

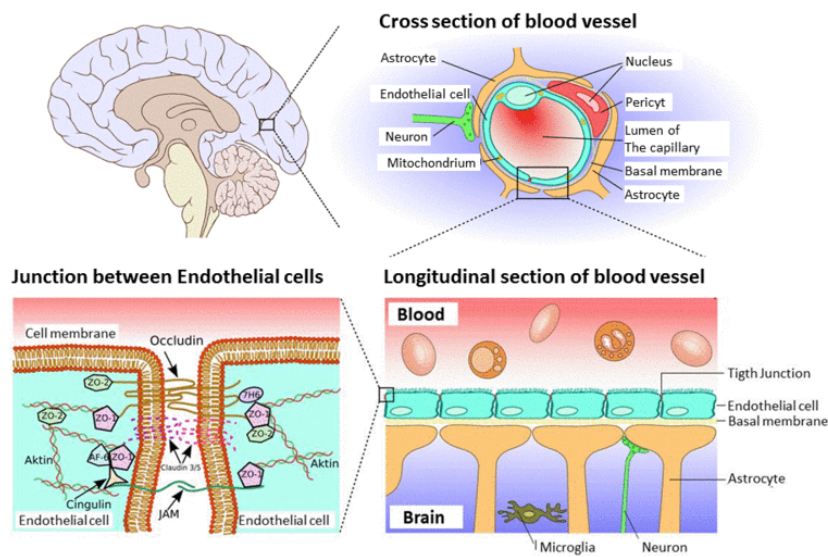


Figure 13: View of the blood-brain barrier; above, a cross-section through the brain; center, a schematic representation of the BBB; below, cellular structure [98]

Superparamagnetic iron oxide nanoparticles can cross the BBB and their ability is based on three strategies. In the first, SPIO-NPs are modified with functional ligands that target specific receptors in brain cells (examples of these ligands are antibodies, peptides, and proteins) (figure 14). In the second, the movement of SPIO-NPs-encapsulated cargo to the brain is directed with the help of an external magnetic field. Finally, the third strategy is applying a regulated radio frequency (RF) field to the SPIO-NPs in order to produce heat and thereby transiently and thus locally open the BBB. Second and the third strategies are specified to the SPIO-NPs; both are based on the physical principles derived from the magnetic properties of this kind of material: the magnetic force and heat generated by the particles under the influence of an external electromagnetic radiation. For the first strategy, it is not different from that adopted with other different nanoparticles to which a specific ligand is attached to the particle surface. First, two strategies can be combined when an external magnet reinforces the vectorization achieved with the ligands [99].

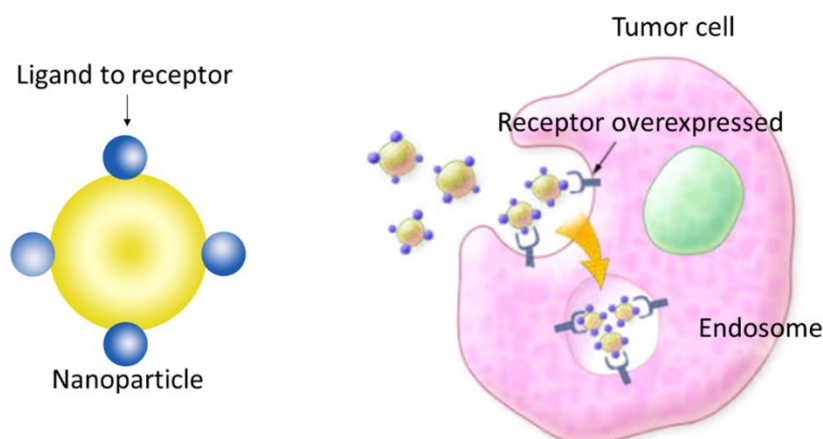


Figure 14: Interruption of NPs in the blood-brain barrier (BBB), which tends to accumulate at the tumor site. Receptor-mediated endocytosis of the functionalized NPs by cells overexpressing a receptor can retain NPs inside the tumor [99]

A number of factors to happen together to cross the BBB for delivery of drugs and other small molecules while considering potential targeting a particular site, for example, a tumor. Systematically administration of nanodelivery-drug complex (for example, intravenously) required in an ideal situation. For minimal systematic effects on CNS, it would be able to cross the BBB and then targeting the cells correctly in CNS, and releasing of drug carry out as its primary function. This is very challenging and technological obstacles and it requires multidisciplinary solutions between different fields, including engineering, chemistry, cell biology, physiology, pharmacology, and medicine. Unfortunately, this ideal situation is still lacking, a pronounced research has been done already to develop nano-technological drug delivery strategies to cross the BBB [89] but transportation of drugs into the brain, however, is still not fully understood [94].

2.4.1.4 *In vivo* confocal neuroimaging (ICON) and BBB

Alzheimer disease, in general speaking, is a neurodegenerative disorder of the elderly and is the most prevalent form of dementia. Alzheimer disease not only impacts on social life but also a financial burden on patients, their families and on the community as a whole. The tight junctions of BBB offer restrictions and an obstacle in its treatment. To overcome this problem, polymeric biocompatible drug carriers are the best implied to the CNS [100]. At the same time, there is still a great demand for innovative drugs in the area of diseases of the CNS (e.g. Morbus Alzheimer, Multiple Sklerose, Stroke, Morbus Parkinson) and the demographic changes add to the urgency to find new treatment solution [101], [102]. The existing methods for studying the BBB are limiting the progress.

The standard method for analyzing pharmacokinetics parameters of the BBB passage is the *in vivo* method of the “brain/plasma” [103]. Other techniques are “in situ brain perfusion”, “brain uptake index” or microdialysis [104]. However, these techniques are rather complex, laborious, and costly and are therefore, not used widely for drug testing. Moreover, they provide data either about the rate or the

amount of the substance entering the brain. *In vivo* confocal neuroimaging (ICON) is rather a new way for visualizing and analyzing the BBB passage of nanoparticles. ICON has been developed and repeatedly shown as reliable and reproducible [105]–[108], similar approaches are being developed by many research groups [109], [110]. The advantages over other methods are that ICON can (i) collect data about the rate of BBB passage and the amount of substance entering the CNS tissue in a single experiment, (ii) detect the spatial distribution of the drug or carrier in the tissue, (iii) analyses particles-induced neuronal death and, (iv) due to repetitive data collection in the same experimental animal, ICON produces data with low statistical variance (because it allows intra-individual comparison over time).

ICON is superior to *in vitro* test system of the BBB. While *in vitro* systems are valuable models for specific (molecular) questions [111], several parameters are responsible for that translation of *in vitro* to *in vivo* findings is poor. For example, concerning the lipid-mediated transport, the BBB permeable was overestimated more than 100-fold by *in vitro* models [112]. Moreover, the complex interaction of, for example, blood constituents with the drug/particles and the brain cannot be mimicked sufficiently.

The blood-retina-barrier is normally used as a model of the BBB which based on the following considerations: (i) the retina is ontogenetically part of the CNS, (ii) neurons and glial cells are present in the retina and information is processed via synaptic transmission, just as in the brain. Therefore, the same strictly controlled extracellular milieu is found in the retina as in the brain. Moreover, (iii) it has been shown [113] that there are identical structures in both the blood-retina-barrier and the BBB and that blood-retina-barrier and BBB have the same effective permeability for various drugs [114]. Therefore, the blood-retina-barrier and the BBB can be considered as very similar, if not identical, and the eye can be used as a “window to the brain” to see how and if nanoparticles enter the CNS tissue.

2.4.2 Magnetic hyperthermia (MHT)

In cancer therapy, the killing of cancer-causing cells without damaging the other normal cells is a preferred goal of cancer treatment [70]. Magnetic hyperthermia (MHT) is a technique to raise the temperature of a particular region of the body affected by the malignancy or due to some other growths. This process is based on the direct cell-killing effect at a temperature above 41-43 °C [68], [115] for treatment about 30 minutes because several different types of cancer cells are sensitive above this temperature range. The successful hyperthermia treatment is dependent on the exposure time and temperature [116]. The damage to normal tissue is referred to reversible, but the damage to the tumor cells is an irreversible [117]. Hyperthermia is one of the most promising methods for cancer treatment among others like hot water usage, capacitive heating, and heat induction. The higher temperature is a cause of cell deaths but tumor-specific hyperthermia is responsible for all types of cell deaths [118]. Four ways to do hyperthermia have been found in the literature: hyperthermia

localized surface, part of the deep body hyperthermia, hyperthermia inside the tumor cavity, and whole body hyperthermia [119]. Ultrasonic or microwave treatments were in use during the past by means of an external heat source but these methods have been replaced by using magnetic fluid injection directly into an artery supplying the tumor. Generation of hyperthermia can take place by a radio frequency, microwave, and laser wavelength. Heating which based on using magnetic nanoparticles is more superior because of the features: (1) non-invasive way to increase the cell temperature up to therapeutic level and (2) magnetic nanoparticles can be compatible with other treatment methods, for example, chemotherapy. The mechanism of hyperthermia involves two steps, magnetic nanoparticles delivery into the target tumor and then heating those nanoparticles using an alternating magnetic field in order to raise the desired temperature level [44].

The magnetic nanoparticles which are employed for magnetic hyperthermia treatment are differentiated into two broad classes which based of their various properties and metallic morphological structures: (1) magnetic alloy nanoparticles which include, for example, Ni-Cr, Fe-Co-Au, and Fe-Cr-Nb-B type's alloy and (2) magnetic metal oxide nanoparticles. These are the oxides of the metals like iron oxide and nickel oxide etc. For more than five decades, iron oxide is considered as one of the most promising candidates for the magnetic hyperthermia among different existing metal oxides because of its numerous notable features especially due to its least toxic effects [120], [121].

The heat generation by magnetic nanoparticles is based on the application of an alternative magnetic field to the delivered magnetic nanoparticles. Superparamagnetic iron oxides are preferred for magnetic hyperthermia because of their extremely small size and unique magnetic properties. SPIO-NPs must be coated with some biocompatible surfactants before applying for such applications [82]. When an alternating magnetic field is applied with enough amplitude and frequency, the magnetization of the particles is continuously reversed, which converts magnetic into thermal energy. This heat is immediately released to the surrounding tumor cells [122]. The heating efficiency of magnetic nanoparticles tends to decrease with a decrease in their respective particles size. This collapse in heating efficiency is due to the loss of vortex magnetic domain structure because the size of nanoparticles affects the hysteresis loop area and thus beside this, a decrease in particle size is also responsible for a slump in their respective magnetic properties. Therefore, a suitable particle size should be tuned to get maximum benefits from the magnetic nanoparticles to use in hyperthermia [123].

Ferrimagnetic nanoparticles release heat by the so-called hysteresis loss mechanism when experiences to an alternating magnetic field. The amount of heat generated or loss by this mechanism is proportional to the frequency applied and to the area inside the hysteresis loop, as shown in figure 15 (left). This implies that nanoparticles with the highest saturation magnetization and coercive field values generate heat more

efficiently [12], [124]. Heat generation of SPIO-NPs explained by two different mechanisms: the so-called Néel relaxation mechanism and the Brown relaxation mechanism, shown in figure 15 (center) and (right) respectively. The Néel relaxation mechanism depends strictly on the value of the magnetic anisotropy energy barrier (ΔE) that needs to be overcome for the reversal of the magnetization of the particle during the application of the alternated magnetic field (B_0 , f). Intrinsic anisotropy of the particle (material, surface, and shape) and the volume of the particle are the two main parameters on which these properties depend. On contrary, the Brown relaxation mechanism is dependent on the capacity of the particle to reverse its magnetization by physically rotating in the physiological medium where it is immersed [12]. Both mechanisms take place simultaneously in the nanoparticles.

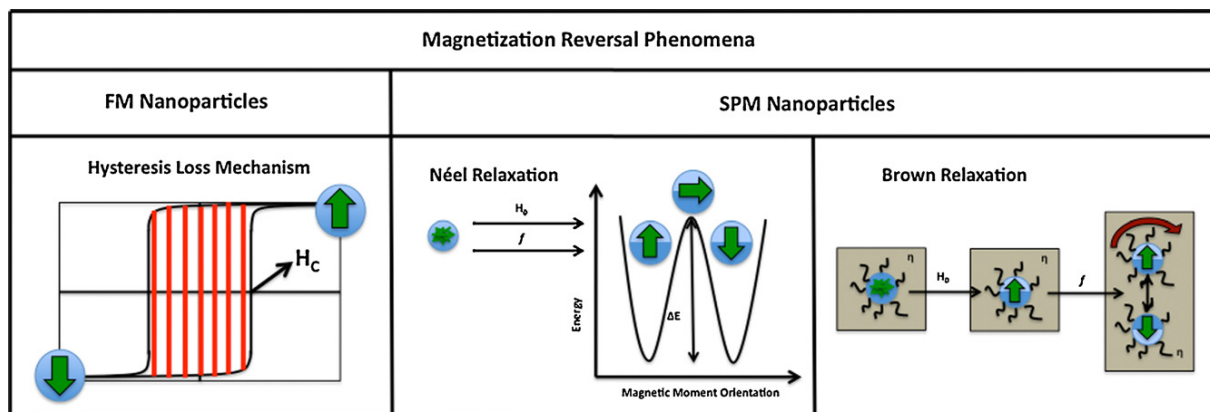


Figure 15: Phenomena of magnetization heat generation when an alternating magnetic field is applied (H_0 , f), (left). A representation of the hysteresis loss mechanism of heat generation [12]

2.4.3 Magnetic resonance imaging (MRI)

Magnetic resonance imaging (MRI) technique was developed during the early 1970s and in 1985, the United States food and drug administration (FDA) approved MRI for clinical use [125], [126]. This technique is based on the principles of nuclear magnetic resonance (NMR) and is widely used in medical and clinical diagnosis to produce high-quality spatial images inside of the human body and also for the molecular structures [127], [128]. Its principle lies in measuring the relaxation of protons under an external magnetic field after they have been excited with a radio-frequency pulse just as in NMR spectroscopy [129]. MRI is considered as the most successful and powerful non-invasive application of the SPIO-NPs as cell tracking among its various other biomedical uses. The ability of high spatial resolutions and for its non-invasive features when compared to X-ray-based imaging technique makes its remarkable development in biomedical science. Magnetic nanoparticles can also be used as an important diagnostics while loading these inside the cell culture with the help of transfection agents. Such a system, therefore, can be utilized inside the body through magnetic resonance imaging technique [130], [131]. This approach based on the magnetic pre-labelling of the cells. With its anticipation in cellular MRI provides the best applications in biology and medicine. Conjugate system of magnetic nanoparticles can be used for both diagnostic and therapeutic purposes. Iron oxide

nanoparticles have been conjugated with chemotherapeutic drug showing enhanced uptake of nanoparticles by cancerous cells through the action of intracellular enzymes [131].

The development in NMR leads to a new class in medical science, so-called magneto-pharmaceuticals. To receive the best quality images one should be: (1) image contrast should be enhanced in between health and diseased tissues and (2) status indication of organ function. SPIO-NPs are the best contrast agents used so far for the MRI. Technological advancement makes it possible to obtain biological and functional information in the form of images which is the result of the interrelation of contrast agents and biological system. Two types of MRI contrast agents are in use, i.e., positive contrast agents (or T_1 -weighted contrast agents) and negative contrast agents (or T_2 -weighted contrast agents). In the absence of contrast agents, it is impossible to get such information [126], [132]. Normally, large size SPIO-NPs behave as T_2 contrast agents but small size SPIO-NPs show their limited T_2 functions and therefore, they are considered as potential T_1 contrast agents [133]. SPIO-NPs being ultra-small in size and having other tremendous features, show in resulting T_2 (spin-spin relaxation process) and T_2^* contrast, as oppose to T_1 effects (spin-lattice relaxation process) at very low concentration for MRI and therefore; widely used as MRI contrast agents in clinical oncology [15], [68], [130]. MNPs which have strong T_1 and T_2/T_2^* relaxation properties have the best use as MRI contrast agents [134]. The R_1 ($= 1/T_1$) and R_2 ($= 1/T_2$) are the relaxivities for the rate of longitudinal magnetization recovery and the rate of transverse magnetization decay, respectively. When a magnetic field B_0 will be applied, the phenomena of magnetic moment induction take into account which perturbs magnetic relaxation. Bright T_1 -weighted MR images will appear for a tissue which has a short T_1 longitudinal relaxation time under such changes and will rapidly recover its longitudinal magnetization. Dark T_2 -weighted MR images will be observed if a tissue will have a short T_2 relaxation time due to quickly lose its transverse magnetization. The rate of transverse magnetization decays is considered as fast as compared to the characteristic R_2 relaxation rate which is normally expressed as R_2^* ($= 1/T_2^*$), and it is higher than the R_2 value [127], [135].

The SPIO-NPs used for MRI contrast agents will be degraded inside the body and subsequently will be incorporated into iron pools or will be used in the metabolic processes. An excessively high R_2 value resulting from the strong magnetization of the conventional iron oxide nanoparticles prevents their use as T_1 contrast agents. However, the R_2/R_1 ratio can be controlled by modulating the size, surface state, and composition of the nanoparticles (figure 16).

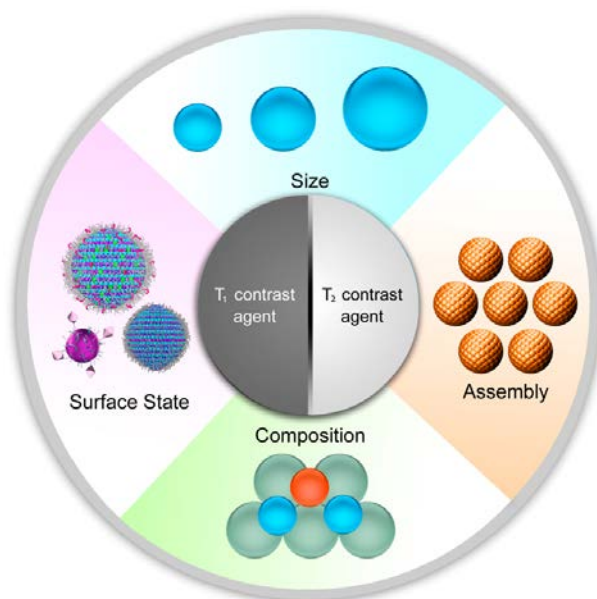


Figure 16: Control of MR contrast effect of magnetic nanoparticles. MNPs can be equally used as T_1 contrast agents or as T_2 contrast agents and this selection of their use depends on their various properties. In addition, the MR contrast effect can be adjusted by changing their core size, surface states including surface atoms and coating, composition, and assembly of multiple nanoparticles [127]

MRI using MNPs as contrast agents has several advantages over other techniques such as lack of irradiation, possibility to generate 3D images, excellent spatial resolution with optimal contrast within soft tissues, and a very good signal-to-noise ratio. Identification of cells and/or disease and/or function-specific biomarkers is the first and one of the major prerequisites of targeted contrast agents. For the best outcomes, the biomarkers should be solely and abundantly expressed on the desired cell types and disease affected biomarkers must be different from other healthy cells. Two components will be required to target the SPIO-NPs: (1) the magnetic iron oxide represents the imaging and (2) the attached molecule represents the targeting or affinity component. MNPs without targeting components are engulfed by monocytes/macrophages [136]. Resolutions of up to 1 mm have been reported through direct signals from the magnetic NPs; bulky full-body scanners are not required in the magnetic particle imaging (MPI) technology so, has a more advantageous than the other techniques [125].

3 Synthesis and stabilization of SPIO-NPs

Nanoparticles can be produced by chemical and mechanical processes. Former is referred as a bottom-up approach and later one to a top-down approach. During a bottom-up approach (chemical process), nanoparticles are synthesized by a chemical reaction and aggregation from dispersed molecular phases distributed in liquid or gaseous dispersants (crystallization of precursors particles or precipitation) in a controlled manner, which is regulated by thermodynamic means [137]. While on contrary in a top-down (mechanical process) approach, fine nanoparticles can be produced by starting with a large material and then further crushing into a nanostructure with the means of mechanical, chemical or by any other form of energy as shown in figure 17. Various techniques to produce nanoparticles from bulk materials include high-energy ball milling, mechano-chemical processing, etching, electro-explosion, sonication, and sputtering. This process can be accelerated by the addition of chemicals or using a laser. Sometimes this process is not preferred because of its huge time consumption and also of large particles size distribution [138], [139]. Concerning the selection of the process among them, it should be pointed out that both processes are equally useful for either gas, liquid, supercritical fluids, solid states, or in a vacuum. Control of (a) particle size (b) particle shape (c) size distribution (d) particle composition and (e) degree of particle agglomeration are important factors of consideration in either of the process chosen [138]. Precipitation method has a low solid concentration as compared to the grinding process. Production of the nanoparticles in a precipitation is fast and also it is a highly economical process with relatively narrow size fractions with tailored product properties. In the grinding process, a large volume of particles can be produced, but with irregular in shape and with a wide size distribution [137].

Stabilization of fine nanoparticles against agglomeration is required in both processes. Stabilization of fine and ultrafine nanoparticles can be achieved by two methods: electrostatic and steric stabilization. Electrostatic stabilization is achieved via potentially forming ions on the particle surfaces which has a repulsive effect. Polymers, thiols, phosphines, or silanes are added to the freshly prepared suspension in case of dispersing agents. These added polymers will perform a steric layer or barrier on the particles surface and will act as a molecular spacer to avoid close contact with MNPs, the so-called steric stabilization [137], [140].

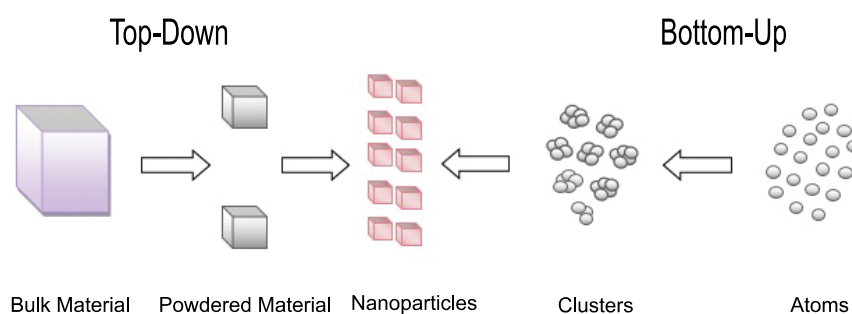


Figure 17: Two basic approaches to nanomaterials fabrication: top-down and bottom-up

3.1 Synthesis of superparamagnetic iron oxide nanoparticles

Superparamagnetic iron oxide nanoparticles can be synthesized either in the liquid phase (chemical methods), gas phase, or through biological methods. Liquid phase synthesis includes [27], [42], [141]–[144]:

- The co-precipitation of an aqueous solution of ferrous and ferric ions by a base
- Sol-gel method
- Hydrothermal preparation
- Thermal decomposition
- Solvothermal process
- Sonochemical reactions
- Colloidal method and
- Emulsion technique

Gas phase synthesis includes aerosol/vapor process, arc discharge, flame hydrolysis, spray pyrolysis, and laser pyrolysis [83]. Biological preparations normally include plant mediation, protein mediation, fungal mediation, and bacterial mediation processes [145]. Bacterial-based synthesis of iron oxide nanoparticles is rather new in biotechnology and at its early development stage. Use of biomaterials with other foreign bodies in this synthesis makes it eco-friendly, low cost, and also green synthesis route. During the biological synthesis, iron oxide nanoparticles are enabling to cap themselves by the protein or biological molecules present in the organism. This biological capping/coating not only prevents them from aggregation but also increases their biocompatibility with no toxic effects. Different bacteria such as *Actinobacter sp.* and *Bacillus* also have been successfully employed in the synthesis of IONPs with good biocompatibility [146], [147]. Aerosol or vapor technology is also in use for the large-scale synthesis of magnetite, maghemite, and wüstite. This technology is based on flame spray and laser pyrolysis. The size of the nanoparticles in this method can be adjusted by controlling the fuel-air-ratio during the combustion process [148]. Liquid phase preparation (chemical methods) of SPIO-NPs is more attractive for the researchers. About 90% attentions have been paid to such methods due to their numerous benefits and only about 2% attention is devoted towards the biological synthesis due to their limitations [145].

All possible magnetic nanoparticles synthesis in a liquid medium and by different physical methods so far is grouped in figure 18.

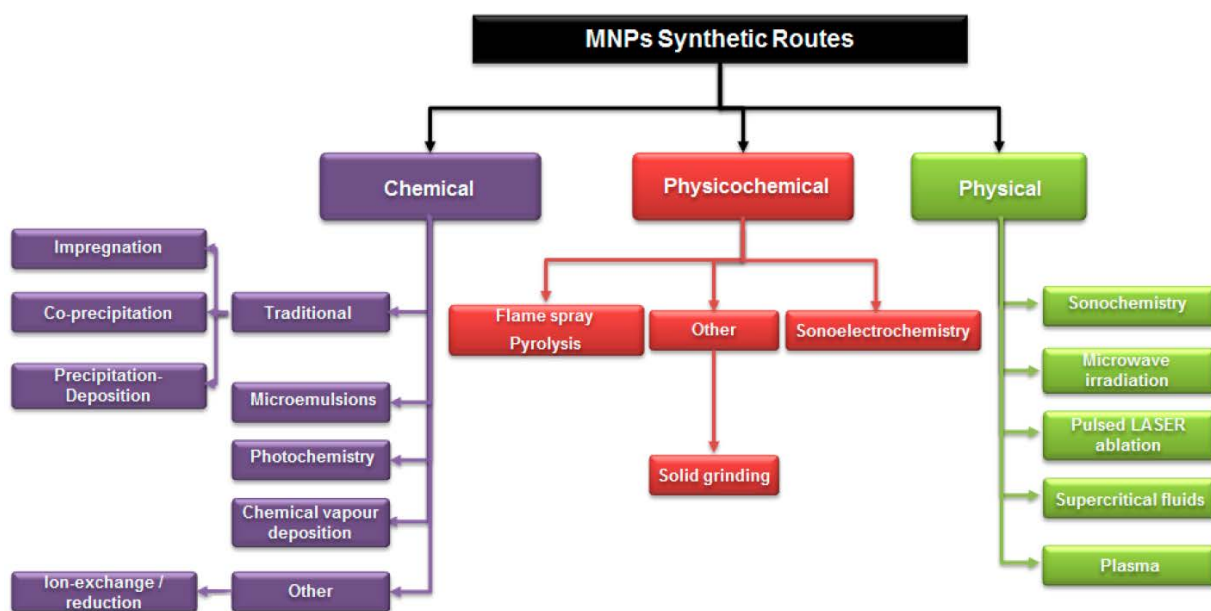


Figure 18: Various other chemical, physicochemical, and physical syntheses methods of magnetic nanoparticles

Synthesis of SPIO-NPs other than liquid phase is not suitable to use them in different biomedical applications. This might be due to their relatively large particle size and wide size distribution. In liquid phase synthesis, control over particle size and size distribution is much easy (figure 19). Usually, it is possible to solubilize with water at final functionalization process or at an intermediate step of NPs synthesis and this water solubilization is basically the coupling colloiddally unstable NPs with hydrophilic ligands in order to form a stable NPs suspension [125].

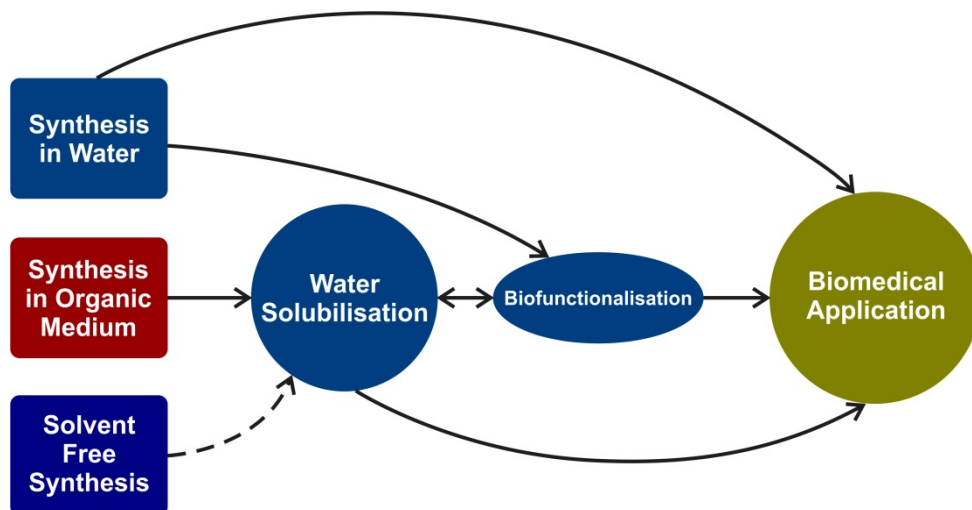


Figure 19: Biomedically applicable nanoparticles are only synthesis in the liquid phase, the dotted line is the indication for that material which synthesized in solid state and non-water soluble, therefore, they may have no suitability for the biomedical applications [125]

3.2 Liquid phase synthesis of Fe₃O₄ nanoparticles

Liquid phase chemical synthesis methods are simple and tractable with appreciable size control, composition, and even the shape of the nanoparticles in a simple way [13].

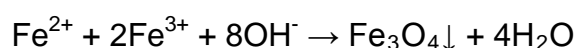
3.2.1 Co-precipitation method

Iron oxide (Fe₃O₄) nanoparticles can be synthesized through a co-precipitation of Fe²⁺ and Fe³⁺ aqueous salt solutions by the addition of a base. Liquid phase synthesis methods other than the co-precipitation, mostly involve special equipment, high temperatures, impurities removal is a tedious job, which makes them time-consuming and their operational cost is high. Among these, co-precipitation is the simplest one and can also be used for a variety of metal oxides [149]. To optimize the precipitation process, various influencing parameters should be controlled. The control of size, shape, and nanoparticles nature during the co-precipitation method strongly depends on the types of salts, pH, temperature, supersaturation, mixing velocity (stirring), and Fe²⁺/Fe³⁺ molar ratio [150]–[152]; with the increase or decrease in a nanoparticles size, eventually their magnetic saturation is affected [153]. Increase in stirring velocity also influence the magnetic properties because NPs size decreases and Fe:O ratio can be disturbed at higher stirring velocity [154].

Among various size controlling factors, alkali and pH are the prominent factors because Fe²⁺ and Fe³⁺ ions are liable to hydrolyze at different pH during the course of a precipitation reaction. When the solution pH > 3, Fe³⁺ ions start to hydrolyze in ferric hydroxide and Fe²⁺ ions hydrolyze at pH 7 but at higher pH 9, the formation of Fe(OH)₂ takes place [155]. Nucleation, growth and some secondary processes such as agglomeration, attrition, and breakage are regarded as the main stages of a co-precipitation method [156], [157]. Synthesis of a large number of magnetic nanoparticles and the involvement of toxic free chemicals are the main advantages of this technique. However, control over the magnetic particles size and size distribution is limited due to the poor control over the nucleation during the nuclei growth [6], [48], [155]–[157]. Spherical magnetic nanoparticles with a size range of 30 to 100 nm can be synthesized by this method. It is possible to prepare various sizes (from 2 to 15 nm) nanoparticles by adjusting the pH and ionic strength of the reaction medium [13].

Fe₃O₄ nanoparticles are prepared by adding a base to an aqueous mixture of Fe²⁺ and Fe³⁺ chlorides at a 1:2 molar ratio. It has been pointed out that Fe₃O₄ nanoparticles precipitated by using NH₄OH instead of NaOH have a better crystallinity, high saturation magnetization and small size [83]. To synthesize the magnetite nanoparticles from a solution of ferrous/ferric mixed salts by a co-precipitation method, there are two different ways of adding precursors: (i) normal co-precipitation and (ii) reverse co-precipitation. In the former method, the pH value gradually increases, because of dropwise addition of an alkali solution to the mixed metal solution. In the later method, pH of the solution is suddenly increases due to

the abrupt addition of mixed metal solutions into an alkaline solution and thus restricts the Fe_3O_4 nanoparticles growth due to better oxidation prevention with closer stoichiometry which leads to much easy control over the particle size and also size distribution [158]–[160]. The precipitate is black in color (figure 20). It is not possible to get monodisperse nanoparticles and also obtained nanoparticles cannot be of same size and shape; these facts cause for the polydispersity in the nano-suspension either synthesized by any method. For many biological applications, it needs to reduce the polydispersity which can be accomplished either during synthesis or by post-synthesis treatment. Usually, post-synthesis purification is employed and for this purpose, magnetic nanoparticles can be separated from their suspension by a magnetic field separation, chromatography, centrifugation, electrophoresis, membrane filtration, or by an extraction [161]. An overall chemical reaction equation representing the Fe_3O_4 precipitation reaction can be written as:



In order to control the reaction kinetics, the oxygen-free environment must be required and this can be achieved by bubbling the N_2 gas through reaction media. Nitrogen gas not only prevents the oxidation of magnetite but also reduces the nanoparticles size as compared with the reactions without removing the O_2 gas [83].

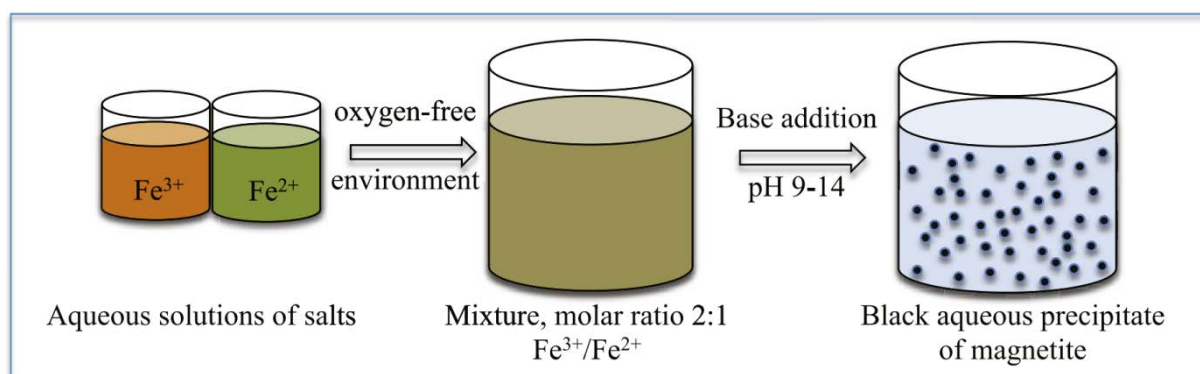


Figure 20: Co-precipitation method using Fe^{2+} and Fe^{3+} aqueous solutions of salts with the addition of a base

The nomenclature of NPs can be categorized into two terms; single-core (individual NPs) and multi-core (collection of single-cores which are held by a matrix lead to a fixed structure) [65]. The pioneer work in the precipitation was done by Massart [162], [163] in the early 1980s and since then it is under an intensive research. FeCl_2 and FeCl_3 salts (with a molar ratio of $\text{Fe}^{2+}/\text{Fe}^{3+}=1:2$) were precipitated in an alkaline media (NaOH , NH_3 , etc.). Particle sizes between 6 nm and 17 nm with a poorly defined morphology and large size dispersion were obtained by this method. Another approach to synthesize magnetite nanoparticles is the precipitation process starting from partially reduced ferric chloride aqueous (FeCl_3) solution. Qu et al. [164] prepared spherical magnetite nanoparticles with a mean diameter of 10 nm. They used Na_2SO_3 as a reducing agent which partially reduced the ferric ions to ferrous before alkanizing. The optimal initial $\text{Fe}^{3+}/\text{SO}_3^{2-}$ ratio was 3 for producing the

nanoparticles with small diameters. The process did not require the rinsing of the reaction system with an inert gas, but there was a release of toxic SO_2 gas. One of the main advantages of using the reduction-co-precipitation process in the presence of Na_2SO_3 as a reducing agent was that the ferrous ions were not used in the starting solution. Thus, further oxidizing of the magnetite nanoparticles was prevented.

In an interesting study by Mahdavi et al. [165] optimum pH, initial temperature, and reaction stirring speed for oleic acid-mediated magnetite precipitation were investigated in order to get small sized nanoparticles and also a narrow size distribution through a simple co-precipitation method. Their results show an increase in crystallite size from 8.3 nm to 13.2 nm when the reaction temperature was in the range of 25-45 °C. When the reaction temperature exceeded from 45-85 °C, reduction in size was observed due to the greater polydispersity in the reaction. In their study, the size of iron oxide nanoparticles was reduced with the increase in pH value but up to 11. After a further increase in pH above 11, size of MNPs increased with the increase in a solution pH above 11, because hydrolysis of Fe^{3+} occurred. When mechanical stirring speed was increased from 400 rpm to 800 rpm (or 1.21 m/s to 2.42 m/s stirrer tip speed), average diameter size was decreased from 9.41 nm to 7.83 nm due to the fact that solution was dispersed into smaller droplets because, at higher stirring speed, energy transformation to the suspension medium is also enhanced. Also, the saturation magnetization (M_s) of the Fe_3O_4 MNPs was increased from 58.60 to 78.00 emu/g with the increase of the nanoparticle sizes from 7.83 to 9.41 nm. On similar grounds, Khan et al. [166], [167] conducted a comprehensive study to get the small particles size with narrow size distribution. The reducing agent was NaOH for their precipitation. Increase in particle size from 8.98 nm to 14.55 nm was investigated with the increase in reaction temperature from 25-90 °C. MNPs size was enhanced directly with the increase in pH of the solution. Stirring speed also had a great influence on MNPs size and size distribution. The decrease in size from 14.55 nm to 9.39 nm was observed with the increase in mechanical stirring velocity from 500 rpm to 1100 rpm (or 1.51 m/s to 3.34 m/s stirrer tip speed).

Lai et al. [168] prepared oleic acid (OA) coated SPIO-NPs to study their colloidal stability by the co-precipitation of ferrous and ferric salts in the presence of ammonium hydroxide as a precipitating agent. Increase in zeta potential values from -29.8 mV to -58.1 mV of the MNPs was observed when 1.2 wt.% oleic acid was used to modify these MNPs. After 21 days, the colloidal stability against agglomeration of oleic acid decorated MNPs was much higher than the undecorated MNPs. Authors attributed that this stability is due to the presence of oleate secondary layer on the OA-decorated MNPs surface. With the increase in a zeta potential of OA-coated MNPs (-58.1 mV), the hydrodynamic MNPs size was also decreased from 61.04 nm to 41.90 nm. Kandpal et al. [169] synthesized iron oxide nanoparticles by a co-precipitation reaction using ammonium hydroxide as a base and their results show that nanoparticles in the range of 5.67-8.16 nm were synthesized. Further, their study

shows that some of the synthesized nanoparticles were tended to agglomerate to make a big one of about 20-50 nm.

Faiyas et al. [170] synthesized Fe_3O_4 nanoparticles by a co-precipitation in an aqueous solution containing ferrous and ferric salts with 1:2 molar ratio. Solution pH was varying with the addition of ammonia as a base. It was found that the value of pH influences the reaction mechanism for the formation of Fe_3O_4 . Furthermore, the addition of mercaptoethanol significantly reduced the crystalline size of Fe_3O_4 nanoparticles from 15.03 to 8.02 nm. Rana et al. [171] worked for MNPs size increment with the increase in a solution pH and found that the physical properties were affected due to the size difference. Wang et al. [172] synthesized Fe_3O_4 nanoparticles with a new route by an oxidation-precipitation method using monoethanolamine (MEA) as a precipitation agent and by a modified co-precipitation method. Average crystallite size from 8.9 to 10.6 nm was recorded by the oxidation-precipitation method and from 6.7 to 8.6 nm for synthesized through a modified co-precipitation method. They concluded that nanoparticles possess larger crystallite sizes at higher pH and at a higher temperature. Eivari et al. [173] manufactured SPIO-NPs by a co-precipitation method with $\text{Fe}^{2+}/\text{Fe}^{3+}$ 1:2 molar ratio using NaOH as a reducing agent. XRD analysis confirmed the crystallite size of 11 nm and the saturation magnetization was 69 emu/g for this size range. In another study by Eivari et al. [174], SPIO-NPs were prepared to have a size of 8 to 17 nm using ammonia as a base solution. The reaction temperature was found to be a significant process parameter for nanoparticle size. In their study, it was revealed that change in ammonia concentration did not show any impact on the particle size.

Magnetite nanoparticles were successfully synthesized by Petcharoen et al. [175] in the size range of 10–40 nm yielding at 0-90 °C. Ammonia solution (25 wt%) as a precipitating media and iron chlorides salts as precursors were used. Freshly prepared MNPs were coated with oleic acid and hexanoic acid. Results they obtained show that the nanoparticle size was influenced by reaction temperature and thus by adjusting the reaction temperature, a narrow size distribution was achieved. It was found that bare and hexanoic acid coated magnetite sizes increased and the oleic acid coated magnetite size decreased with the increase in reaction temperature.

The effect of pressure on the size of magnetite nanoparticles synthesized by a co-precipitation is not studied well. Yazdani et al. [176] performed a study to show the significant effect of pressure on the MNPs size. Precursors of their study were $\text{Fe}_2(\text{SO}_4)_3 \cdot 5\text{H}_2\text{O}$ and $\text{FeSO}_4 \cdot 7\text{H}_2\text{O}$ salts and NaOH was used as a precipitating agent. When the reaction pressure was raised from 300 to 6000 mbar, an increase in particle size from 8.3 to 16.8 nm was recorded accordingly at 25 °C. So, by adjusting the pressure during the magnetite nanoparticles synthesis, it is possible to control the crystals size. In their work by Palanisamy et al. [177], olive oil coated MNPs were synthesized with NaOH as a basic solution. The average particle size obtained was 19.2 nm which was also confirmed by XRD and TEM analysis. The saturation

magnetization 40 emu/g was recorded with the superparamagnetic behavior of their prepared samples.

To study the effect of different bases like NaOH, KOH, and $(C_2H_5)_4NOH$ (tetraethylammonium hydroxide), a comprehensive study was performed by Mascolo et al. [178] with $FeCl_3 \cdot 6H_2O$, $FeCl_2 \cdot 4H_2O$ as starting solutions at room temperature. The average particle size was 11 nm for their experiments. The decrease in size with different choices of bases was directly related to the factors of pH and the slow/fast addition of the basic solution to a mixture of Fe^{2+} and Fe^{3+} ions. The decrease in MNPs size was dependent on the nature of the basic solution in accordance with the sequence $(C_2H_5)_4NOH < KOH < NaOH$. First ever synthesis of octanoic acid coated MNPs was conducted by Salavatri-Niasari et al. [179]. The pH of the reaction solution was monitored by dropwise addition of NaOH at 80 °C. The particle diameter they obtained was 25 nm with a saturation magnetization of 15.92 emu/g. Forced mixing in precipitation method was studied by Zhu et al. [28] and their findings revealed that magnetic iron oxide nanoparticles with size less than 6 nm were achieved under the condition of $Fe^{2+}/Fe^{3+} = 0.5$.

In an innovative method, Khalil [180] prepared Fe_3O_4 NPs using only one precursor of iron (III) salt. In his method, the iron salt molar ratio was achieved by reducing iron (III) using a potassium iodide solution. Iodine formed was filtered and then hydrolyzed the filtrate using 25% NH_4OH solution at pH 9-11. Magnetic nanoparticles were of 6.3 ± 0.2 nm in size. Influence of stirring velocity during the precipitation of iron (II) and iron (III) salt was studied by Valenzuela et al. [181]. The stirring speed they chose was 10,000 rpm, 18,000 rpm, and 25,000 rpm and precipitation were carried out in an N_2 gas environment. The obtained nanoparticles were around 10 nm. Riaz et al. [182] synthesized SPIO-NPs via a co-precipitation route in the absence of nitrogen gas and also without using any surfactant. Effect of pH on the particle size was studied and the solution pH was controlled by adding sodium hydroxide specifically. Vibrating sample magnetometer and SEM analysis confirmed that synthesized NPs were in the superparamagnetic regime. Nanoparticles size was increased with the increase in pH that might be due to some agglomeration. Another surfactant-free synthesis of monodispersed IONPs was conducted by Yang et al. [183]. They used 5.4M NaOH and 1.34M $NH_3 \cdot H_2O$ solutions as precipitating agents. Size of the obtained IONPs was about 10 nm and they concluded that IONPs with $NH_3 \cdot H_2O$ as a precipitant was smaller than those synthesized by NaOH but on a contrast, magnetic properties of the IONPs synthesized through NaOH were much better. The effect of pH on a structure and magnetic properties of MNPs was also studied by Ramadan et al. [184]. Main precursors were iron chlorides salts; 33% ammonia and 1.5M NaOH were used as precipitating agents. The reaction was carried out in the presence of nitrogen gas to avoid any agglomeration. The large variation in the pH value, from 8 to 12.5, showed the insignificant effect on the particle size, which changed from 10 to 13 nm in their results. Decrease in the saturation magnetization of synthesized magnetite nanoparticles from 72 emu/g at pH 8 down to 44 emu/g at pH 12.5 was

recorded. SPIO-NPs with less than 10 nm size were manufactured by Liu et al. [185] through the co-precipitation of Fe^{2+} and Fe^{3+} ions in the presence of NH_4OH basic media. Nanoparticle size was increased directly with the increase in reaction temperature. Corresponding saturation magnetizations were also increased due to the increase in a nanoparticle size.

Entire transformation to Fe_3O_4 NPs involved during precipitation is not well described in all above and similar to these studies; only a small part of information related to this transformation is available. First ever phase transformation of the intermediates of goethite ($\alpha\text{-FeOOH}$), akaganeite ($\beta\text{-FeOOH}$), and lepidocrocite ($\gamma\text{-FeOOH}$) was studied by Ahn et al. [186]. Main precursors were iron salts and aqueous ammonia and pH of the solution was monitored by slightly addition of ammonia. The molar ratio of ammonia to iron ions ($R = [\text{NH}_3]/[\text{Fe}^{2+} + \text{Fe}^{3+}]$) was varied with the sampling intervals of 0.5 or 0.1 in R. At $R=2$, TEM and FTIR confirmed the formation of akaganeite and goethite and indicates that akaganeite and goethite are the intermediates for magnetite (Fe_3O_4). Goethite was dissolved at $R=2.1$ and indicates that continuous addition of a base may be expressed as “akaganeite \rightarrow goethite \rightarrow magnetite”. Transformation of goethite to hematite is due to the dehydration and local rearrangement processes. When an abrupt base was added and $R < 2.67$, it was found that the transformation (taking place with changes from low pH to high pH) occurred as “akaganeite \rightarrow goethite \rightarrow (hematite \rightarrow maghemite) \rightarrow magnetite” on continuous addition of a base. This complete transformation of Fe_3O_4 NPs during the precipitation process can be explained through a complete reaction in figure 21.

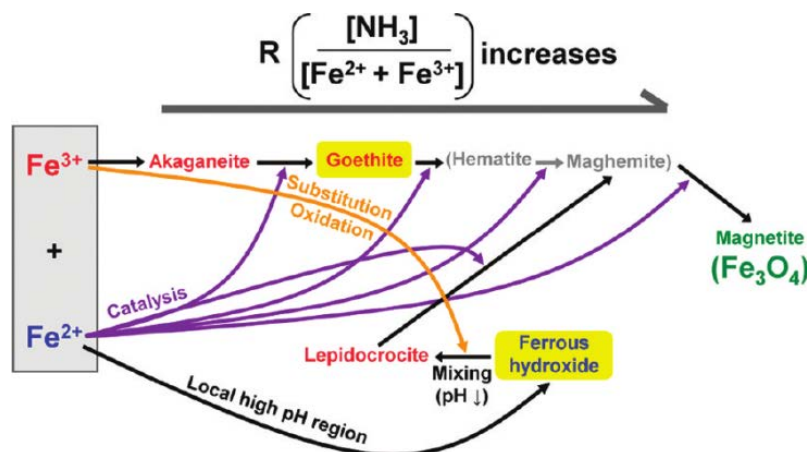


Figure 21: A representation of formation pathways of magnetite nanoparticles by a co-precipitation method. Yellow areas indicate the main intermediate phases [186]

3.2.2 Sol-gel method

The synthesis of metal oxide nanoparticles by a sol-gel method has proven a versatile one because it allows the large variety of metal oxide relatively at a low temperature via the processing of metal salt or metal alkoxide precursors. The structure and composition of nano-oxides by this method depends on the preparation conditions, the nature of precursors, the ion source, and pH [187]. This method is

based on the hydroxylation and condensation of molecular precursors in the solution, originating a “sol” of nanometric particles. This “sol” is then dried or “gelled” by a solvent removal or by a chemical reaction to get three-dimensional metal oxide network. Gel properties depend upon the structure created during the sol stage of the sol-gel process [13]. It offers various *advantages* [13], [187] like: (i) tailor-made materials due to good control over the process, (ii) homogeneous multicomponent system due to the mixing in a liquid medium, (iii) low temperature for material processing, (iv) monodispersity, and (v) possibility to obtain pure amorphous phase. The *drawback* of this method is that it generates 3D oxide networks, and hence, it is limited in its efficiency regarding the formation of independent, disconnected nanosized particles. It may also have contamination from a by-product of reactions so, the post-treatment should be done [13].

Kayani et al. [188] conducted a study to see the effect of annealing temperature on the synthesis of magnetic nanoparticles using the sol-gel method and then characterized by XRD, SEM, and FTIR to confirm their findings. Their results show that the magnetic nanoparticle size was increased from 34 nm to 36.7 nm on increasing the annealing temperature from 400 to 1000 °C. Xu et al. [141] synthesized magnetic nanoparticles by sol-gel method and they characterized phase structure, morphology, particle size, and chemical composition of the synthesis product. They concluded that particle size increased with the increase in synthesis temperature and can be easily tailored by controlling the synthesis temperature.

Lu et al. [189] presented a sol-gel approach for superparamagnetic iron oxide nanoparticles with an amorphous silica. Commercially available ferrofluids were successfully employed for this coating. The important finding in their results was that the silica coating can be controlled in the range of 2-100 nm by changing the concentration of the sol-gel solution.

3.2.3 Hydrothermal method

The hydrothermal method follows a heterogeneous reaction system in the presence of an aqueous solvent or mineralizers under high pressure greater than 2000 psi and temperature can be above 200 °C [187]. Nanoparticle size is greatly affected by the nature of the solvent, temperature, reaction, and the aging time. Nanoparticles size increases when the time of reaction increases and also with the increase in the amount of water. The formation of the particles follows two steps: nucleation and crystal growth. For higher temperatures, the nucleation process is faster than the crystal growth followed by the decrease in particle size. Crystal growth dominates at longer reaction time so, liable to larger particles [83], [117]. A detailed study has been carried out to investigate the effects of precursor concentration, temperature, and residence time on particle size and morphology in this method. The hydrothermal method also relies on the ability of water to hydrolyze and dehydrate metal salts on elevated conditions, and very low solubility of the resulting metal oxides in water at

these conditions to generate supersaturation. The particle size and size distribution increase with the precursor concentration.

3.2.4 Microemulsion method

Microemulsions are a transparent and stable mixture of oil (small droplets), water and amphiphilic molecule, a so-called surfactant which frequently makes a combination with the co-surfactant [15] and is under research for the synthesis of iron oxide nanoparticles with a narrow size distribution [10]. The role of surfactant is to lower down the interfacial tension in order to stabilize the droplets [187]. Reagents lie in water droplets which react as nanoreactors. Microemulsions can be categorized into two classes: (i) direct (oil dispersed in water, o/w) (figure 22a) and (ii) reversed (water dispersed in oil, w/o) (figure 22b), subsequently used for the synthesis of iron oxide nanoparticles with tailored shape and size [15]. Among various synthesizing techniques of iron oxide nanoparticles, the microemulsion method is considered as the most powerful one due to its transparent and importantly thermodynamically stable colloidal dispersion of two immiscible liquids [190]. Iron oxide nanoparticles of size range 1-100 nm with a narrow size distribution can be achieved by varying the concentration of the dispersed phase and surfactant. This can be attributed that surfactant molecules surrounded the spherical droplets of water and thus act like cages for growing particles and thereby reduces the particle size. So, in this way it is possible to control the size of spherical iron oxide nanoparticles by controlling over the size of the water pool (W_o value, the water-to-surfactant molar ratio) [83]. Simply speaking, higher the W_o value, larger will be the particles size [10], [83]. Common investigated surfactants used in microemulsion process for the synthesis of iron oxide nanoparticles are sodium bis(2-ethylhexylsulfosuccinate) (AOT), cetyltrimethylammonium bromide (CTAB), sodium dodecyl sulfate (SDS), and poly(vinylpyrrolidone) (PVP) [15], [82].

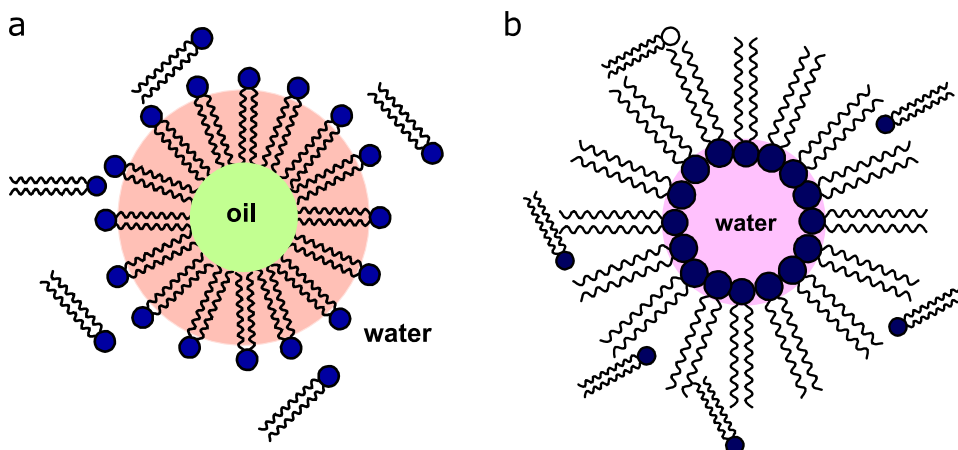


Figure 22: Typical microemulsion process: a) oil in water microemulsion b) water in oil microemulsion [191]

The advantages, disadvantages, and other characteristics of the above four synthesis methods are briefly summarized in the following table 5. No doubt, co-precipitation is considered a preferred route by many researchers due to its low cost and simplicity of the synthesis. In terms of size control and narrow size distribution, the sol-gel method seems to have some advantages. Alternatively, microemulsions can also be used to synthesize monodispersed nanoparticles with various morphologies. The requirement of a large amount of solvent is among its main disadvantages. Little attention is devoted to the hydrothermal synthesis method, therefore, a relatively little-explored method for the magnetic nanoparticles synthesis, although high-quality nanoparticles can be obtained by this method. In short, co-precipitation and microemulsions are the most studied, and they can be industrialized for a large-scale synthesis.

Table 5: Comparison of different characteristic features of the iron oxide nanoparticles fabricated through different methods

Method	Reaction conditions	Characteristics of the obtained products	Advantages	Disadvantages
Co-precipitation	Temperature: 20-90 °C Duration: minutes Solvent: water	Shape control: not good Size distribution: broad Crystallinity: poor polydispersity Magnetization value: 20-80 emu/g	Simple, easy, and low-cost method to obtain large quantities of products	Difficult to avoid nucleation during the reaction and the obtained particles have a weak magnetic response
Sol-gel	Temperature: 200-400 °C Duration: hours Solvent: organic compounds	Shape control: good Size distribution: narrow Crystallinity: high polydispersity Magnetization value: 10-40 emu/g	Particles of desired shape and length can be synthesized, useful making hybrid nanoparticles	Product usually contains sol-gel matrix components at their surfaces
Hydrothermal	Temperature: 150-220 °C Duration: hours-days Solvent: water-ethanol	Shape control: very good Size distribution: very narrow Crystallinity: high monodispersity Magnetization value: up to 93 emu/g	The use of organic reagents are waived, relatively cost-effective and high yield of products	Relative slow kinetic due to the relatively low temperature used
Microemulsion	Temperature: 20-50 °C Duration: hours Solvent: organic compounds	Shape control: good Size distribution: narrow Crystallinity: low monodispersity Magnetization value: up to 113 emu/g	The particles obtained are generally very uniform without going through and size-selection process	A large amount of solvent to synthesize appreciable amount of nanomaterials

3.3 Surface coating of SPIO-NPs

The following step after the synthesis of SPIO-NPs core is their coating. In an aqueous phase, iron atoms on the SPIO-NPs surface act as Lewis acids, and coordinate with water molecules to accept lone-pair electrons; therefore, the SPIO-NPs surface possesses hydroxyl groups, due to water dissociation. Consequently, with the change in a solution pH, their surface charge tends to change. It has already been discussed that NPs have a greater surface-to-volume ratio; so, the combination of hydrophobic interactions and van der Waals forces may lead to the SPIO-NPs aggregation, following by minimizing the total surface and interfacial energy. Beyond

a critical size, the phenomena of precipitation happen which is due to the growth of the progressive cluster and the role of gravitation is dominant. When NPs injected intravenously for biomedical use, this aggregation could be dangerous; thus such surface properties are not compatible with the biological applications, even though the magnetic susceptibility increases with the cluster size. To avoid such danger of aggregation and also to become suitable candidates for theragnostic applications, the surface of SPIO-NPs must be modified. In order to avoid aggregation, strategies for the stabilization of the NPs surface mainly use organic molecules [192]. For a successful coating of MNPs, the coating materials must be non-toxic in nature and also biocompatible. The coating material must provide a straightforward targeted drug delivery and should be capable to attach different molecules like enzymes, proteins, and various drugs [193]. The small size of the nanoparticles is very important for their numerous applications rather in biomedical or industrial so, during the recent time, a number of different novel surface coating strategies have been developed in order to coat small sized NPs with different small molecules without altering their small size and also their stability [194].

Another reason for nanoparticles coating is that surface atoms increases with a decrease in size below 100 nm, so, reactivity increases and makes these NPs highly reactive sites. At a point when the percentage of atoms on the NPs surface increases, they become more reactive yet less stable. That's the reason that NPs are liable to undergo agglomeration [195]. The strong magnetic attraction between the NPs, van der Waals forces, and high energy surfaces are responsible for the bared surface NPs agglomeration. These agglomerated NPs are easily eliminated by the reticuloendothelial system (RES). High concentration of Fe ions is very toxic to many organisms from Fe dissolution. These disadvantages are minimized by providing a shell around the NPs surfaces which makes them hydrophilic, compatible with bio-environments, and also functionalized [145].

The other advantages of NPs surface coatings are: protection of NPs surface from oxidation in order to avoid their agglomeration, increases the blood circulation time by avoiding rapidly clearance by the reticuloendothelial system; and increases the internalization efficiency by target cells [11], [196]. No doubt, naked SPIO-NPs are stable in high- and low- pH suspensions and not in the neutral pH, for biomedical (*in vivo*) applications, SPIO-NPs must be coated preferably with the polymers.

For monodisperse NPs to have a hydrophobic surface, they are usually coated with the long-chain hydrocarbons. Surfactant addition is achieved through the adsorption of amphiphilic molecules that contain both a hydrophobic segment (forms a double layer structure with the original hydrocarbon chain) and a hydrophilic component (to render NPs water soluble) [135].

In view of many strategies and their potential uses, efforts have been made to synthesize IONPs-based materials (figure 23) [15], [197]: (1) core-shell structure

(encapsulation of iron oxide core-shell takes place with an inorganic or organic coating for tendering this core-shell biocompatible. Sometimes it is also referred to yolk structure because core on NPs not located in the center), (2) matrix-disperse structure (magnetic nanoparticles are likely to be dispersed in a continuous amorphous matrix in order to prevent SPIO-NPs from aggregation into large ferromagnetic species), (3) Janus structure (for Janus structures, one side consists on magnetic iron oxide nanoparticles and the other side is a functional material, and (4) colloidal structure (in this type of structure, nanoparticle core is located right in the center of two functional materials).

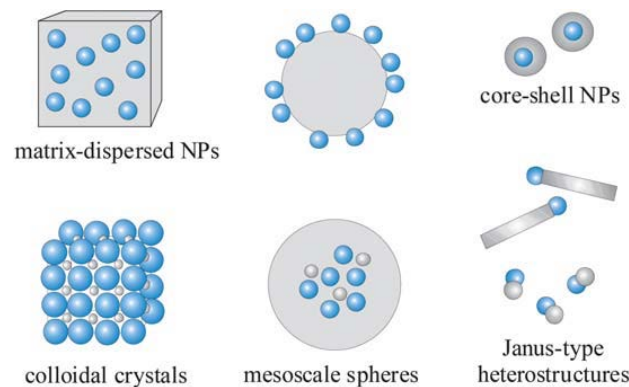


Figure 23: Morphologies of magnetic nanocomposite materials are depicted. Blue spheres representing magnetic NPs. Grey color is for the non-magnetic entities and matrix materials. The nonmagnetic entity may provide the composite material with further functionalities and properties, providing multifunctional hybrid system [197]

Coating of the SPIO-NPs can be achieved by two ways; either during their synthesis (*in-situ*) or by post-synthesis (*ex-situ*). For *in-situ* coating approach, nanoparticles growth can be eliminated [83]. Post-synthesis addition of coating materials is a most common way for inorganic NPs cores, introducing an electrostatic or a steric hindrance. While during coating, apart from the favorable characteristics of the SPIO-NPs, care must be taken to preserve the desired properties of uncoated SPIO-NPs. During the post-synthesis strategy, re-aggregation of nanoparticles is usually observed and therefore, the stabilization of nanoparticles is very limited (figure 24). For this reason, *in-situ* strategies are preferred over the *ex-situ* strategies due to their number of technological advantages [63].

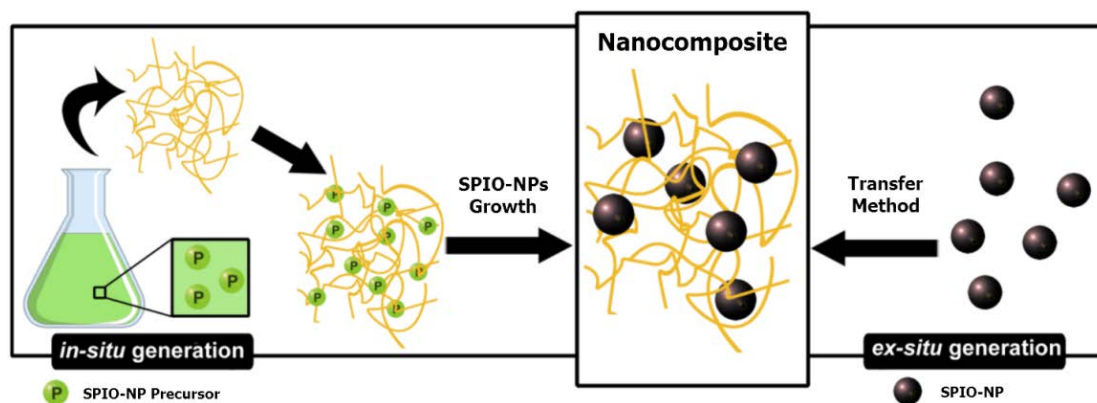


Figure 24: Comparison of *in-situ* and *ex-situ* surface coating strategies of SPIO-NPs [63]

Functionality and biological fate of drug delivery systems (DDSs) are largely influenced by the suitable coating of SPIO-NPs to be used for *in vivo* applications. For instance, iron oxide nanoparticles coated with hydrophilic polymers, including PEG, poloxamers, polysorbate 20 and 80, tocopheryl PEG succinate and dextran, can form a protein layer at the particle's surface by providing a hydrophilic cloud and neutral chains. As an example, PEGylation improves the pharmacokinetic profile of DDSs and thus enhances the accumulation of nanoscale DDS in the tumor, coating with polysorbates, dextran, and DEAE-Dextran has been shown to improve the blood-brain barrier (BBB) transport of NPs [76]. Silica, carbon, gold and other polymer coating materials of lipids, proteins, dendrimers, gelatin, dextran, chitosan, pullulan, poly(ethylene-co-vinyl acetate), poly(vinylpyrrolidone) (PVP), poly(lactide-co-glycolide acid) PLGA, or poly(vinyl alcohol) (PVA) are often employed for NPs coating. Other special molecules, such as bifunctional 2,3-dimercaptosuccinic acids (DMSA), dopamine, and silanes, are also investigated for the NPs functionalization. Alginate and poly(acrylic acid) (PAA) can also be used to stabilize nanostructures which offer long-term stability and biocompatibility [76], [135].

In the first section of this chapter, it already has been discussed that stabilization of fine magnetic nanoparticles is the result of two acting forces on these: electrostatic and steric forces. It is tedious to predict and quantity of steric forces. But diffusion knowledge can lead to electrostatic forces [198]. Figure 25 shows the different organic and inorganic materials used for (above) coating and stabilization of MNPs. For the present work, Tween 80, Dextran 70,000, and DEAE-Dextran are chosen for the surface coating of the synthesized SPIO-NPs. These surface masking agents are non-toxic, biocompatible, and also biodegradable with the human and animal body and with the extended vascular retention. These compounds also show the prolonged blood residence time so, they are promising candidates for biomedical applications. Further, FDA already approved such coated nanoparticle systems for the human trials.

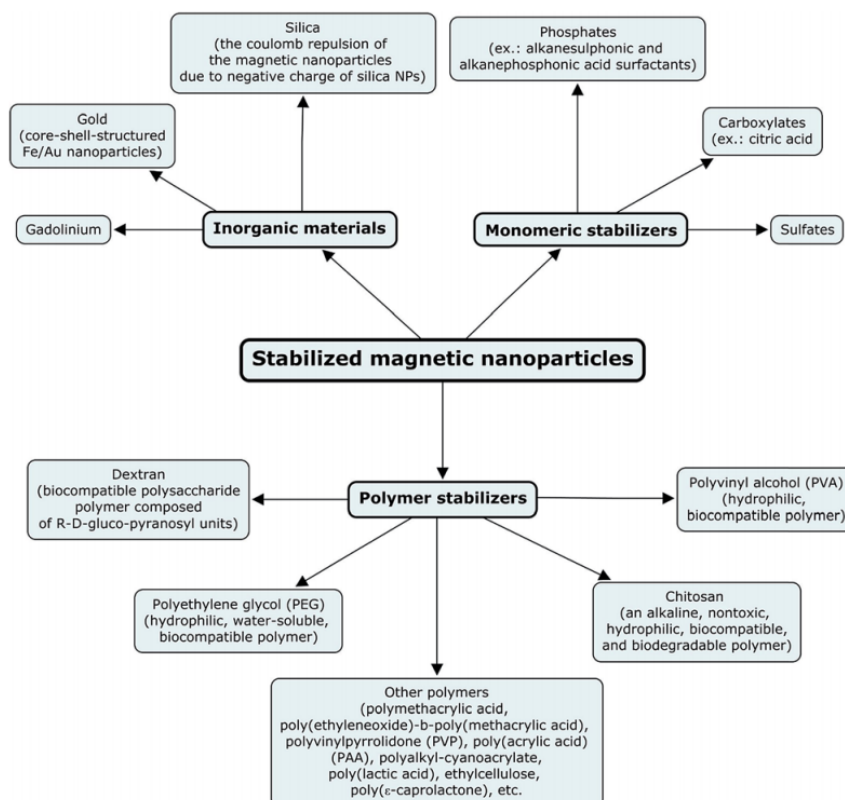


Figure 25: A plethora of different compounds which are used for the coating and stabilization of magnetic nanoparticles [198]

3.3.1 Polymeric superparamagnetic iron oxide nanoparticles

Properties of SPIO-NPs can be altered by their polymeric coating. Polymers improve the biocompatibility and also act as stabilizers [197]. For the situation of stabilization of SPIO-NPs with polymers, the polymers on the surface act as a protective barrier to avoid the interaction between the particles. Such protection is the most efficient when using amphiphilic copolymers bearing a hydrophilic segment with a tendency to spread into the aqueous medium and a hydrophobic segment anchoring onto the particle surface [199]. Coating with polymers not only increases the repulsive forces but also used for a well-defined material composite for their potential applications in various fields. Polymeric coating can be done by any of the two approaches: (1) irreversible attachment of polymers can be achieved by chemisorption and (2) initiation of polymers is the directly from the particle surface. A thin layer of polymer over the magnetic nanoparticles is not enough and NPs coated with single or double layers are not very protective to air and thus liable easily to leach by an acidic solution [83].

For polymeric NPs, nanocapsules are linked to vesicular systems in which a drug is confined in a cavity consisting of an inner liquid core surrounded by a polymeric membrane. In this case, the active substance is likely to be usually dissolved in the inner core, but may also be adsorbed to the capsule surface [200], [201] (figure 26).

Generally, nanospheres are a type of matrix particles (entire solid mass particles). The characteristics of these nanospheres are based on their size from several tenths to nanometers [202].

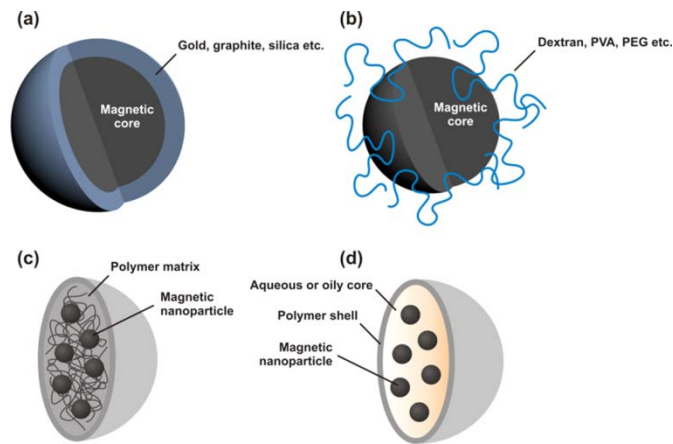


Figure 26: Schematic representation of the stabilization of MNPs by surface coating with inorganic (a) or organic materials (b) or by encapsulation into nanospheres (c) or nanocapsules (d) [199]

Polymeric NPs should have easy to synthesize under the form of polymer nanoparticles, inexpensive, biocompatible, non-toxic or non-immunogenic, and biodegradable or it should be eliminated in a shorter time from the body [202], [203]. Other advantages associated with the polymeric NPs are listed below [204]:

- They increase the stability and of any volatile pharmaceutical agents;
- Offers a significant improvement over traditional oral and intravenous methods of administration for more efficiency and effectivity;
- Particularly delivers a higher concentration of medicines to a targeted site;
- Due to the choice of various polymers and ability of drug release, polymeric nanoparticles are the best candidates for the drug delivery applications and for the cancer treatment.

Different polymers used for the polymeric nanoparticles preparation are [200], [205]:

- Natural biodegradable polymers;
- Synthetic biodegradable polymers;
- Non-biodegradable polymers.

Table 6 consists of various possible examples of such above different polymers.

Table 6: Polymers used for polymeric nanoparticles

Classification of polymers	Examples
Natural biodegradable polymers	Alginates, Chitosan, Gelatin, Dextran, Pullulan, Gliadin
Synthetic biodegradable polymers	Pre-polymerized: poly (ϵ -caprolactone) (PECL), poly (lactic acid) (PLA), poly (lactide-co-glycolide acid) (PLGA), polystyrene, poly (isobutylcyanoacrylates) (PICA), poly (butylcyanoacrylate) (PBCA), polyhexalcyanoacrylate (PHCA), and copolymer of aminoalkylmethacrylate
Nonbiodegradable polymers	Polymethylmethacrylate(PMMA),Polymethylacrylate (PMA)

Among the noninvasive approaches, polymeric nanoparticles, especially poly (butylcyanoacrylate) (PBCA) play an important role and therefore, have attained much attention of the researchers. PBCA nanoparticles are considered as low toxic and most rapidly biodegradable synthetic polymers and thus used for *in vivo* applications. As a result of this rapid degradation and the low molecular weight of the polymer in the nanoparticle, the polymer material has a tendency to rapidly eliminate from the body. Delivering the drug to an infected part without changing the drug characteristics is considered as the main advantage of PBCA nanoparticles.

3.3.2 Synthesis methods of polymer coated NPs

Polymeric nanoparticles can be synthesized either by performed polymers or through monomers for classical polymerization or poly reactions. Nanoparticles from the dispersion of performed polymers can be accomplished by a solvent evaporation, salting-out, dialysis, and a supercritical fluid technology. Directly, polymeric nanoparticles can also be synthesized by the polymerization of monomers using various polymerization techniques such as microemulsion, mini-emulsion, surfactant-free emulsion, and an interfacial polymerization. Illustration of these different synthesis techniques is depicted in figure 27. Different factors like type of polymeric system, the area of application, size requirement, etc. should be kept in account while the selection of suitable methods. For a polymeric system that needs to be developed for an application in the biomedical or environmental fields where it should be completely free from the additives or reactants such as surfactants or traces of organic solvents. In such case, techniques like RESS (rapid expansion of a supercritical solution) or RESOLV (rapid expansion of a supercritical solution into a liquid solvent) can be selected, as they do not utilize any surfactant or an organic solvent during the polymeric nanoparticles preparation [204], [206].

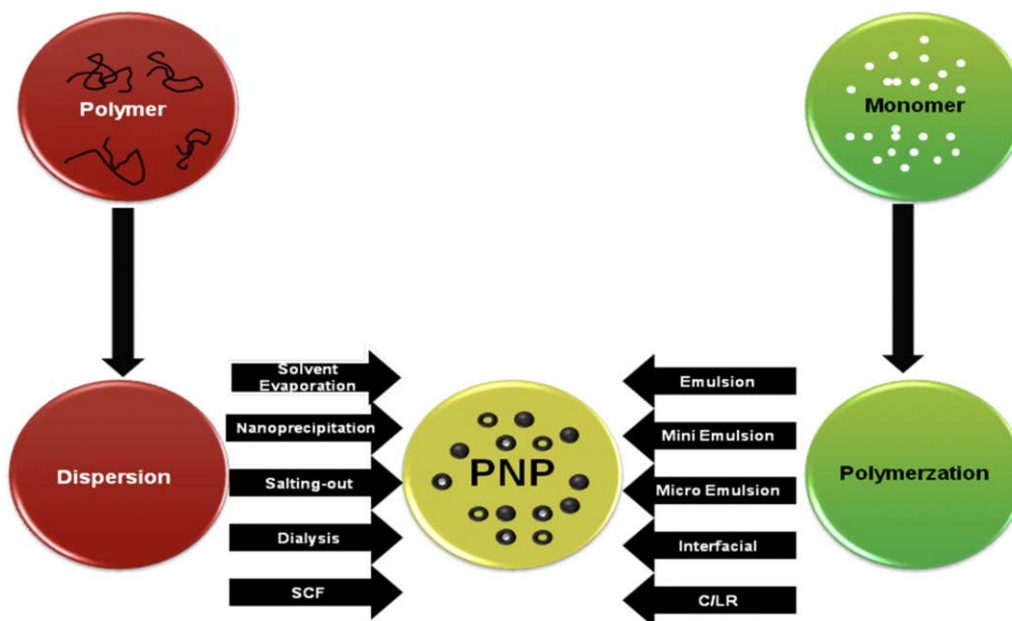


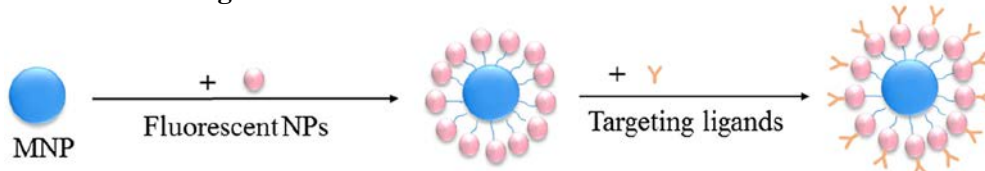
Figure 27: Various techniques used for the preparation of different polymer nanoparticles. SCF: supercritical fluid technology, C/LR: controlled/living radical [206]

3.3.3 Fluorescent magnetic nanoparticles

It already has been demonstrated that for various biomedical applications, SPIO-NPs need to be coated with the special surface coating materials, which must be not only non-toxic and biocompatible but also allowing a targeted delivery with the particle localization in a cell. These surface coated NPs can also be conjugated with another functional biomolecule like fluorescent markers. Combination of superparamagnetic iron oxide nanoparticles with fluorescent properties in one nanocomposite is extensively applicable in *in vitro* and *in vivo* applications like cell migration monitoring in the body, guide magnetically the site-specific targeting of drug loaded MNPs [207], biodetection, and biosensing in various medicinal and biological applications for different targeted nanoscale photonic devices monitor by an external magnetic field. Fluorescent-magnetic nanocomposites are also used in other multimodal diagnostic and therapeutic applications like MRI, fluorescent microscopy, cancer therapy, and in the magnetic hyperthermia treatment. Besides these advantages, there are some disadvantages associated with them; namely lack of photostability and broad emission spectra which is responsible for their multiplexing ability [208]. Fluorescent iron oxide nanoparticles are also referred as Quantum Dots (QDs) and these QDs are used as 'quantum dots imaging' which was introduced in 1980 and it allows the cell tracking which makes them potential candidates in different biological and various medical applications [209], [210]. The significant biomedical applications of these QDs are because of their broad absorption band, narrow emission spectra, high photoluminescence intensity, and an active surface area [211]. Basically, QDs are nanometer-size crystals of inorganic semiconductors. Development of fluorescent-magnetic nanocomposites is at a relatively early stage and a still challenging. Generally, surface modification with fluorescence dyes is possible during as well as after finishing the precipitation process. In the first process, simultaneously

incorporation and adsorption of the added modifying chemicals, in the second process option, the adsorption process is studied. Among the several synthesis approaches, the first approach (figure 28) involves the synthesis and functionality of fluorescence and magnetic species individually and then conjugates with each other either by a covalent binding or by an electrostatic interaction directly (inorganic or coupling synthesis).

Covalent bonding



Electrostatic interaction

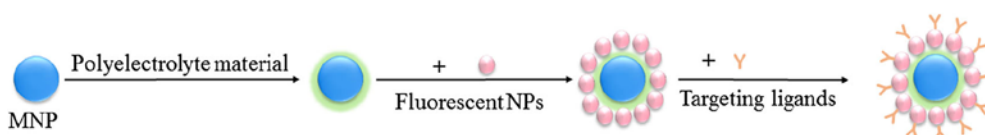


Figure 28: Schematic representation of targeted magnetic fluorescent nanoparticles. Covalent bonding (top) and electrostatic interaction (bottom) with conjugation of targeted ligands [212]

A second route (figure 29) involves the incorporation of magnetic and fluorescent nanoparticles into polymeric or silica scaffolds (encapsulation) because fluorescent materials form a core-shell structure onto the surface of the magnetic core. The third approach is the direct reaction between the fluorescent and the magnetic domain. To combine fluorescence and superparamagnetism into a single nanosystem, covalent immobilization through targeted surface functionalization is one of the most widely used approaches [212]–[216].

Encapsulation

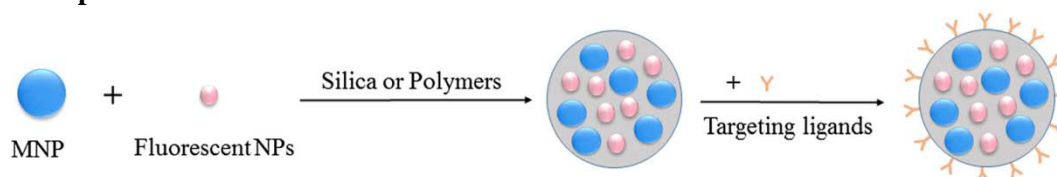


Figure 29: Fluorescent magnetic nanoparticles synthesis by encapsulation. The magnetic core is encapsulated with silica or polymers to form a new composite in which targeted ligands are conjugated onto the surface of magnetic-fluorescent nanoparticles [212]

Different features of the fluorescence labelled MNPs are strongly dependent on their preparation method and these two important aspects are sketched out in a proceeding figure 30.

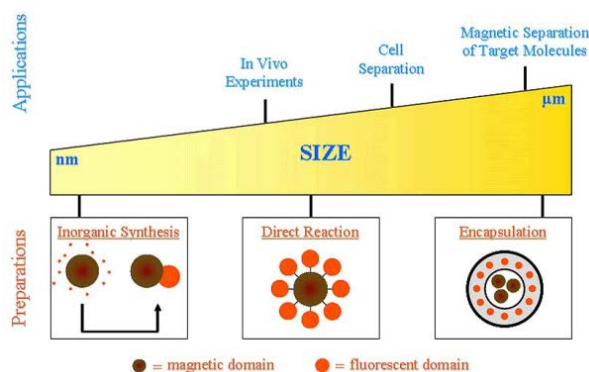


Figure 30: Preparation of fluorescent magnetic nanoparticles with the relation and focusing to their fields of applications [215]

For the synthesis of fluorescent magnetic nanoparticles, quenching of the fluorophore and oxidation on the metal particle surface by the magnetic core is a vital risk and therefore, they would have less stability at a higher temperature. Coating the magnetic core with a stable isolating shell such as polymer matrix prior to the introduction of the fluorescent molecule or by attaching an appropriate spacer to the fluorophore can be used for this problem. Most fluorescent magnetic nanoparticles thus have a core-shell structure [217], [218]. Different fluorescence markers – rhodamine B [213], [219], 4',6-Diamidino-2-phenylindole (DAPI) (to prove the NPs in the cell tissue) [214], and fluorescein isothiocyanate FITC [217], [220] have been reported in the literature. Recently, Sarkar et al. [221] synthesized surface modified SPIO-NPs using eucalyptus leaves as a source of carbon with the size range of 10-42 nm at higher temperatures. They showed that carbon-NPs composite became fluorescent and hydrophilic due to change in physical and chemical properties of SPIO-NPs.

3.4 Liquid-liquid phase transfer of magnetic nanoparticles

The phenomenon of agglomeration of nanoparticles is due to the salt concentration and a resulting zeta potential because the liquid aqueous phase is highly unstable [222]. Water-based nanoparticles synthesis has a problem with ionic interactions which are typically overcome by using low reactant concentration or the fact of use of stabilizers which are difficult to remove from final suspension [223]. Further, many specific applications of MNPs are dependent on the transferring of newly synthesized nanoparticles to a non-polar environment from a polar environment, or vice versa, for the advantages offered by in this specific environment which based on processing considerations. It is possible to synthesize magnetic nanoparticles directly into the organic phase, or inversely from the aqueous phase to the organic phase [224]. To convert micron-scale particles in a non-aqueous liquid phase, in conventional strategies includes after synthesis filtration, drying and then disperse again in the non-aqueous liquid. For the case of nanoparticles, this strategy is not applicable due to the quality and functionality of the nanoparticles and thus a different strategy must be applied for the nanoparticles less than 100 nm which is direct liquid-liquid phase transfer. Some fundamental work has been done in this field in the presence of a

suitable surfactant and this surfactant makes possible the wetting of iron oxide nanoparticles surface from hydrophilic to hydrophobic and also avidness of nanoparticle agglomeration is possible in an organic phase by using this surfactant. For the successful phase transfer, surfactant introduces in a non-aqueous phase [225].

3.4.1 Theoretical background of liquid-liquid phase transfer process

The phase transfer by sedimentation through a liquid-liquid interface uses the gravitational or the centrifugal force to create a relative movement of the particles within the suspension liquid. The second liquid, which receives the particles, must have a higher specific weight than the releasing liquid and the receiving and releasing liquids have to be non-miscible. Due to this immiscible behavior, the aqueous suspension (releasing liquid) is laminated above the receiving organic liquid. The gravitational or centrifugal field is responsible to start the sedimentation process started. Destabilization of the dispersion must be carried out in order to increase the sedimentation speed in the releasing aqueous phase. By adjusting the pH to change the surface charge and the zeta potential, this goal can be achieved [225]. It must be considered in account that high pH in the aqueous phase and a threshold surfactant concentration is a core of the phase transfer process [222]. The deagglomeration is a function of the geometry, the surface coverage, the adsorption equilibrium, and the solubility of a surfactant in the organic phase.

For a successful phase transfer process and liquid-liquid interface deagglomeration, surfactant plays a vital role thus; selection of suitable surfactant is a key point for the phase transfer. The chosen surfactant must be adsorbed at the particle surface and due to this adsorption, surface properties change from hydrophilic to hydrophobic. To achieve this desired hydrophobicity, the applied surfactants are mainly non-soluble or poorly soluble in the releasing water phase. It is important that the surfactant is dosed into the organic phase and vigorous stirring is required for the mass transport of the particles to the liquid-liquid interface [222]. The adsorption isotherm of the surfactant on the particle surface determines the required concentration in the receiving organic liquid. The adsorption isotherm of the surfactant on the particle surface determines the required concentration in the receiving organic liquid.

It is impossible to conduct a phase transfer in the absence of surfactant molecules because wetting of particles cannot take place due to the missing adsorption of the surface of nanoparticles and thus change from hydrophilic to a hydrophobic is impossible [222].

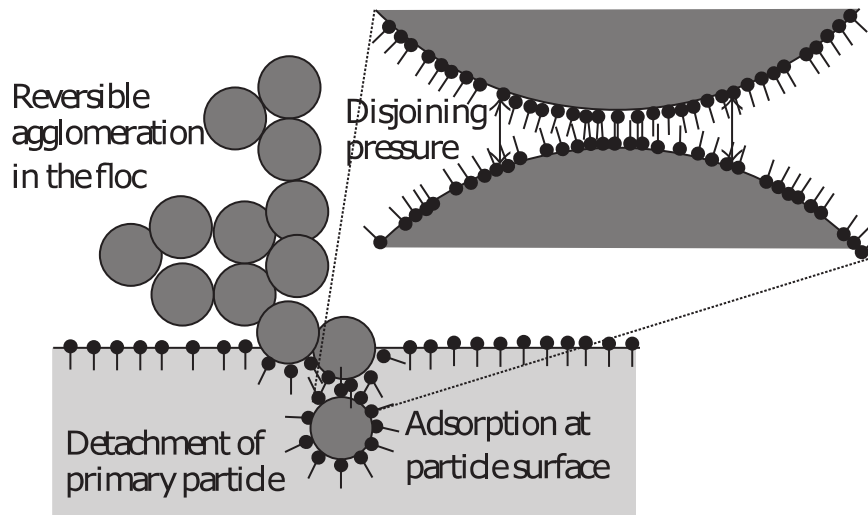


Figure 31: Phase transfer mechanism and deagglomeration in the presence of surfactant molecules present at the interface [225]

The phase transfer begins when the sedimenting floc arrives at the liquid-liquid interface. The surfactant concentration is enriched at the interface. The hydrophilic end of the surfactant reaches into the aqueous phase. This end adsorbs at the surface of the primary particle which is still incorporated in the floc. It is supposed that the adsorption occurs at the entire particle surface including that area, which is in closest distance to the neighboring primary particle (figure 31). The adsorption of surfactant molecules in this narrow gap creates an additional repulsive force, the disjoining pressure. When a certain surface coverage with surfactant molecules is reached, the disjoining pressure has the possibility to liberate the primary particles from the floc [225]. Fundamental steps involved in the liquid-liquid phase transfer process are shown in figure 32.

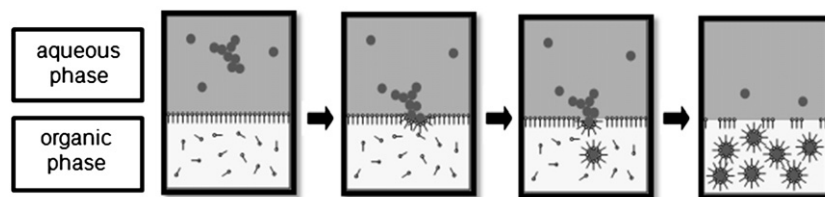


Figure 32: Fundamental steps which are used in the mechanism process during the phase transfer [222]

3.4.2 Preliminary work of liquid-liquid phase transfer of magnetic nanoparticles

A precise research already has been conducted on the phase transfer of silver and gold nanoparticles [226]–[228]. Most of the methods of nanoparticles phase transfer focus on the transfer of particles from aqueous to an organic phase [223]. On the other side, only few literature deals with the iron oxide nanoparticles phase transfer study. Machunsky et al. [229] presented the first experimental results on this topic. The magnetite NPs were synthesized through a co-precipitation method of iron salts with a $\text{Fe}^{3+}/\text{Fe}^{2+}$ molar ratio of 2:1. The precipitation medium was a concentrated

ammonium hydroxide. Phase transfer phenomenon was strongly dependent on the ammonia concentration in the aqueous phase. At low ammonia concentration, no any phase transfer was observed and at higher ammonia concentration, the particles were more hydrophobized and thus transferred completely into dichloromethane. For the phase transfer study, two setups were used; measuring beaker (study under gravitational field) and a laboratory scale centrifuges. In their experiments, the aqueous phase was laminated above the organic phase which was dichloromethane and oleic acid used as a surfactant was introduced into the organic phase. The resulting suspension had a pH-value of 5 and a zeta potential of +10 mV. For experiments in centrifuges, the studies different concentration and fatty acids (linoleic and ricinoleic acid) in dichloromethane phase and 0.02 mass % ammonia was used in the aqueous phase. Fatty acids and magnetite had a legend exchange reaction which further leads to the adsorption of the fatty acids on the particles surfaces. Their experimental setups are shown in the following figure 33.

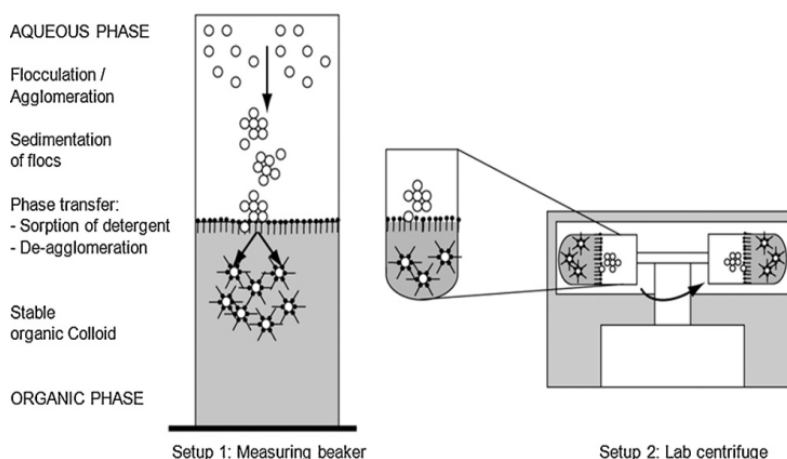


Figure 33: Experimental setups for the phase transfer in the gravitational field (1) and centrifuge field (2) [229]

Presence of ammonia in an aqueous phase plays a vital role during the liquid-liquid phase transfer. A white layer was formed in the dichloromethane phase at a higher ammonia concentration of about 10 mass % (figure 34a) which produces a negative impact on phase transfer. Centrifugation leads to a kind of phase inversion: the entire aqueous phase then contains the described white layer (figure 34b). This white layer was due to the reaction between the ammonia and fatty acids and as a result, an oleate formed which leads to the formation of an emulsion consisting of the two liquid phases. Determination of the ammonia concentration in a dichloromethane after centrifugation confirmed the phase transfer yield of 100%.

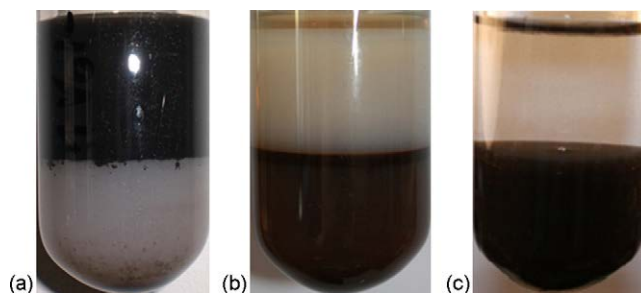


Figure 34: A view of the phase behavior at 10 mass % (a, b) comparison with 0.01 mass % (c) ammonia in the aqueous phase [229]

Erlar et al. [222] conducted a comprehensive study to find the surfactant concentration in an organic phase for magnetite nanoparticles phase transfer. Being a decision step that either phase adsorption will happen or not, surfactant concentration is a key factor. Their synthesis strategy was also based on the co-precipitation reaction of iron salts. Phase transfer study was done in dichloromethane as the organic phase. The interesting part of their study was the evaluation of different surfactants like ricinoleic and caprylic acids. Their study concluded that an increase in surfactant concentration of ricinoleic acid in the organic phase, increase in the stabilization of primary particles was observed. Also, with an increase in surfactant concentration, the rise in fatty acids ability to disintegrate the primary particles was observed. The study also concluded that 3 mass % of the ricinoleic acid is the optimal concentration at which primary particles mass transfer was observed and beyond this optimal concentration, no further yield of primary particles was recorded and a further increase in concentration leads to less yield of primary particles. In contrast, by using threshold level of 3 mass % of caprylic acid as a surfactant, only about 5% primary particles transfer was observed and with an increase in surfactant concentration up to 4 mass %, increase in primary particles was prominent and beyond the increase in surfactant concentration, no primary particles yield was recorded. This is because of the fact that caprylic acid has a different structure than the ricinoleic acid. Caprylic acid is a fatty acid with no additional functional group and ricinoleic acid has a shorter carbon-chain length and therefore, noticeably higher threshold concentration. Consequently, these structural differences have an effect on the adsorption mechanism at the liquid-liquid interface and also on the particle size distribution.

Rudolph et al. [230] also conducted a phase transfer study of magnetite nanoparticles synthesized with the help of a co-precipitation method of iron salts followed by a phase transfer from an aqueous to dichloromethane (DCM) in the presence of a ricinoleic acid as a surfactant. The surfactant ratio (mass of ricinoleic acid per mass of magnetite) was 0.2. By using the surfactant concentration 2% in the organic phase, they observed 100% particles transfer.

Mériguet et al. [231] tested various pure surfactants in their phase transfer study of maghemite nanoparticles. An anionic surfactant, the sodium hexadecylsulfonate and several cationic surfactants didodecyldimethylammonium bromide (DDAB),

benzyltrimethylhexadecylammonium bromide (BHAB), and octadecyltrimethylammonium bromide (OTAB) were chosen. Two solvents were tested: cyclohexane and a nonane. In the case of cyclohexane, it was known that the studied particles can be stabilized using oleic acid or phosphate esters as surfactants. The study concluded with the remarks that didodecyldimethylammonium bromide (DDAB) was an appropriate surfactant to stabilize maghemite nanoparticles. A direct liquid-liquid phase transfer method was developed to transfer these nanoparticles from a water-based suspension to a cyclohexane-based media. Further, their method was reproducible and controlling of free and adsorbed surfactant was possible and no agglomeration was observed.

In an interesting study by Wang et al. [232], oleic acid stabilized iron oxide nanoparticles irreversibly transferred into α -cyclodextrin (CD) containing aqueous media from hexane suspension. Iron oxide nanoparticles were synthesized by a thermal decomposition of iron pentacarbonyl in octyl ether in the presence of oleic acid as a surfactant. Phase transfer phenomenon was studied by vigorous stirring the hexane suspension of iron oxide nanoparticles and equal volume of the α -cyclodextrin aqueous solution under room temperature. After 20 hours stirring, the top hexane layer became colorless and was discarded; while the bottom aqueous layer collected and centrifuged twice to obtain the transparent yellowish nanoparticles suspension. Their experimental scheme is illustrated in figure 35.



Figure 35: Chemical structure of (a) oleic acid, (b) α -cyclodextrin (CD), and (c) organic to aqueous phase transfer process of oleic acid modified nanoparticles when using α -CD as surface modifying agent [232]

Figure 36 is a dispersion of iron oxide nanoparticles in hexane and their phase transfer was achieved by the centrifugation. After a successful phase transfer, the yellowish color was disappeared to a pellucid liquid and vice versa (figure 36a and figure 36b). If the aggregation of nanoparticles takes place, then the solution appeared as a blur liquid and solid nanoparticles were collected by the centrifugation, figure 36c.

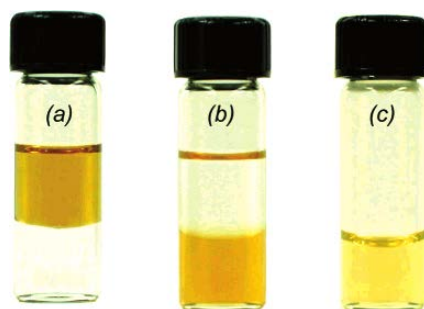


Figure 36: Photographs of a two-phase mixture of iron oxide nanoparticles (a) before and (b) after phase transfer, and (c) aqueous suspension after centrifuge. The top layers were hexane and bottom layers were α -CD aqueous solutions [232]

3.5 Toxicity of magnetic nanoparticles

Initially, it was considered that iron oxide nanoparticles are biocompatible and non-toxic in nature. The reason for this consideration was that these nanoparticles resemble with the endogenous iron of a human body. With the introduction of IONPs as MRI contrast agents first time during the late 1980s, subsequently their toxic studies initiated during this period [233]. It has been mentioned that FDA only approved the IONPs for their biomedical uses, but their pharmaceutical applications are somehow limited because the knowledge is still lacking to understand the mechanism of these magnetite NPs penetration into tissues, organs and tumors, and especially about their degree of toxicity [234]. Excessive accumulation of iron in the cells not only contributes as a catalyst but also a reactant to free-radical generation which is a cause of toxicity and it is discussed in the next section.

For the development of safe MNPs system, it should be considered that there is no any threat to the patients after the nanoparticles administration. Individual component toxicity and also the toxicity of whole nanoparticles need to be carefully evaluated before such administrations in patients. There are two factors for evaluating the NPs toxicity: (1) how the synthesized nanoparticles system will interact with the body during its functional lifetime, and (2) how independent components will effect during the biodegradation and liver processing [85]. SPIO-NPs have the ability to cross the blood-brain barrier but with damaging the neural functions. These nanoparticles also produce mutations when crossing the nuclear membrane [235]. Apart from the various pros and cons of *in vivo* utilization of iron oxide nanoparticles, only SPIO-NPs are the promising magnetic nanoparticles for their clinical applications to date [236]. Many researchers have been demonstrated that SPIO-NPs having varying physicochemical characteristics are responsible for low toxicity or cytotoxicity. Due to very small SPIO-NPs size, they can enter into the human body through many means; inhalation, ingestion, skin penetration etc. and ultimately to the body tissues and then to body organs [237]. It is a point to ponder that SPIO-NPs does not show profound toxic effects to the human body so, to get maximum benefits from their biomedical applications, it is an attractive field of research [235]. All possible side effects to the human body through various inlet means are summarized in figure 37.

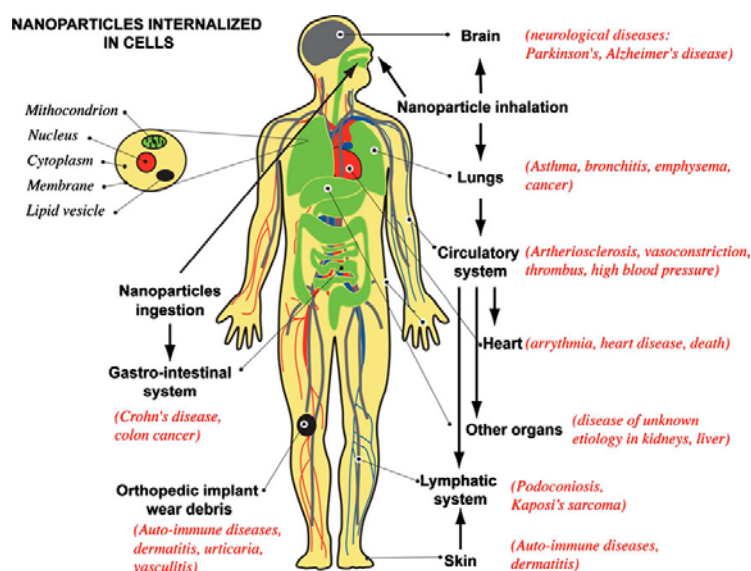


Figure 37: Possible exposure pathways of NPs to the human body, different affected organs, and associated diseases from epidemiological, *in vivo* and *in vitro* studies are shown [237]

3.5.1 Mechanism of toxicity

It has been established that excessive reactive oxygen species (ROS), including free radicals such as the superoxide anion, hydroxyl radicals, and the non-radical hydrogen peroxide are the cause of most intracellular and *in vivo* toxicities from SPIO-NPs. As SPIO-NPs possess very small size but the large surface area, thus it is liable to generate free radicals due to the redox cycling process at their surface. Production of ROS with a high chemical reactivity is the result of exposure of cells to NPs at a higher dose. Greater will be the chemical reactivity, larger will be the ROS production. Generation of ROS is also possible when leaching of iron ions takes place because of enzymatic degradation from NPs surface. Generated ROS then transferred into the cell interiors and produces oxidative stress responsible for pro-inflammatory mediators. The oxidative stress reflects an imbalance between the systemic manifestation of ROS and a biological system's ability to readily detoxify the reactive intermediates or repair the resulting damage. A higher level of ROS produced in the body will be liable to damage cells by peroxidizing lipids, disrupting DNA, modulating gene transcription, altering proteins, and resulting in a decline in a physiological function and cell apoptosis/death (figure 38) [238], [239]. There are four primary sources of oxidative stress in response to iron oxide nanoparticles: (1) direct ROS generation from the nanoparticle surface, (2) ROS production via leaching of iron molecules from nanoparticle surface, (3) altering mitochondrial and other organelle functions, and (4) induction of cell signaling pathways [239], [240]. When SPIO-NPs are magnetically guided to a particular tissue or an organ, then it could be possible that accumulation or overloading of these magnetic particles due to the high concentration and localization on the surface of that specific tissue/organ induce toxicity which is grouped as non-ROS toxicity [240], [241]. This excessive accumulation of the SPIO-NPs may cause a risk of liver cancer [240].

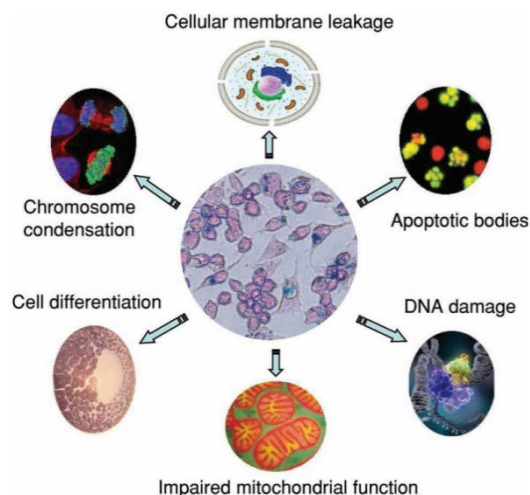


Figure 38: Potential toxic effects of superparamagnetic iron oxide nanoparticles due to the ROS generation [239]

3.5.2 *In vitro* toxicity of magnetic iron oxide nanoparticles

The *in vitro* methods are highly valuable for the safety assessment of SPIO-NPs. The *in vitro* models for the toxicity of MNPs are considered as the best models in respect of their ability to reproduce results and also of inexpensive. It also has the main advantage that the use of animals in such models can be avoided. Four main techniques are in use for the evaluation of nanoparticles cytotoxicity: (1) *in vitro* assays for the cell viability differentiation (3-(4,5-dimethylthiazol-2-yl)-2,5-diphenyltetrazolium bromide (MTT) and lactate dehydrogenase (LDH) assays of cell membrane), (2) electronic microscopy and atomic force microscopy intracellular localization, (3) *in vitro* hemolysis, and (4) gene expression analysis [239], [242]. Large surface area and chemical nature of the SPIO-NPs are also responsible for affecting the *in vitro* assays. Further, size, shape, charge, and aggregation of SPIO-NPs produce significant impacts on *in vitro* toxicity studies [233].

Choices of cells, growing conditions, and sample preparation assay are important factors to get the possible toxicity of SPIO-NPs. For a successful SPIO-NPs toxicity assessment, four tests are employed; cytotoxicity, oxidative stress, inflammatory reactions, and genotoxicity. If there is no any significant or minor outcome of these tests, then samples are forwarded for their *in vivo* toxicity assessment in animal models. In case of good findings of these *in vivo* tests, then it is possible to register the products with federal drug administration (FDA) for their clinical approval trials in humans [243].

3.5.3 *In vivo* toxicity of magnetic iron oxide nanoparticles

The term of biocompatibility is associated with SPIO-NPs, which means that no any dangerous effects when employed in *in vivo*. Use of SPIO-NPs in *in vivo* studies is very complex. On the penetration of SPIO-NPs into the body system, they distributed into various organs and they remain in same nanostructure or liable to become

metabolized. When iron oxide nanoparticles are introduced into the body through many administrative routes, then these NPs start to accumulate in liver, spleen, testis, and brain after intravenous injection. This phenomenon occurs due to the adsorption of SPIO-NPs on the interaction with biological components like proteins and cells. To design a successful and biocompatible with least or zero toxic effect of SPIO-NPs, a thorough pharmacokinetics study (absorption, distribution, metabolism, and excretion) would be required [239], [241]. Besides the involvement of many ethical issues and also of an expensive process, *in vivo* understanding of the SPIO-NPs is an integral part of research today [233].

Apart from the toxicity evaluation of NPs, good manufacturing practice (GMP)-compliance synthesis and SPIO-NPs production costs are also considered for the successful bench-to bedside clinical approvals in humans [244]. All these step-to-step regulatory approval processes are shown in figure 39 with important deliberations of each approval route. Toxicity plays a crucial role in the decision making process.

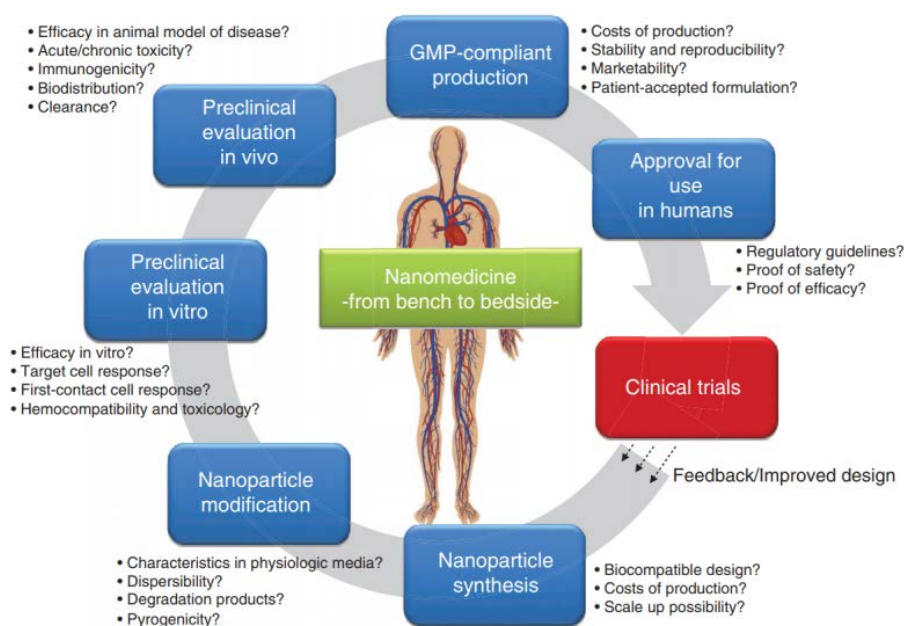


Figure 39: Step-to-step NPs-based bench-to bedside approval procedure in humans. Important deliberations of each approval route are highlighted [244].

MTT assay (3-(4,5-dimethylthiazol-2-yl)-2,5-diphenyltetrazolium bromide) is a widely and effectively used technique for *in vitro* qualitatively and quantitatively cytotoxicity of iron oxide nanoparticles [245]–[248], but it is still very crucial to estimate about the toxicity of the SPIO-NPs in an appropriate model [249]. The MTT assay principle is based on the estimation of the number of living cells by determining the capacity of cell mitochondrial reductase on converting the yellow MTT agent into purple formazan crystals by mitochondrial succinate dehydrogenases in viable cells [250], [251]. The cellular uptake of the fluorescent iron oxide nanoparticles is extensively studied in C6 cells for use in imaging and drug delivery of magnetite nanoparticles [252]–[254].

To see the localization of SPIO-NPs within the cells, various techniques are in use like; transmission electron microscopy (TEM), confocal microscopy, and fluorescence microscopy. The cell track and internalization can easily examine by these techniques. But to quantify the amount of SPIO-NPs within the hundreds of cells is not possible by using these techniques [249]. For the SPIO-NPs quantification, ultraviolet spectroscopy (UVS), magnetic particle spectroscopy (MPS), and atomic absorption spectroscopy (AAS) are of particular interest. However, these methods are time consuming and cost-effective [249].

3.5.4 Factors affecting the SPIO-NPs toxicity

In order to find possible toxic effects, it is necessary to measure toxicological end point and starting point, otherwise; it would not be easy to attribute certain nanoparticles properties. Nanoparticle size, dose or concentration, shape, charge, and surface chemistry are among the important factors which directly affects the nanoparticles toxicity. Many crude production processes were liable to produce many industrially used nanoparticles with their huge properties variation. That's why different size and shaped nanoparticles were produced with many toxicological effects. These properties also contribute to the ROS induction in the cells [233], [241], [255]. The concentration of IONPs, the solubility of IONPs, and bilateral interaction of IONPs with bacterial biofilms, tissue or cell type are also produced cell toxicity. According to some published reports, liver, kidney, and lungs are directly affected due to the toxic effects of iron oxide nanoparticles [157], [241].

3.5.4.1 Effect of size

Particle surface is directly in contact with the biological system of the body. So, the size and surface area have significant effects on nanoparticles toxicity. Increase in toxicity is directly linked to the large surface area of SPIO-NPs. Reason for this increase in toxicity is that more chemical molecules will attach this extended surface, so, as a result, reactivity will be enhanced which lead to more toxic effects [256]. There is no any significant difference however in findings of some research in the size-dependent toxicity of the IONPs. For instance, the bare Fe_3O_4 (20–30 nm, surface area: 42 m^2/g) and Fe_3O_4 (5 μm , surface area: 6.8 m^2/g) have toxicity in A549 cells in terms of cell death, mitochondrial damage, and deoxyribonucleic acid (DNA) damage. But, no significant difference was found between the toxicity response by Fe_3O_4 (20–30 nm) and Fe_3O_4 (5 μm) [233]. Nanoparticles of 10-100 nm size are believed to be optimal for intravenous administrations.

3.5.4.2 Effect of dose

For a clinical study and also for real implementations of IONPs, their dose-dependent administration is very crucial in determining the toxic effects; IONPs with higher concentration or dose produces higher toxic risks to the living organisms. For a reliable cytotoxicity data, dose or concentration of incubated IONPs, and their internalization amount over the time is very important [240].

Although SPIO-NPs are approved for the various promising *in vivo* biomedical applications such as drug delivery and MRI; so, it is important to get knowledge about the safe upper threshold limit for their use in such applications. For a cellular uptake of IONPs, their high dose or concentration and longer incubation period will lead to higher cellular iron content which is a toxic sign. In contempt of these side effects, SPIO-NPs produce the least influence on the cell viability and bring out only a very less cell increment in an undergoing apoptosis. For a safe hand and precisely, an optimum low dosage of SPIO-NPs is paramount in preventing the oxidative stress which may cause cell injury and also death [240].

3.5.4.3 Effect of shape

The shape of NPs with varying shapes has response towards toxicity. Nanoparticles exist in different shapes like fibers, spheres, tubes, rings, and planes. The shape of NPs is more important in *in vitro* studies than *in vivo* applications. For *in vivo* application, adverse effects recorded on clearance by macrophages. Cellular uptake is also influenced by the nanoparticles shape. Rounded particles are more easily able to internalize into cells when they compared with the large length-to-radius ratio particles [97].

3.5.4.4 Effect of surface chemistry

The toxicity of SPIO-NPs is also due to the surface chemistry of bare and coated SPIO-NPs. When bare SPIO-NPs interact with the biological system, they are responsible for leaching of more iron, resulting in iron overload. Various studies involved SPIO-NPs synthesized by different methods, coating agents, types of tissues/cells, and cytotoxicity assays. It has been reported that higher toxicity of bare SPIO-NPs than coated SPIO-NPs, however, some research studies have found the toxicity of bare SPIO-NPs is less than that of the (oleate) coated SPIO-NPs. Oleate does not show any toxic effects and cytotoxicity itself but shows toxicity when SPIO-NPs incorporating a layer on bare SPIO-NPs [233].

All biomedical applications associated with SPIO-NPs are increasing in terms of numbers and benefits but the knowledge about their toxicity is still very rare when compared with the fast production of these nanoparticles. Also, the toxicity mechanism is still lacking due to the large variability of particles in different studies. When SPIO-NPs are employed in various biomedical applications, then there is a direct interaction of these particles with the human body and also with the cellular systems so, there is a need to more exposure the nanoparticles adverse effects on human health [257]. Besides these, iron oxide nanoparticles are also responsible for many risks to the environment and to our ecosystems when they are disposed of after their emerging applications. Still, no any reference index is available which can be used as their exposure limits to the environment. To solve all these issues, IONPs toxicity must be evaluated or estimated before their exposure [258].

3.6 Nucleation and growth of nanoparticles

Preparation of monodisperse magnetic nanoparticles in the liquid phase is very challenging because the formation of nanocrystals and their synthesis mechanism is one of the major issues. There are a number of different nanoparticles synthesis methods are in use, but still, very limited knowledge for the nanoparticles generation along with their nuclei structures is available in existing procedures [259]. However, the formation of nuclei in nucleation event is strictly system dependent. For a closed system with a finite number of heterogeneous sites, the nucleation associated with these sites may be transitory, lasting only until all such sites have been titrated by nuclei. For a system with a mechanical agitation aid, a secondary nucleation is expected because daughter fragment growth may form from parent crystals which accelerate the nucleation rate. Here, burst nucleation comes into play which is the difference in rate constants of slow and continuous nucleation with fast autocatalytic surface growth during magnetic nanoparticles synthesis. For a homogeneous nucleation system, the burst nucleation is studied within a system with fresh monomers impart and having least heterogeneous or secondary nucleation [260]. LaMer in the 1950s developed a mechanism to understand the colloidal formation or nanocrystals ideally from a homogeneous supersaturated medium and this mechanism is based on the nucleation and growth study of colloidal sulfur. According to their suggested mechanism, the rapid increase in the concentration of precursors (stage I, figure 40) was observed creating a degree of supersaturation for a time in which larger numbers of nuclei were produced for which the supersaturation surpasses the nucleation at a threshold level (stage II) which reduces the degree of supersaturation. For all particles which grow rapidly and still their concentration are lower the nucleation level, they will continue to grow by the Ostwald ripening; whereby, small nuclei are disfavored and re-dissolve into thermodynamically more stable large nuclei (stage III). The rate of the whole reaction is determined with the slowest step of their growth process [261], [262].

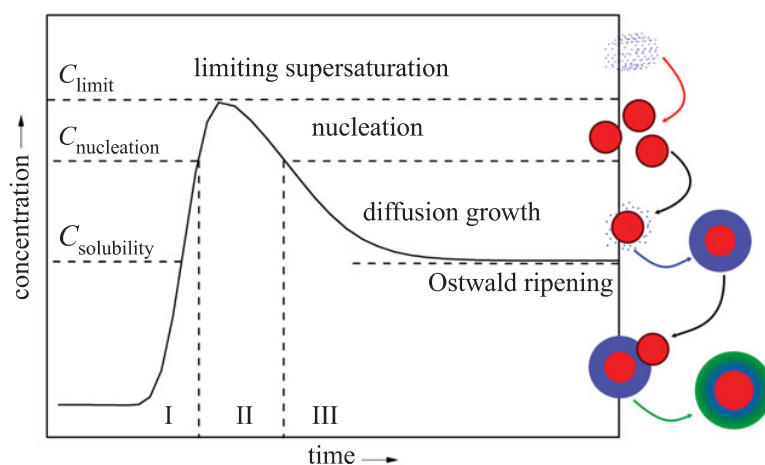


Figure 40: A diagram illustrating the LaMer nucleation and growth model [262]

In order to get monodisperse particles, two basic factors should be considered in their suggested model: (1) high nucleation rate followed by the burst nucleation

formation in short interval of time, thus limiting the Ostwald ripening, and (2) initially nucleation growth rate should be fast in order to reduce the concentration which must be below the rapid nucleation concentration. Low monomer concentration is favored the large critical size and small for higher monomer concentration. For a monomer concentration just below the critical threshold point, small nanocrystals are deposits into larger ones by the Ostwald ripening for broadening the large size distribution. For particles grow at higher monomer concentration, there will be the smaller critical size and small particles will have a fast growth rate which results in the formation of monodisperse particles [262], [263]. Vreeland et al. [264] proposed a new “extended LaMer mechanism” which based on the continuous addition of precursor to the reaction media. In this new mechanism, they introduce a new stage IV with an existing stage III in the LaMer mechanism. The decrease in precursor concentration becomes equal to the monomer consumption as the result of growing nanoparticles at a certain point where monomer concentration is at steady state. This is the start of new stage IV, the steady-state growth of nanoparticles. The new stage IV can be extended for an arbitrarily long time for a sufficient particle growth for a range of particles sizes with low size dispersity. The advantage of a new idea in stage IV is that reaction is reproducible and also predictable due to the constant growth rate. Ostwald ripening is also avoided by a continuous and controlled precursor addition. No further nucleation is occurring in this new stage which leads to a low size dispersity. So, the size controlling is possible systematically by just varying the reaction time.

Nucleation follows thermodynamics laws and therefore, it is a strictly thermodynamic model in which the apparent phenomenon of a new phase, the nucleus, in the metastable primary phase is discussed. When nucleation occurs on solid surfaces contacting liquid or vapor, then it is referred to heterogeneous nucleation. On contrary, homogeneous nucleation occurs spontaneously and randomly but requires a supercritical state such as a supersaturation. In the case of the nanoparticle synthesis, it is assumed that above both kinds of nucleation occur, consecutively and in parallel [265].

Gibbs free energy of a cluster (ΔG) can be evaluated in the case of homogeneous nucleation with the help of an equation 3.1:

$$\Delta G = -\frac{4}{3}\pi r^3 |\Delta G_v| + 4\pi r^2 \gamma \quad (3.1)$$

Where r is the radius, $|\Delta G_v|$ is the difference in Gibbs bulk free energy per unit volume and γ is the interfacial surface energy per unit area. The negative bulk energy and positive surface energy terms are displayed in the curve of the cluster Gibbs free energy in figure 41. The cluster free energy depends on the cluster radius. When $r < r^*$, nuclei dissolve, when $r > r^*$, nuclei occur due to the reduction of the Gibbs free energy.

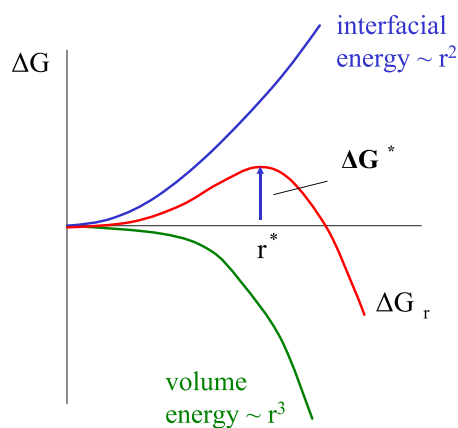


Figure 41: Dependence of the cluster free energy, ΔG , on the cluster radius, r . The curve has a maximum free energy ΔG at a critical cluster size, r^* , which defines the first stable particles – the nuclei

3.7 Inter-particles forces

When nanoparticles are in the colloidal state, they observe three types of intermolecular forces; van der Waals attractive forces, electrostatic repulsive forces, and a steric interaction. These three forces are necessary to avoid particles agglomeration.

3.7.1 van der Waals attractive forces

In 1873, van der Waals discovered a general attractive interaction between the neutral atoms, in order to study anomalous phenomena occurring in non-ideal gases and liquids. For nanoparticles dispersion in a solvent, van der Waals attraction force and Brownian motion play a crucial role. The influence of gravity becomes negligible in this case. van der Waals forces are considered as weak forces and are influential for a very short distance. Brownian motion is responsible for the collision of NPs with each other for the whole process time. A combined van der Waals attractive force and Brownian motion may lead to the agglomeration and disintegration of the nanoparticles.

3.7.2 Electrostatic repulsive forces

Charge on the particle surface and their electrostatic potential is directly responsible for the inter-particles attractions. The electric surface charge also produces electrostatic repulsion between the particles, which is the cause of a double layer found on the particles. For a case where particles are far from each other, there will be no any chance for double layers overlapping and thus net repulsion will be zero in this case. On the other side, when particles come closer to each other, their double layers overlap and phenomenon of repulsion takes place. An electrostatic repulsion $v(d)$ between two equally sized spherical particles is given by an equation 3.2:

$$V(d) = 2\pi\epsilon r\zeta^2 \exp[-kd] \quad (3.2)$$

In this equation, $\epsilon = \epsilon_0 \epsilon_r$ and ϵ_r is the dielectric constant of the solvent, ϵ_0 is the permittivity of vacuum, r is the particle radius, π is the solvent permeability, k is a Debye-Hückel parameter and ζ is the zeta potential.

3.7.3 DLVO theory

Two Russian (Derjaguin and Landau) and two Dutch (Verwey and Overbeek) scientists developed a theory of colloidal stability which is still seen as one of the groundbreaking characterization and our understanding of colloidal interparticle – the DLVO theory [265], [266]. This landmark theory lies on an assumption that total colloidal particles forces are the net result of van der Waals attractive force and repulsive electrostatic double layer, so in this way, total potential interaction (V_T) acting on two particles surface in a liquid phase is the sum of the van der Waals and the electrostatic repulsive forces [265]. Mathematically this can be exploded by an equation 3.3.

$$V_T = V_A + V_R + V_S \quad (3.3)$$

In the above equation, V_S denoted for potential energy in a solvent, V_A is van der Waals attraction, and V_R is electrostatic double layer repulsive energies. It is important to balance between V_A and V_R . In general, the stability of particles when they come closer to each other can be determined by the sum of van der Waals attraction and the electrostatic double layer repulsive forces according to DLVO theory. So, in short, equation 3.3 will become:

$$V_T = V_A + V_R \quad (3.4)$$

Figure 42 is the explanation of the relationship between interaction potential energy and the separated distance of the particles.

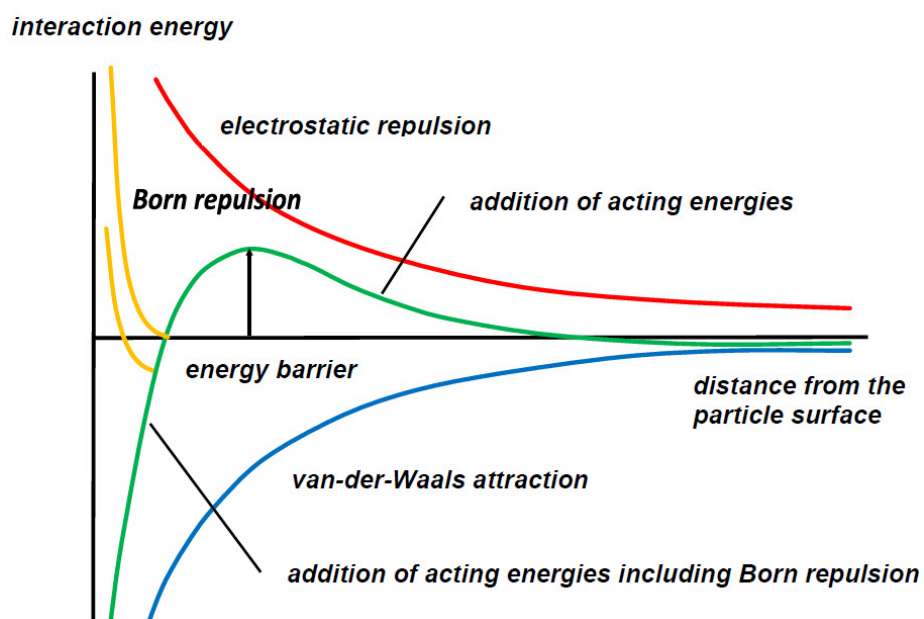


Figure 42: Graphical demonstration of interaction energies in the approach of the particles

In the above figure, V_A increases rapidly when the particles approach each other, while a decrease in V_R is not as fast. When the distance between the particles increases, both van der Waals attraction energy, and the electrostatic repulsion energy become zero. There is a maximum, V_{max} , point from where total potential energy crosses and it constitutes an energy barrier against the adherence of the particles. When particles come closer to each other, they liable to overcome this V_{max} , the repulsive barrier, then the particles are attracted strongly and the potential energy falls rapidly into the primary minimum. For lower the height of V_{max} , there will be more particles, which can potentially come close enough to adhere.

3.7.4 Stabilization of magnetic nanoparticles

MNPs are synthesized either in aqueous media or in an organic solvent. Without the surface coating, MNPs will have more hydrophobic surfaces and thus will be liable to agglomerate. Stabilization of the MNPs is favored by their coating. For their industrial use, the mobility and reactivity are seriously affected by the sedimentation of the MNPs which is a crucial factor. So, in order to study the interaction of the MNPs with other contaminants, bare MNPs should be dispersed into a stable suspension. There are two forces which are helpful for the stabilization of the MNPs: electrostatic and steric forces. Particles stability depends on the controlling these two forces. It is not easy to predict and quantify the steric forces [198], [267]. Polymeric matrix or an inorganic coating is used for the steric stabilization of MNPs [125]. Electrostatic repulsive force can be followed through the knowledge of the diffusion potential, which may be close to the zeta potential and Debye-Huckel length. Phase, chemical environment, and physical environment are the most influencing parameters affecting the stabilization of the nanoparticles [268] and these are all illustrated in figure 43. These are dependent on the pH and the ionic strengths [198].

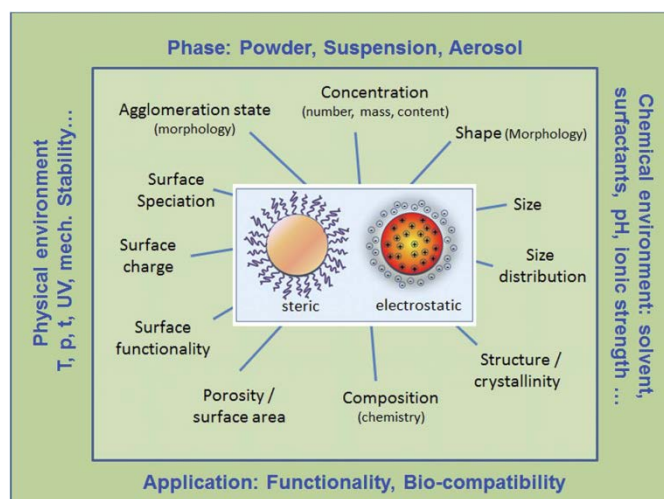


Figure 43: The role of two paramount stabilization types of nanoparticles: most important properties and the relevant forms, influencing factors, and applications are illustrated [268]

Surfactants used for the stabilization of the MNPs are always forming a double layer over MNPs for turning them more stable. The interactions between the ions and

particles forming electrical double layers and potential differences as a function of distance from the charged surface are explained in figure 44.

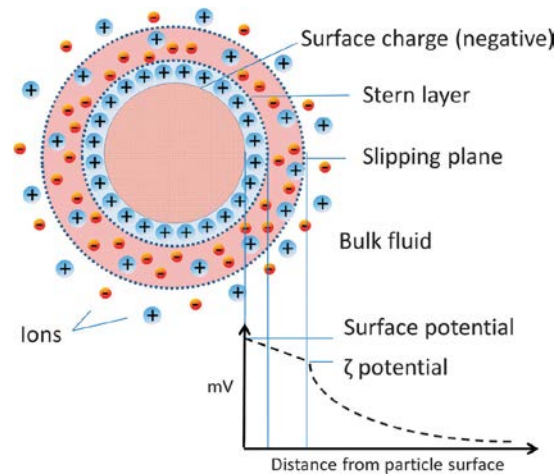


Figure 44: Electrical double layer representation: ionic concentration and potential differences as a function of distance from the charged surface

Considering a negative particle inside the fluid as an example and the surface potential named as Nernst potential. The fluid contains ions with different signs and with particles called counter-ions (here, positive sign) and ion with the same sign called co-ions (here, negative sign). Because of the electro-neutrality principle, counter-ions are attracted toward the particle surface. A part of these counter-ions called potential determining ions is adsorbed directly on the particle surface to form a Stern layer. The Stern layer is a fairly immobile layer of ions that adhere strongly to the surface of the colloidal particles and most of the surface charges are distributed in this layer, which is different from the bulk solution. The rest of the counter-ions together with the co-ions are in the Brownian motion region and counter-ions have the highest concentration near the surface particles; however, it is vice versa with the co-ions. The area of shear plane exists between the Stern layer and the layer (Gouy-Chapman layer) around it. This is the area where ions stick to particles and move along with the particles when an external electric field is applied, thus creating a phenomenon of electrophoresis. The electric potential at the surface of the shear that is relative to its value in the distant, bulk medium is called the zeta potential (ζ) or the electro-kinetic potential. The primary role of the electric double layer is to confer the kinetic stability to the colloidal particles.

The magnitude of the repulsion or attraction is calculated by a zeta potential (ζ) (figure 45, the zeta potential cell). However, the stability of suspension based on the measurement of zeta potential itself provides not a guaranty for its stabilization, but an accurate zeta potential measurement can provide a guidance towards the stabilization or destabilization of the colloidal system [269].

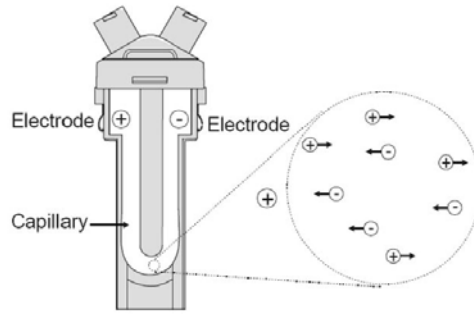


Figure 45: Zeta potential measurement [270]

For zeta potential measurement, movement of the nanoparticles under an applied electrical field is measured by the light scattering of the particles. Zeta potential (ζ) can be calculated by using Henry's equation 3.5:

$$U_e = \frac{2\varepsilon\zeta f(\kappa a)}{3\eta} \quad (3.5)$$

In above equation, U_e is the electrophoretic mobility, ε is the dielectric constant, η is the absolute zero-shear viscosity of the medium, $f(\kappa a)$ is the Henry function, and κa is the measuring of the ratio of the particle radius to the Debye length.

4 Material properties and characterizations of iron oxide nanoparticles

Different chemicals and materials used to synthesize the SPIO-NPs in a co-precipitation method are discussed in this chapter and are summarized in the following table 7.

Table 7: Chemicals used

Chemicals	Source	Purity
Ferric chloride hexahydrate	Carl Roth, Germany	98%
Ferrous chloride tetrahydrate	Carl Roth, Germany	98%
Sodium hydroxide		99.9%
Ammonia solution		25%
Tween 80	VWR, Germany	99%
Dextran 70,000	AppliChem, Germany	99%
DEAE-Dextran	Alfa Aesar, Germany	99%
Rhodamine 123	AppliChem, Germany	99.9%
Propidium iodide	AppliChem, Germany	99.9%
Ethanol		75%
Thiazolyl blue tetrazolium bromide	Sigma Aldrich, Germany	98%
Dimethyl sulfoxide	Sigma Aldrich, Germany	99.9%
Phosphate buffered saline (pH=7.2)	Gibco/Thermo Fisher Scientific	
Trypsin-EDTA solution	Sigma Aldrich, Germany	
Penicillin-streptomycin	Biochrom, Germany	
Fetal bovine serum	Sigma Aldrich, Germany	
Horse serum	American Type Culture Collection (ATCC), USA	
F-12K nutrient mixture	Gibco/Thermo Fisher Scientific	
Hoechst 33342 (hydrochloride)	Cayman Chemicals (Biomol) Germany	98%
HEPES buffer solution	Sigma Aldrich, Germany	

All chemicals were of analytical grade and used as received without any further purification. Deionized water was a dilution medium and was throughout used for making all types of solution. A stock solution of sodium hydroxide was prepared just before its utilization. All biological tests were performed in a biological safety cabinet (BSC).

4.1 Experimental equipment

Following different types of laboratory equipment were used for the SPIO-NPs synthesis and their various pharmaceutical tests:

- Three-neck glass reactor
- Thermostatic water bath
- Mechanical stirrer
- Magnetic stirrer plate
- Thermometers
- Electronic balance
- Serological pipettes
- Microcentrifuge tubes
- Microliter pipettes
- Syringes
- Multichannel micropipettes
- Haemocytometer (cells counting)
- Cell culture flasks
- 96-well plates
- 6-well plates
- pH meter
- Measuring cylinders (5-500 ml)
- Glass beakers (100, 250, 500 ml)
- Volumetric flasks

4.2 Reactor set-up

For the purpose of reproducible SPIO-NPs synthesis by a co-precipitation method, a semi-batch three-neck round bottom glass reactor was used. Various operating parameters for the bulk phase iron salts precipitations were easily controlled with the help of this standard semi-batch glass reactor (figure 46). The reactor consisted of a 250 ml three-neck glass flask placed in a water jacket (Lauda thermostat) for temperature control during the reaction. Two blades mechanical stirrer was equipped for mechanical agitation and its revolutions per minute (rpm) were controlled using IKA overhead mechanical stirrer. Feeding in the three-neck reaction flask was carried out by using its right and left necks and these necks were keeping covered during the entire course of the reaction. Afterwards, sonication at different intensities was carried out immediately after the termination of the reaction.

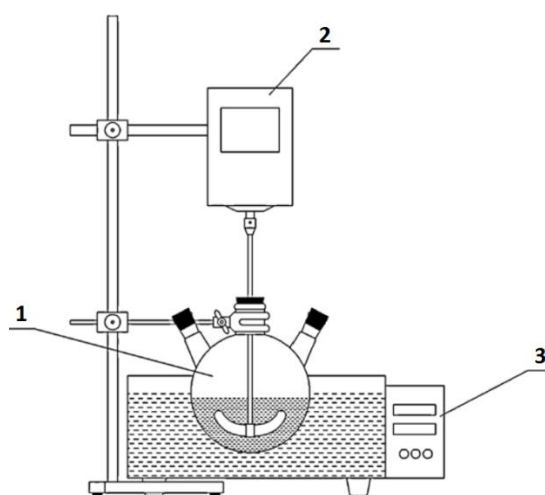


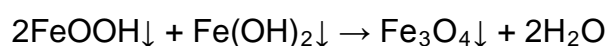
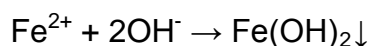
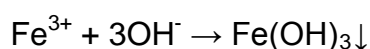
Figure 46: Experimental set-up (1- three-necked round bottom glass reactor, 2- overhead mechanical stirrer, 3- thermostatic water bath)

4.3 Synthesis of SPIO-NPs

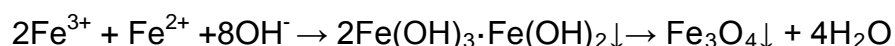
Preparation of SPIO-NPs was carried out through a bulk co-precipitation method of iron salts solution. Typically, specific stoichiometric quantities (in grams) of ferric

chloride ($\text{FeCl}_3 \cdot 6\text{H}_2\text{O}$) and ferrous chloride ($\text{FeCl}_2 \cdot 4\text{H}_2\text{O}$) with 2:1 molar ratio were dissolved in deionized (DI) water in a three-neck reactor under vigorous stirring. Stoichiometric calculated amounts (in grams) of surfactants (Dextran 70,000, DEAE-Dextran, and Tween 80) were solubilized in DI water separately in a glass beaker and then added into the three-neck reaction flask. The reaction temperature was adjusted to 40-100 °C at which NaOH or 25% NH_3 solution was quickly injected into the glass reactor to increase the solution pH. The dispersion quickly turned to dark black which was the evidence of the magnetite formation. The reaction was carried out at 400 rpm to 1000 rpm (stirrer tip speed from 1.21 m/s to 3.03 m/s) for nucleation and growth of iron oxide nanoparticles under the same temperature for one hour. Nanoparticles syntheses were then probed to a sonication for 10 minutes. For labelling with the fluorescence marker, fluorescence dye was dissolved separately in DI water and then introduced with the stoichiometric amount of iron oxide nanoparticles followed by a magnetic shaker. Afterwards, the nanoparticles were separated from the unlabeled solution by a centrifugation and re-dispersed in DI water. Nanoparticles size was controlled/adjusted through a suitable choice of process and apparatus parameters during the synthesis process.

Co-precipitation of iron salts solution is extensively studied. Following reaction mechanism takes place during the bulk co-precipitation process containing Fe^{3+} and Fe^{2+} ions.



An overall reaction gives:



Nanoparticles size, particle size distribution, morphology, and magnetic properties were controlled through a solution pH adjustment, reaction temperature, reaction time, mechanical stirring velocity, strength and amount of basic solution, and $\text{Fe}^{3+}/\text{Fe}^{2+}$ molar ratios.

4.3.1 Cell culture of C6 glioma cells

C6 cells are glioma cells that were extracted from a rat glial tumor and recovered by taking the horse serum, fetal bovine serum, and Ham's F-12K medium. The cells were then incubated at 37 °C in a 5% CO_2 atmosphere (ca. 30 min). The medium (for complete growth) consisted of:

- 15% horse serum
- 2.5% fetal bovine serum

- 1% antibiotics (penicillin-streptomycin solution)

For a **subculture**: medium (complete growth medium) and Trypsin-EDTA solution was used. Medium and the Trypsin-EDTA solution were warmed (from -20 °C) in an incubator (37 °C) for 30 minutes. The old medium was removed from it with a serological pipette and then 0.5 ml Trypsin-EDTA was added to it. It was washed for a short time to remove the Trypsin-EDTA solution from it, which was then replaced by a fresh quantity of 1 ml of Trypsin-EDTA solution. The cells were checked under the microscope until the cell layer was completely dispersed. Afterwards, the medium was added and the cells aspirated by gentle pipetting (total volume = 8 ml). The cells were washed down from the surface (bottom) by pipetting (maximum 10 times) and then added into a 6-well plate.

For a **cryopreservation**: medium and dimethyl sulfoxide (DMSO) were utilized. For this, 2 ml of cell solution (from subculture) was taken in a 15 ml centrifuge tube and centrifuged for 5 minutes at 900 rpm. The supernatant was removed from it, followed by the addition of 1.9 ml medium (95%) and 100 µl DMSO (5%) in it. This cell solution was transferred into a cryopreservation tube and placed at -20 °C for 2-4 hours and then stored at -80 °C.

After that C6 glioma cells were taken from -80 °C and warmed up in a water bath at 38-39 °C. This process was performed at a very fast speed to maximize the number of cells' viability. Cell solution was transferred from the cryopreserving tube into a 15 ml centrifuge tube and then added 10 ml medium in it. Afterwards, centrifugation was carried out for 5 minutes at 900 rpm and the supernatant was removed. Then 3 ml of medium was added to it, followed by a thorough mixing by pipetting. The cell solution was transferred to a small cell culture bottle (25 cm²). The cells were incubated overnight at 37 °C in a 5% CO₂ humidified atmosphere.

Next day, those cells were examined under the microscope. In accordance with the general practice, the cells that were in one layer were regarded as good, while those that formed agglomerates were regarded as bad. For good and well-growing cells, the medium was changed. For this, the medium was warmed at 4 °C in the incubator (37 °C) for 30 minutes. The old medium was removed with the help of a serological pipette, followed by the addition of medium in a cell culture bottle with 5 ml serological pipette. The cells were allowed to grow in an incubator for ~ 2 days.

4.3.2 MTT assay with iron oxide nanoparticles and C6 glioma cells

Recovery of C6 glioma cells (2 tubes in 2 cell culture flasks (25 cm²)) was carried out and when the cells started to grow, the medium immediately changed for the preparation of MTT test.

First, the cells were dispersed with Trypsin-EDTA solution and the number of cells was counted. Then this cell solution (having ~200,000 cells) was randomly

transferred into a 96-well plate. After the cells' overnight incubation, the preparation for MTT test started. Afterwards, the cells were exposed to various concentrations (with and without fluorescent) of NPs (in $\mu\text{g}/\text{ml}$) with different dilution/group for the final concentration in the 96-well plate. For a positive control, C6 cells were exposed only with medium and for a negative control, C6 cells were exposed with medium and 75% ethanol. The real concentration was doubled but the final/right concentration was reached by adding 100 μl medium to each well.

After the incubation, the old medium was discarded via pipette (with the prevention that cells were not dry) and fresh 100 μl was added to each well (with cells); after washing (sterile) with 100 μl of phosphate buffered saline (PBS) (pH 7.2 to 7.6 for C6 cells), PBS was completely removed. Afterwards, 100 μl cell culture medium was added in 5 wells, and the different dilutions, each with 100 μl in 5 wells (5 replicates per group with total volume of each well = 200 μl as shown in figure 47), were then incubated for 16 hours and 24 hours.

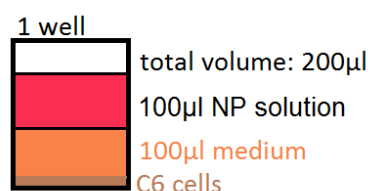


Figure 47: Schematic representation of one well: the portion of each solution over C6 glioma cells is shown

After the incubation, thiazolyl blue tetrazolium bromide was dissolved in PBS (pH 7.2) (usually, PBS with pH 7.2-7.6 for C6 and HEK cell is used) with the concentration of 5 mg/ml (0.5 $\text{mg}/100$ μl). After adding 190 μl cell culture medium to each well, 10 μl of MTT solution was added to each well to solubilize the formazan crystals that were thus formed. They were then incubated for another four hours. In accordance with the principle, the MTT solution reacted with living cells and became yellow. The solution was removed from all wells with special care that cells or particles could not escape (from the bottom). To avoid any contamination, pipette tubes were changed for each group. 100 μl of dimethyl sulfoxide (DMSO) was added in each well and the 96-well plate was shaken at 5-6 rpm for approximately 10 minutes. When the particles dissolved in the solution, it turned from yellow to violet. DMSO destroyed the cells and released the NPs that were detected by an optical density (OD) value. The process of the change of color was analyzed with the help of a plate reader (spectrophotometer) on different wavelengths.

The cell viability is calculated in percentage and it is the ratio of mean absorbance (I_{sample}) of all three experimental readings to the mean absorbance of control cells (I_{control}). Mathematically this may write as:

$$\text{Cell viability} = \left(\frac{I_{\text{sample}}}{I_{\text{control}}} \right) \times 100 \quad (4.1)$$

For confocal imaging, SPIO-NPs were treated with the C6 glioma cells for one day and then after adding Hoechst 33342 (in medium), cells were incubated for at least 40 minutes. Just before imaging, the medium was removed and replaced with fresh phosphate buffered saline. Magnification 50X was chosen for all images and laser used for images was: 405 nm for Hoechst, 514 nm for rhodamine 123, and 543 nm for propidium iodide.

4.3.3 Animal models

For *in vivo* toxicity, male adult Wistar rats of 9-12 weeks age were used. They were maintained in group cages at 12 hours light : dark cycle under 24-26 °C and 50-60% humidified conditions. All rats had access to their food and water, however, one day before experiment; food was removed to facilitate the narcosis. Narcosis solution (5 ml/kg body weight of a mixture of 2 ml Ketamine 100 mg/ml, 3 ml Medetomidine 1.0 mg/ml, and 15 ml of 0.9% saline) was prepared and stored in a fridge at 4 °C. Rats were weighed and put under the heating lamp for five minutes before treatment with narcosis injection. After intraperitoneal narcosis injections, the rats were randomly divided into three groups with three animals per group for retrograde labelling of retinal ganglion cells (RGCs), intravitreal SPIO-NPs injections, *in vivo* confocal neuroimaging, and *ex vivo* (whole mount) confocal imaging. Two animals were placed in the vehicle (control) group.

For all procedures, ethical approval was obtained according to the requirement of the German national act on the use of experimental animals (Ethic committee Referat Verbraucherschutz, Veterinärangelegenheiten; Landesverwaltungsamt Sachsen-Anhalt, Halle, Germany).

In vivo confocal neuroimaging (ICON):

The rats were fixed on a purpose-built stage underneath a standard confocal laser scanning microscope with a large probe space and a long working distance objective lens. For the uptake study, fluorescent labelled Dextran coated SPIO-NPs (3 µl labelled with rhodamine 123) were diluted in phosphate buffered saline and were slowly injected into eyes' vitreous body (superior colliculi) of deeply anaesthetized rats. To prevent drying of the eye cornea of anaesthetized rats, the optical gel was applied. Rat behavior, weight, and appearance were strictly followed during the whole experimental procedure. The eye was positioned directly underneath the 5X objective lens of a Zeiss LSM 880 and a -80 dioptr plan-concave lens was placed directly onto the surface of the cornea to adjust the path of the laser rays to rat's eye. Images (ICON and *ex vivo*) were taken after two days of the intravitreal injections of the nanoparticles.

For the *ex vivo* (whole mount) retinas, the rat under deep Ketamine / Medetomidine narcosis was decapitated. Eyes were enucleated and placed in cold HEPES buffered Ca²⁺ free solution containing 135 mM, NaCl, 5 mM NaOH, 2.5 mM KCl, 7 mM MgCl₂,

10 mM HEPES, 10 mM glucose; pH 7.4. The excess of connective tissues and muscles were removed. The cornea was removed by cutting on the rim with the sclera. The lens and most of vitreous were removed, and the retina was separated from the pigment epithelium. Residuals of vitreous were removed either by small forceps or wooden toothpick. 3-4 small cuts from the edge direction to optic nerve were done, and retina was flattened on the hydrophilic polytetrafluoroethylene (PTFE) membrane (0.4 μm pore). To fix retina, the 4% paraformaldehyde solution was applied for 10 minutes.

Retina was washed with HEPES (4-(2-hydroxyethyl)-1-piperazineethanesulfonic acid) buffer and then Hoechst 33342 (0.005 mg/ml) was added to counterstain the nuclei. The imaging was done using Zeiss LSM 880 confocal microscope with 50X magnification.

Characterization of prepared samples for nanoparticle size, particles size distribution, and zeta potential can be employed using zetasizer. Morphology of the samples can be determined using scanning electron microscopy (SEM) and transmission electron microscopy (TEM), magnetic properties can be observed using vibrating sample magnetometer (VSM), and absorption of light is usually observed by spectrophotometry method.

4.3.4 Effect of pH on the particle size of SPIO-NPs

The general pH range during the SPIO-NPs synthesis is in between 8-11 and the corresponding $\text{Fe}^{3+}/\text{Fe}^{2+}$ molar ratio is 2:1. Size of the nanoparticles tends to decrease with the rise in a solution pH below 11 and particle size increases when pH increases above the 11 [165]. This increase in SPIO-NPs size after pH 11 is due to the fact that hydrolysis of Fe(III) ions and formation of $\text{Fe}(\text{OH})_3$ takes place in the first stage of the magnetite synthesis. This is followed by the generation of $\text{Fe}(\text{OH})_2$ with an increase in solution pH, because of the hydrolysis of iron(II) ions. Magnetite is then formed when the solution pH is further increased. This implies that nucleation of magnetite is easier when the pH is <11, whereas the growth process of the magnetite nucleus is easier when the solution pH is >11. Formation of the FeOOH phase should occur first, then the $\text{Fe}(\text{OH})_2$ - FeOOH composite would be converted to magnetite [166]. Therefore, an optimum pH is 11 for SPIO-NPs synthesis by using a co-precipitation method.

4.3.5 Effect of temperature on the particle size of SPIO-NPs

The reaction temperature is a very important parameter for SPIO-NPs synthesis in a co-precipitation method. Nanoparticle size is directly related to the reaction temperature; when the reaction temperature rises, more energy is transferred within the reaction system and thus, particles mobility increases and therefore, particles observe greater numbers of collisions which favored the increase in particles size [165]. Further, when the reaction temperature increases, the nucleation rate is also

reduced and ultimately their growth rate accelerates [166]. That's why large sized particles are produced at higher temperatures.

4.3.6 Effect of stirring velocity on the particle size of SPIO-NPs

To synthesize the SPIO-NPs through a co-precipitation method, stirring velocity is a paramount and a decision making step. Throughout the course of a co-precipitation reaction, care should be taken that the disperse phase must be largely distributed in a well uniform manner over the entire liquid height. This is most important for the NPs crystallization growth. Solution uniformity improves with the increase in stirring velocity so, smaller size NPs with a narrow size distribution are achieved [181]. The decrease in particle size is also due to the occurrence of irregular diffusion of the particles. Increase in agitation impedes the growth of the particles, and hence smaller the particles size [166]. Also, the energy transfer to the nanoparticles suspension medium also increases with the increase in stirring speed; as a result, the reaction solution disperses into smaller droplets and therefore, particle size reduces. Another explanation for this size reduction is that anomalous diffusion of particles at a higher degree of agitation reduces the growth kinetics of the particles, and hence results in the smaller sized nanoparticles [165].

4.3.7 Effect of precursors concentration on the particles size of SPIO-NPs

Normally, in a co-precipitation method, the $\text{Fe}^{3+}/\text{Fe}^{2+}$ molar ratio is 2:1. Particle size tends to increase when the $\text{Fe}^{3+}/\text{Fe}^{2+}$ molar ratio exceeds from 2:1. The concentration of alkali also plays its role in size controlling of NPs. It is observed that particle size increases with the increase in a concentration of alkali. Reducing the concentration of the solution of iron salts enhances product quality but reduces the yield. It has been demonstrated that deviation from the standard $\text{Fe}^{3+}/\text{Fe}^{2+}$ molar ratio (2:1), may lead to the synthesis of maghemite [158].

4.3.8 Effect of surfactants on the particles size of SPIO-NPs

Magnetic nanoparticles obtained with the different amount of surfactants have a better size distribution than synthesized in the absence of surfactants. Surfactants coated MNPs are monodisperse and with a narrow size distribution because their surfaces are coated with surfactants. The coating restricts agglomeration of magnetic NPs, thus increasing the monodispersity of the prepared materials. The thickness of the coating layer can be controlled by adjusting the stoichiometric amount of the surfactants. The monodispersity of the MNPs is also enhancing by increasing the quantity of the surfactants because this increases the thickness of the coating layer. The bare magnetite nanoparticles are more liable to agglomerate because the uncoated nanoparticles are not monodispersed throughout the solution.

4.3.9 Effect of sonication on the particle size of SPIO-NPs

The energy supplied to the nanoparticles mixture is dependent on time and sound intensity. Ultrasound intensity is simply ultrasonic energy per unit time. The percentage specified by manufacturer refers to relative amplitude and it is a setting of the device. Usually, a high shear force is required to produce miniemulsion. With lower intensity, NPs have comparatively broad particle size distributions which might be due to the insufficient input energy to produce monodisperse particle size distribution in the nanoparticles suspension. With the increase in an ultrasonic intensity, particle size and the particle size distribution get better and NPs will be monodisperse. This is suggested that too high input energy will tend to produce too many small droplets and also produces enough heat and disturbs the nanoparticles production along which may lead to many side reactions.

4.4 Physicochemical characterizations of magnetite nanoparticles

To understand the process optimization and relative operation, their knowledge about the physical properties come into play. For a nanoparticles colloidal system where a number of individual particles form such system, an accurate characterization of their physical properties is very important before their further applications. Sometimes, these physical properties are also referred to as granulometric properties. As a number of individual particles forms such colloidal system and these individual particles are of different sizes and also of different shapes; so their particle size analysis is of great importance for their handling [271]. A cumulative particle size distribution of spherical particles with a diameter 'd' can be described by a mathematical expression 4.2 [271]:

$$Q_r(d) = \int_{d_{\min}}^{d_{\max}} q_r(d) d(d) \quad (4.2)$$

Herein,

$$q_r(d) = \frac{dQ_r(d)}{d(d)} \quad (4.3)$$

Here, index r denotes the quality measured

Short descriptions of various characterization techniques like DLS, SEM, TEM, VSM, and spectrophotometry are described in the proceeding sections.

4.4.1 Dynamic light scattering (DLS)

DLS, also known as photon correlation spectroscopy (PCS) is a fast way to study the colloidal system. In DLS operation, a light beam is allowed to direct for a period of time (before its statistical analysis) onto a liquid sample that scatters the light elastically (figure 48). When a monochromatic light hit the particles, it scatters in all directions and the rate of scattered light depends on the particle size and smaller particles are kicked further and hence move more rapidly. Nanoparticles observe

Brownian motion in the liquid phase and the relative position of the particles alters with time and thus, causes the time fluctuation in scattered light intensity. These two variations in light scattering yield the Brownian motion velocity and for this reason, the particle size (r_k) is calculated by the Stokes-Einstein relationship [272]:

$$r_k = \frac{KT}{6\pi\eta D} \quad (4.4)$$

In the above equation, K is the Boltzmann's constant; T is the temperature in K; η , is the viscosity; and D , the diffusion coefficient.

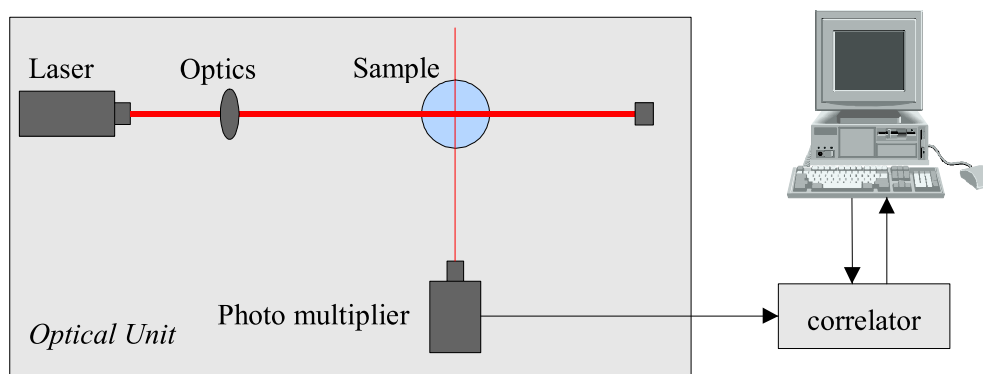


Figure 48: Working principle of the dynamic light scattering

Two main applications associated with the DLS are the study of system dynamics in real time and the particle size measurement. DLS also measures the monodispersity and polydispersity index (PDI) of nanoparticles system and also calculates the “mean particle” diameter when some changes occur in the form of coated nanoparticles. It is very important that NPs must have monodisperse in an aqueous phase. PDI is mainly used to calculate the molecular breadth distribution and is the ratio of the average molecular weight (M_w) to the average number of molecular weight (M_n) as expressed by the following expression:

$$\text{Polydispersity index (PDI)} = \frac{M_w}{M_n} \quad (4.5)$$

Even DLS is widely used tool for nanoparticles characterization, but it is still not completely understood the precision of the measurement due to the numerous unevaluated effects, for instance, scattering angle, the concentration of the suspension and physical properties like shape and anisotropy of the synthesized nanoparticles [273], [274]. As an advantage, DLS measurement involves non-ionizing lower energy light source and is carried out at room pressure. DLS also provides an excellent time-dependent for nanocrystal growth study in a solution. Despite these advantages, DLS also have some limitations; only useful for the particle system that exhibits Rayleigh scattering; in most of the cases, a dilute suspension is required for minimizing the multiple scattering; almost impossible to differentiate between light scatterings from single primary particle agglomerate.

4.4.2 Scanning electron microscopy (SEM)

Scanning electron microscopy is a type of an electron microscope and it uses high electrons beam to take the sample images by scanning the surface [272]. SEM is used for morphological examination of the nanoparticles with direct visualization [275].

Basic principle: An interaction takes place between the target sample atoms and strikes electron beam resulting in the secondary electron image, backscattered electrons with the generation of X-rays having the sample surface morphology and composition analysis (figure 49). High sample resolutions are possible to obtain even 1-5 nm sized particle size can be characterized in the form of the secondary image through this technique with typical so small energies less than 50 eV and this energy emission is dependent on the surface geometry, surface chemical characteristics, and also bulk chemical composition. Therefore, the chemical composition of the sample can also be evaluated through SEM [272], [276]. To get SEM images, it is vital to make a sample conductive for the electron beam to scan the sample surface. If a sample is non-conductive in nature then first the sample surface is coated with the conductive material using low vacuum sputter coating or high vacuum evaporation. This is done in order to prevent the accumulation of static electric charge on the sample during the electron irradiation.

SEM also has some limitations like very less information about the particles size distribution and true particles population. The results regarding the mean particle obtained from SEM are comparable with DLS [275].

4.4.3 Transmission electron microscopy (TEM)

Although same kind of data is examined in TEM and in SEM but the operating principle of both TEM and SEM are different. Sample preparation in TEM is also a complex way due to the requirement of transmittance of the electron beam through a thin media [275]. Transmission electron microscopy is an efficient technique to determine the particle size, shape, and particle morphology [277]. Transmission electron microscopy is specially designed to investigate very thin samples with a thickness of about 10-100 nm and an electron accelerating voltages of up to 200 KV [278]. TEM has an advantage over SEM in such a way that spatial resolution of 1 nm or better can be obtained. Physical and chemical properties of nanomaterials depend on both chemical composition and also on their structure and TEM provide an understanding of such structures. Atomic-resolution real-space imaging of nanoparticles is better revealed by this technique.

Operation of TEM is similar to a slide projector. When the electron beam is allowed to pass through the sample under investigation, then only its part is transmitted which make an amplitude contrast agent (figure 49). The obtained image then passes through a magnifying lens and then projected onto a phosphor screen or a charged

coupled device (CCD). Because Broglie wavelength of an electron is much smaller as compared to the wavelength of visible light, therefore, TEM resolution experience a much smaller than 1 nm. As the TEM is carried out in a high evacuated chamber so the sample structure can be suspected through an interaction with electrons and the vacuum so, this factor should be focused during TEM examination [276].

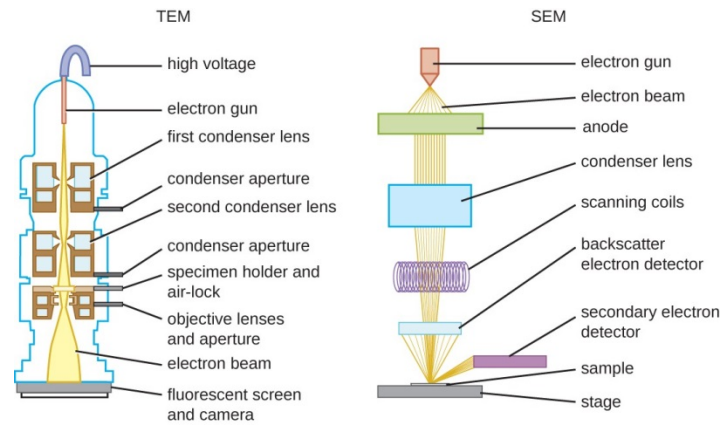


Figure 49: Schematic illustrations of both TEM and SEM components [279]

4.4.4 Vibrating sample magnetometer (VSM)

Vibrating sample magnetometer is a perfect technique to determine the magnetic moment of the magnetite nanomaterials with high precision. The magnetite nanomaterials are characterized using this versatile technique for magnetic hysteresis and demagnetization. VSM working is based on Faraday's law which stated that "generation of an electromagnetic in a coil follows the change in flux through the same coil."

The working principle of vibrating sample magnetometer is that when a uniform magnetic field is produced in a test sample, there will be a dipole moment which is proportional to the product of the sample susceptibility times the applied field is induced in that test sample [280].

The sample to be investigated is placed in a constant magnetic field and if the sample is magnetic in nature, then the sample will be magnetized by aligned magnetic domains produced by that applied constant magnetic field. The magnitude of this induced magnetic field strongly depends on the applied constant field. A magnetic field around the sample is produced by the sample dipole moment which referred to a magnetic stray field. When the sample is allowed moving up and down (vibrate) with the help of oscillator output (figure 50), change in a magnetic stray is the time-dependent function and is sensed by a set of pick-up coils and these coils will observe an electric current due to the alternating magnetic field according to Faraday's law. Generated electric current is directly proportional to the magnetization and amplified by a trans-impedance amplifier and lock-in amplifier. There are various softwares which are frequently used for the magnetization magnitude [280]. The output of vibrating sample magnetometer is a hysteresis curve, which is the relation

in between induced magnetic flux density and magnetization force. This hysteresis curve provides information about magnetic saturation, the remanence, the coercivity, and the level of residual magnetism left in the sample.

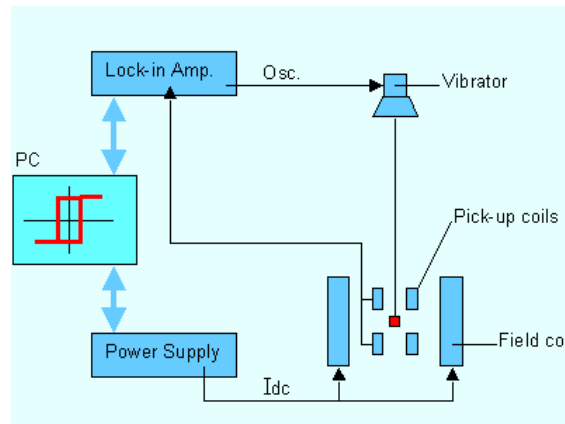


Figure 50: Vibrating sample magnetometer setup [281]

4.4.5 Spectrophotometry

Spectrophotometry is a method to measure how much a chemical substance absorbs light by measuring the intensity of light as a beam of light passes through the NPs sample solution. The basic principle is that each compound absorbs or transmits light over a certain range of wavelength.

When light passes through NPs sample material from a light source, then this light is transmitted through the NPs sample solution or absorbed by that sample. This transmission or absorbance is measured by a spectrophotometer. The absorption or transmission of light is directly proportional to the distance which light covered through NPs sample solution and also to the concentration of absorbing compound in that particular NPs sample solution. To work with a spectrophotometer, NPs sample solution is placed inside the cuvette which is then placed in a cuvette holder of the spectrophotometer. When a beam of light with a particular wavelength is allowed to pass through that cuvette, the magnitude of light transmission or absorbance is electronically recorded. For a reference, a reference blank is used to quantify the transmission or absorbance through that NPs sample solution. Transmittance (T) is referred to the magnitude of transmitted light through a particular NPs sample solution. Transmittance is the ratio of light which is transmitted through NPs sample solution (I_t) to the light transmitted by a reference blank (I_0).

$$T = \frac{I_t}{I_0} \quad (4.6)$$

When a light comes out from a light source, it does not consist of a single wavelength and is reflected in different directions. A prism or diffracting grating is thus used to separate the light into specific portions (monochromatic) of the spectrum and a small portion of it also passes through a small slit as shown in figure 51. For most of the

biological applications, the absorbance of light by NPs sample solution is measured which is also referred to an optical density (OD) and it is a negative logarithm of the transmittance.

$$A = -\log T \quad (4.7)$$

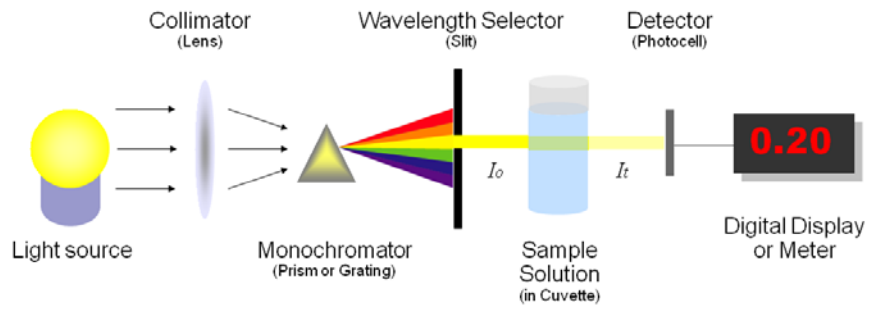


Figure 51: Working principle of the spectrophotometer [282]

5 Influence of process parameters on the properties of SPIO-NPs

Many process parameters play a vital role in the synthesis of the SPIO-NPs. Our aim was to determine the most influential parameters in order to adjust the desired properties of particles size, particles size distribution, monodispersity, morphology, and surface properties. Process parameters such as temperature, mechanical stirring velocity, pH, precursor's ratio ($\text{Fe}^{3+}/\text{Fe}^{2+}$ molar ratio) were varied for the required purpose. The coating agents are only required on the surface since the surface texture is to be decisive for the transport across the blood-brain barrier and thus coating agents adsorb on the nanoparticles surface.

5.1 Experiments with Tween 80 as a surface coating material

Preparation of Tween 80 coated iron oxide nanoparticles has already been discussed in previous chapter 4.

5.1.1 Effect of temperature on the synthesis of Tween 80-SPIO-NPs

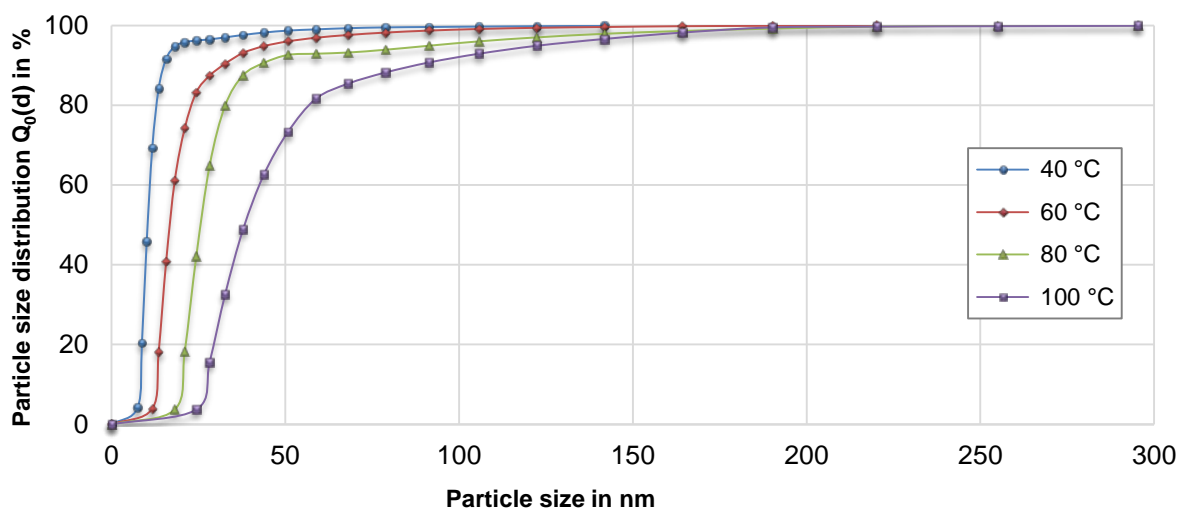


Figure 52: Cumulative particle size distribution $Q_0(d)$ of Tween 80-SPIO-NPs for the reaction temperatures between 40 °C to 100 °C at a $\text{Fe}^{3+}/\text{Fe}^{2+}$ molar ratio of 2:1 and 400 rpm

Particles size distribution of change in SPIO-NPs size at temperature interval from 40 °C to 100 °C is drawn in figure 52. With the increase in a temperature, the median particle size ($d_{50,0}$) was increased from 11.7 nm to 37.84 nm, the zeta potential (ZP) rose from 26.1 mV to 28.6 mV and pH of the solution varied from 8.43 to 8.96. The best polydispersity index (PDI) value was achieved 0.40 at 40 °C. For an effective drug delivery application, it is important to have some effective size distribution and in order to determine the mean nanoparticle size, a proper particle size distribution is required [283]. We synthesized iron oxide nanoparticles with an average of less than 100 nm in size and synthesis of nanoparticles at 40 °C and 60 °C were of very small in size and in superparamagnetic regime. A term 'span' is used for the measurement of the width of size distribution. As smaller the span value (equation 5.1), narrow will be the distribution. Reaction characteristics are given in table 8.

$$\text{Span} = \frac{d_{90,0} - d_{10,0}}{d_{50,0}} \quad (5.1)$$

Table 8: Reaction characteristics at temperatures 40 °C to 100 °C

Temperature (°C)	pH	PDI	Zeta potential	Span
40	8.43	0.40	+26.1 mV	0.59
60	8.56	0.42	+28.4 mV	1.05
80	8.78	0.43	+29.7 mV	0.80
100	8.96	0.45	+28.6 mV	1.67

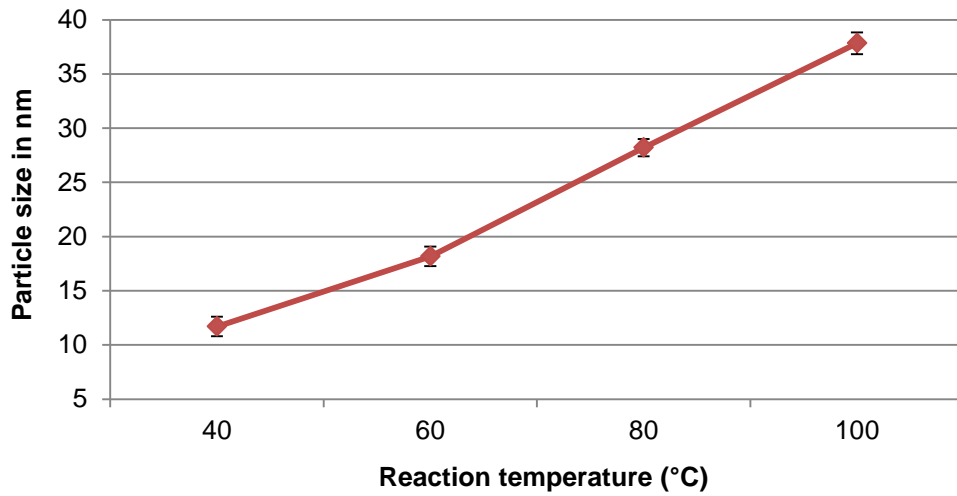


Figure 53: Effect of temperature on the median ($d_{50,0}$) particle size of Tween 80-SPIO-NPs

It was observed that with the increase in reaction temperature from 40 °C to 100 °C, SPIO-NPs size also tended to increase as shown in figure 53.

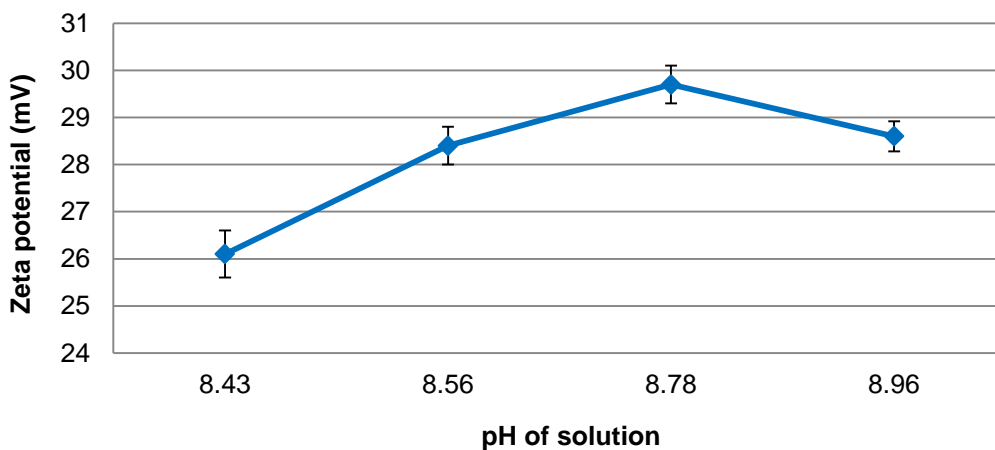


Figure 54: Change of zeta potential with the solution pH of Tween 80-SPIO-NPs

Change of zeta potential with the solution pH is depicted in the above figure 54. We had positive values of zeta potential when Tween 80 coated SPIO-NPs were synthesized because Tween coated SPIO-NPs have positively charged surface. Zeta

potential increased with the increase in the solution pH. The highest value of zeta potential was achieved at pH 8.78. It is suggested that at pH 8.78, more H^+ ions are produced and due to the adsorption of these H^+ ions, the zeta potential value was increased. After this pH of 8.78, the OH^- ions are produced more rapidly and thus trend in a decrease in the zeta potential was observed.

All synthesized nanoparticles with some exception were stable at pH values indicating that these SPIO-NPs have good potential for *in vivo* use.

5.1.2 Effect of stirring velocity on the synthesis of Tween 80-SPIO-NPs

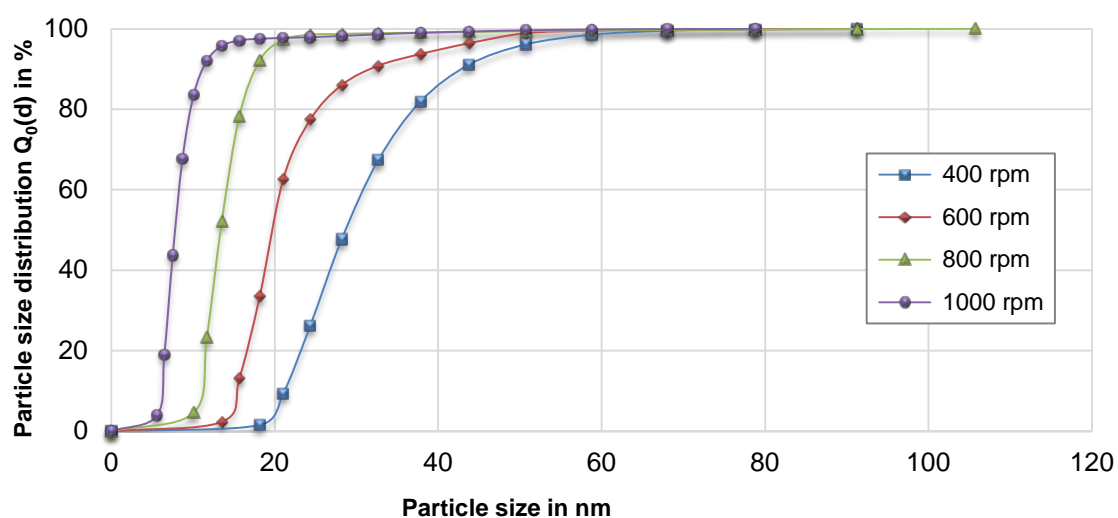


Figure 55: Cumulative particle size distribution $Q_0(d)$ of Tween 80-SPIO-NPs at stirring velocities between 400 rpm to 1000 rpm (1.21 m/s to 3.03 m/s stirrer tip speed) with a Fe^{3+}/Fe^{2+} molar ratio of 2:1 and at 40 °C

Figure 55 is a representation of the particles size distribution from 400 rpm to 1000 rpm stirring speeds. Maximum nanoparticle size was less than 40 nm. The nanoparticle size was going to decreasing with increase in stirring velocity. The median particle size ($d_{50,0}$) 28.21 nm, 21.04 nm, 13.54 nm, and 8.72 nm at 400 rpm, 600 rpm, 800 rpm, and 1000 rpm stirring velocities respectively (1.21 m/s, 1.82 m/s, 2.42 m/s, and 3.03 m/s stirrer tip speed respectively) were observed. At 1000 rpm, best zeta potential +55.5 mV was obtained which elucidate that nanoparticles obtained at 1000 rpm are most stable and also of narrow size distribution. At higher stirring speeds, dispersion phase is largely distributed in a well uniform manner over the entire liquid height which is crucial for the NPs crystallization growth. Increased agitation impeded the growth kinetics of particles and hence results in smaller particle size. Higher stirring speed is also responsible for the increase in energy transfer to the nanoparticles suspension and the reaction solution disperses into smaller droplets which also causes a decrease in the particles size. Reaction characteristics for this reaction phase are given in table 9.

Table 9: Reaction characteristics at stirring velocities from 400 rpm to 1000 rpm (1.21 m/s to 3.03 m/s stirrer tip speed)

Stirring (rpm)	pH	PDI	Zeta potential	Span
400	8.47	0.52	+15.5 mV	0.80
600	8.56	0.49	+21.2 mV	0.80
800	8.31	0.47	+33.6 mV	0.47
1000	8.50	0.44	+55.5 mV	0.59

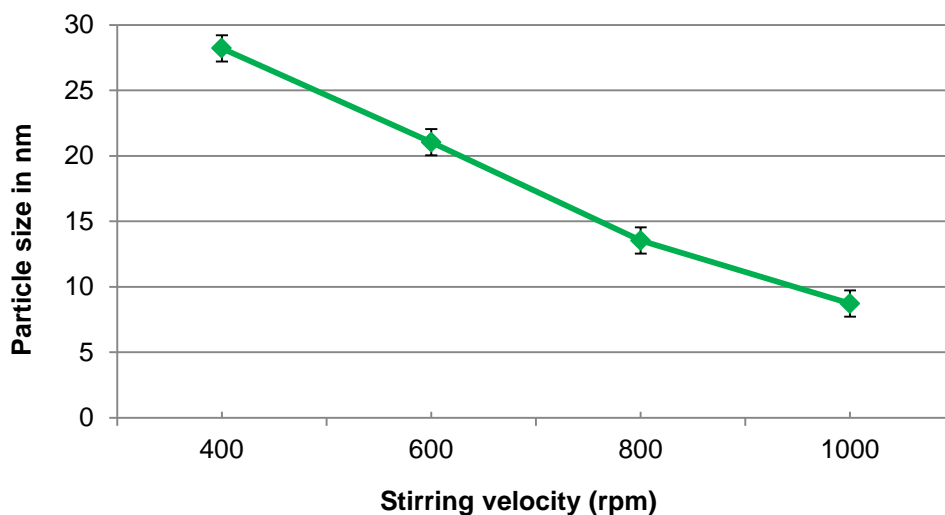


Figure 56: Effect of stirring velocity on the median ($d_{50,0}$) particle size of Tween 80-SPIO-NPs

The median nanoparticle size was tended to decrease with the increase in stirring velocity as shown in the above figure 56.

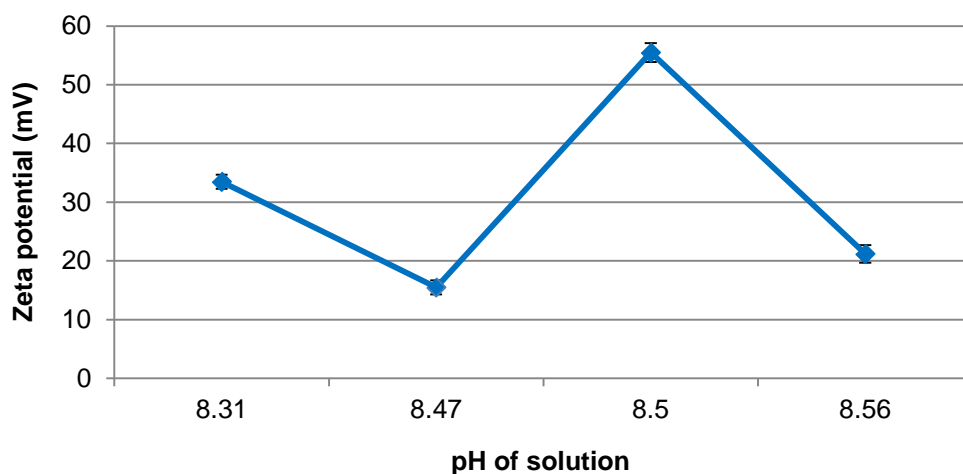


Figure 57: Variation of zeta potential with the solution pH of Tween 80-SPIO-NPs

Positive values of zeta potential were obtained and their trend is shown in the above figure 57. It is cleared that zeta potential is significantly changing with the respective solution pH.

5.1.3 Effect of pH variation on the synthesis of Tween 80-SPIO-NPs

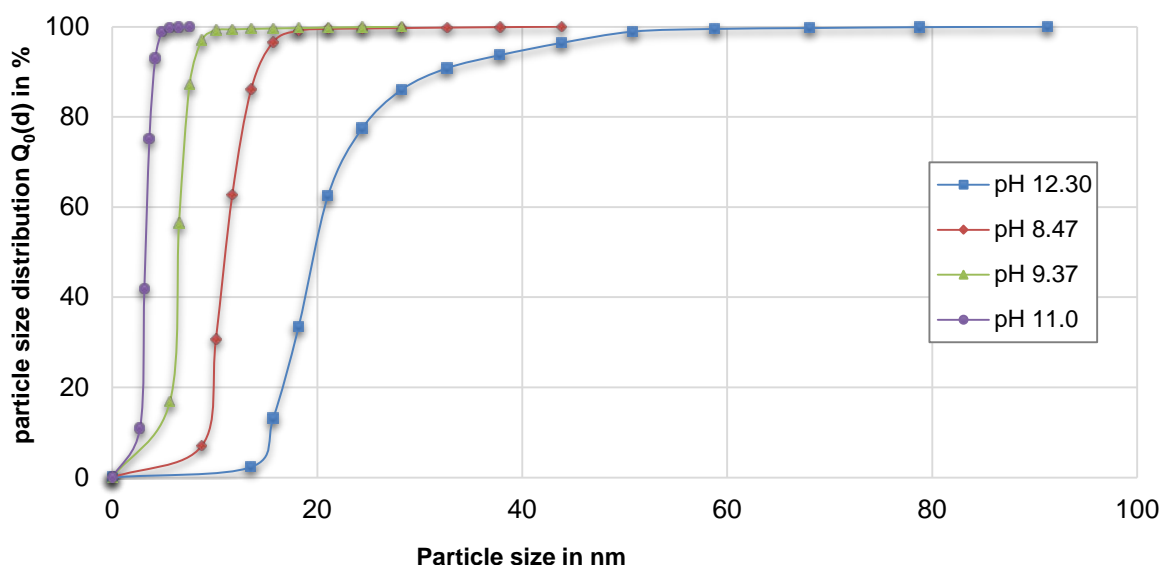


Figure 58: Cumulative particle size distribution $Q_0(d)$ of Tween 80-SPIO-NPs for the solution pH 11.0 to 12.30 with a Fe^{3+}/Fe^{2+} molar ratio of 2:1, 400 rpm, and at 40 °C

With the increase in a solution pH, a decrease in nanoparticles size was observed (figure 58). At pH 12.30, 11.0, and at 9.37, NPs were of very small in size less than 30 nm. Tween 80 coated NPs had zeta potential -59.7mV at pH 8.47. With the increase in pH up to 9.37, the zeta potential was -46.7 mV. Interestingly, at higher pH 12.30, the zeta potential was -24.2 mV. The median size ($d_{50,0}$) for Tween 80 coated NPs was 3.61 nm at pH 11.0 and 21.04 nm at pH 12.30 was recorded. With the increase in pH, the particle size was also decreased and particle size increased after pH 11. Here it is further suggested that the zeta potential is positive at low pH and a high pH value is connected to a negative zeta potential. Reaction characteristics for the effect of solution pH on Tween coated SPIO-NPs syntheses are provided in the following table 10.

Table 10: Reaction characteristics at various solution pH

pH	PDI	Zeta potential	Span
8.47	0.51	-59.7 mV	0.80
9.37	0.49	-46.7 mV	0.47
11.0	0.51	-37.4 mV	0.29
12.30	0.46	-24.2 mV	0.41

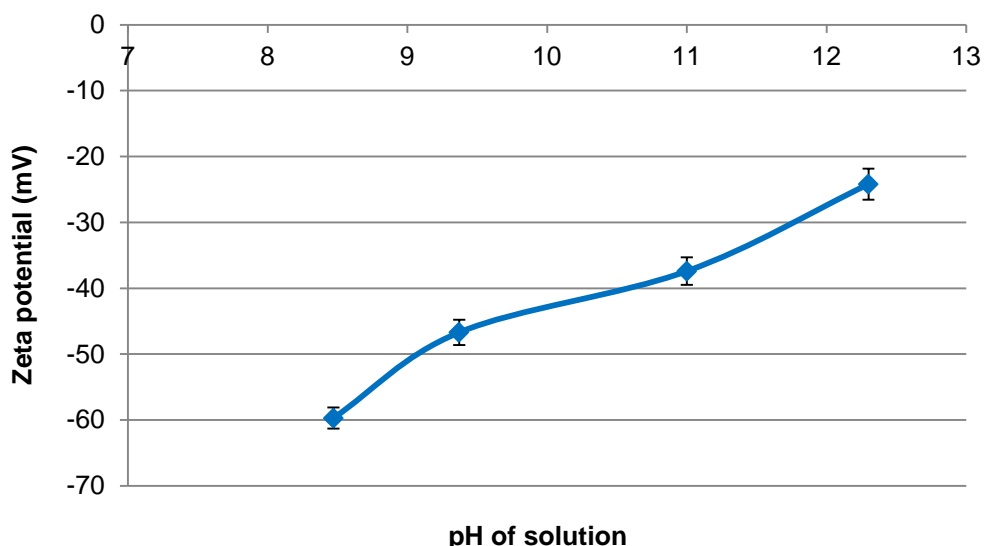


Figure 59: Variation of zeta potential with the solution pH of Tween 80-SPIO-NPs

With the increase in a solution pH, the zeta potential decreased and we had negative zeta potential values during this reaction parameter as shown in figure 59.

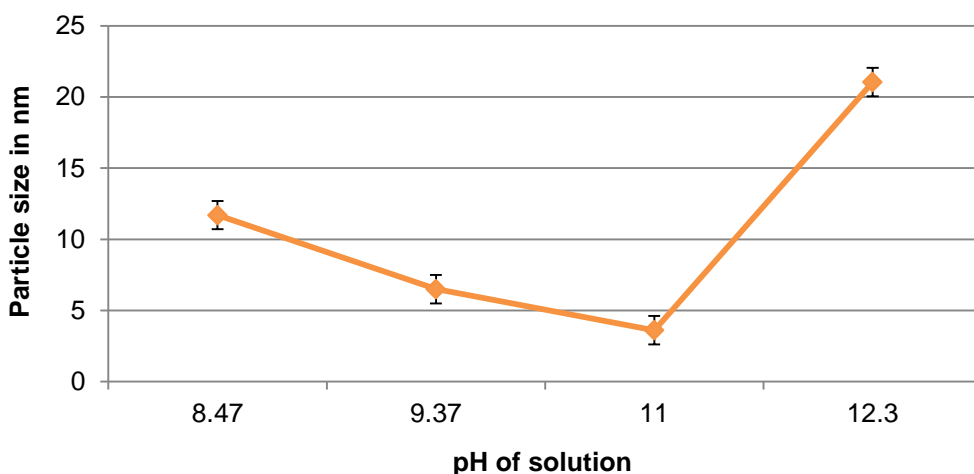


Figure 60: Effect of the solution pH on the median ($d_{50,0}$) particle size of Tween 80-SPIO-NPs

With the increase in a solution pH up to 11, the median ($d_{50,0}$) nanoparticle size was decreased to 3.61 nm because of the nucleation of the nanoparticles during a chemical reaction. On further increase in pH up to 12.30, the median particle size was also increased due to the growth of nanoparticles. Normally, the nanoparticles growth process starts after pH 11 as given in above figure 60. When the solution pH exceeds from 13, then the production rate of magnetite is reduced to 30-40 vol% and a maghemite structure like layer is formed on the nanoparticles surface. Therefore, a medium pH range (8-12) is very effective for the magnetite synthesis and this pH range also do not effect on the nanoparticle size [155].

5.1.4 Effect of $\text{Fe}^{3+}/\text{Fe}^{2+}$ molar ratio on the synthesis of Tween 80-SPIO-NPs

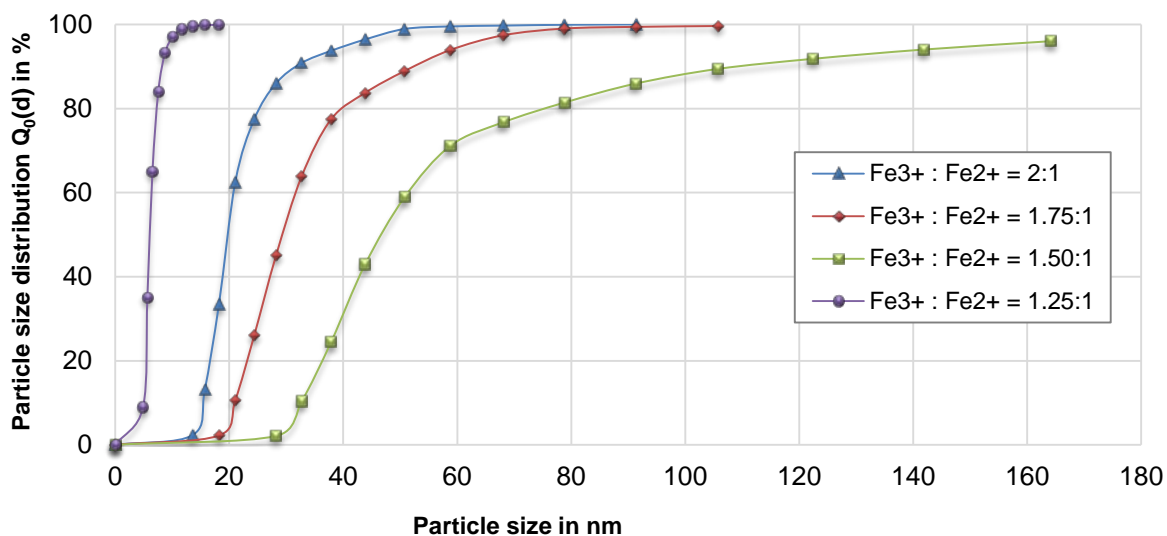


Figure 61: Cumulative particle size distribution $Q_0(d)$ of Tween 80-SPIO-NPs for $\text{Fe}^{3+}/\text{Fe}^{2+}$ molar ratios 1.25:1 to 2:1 at 40 °C and 400 rpm

The molar ratio of $\text{Fe}^{3+}/\text{Fe}^{2+}$ had a significant influence on the particle size as shown in the above figure 61. For Tween 80 coated NPs with iron salts concentration of 2:1 the pH 8.47, PDI 0.45 and zeta potential +15.5mV was recorded. When the iron salt concentration was changed to 1.75:1 the resulted values were increased to pH 8.50, PDI 0.43, and zeta potential +24.8mV; the highest zeta potential achieved for iron salt concentration for tween 80 coated NPs. There was no any prominent difference observed on changing the iron salts concentration to 1.75:1 and 2:1. The median size diameter was also increased from 6.50 nm to 21.04 nm from 1.25:1 to 2:1 $\text{Fe}^{3+}/\text{Fe}^{2+}$ molar ratios. The least median size diameter (6.50 nm) was measured at 1.25:1 $\text{Fe}^{3+}/\text{Fe}^{2+}$ molar ratio as shown in figure 63.

Normally, in a co-precipitation process, the $\text{Fe}^{3+}/\text{Fe}^{2+}$ molar ratio is 2:1. Particle size tends to increase when the $\text{Fe}^{3+}/\text{Fe}^{2+}$ molar ratio exceeds from 2:1. While Fe^{2+} tends to be oxidized to Fe^{3+} in the air, the $\text{Fe}^{3+}/\text{Fe}^{2+}$ molar ratio 2:1 is very difficult to be maintained during the precipitation. Therefore, excessive dosage of ferrous salts should be required for pure magnetite phase formation. In some experiments, an initial molar ratio of $\text{Fe}^{3+}/\text{Fe}^{2+}$ smaller than 2:1 has been utilized to compensate for the oxidation of Fe^{2+} . The decrease in a $\text{Fe}^{3+}/\text{Fe}^{2+}$ molar ratio from 2:1 causes a decrease in the chemical and physical properties because it is a possibility that some other forms of iron oxide can be formed when the standard $\text{Fe}^{3+}/\text{Fe}^{2+}$ molar ratio is disturbed from 2:1. Reaction characteristics for the different $\text{Fe}^{3+}/\text{Fe}^{2+}$ molar ratios on Tween coated SPIO-NPs syntheses are provided in the following table 11.

Table 11: Reaction characteristics at different Fe³⁺/Fe²⁺ molar ratios

Fe ³⁺ /Fe ²⁺ molar ratios	pH	PDI	Zeta potential	Span
1.25:1	8.66	0.44	+21.7 mV	0.59
1.50:1	8.46	0.47	+24.4 mV	1.76
1.75:1	8.50	0.43	+24.8 mV	0.90
2:1	8.47	0.45	+15.5 mV	0.80

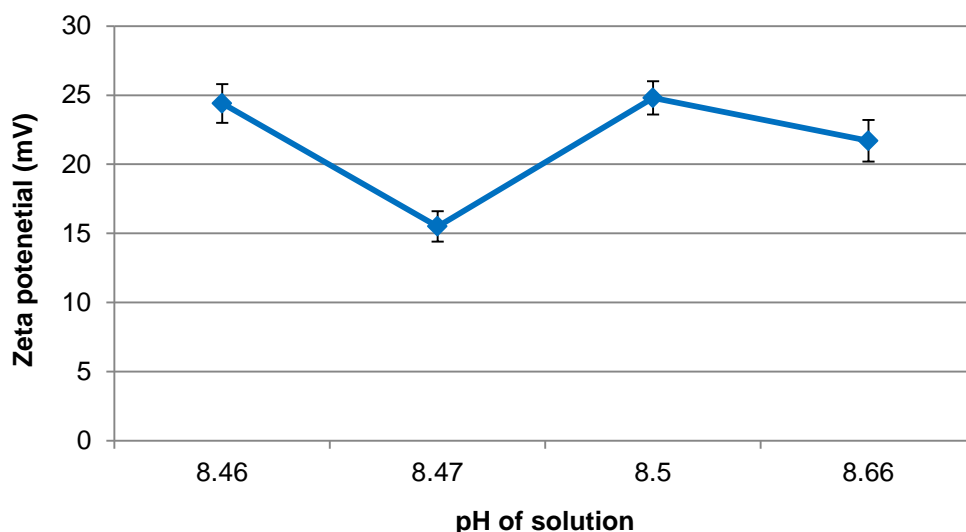


Figure 62: Change of zeta potential with the solution pH for different Fe³⁺/Fe²⁺ molar ratios

As depicted in the above figure 62, the zeta potential changed with the increase in a solution pH. Initially, it decreased with the rise in the solution pH and then afterwards, it increased to +24.8 mV.

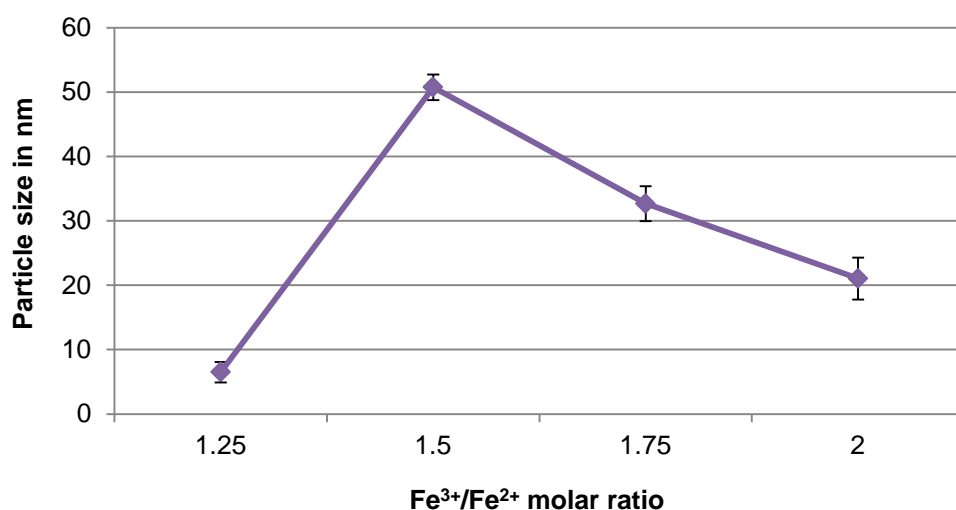


Figure 63: Effect of Fe³⁺/Fe²⁺ molar ratios on the median ($d_{50,0}$) particle size of Tween 80-SPIO-NPs

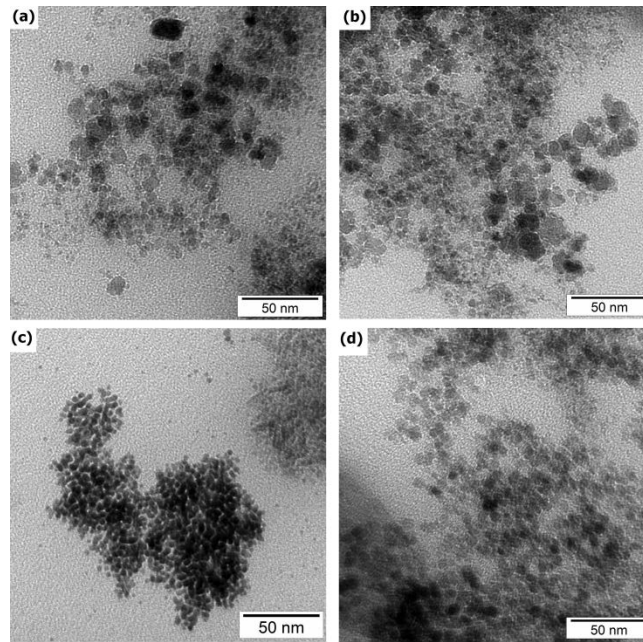


Figure 64: TEM images of Tween 80 coated SPIO-NPs (a) SPIO-NPs at 40 °C (b) SPIO-NPs at 1000 rpm (3.03 m/s stirrer tip speed) (c) SPIO-NPs at pH 11 (d) SPIO-NPs at $\text{Fe}^{3+}/\text{Fe}^{2+}$ molar ratio = 2:1

TEM results of Tween 80 modified SPIO-NPs confirm the morphology and size of the synthesized SPIO-NPs. Morphology of the SPIO-NPs is nearly spherical with an average hydrodynamic diameter 50 nm of the NPs for different reaction parameters.

5.2 Experiments with Dextran 70,000 as a surface coating material

5.2.1 Effect of temperature on the synthesis of Dextran 70,000-SPIO-NPs

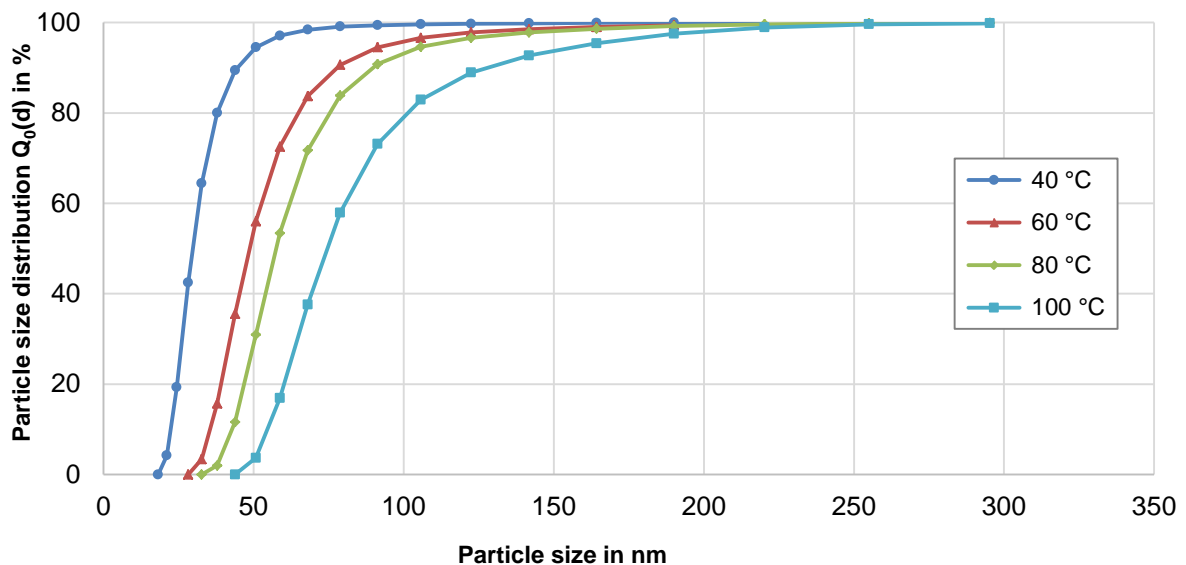


Figure 65: Cumulative particle size distribution $Q_0(d)$ of Dextran 70,000-SPIO-NPs for the reaction temperatures between 40 °C to 100 °C at a $\text{Fe}^{3+}/\text{Fe}^{2+}$ molar ratio of 2:1 and 400 rpm

Figure 65 is a particle size distribution and the particle size was increased with the increase in reaction temperature from 40 °C to 100 °C while keeping all the other parameters constant. The median particle size ($d_{50,0}$) was increased from 32.67 nm to 78.82 nm (figure 66). Best PDI of 0.40 was achieved at a temperature of 80 °C with a particle size $d_{50,0} = 58.77$ nm. At higher temperature, the curve became steeper and became flat for all higher temperature of 60 °C, 80 °C, and 100 °C. This shows the little polydispersity of nanoparticles in the reaction solution. At higher temperatures, too much higher input energy disturbs the reaction temperature and also many side reactions take place. So, a low temperature of 40 °C is favorable for the synthesis of iron oxide nanoparticles. Reaction characteristics are provided in table 12.

Table 12: Reaction characteristics at temperatures between 40 °C and 100 °C

Temperature (°C)	PDI	Zeta potential
40	0.48	-1.90 mV
60	0.47	-1.53 mV
80	0.40	-1.75 mV
100	0.45	-1.16 mV

There was a significant decrease in the zeta potential for iron oxide nanoparticles coated with Dextran 70,000. The recorded zeta potential was -1.90 to -1.16 mV. It has been well established that negative zeta potential for magnetic nanoparticles is due to the existence of OH^- groups on the surface of nanoparticles which reasoned that coating with Dextran 70,000 is responsible for hydrogen bonding between O^- groups of Dextran 70,000 and a hydroxyl group of the magnetic nanoparticles. Apparently, the value of zeta potential tends to decrease when the SPIO-NPs are coated with dextran [284]; our results are in agreement with Khalkhali et al. [284].

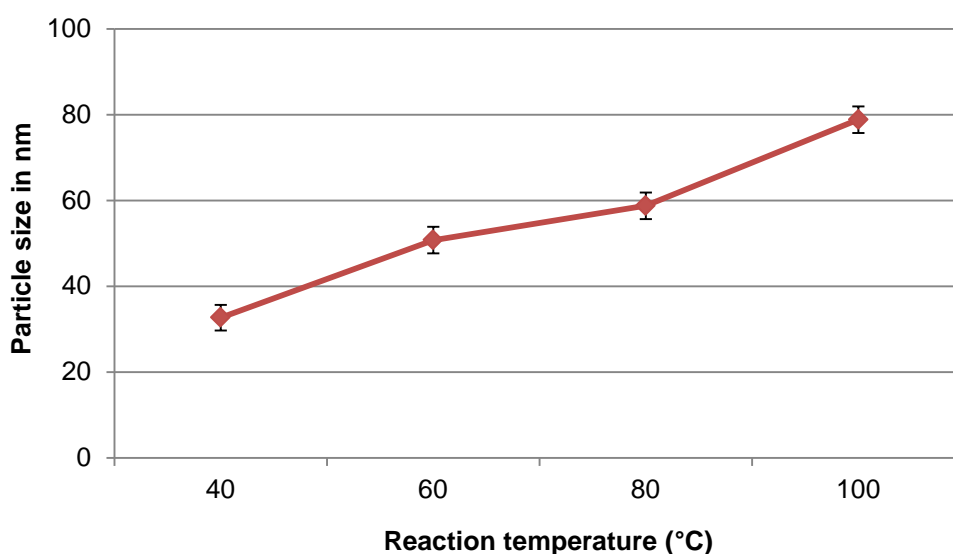


Figure 66: Effect of temperature on the median ($d_{50,0}$) particle size of Dextran 70,000-SPIO-NPs

Clearly it can be observed that the median particle size was increased with the increase in reaction temperature.

5.2.2 Effect of stirring velocity on the synthesis of Dextran 70,000-SPIO-NPs

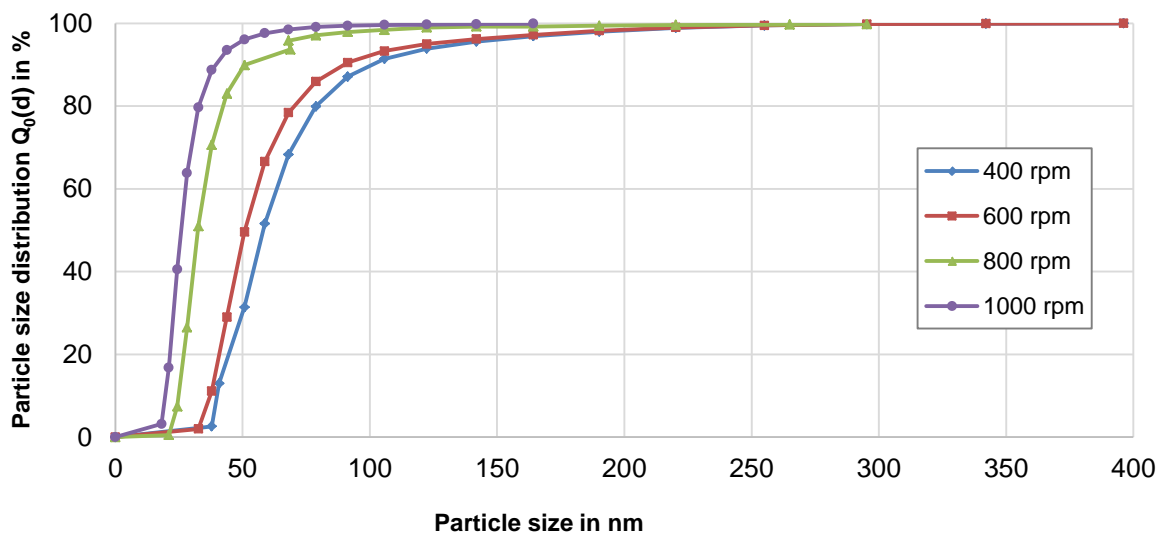


Figure 67: Cumulative particle size distribution $Q_0(d)$ at stirring velocities between 400 rpm to 1000 rpm (1.21 m/s to 3.03 m/s stirrer tip speed) with a Fe^{3+}/Fe^{2+} molar ratio of 2:1 and at 40 °C

Above figure 67 shows the effect of stirring velocity on particle size distribution. The median particle size was reduced from 58.77 nm to 28.21 nm when the stirring velocity was increased from 400 rpm to 1000 rpm (1.21 m/s to 3.03 m/s stirrer tip speed) under the same conditions of temperature. This decrease in particle size is due to the occurrence of irregular diffusion of the particles when agitation was increased, impeded the growth of the particles and hence smaller particles were achieved. Also, the energy transferred to the nanoparticles suspension medium was increased with the increase in stirring velocity and hence the reaction solution was dispersed into smaller droplets and therefore, the particle size was reduced. When the reaction solution was stirred at 400 rpm, the size distributions were broad which is due to the agglomeration of the particles. The size distribution of the sample was improved by stirring the reaction solution at 1000 rpm. Best PDI of 0.24 was achieved at 600 rpm provided the median diameter 50.75 nm and highest PDI of 0.32 was at 1000 rpm provided the median diameter 28.21 nm (figure 68). It is suggested that at low stirring velocity, the synthesized particles are liable to agglomerate.

Table 13: Reaction characteristics at stirring velocities between 400 rpm to 1000 rpm (1.21 m/s to 3.03 m/s stirrer tip speed)

Stirring velocity (rpm)	PDI	Zeta potential
400	0.26	-4.33 mV
600	0.24	-1.86 mV
800	0.25	-4.85 mV
1000	0.32	-1.70 mV

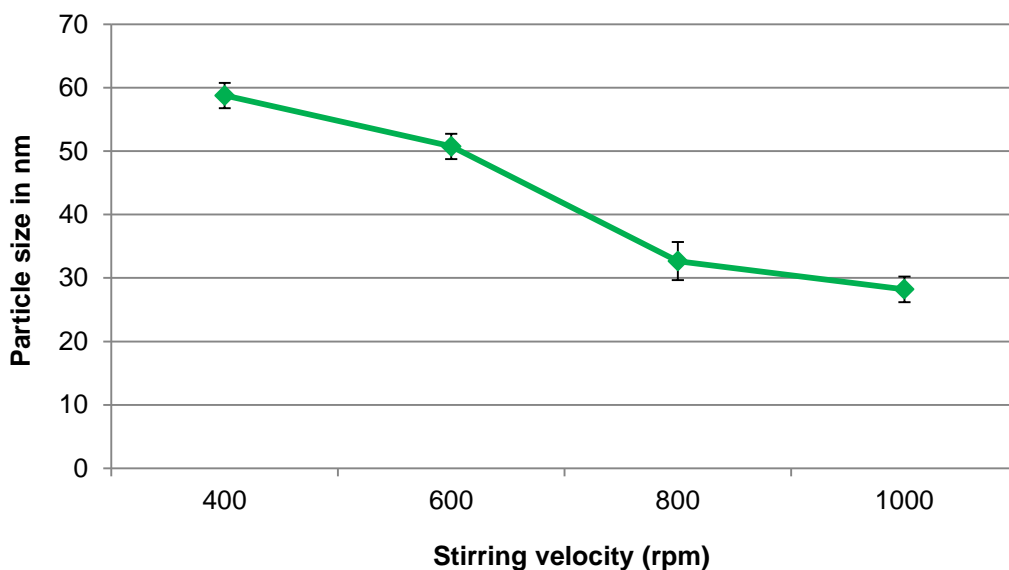


Figure 68: Effect of stirring velocity on the median ($d_{50,0}$) particle size of Dextran 70,000-SPIO-NPs

5.2.3 Effect of pH variation on the synthesis of Dextran 70,000-SPIO-NPs

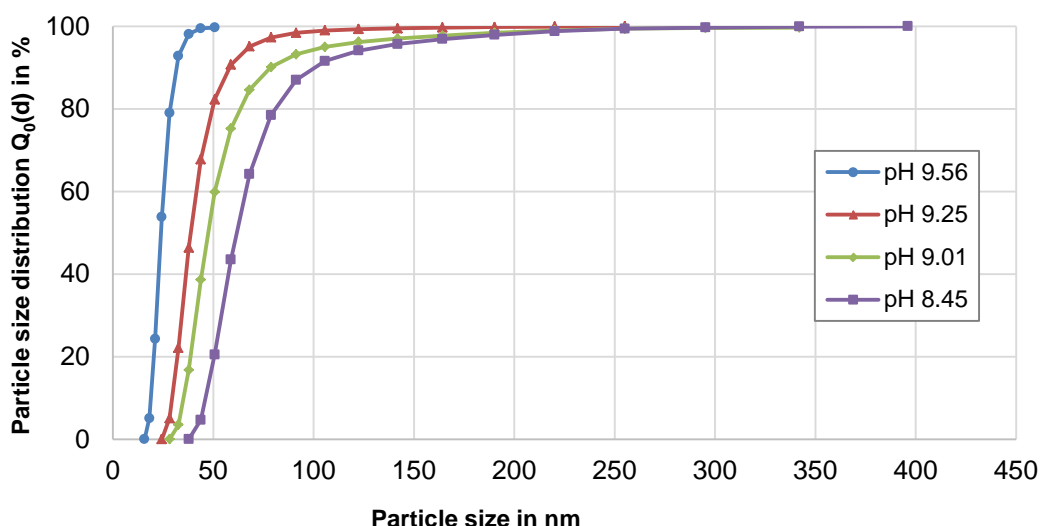


Figure 69: Cumulative particle size distribution $Q_0(d)$ of Dextran 70,000-SPIO-NPs for the solution pH 8.45 to 9.56 with a Fe^{3+}/Fe^{2+} molar ratio of 2:1, 400 rpm, and at 40 °C

Above figure 69 is the particle size distribution when the solution pH was increased from 8.45 to 9.56 keeping all other parameters constant. The respective median particle size ($d_{50,0}$) was reduced from 68.06 nm to 24.36 nm during the pH from 8.45 to 9.56. At the lowest pH of 8.45, the median particle size was 68.06 nm with a PDI of 0.43. With the further increase in pH to 9.01, the better median particle size 50.75 nm with best PDI of 0.38 was obtained. At pH 9.25, we had optimum values 0.43 and 43.82 nm of PDI and particle size respectively. The best median particle size 24.36 nm was obtained at pH of 9.56 with slightly high PDI of 0.46. So, the particle size was decreased as the solution pH increased as shown in figure 70. Reaction characteristics for this case are provided in table 14.

After increasing the solution pH, the hydrolysis of Fe^{3+} occurs and $\text{Fe}(\text{OH})_3$ is generated in the first step. These reactions are very fast and high yielding. In the second step, the ferric hydroxide decomposes to hydroxyl iron oxide (FeOOH) due to the low water activity in a relatively slower reaction step. With the further increase in a solution pH, $\text{Fe}(\text{OH})_2$ produces and a solid state reaction takes place between this ferrous hydroxide and FeOOH to form a $\text{Fe}(\text{OH})_2\text{-FeOOH}$ composite and this composite is converted to Fe_3O_4 nanoparticles. The final concentration of OH^- ions is related to the solution pH and base amount used during the co-precipitation reaction. The OH^- ions concentration is responsible to control the nucleation and growth of the synthesized Fe_3O_4 nanoparticles and eventually influences the nanoparticle size and also their corresponding magnetic properties.

Table 14: Reaction characteristics at pH 8.45 to 9.56

pH	PDI	Zeta potential
8.45	0.43	-6.06 mV
9.01	0.38	-4.16 mV
9.25	0.43	-7.49 mV
9.56	0.46	-5.57 mV

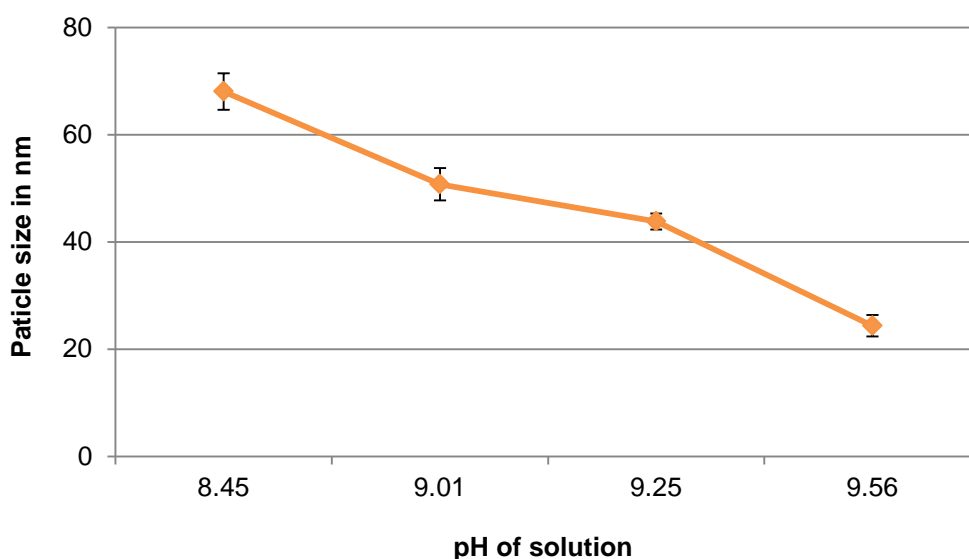


Figure 70: Effect of the solution pH on the median ($d_{50,0}$) particle size of Dextran 70,000-SPIO-NPs

5.2.4 Effect of $\text{Fe}^{3+}/\text{Fe}^{2+}$ molar ratio on the synthesis of Dextran 70,000-SPIO-NPs

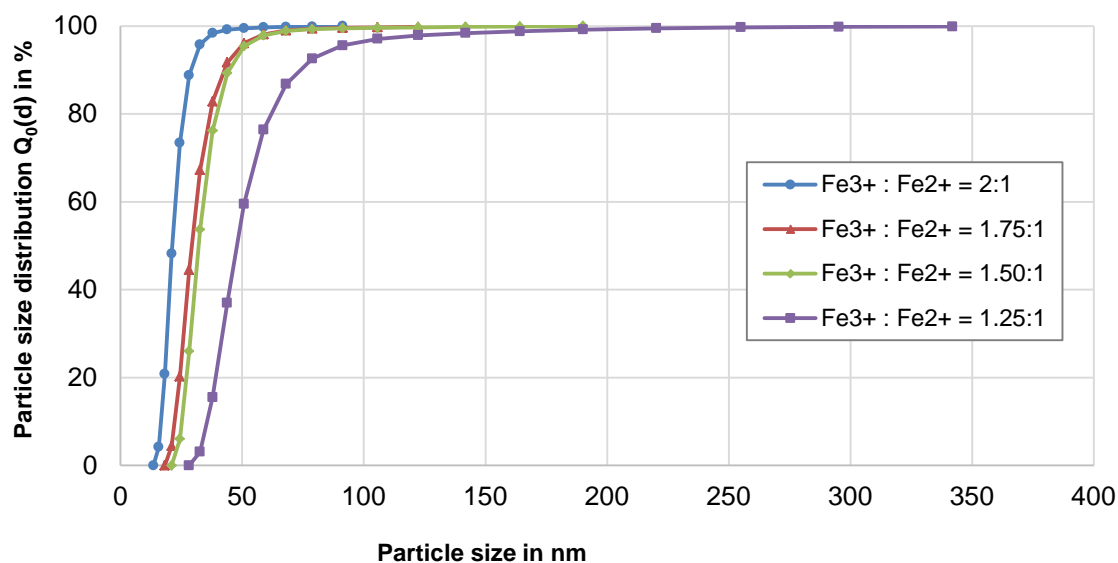


Figure 71: Cumulative particle size distribution $Q_0(d)$ of Dextran 70,000-SPIO-NPs for $\text{Fe}^{3+}/\text{Fe}^{2+}$ molar ratios 1.25:1 to 2:1 at 40 °C and 400 rpm

The results in the above figure 71 explained the effect of precursor's concentration on the particles size distribution keeping all other parameters constant, there is a continuous decrease in the particle size and particle size distribution is no longer broader. The median particle (size $d_{50, 0}$) was decreased from 50.75 nm with PDI of 0.39 to 21.04 nm with a PDI of 0.42 as given in figure 72. At ratio $\text{Fe}^{3+}/\text{Fe}^{2+} = 1.25:1$, the particle size distribution was much broader. By increasing the $\text{Fe}^{3+}/\text{Fe}^{2+}$ ratios, the particle size distribution was much narrower than the previous ratio and we got optimum values of particle size and also particle size distribution. The best particle size was obtained at the $\text{Fe}^{3+}/\text{Fe}^{2+}$ ratio of 2:1 with a PDI of 0.42. Table 15 is the reaction characteristics for the effect of $\text{Fe}^{3+}/\text{Fe}^{2+}$ molar ratios on the synthesis of Dextran 70,000 coated SPIO-NPs.

Table 15: Reaction characteristics at different $\text{Fe}^{3+}/\text{Fe}^{2+}$ molar ratios

$\text{Fe}^{3+}/\text{Fe}^{2+}$ molar ratios	PDI	Zeta potential
1.25:1	0.39	-5.97 mV
1.50:1	0.41	-3.17 mV
1.75:1	0.47	-3.87 mV
2:1	0.42	-1.13 mV

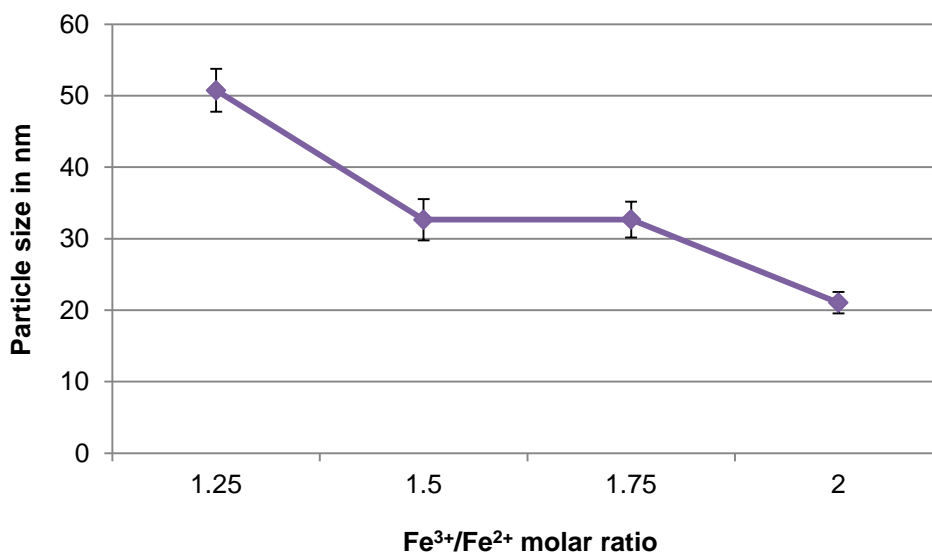


Figure 72: Effect of Fe³⁺/Fe²⁺ molar ratios on the median ($d_{50,0}$) particle size of Dextran 70,000-SPIO-NPs

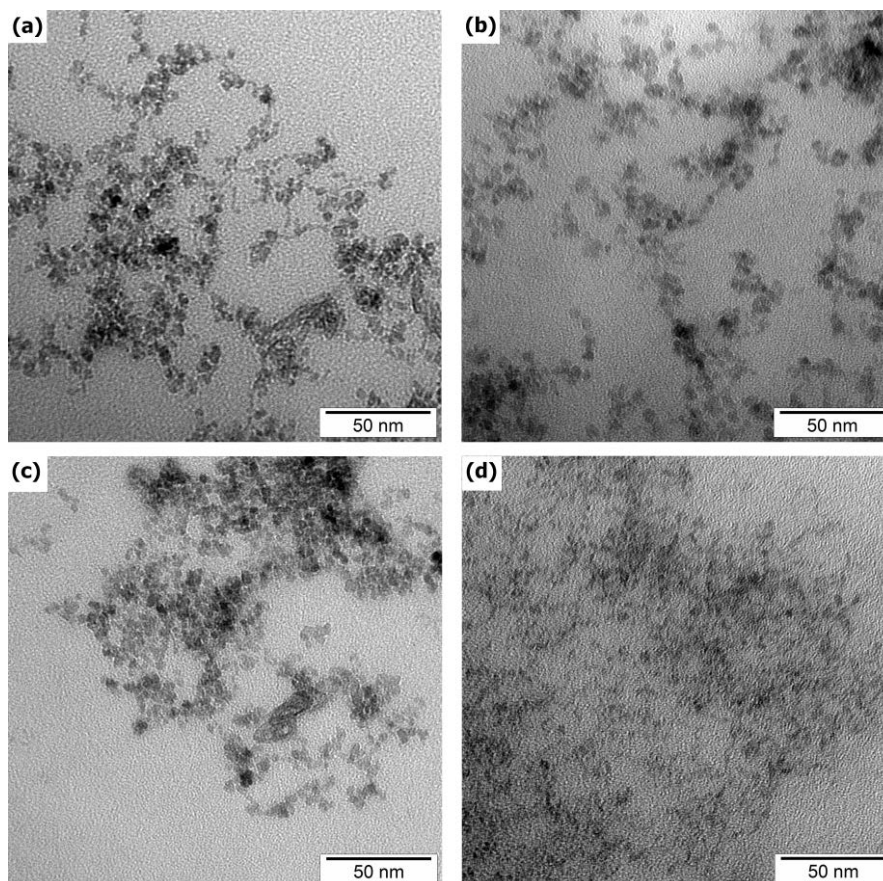


Figure 73: TEM micrographs of Dextran 70,000 coated SPIO-NPs (a) SPIO-NPs at 40 °C (b) SPIO-NPs at 1000 rpm (3.03 m/s stirrer tip speed) (c) SPIO-NPs at pH 9.56 (d) SPIO-NPs at Fe³⁺/Fe²⁺ molar ratio = 2:1

TEM images of Dextran 70,000 coated SPIO-NPs are shown in the above figure 73. Average SPIO-NPs sizes are 50 nm with a little tendency to agglomerate. Morphology of the synthesized SPIO-NPs is nearly spherical at different reaction

parameters. Primary particles having a size less than 40 nm can be considered as single domain particles with superparamagnetic properties.

5.3 Experiments with DEAE-Dextran as a surface coating material

5.3.1 Effect of temperature on the synthesis of DEAE-Dextran-SPIO-NPs

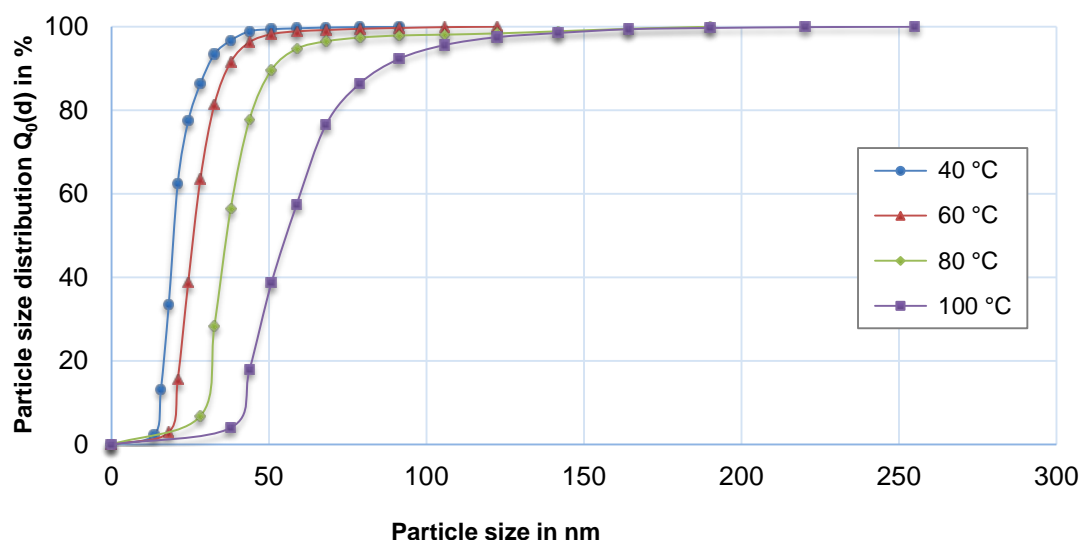


Figure 74: Cumulative particle size distribution $Q_0(d)$ of DEAE-Dextran-SPIO-NPs for the reaction temperatures between 40 °C to 100 °C at a Fe^{3+}/Fe^{2+} molar ratio of 2:1 and 400 rpm

Particle size distribution of DEAE-Dextran coated nanoparticles at various reaction temperatures is given in the above figure 74. At 40 °C, the pH 8.75 with PDI 0.33 and zeta potential +16.2 mV was observed and at higher temperatures, 60 °C, 80 °C, and 100 °C not much difference was recorded. For DEAE-Dextran coated NPs, the minimum median particle size ($d_{50,0}$) was 21.04 nm at 40°C and the maximum median particle size 58.77 nm was achieved at 100 °C. The effect of temperature on the median particle size is given in figure 75 and variation of zeta potential with the solution pH is illustrated in figure 76. Reaction characteristics for the effect of temperatures in this synthesis phase are given in the following table 16.

Table 16: Reaction characteristics at different temperatures in case of coating with DEAE-Dextran

Temperature (°C)	pH	PDI	Zeta potential	Span
40	8.75	0.33	+16.2 mV	0.80
60	8.59	0.44	+17.7 mV	0.59
80	8.10	0.41	+19.2 mV	0.47
100	8.84	0.42	+16.8 mV	0.80

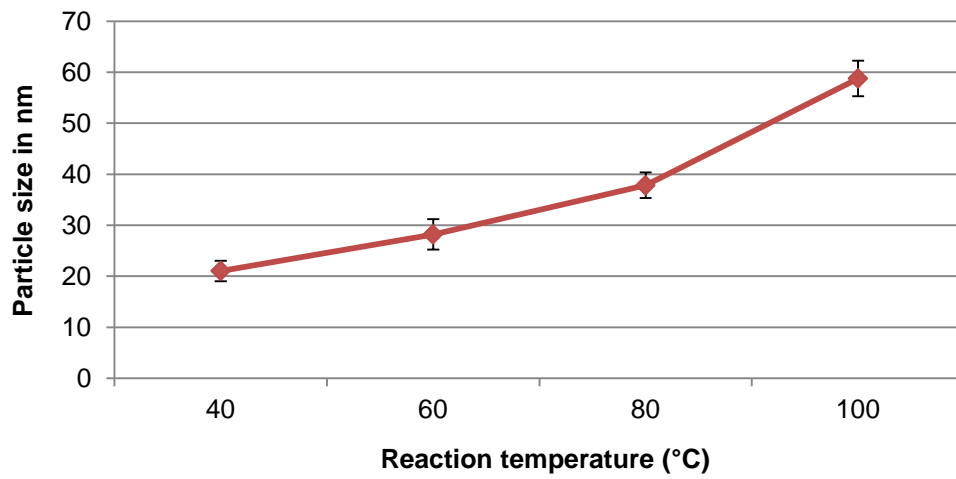


Figure 75: Effect of temperature on the median ($d_{50,0}$) particle size for DEAE-Dextran coated SPIO-NPs

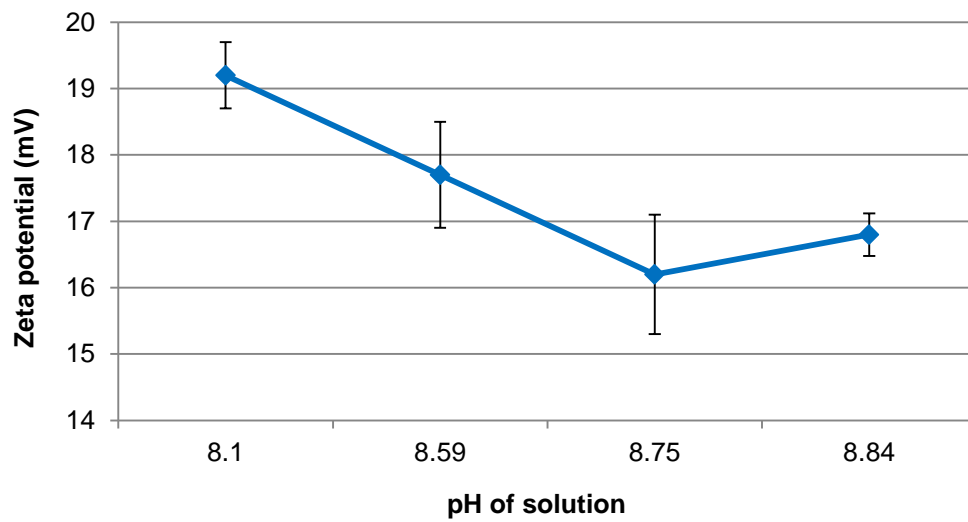


Figure 76: Change of zeta potential with the solution pH for DEAE-Dextran coated SPIO-NPs

5.3.2 Effect of stirring velocity on the synthesis of DEAE-Dextran-SPIO-NPs

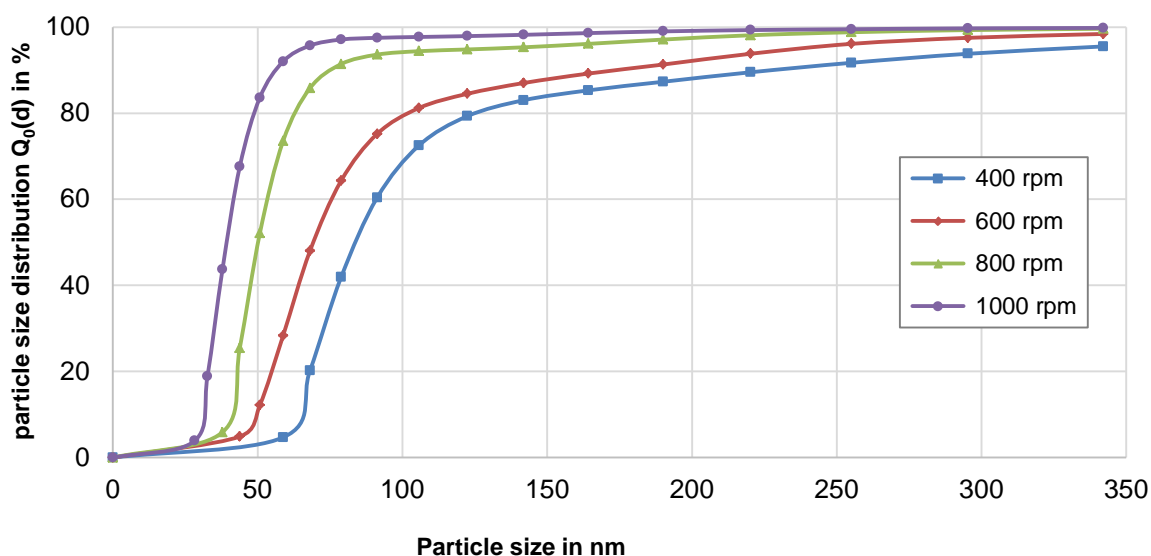


Figure 77: Cumulative particle size distribution $Q_0(d)$ of DEAE-Dextran-SPIO-NPs at stirring velocities between 400 rpm to 1000 rpm (1.21 m/s to 3.03 m/s stirrer tip speed) with a Fe^{3+}/Fe^{2+} molar ratio of 2:1 and at 40 °C

At stirring speeds 400 rpm to 1000 rpm (1.21 m/s to 3.03 m/s stirrer tip speed), the size distribution curves are shown in figure 77. Best particle size and the respective particle size distribution were achieved at 1000 rpm and least size and size distribution was obtained at 400 rpm. The median particle size ($d_{50,0}$) was decreased from 91.28 nm to 43.82 nm when the stirring velocity was increased from 400 rpm to 1000 rpm respectively and is clearly illustrated in figure 78 and the next figure 79 is the variation explanation of zeta potential with the solution pH. Reaction characteristics for the effect of different stirring velocities in this phase are given in the following table 17.

Table 17: Reaction characteristics at different stirring velocities between 400 rpm to 1000 rpm (1.21 m/s to 3.03 m/s stirrer tip speed) for DEAE-Dextran-SPIO-NPs

Stirring (rpm)	pH	PDI	Zeta potential	Span
400	8.11	0.52	+21.2 mV	2.04
600	8.19	0.50	+19.1 mV	2.04
800	8.25	0.42	+18.5 mV	0.69
1000	8.33	0.46	+16.9 mV	0.60

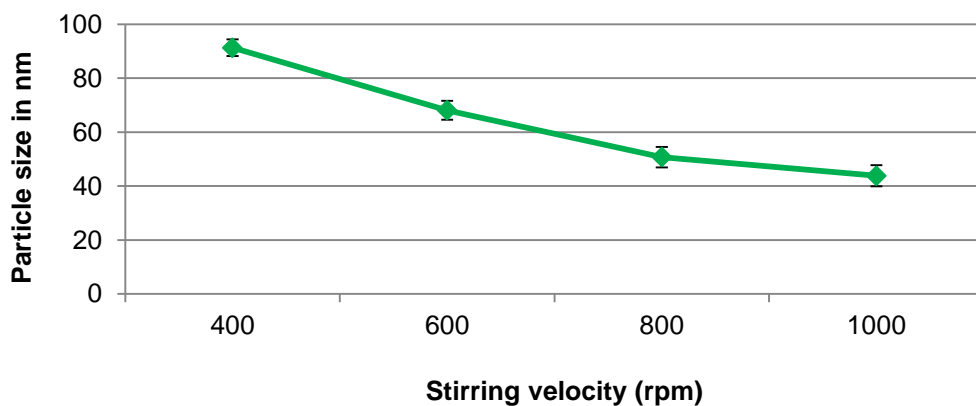


Figure 78: Effect of stirring velocity on the median ($d_{50,0}$) particle size for DEAE-Dextran-SPIO-NPs

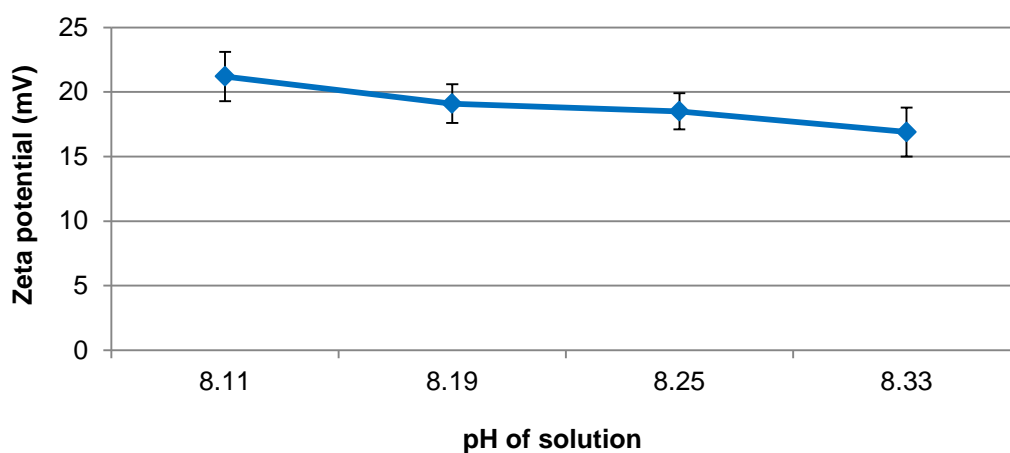


Figure 79: Effect of the solution pH on zeta potential for DEAE-Dextran-SPIO-NPs

5.3.3 Effect of pH variation on the synthesis of DEAE-Dextran-SPIO-NPs

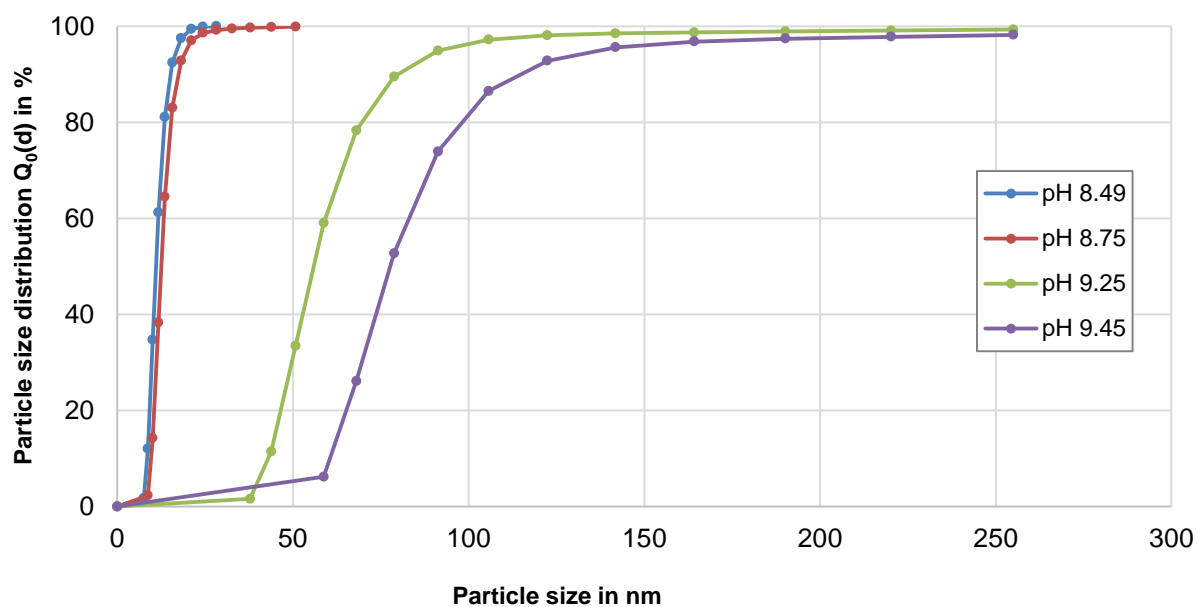


Figure 80: Cumulative particle size distribution $Q_0(d)$ of DEAE-Dextran-SPIO-NPs for the solution pH 8.49 to 9.45 with a Fe^{3+}/Fe^{2+} molar ratio of 2:1, 400 rpm, and at 40 °C

The effect of a solution pH on DEAE-Dextran coated SPIO-NPs is explained in the above figure 80. The lowest median particle size for DEAE-Dextran coated SPIO-NPs was 11.7 nm at pH 8.49 and with the increase in pH, the particle size increased for DEAE-Dextran coated NPs as given in figure 81 and their reaction characteristics are given in the following table 18. At pH 8.49, the zeta potential was +19.5 mV and at pH 8.75, the recorded zeta potential was +18 mV. When the solution pH was reached at 9.45, the ZP was +13.1 mV with PDI 0.49. This can be suggested that with the increase in pH, zeta potential decreased in the case of DEAE-Dextran coated SPIO-NPs (figure 82).

Table 18: Reaction characteristics at pH from 8.49 to 9.45 for DEAE-Dextran coated SPIO-NPs

pH	PDI	Zeta potential	Span
8.49	0.51	+19.5 mV	0.59
8.75	0.49	+18.0 mV	0.59
9.25	0.42	+16.2 mV	0.59
9.45	0.49	+13.1 mV	0.68

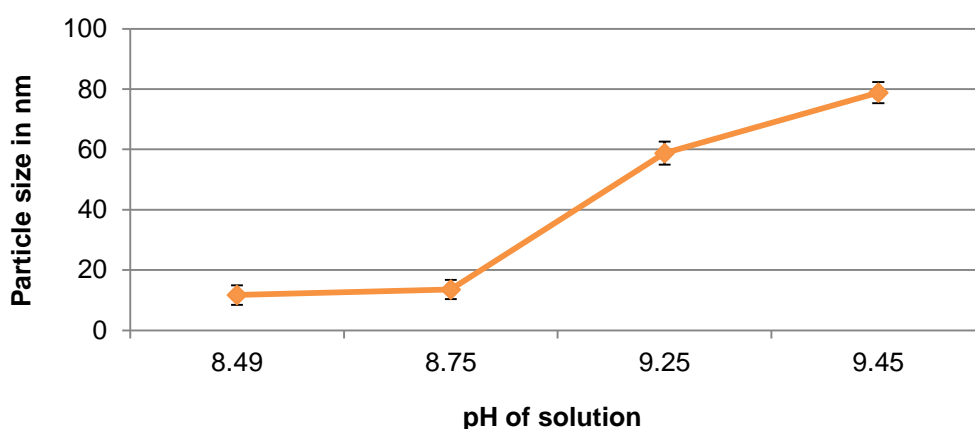


Figure 81: Effect of the solution pH on the median ($d_{50,0}$) particle size for DEAE-Dextran coated SPIO-NPs

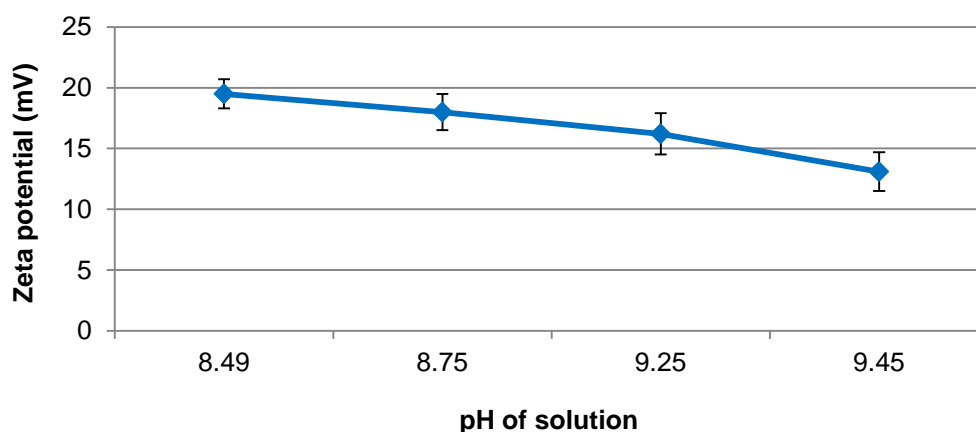


Figure 82: Effect of the solution pH on zeta potential for DEAE-Dextran coated SPIO-NPs

5.3.4 Effect of $\text{Fe}^{3+}/\text{Fe}^{2+}$ molar ratio on the synthesis of DEAE-Dextran-SPIO-NPs

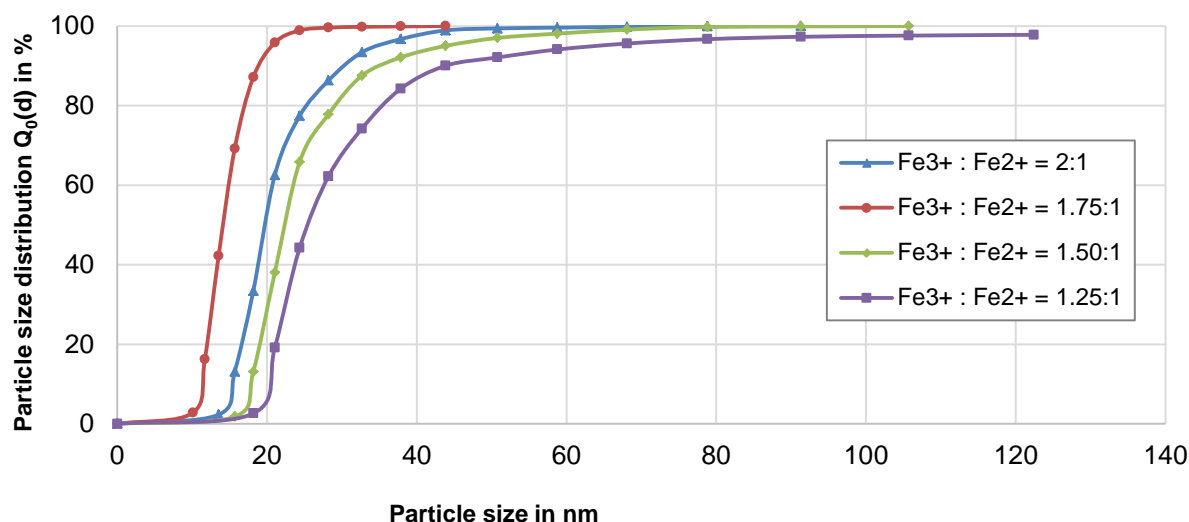


Figure 83: Cumulative particle size distribution $Q_0(d)$ of DEAE-Dextran-SPIO-NPs for $\text{Fe}^{3+}/\text{Fe}^{2+}$ molar ratios 1.25:1 to 2:1 at 40 °C and 400 rpm

In these experiments, the Fe(III) concentration was changed while the concentration of Fe(II) was kept constant. Their particle size distributions are given in the above figure 83. For DEAE-Dextran coated NPs at $\text{Fe}^{3+}:\text{Fe}^{2+} = 2:1$, the pH was 8.47 with PDI 0.45 and zeta potential +15.5 mV. When the iron salt concentration was changed to 1.75:1 the values increased to a slightly high pH 8.50, PDI 0.49, and zeta potential +22.3 mV, which was the highest zeta potential achieved for these experiments for DEAE-Dextran coated NPs. When the iron salt concentration was further changed to 1.50:1 and 1.25:1 there was no any significant change observed but with the best PDI 0.33 at 1.50:1 molar ratio. The minimum median particle size achieved for DEAE-Dextran coated SPIO-NPs at 1.75:1 iron salt concentration was 15.69 nm and the maximum median particle size 28.21 nm was achieved at 1.25:1 iron salt concentration as shown in figure 84. The effect of solution pH on zeta potential is given in figure 85.

Normally, in a co-precipitation process, the $\text{Fe}^{3+}/\text{Fe}^{2+}$ molar ratio is 2:1. Particle size tends to increase when the $\text{Fe}^{3+}/\text{Fe}^{2+}$ molar ratio exceeds from 2:1. While Fe^{2+} tends to be oxidized to Fe^{3+} in the air, the $\text{Fe}^{3+}/\text{Fe}^{2+}$ molar ratio of 2:1 is very difficult to be maintained during the precipitation. Therefore, excessive dosage of ferrous salts should be required for pure magnetite phase formation. In some experiments, an initial molar ratio of $\text{Fe}^{3+}/\text{Fe}^{2+}$ smaller than 2:1 has been utilized to compensate for the oxidation of Fe^{2+} . The decrease in a $\text{Fe}^{3+}/\text{Fe}^{2+}$ molar ratio from 2:1 causes a decrease in the chemical and physical properties because it is a possibility that some other forms of iron oxide can be formed when the standard $\text{Fe}^{3+}/\text{Fe}^{2+}$ molar ratio is disturbed from 2:1. Reaction characteristics for the effect of $\text{Fe}^{3+}/\text{Fe}^{2+}$ molar ratios on DEAE-Dextran coated SPIO-NPs syntheses are given in the following table 19.

Table 19: Reaction characteristics at different Fe³⁺/Fe²⁺ molar ratios for DEAE-Dextran coated SPIO-NPs

Fe ³⁺ /Fe ²⁺ molar ratios	pH	PDI	Zeta potential	Span
1.25:1	8.90	0.37	+18.3 mV	0.80
1.50:1	9.06	0.33	+19.4 mV	0.80
1.75:1	8.50	0.49	+22.3 mV	0.59
2:1	8.47	0.45	+15.5 mV	0.80

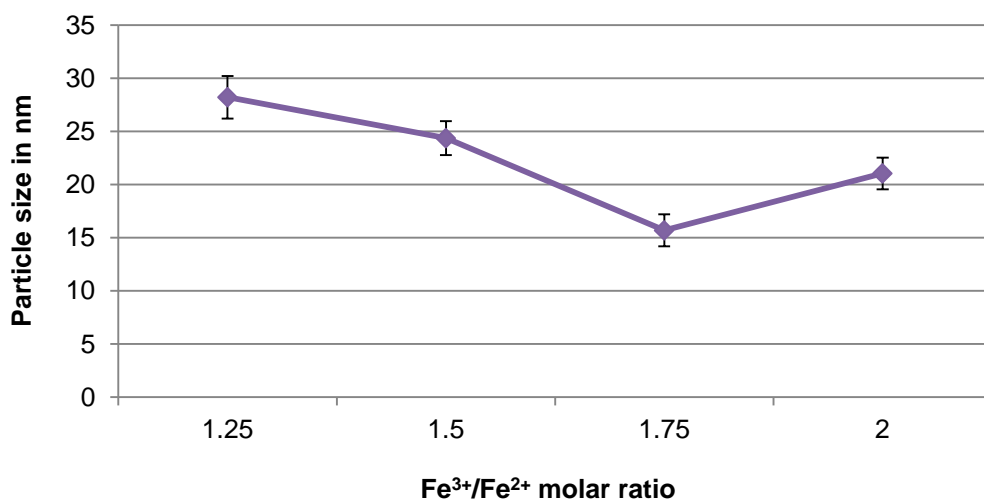


Figure 84: Effect of different Fe³⁺/Fe²⁺ molar ratios on the median (d_{50, 0}) particle size for DEAE-Dextran coated SPIO-NPs

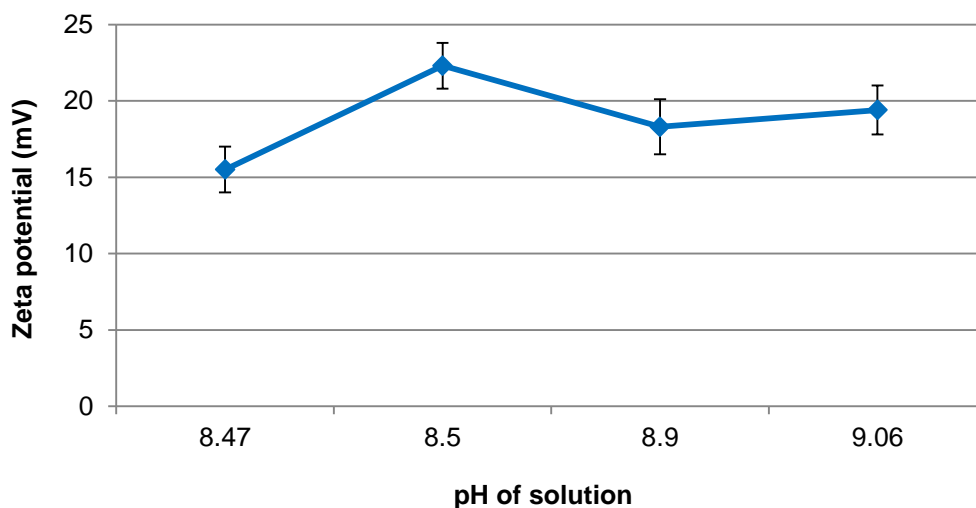


Figure 85: Effect of the solution pH on zeta potential for DEAE-Dextran coated SPIO-NPs

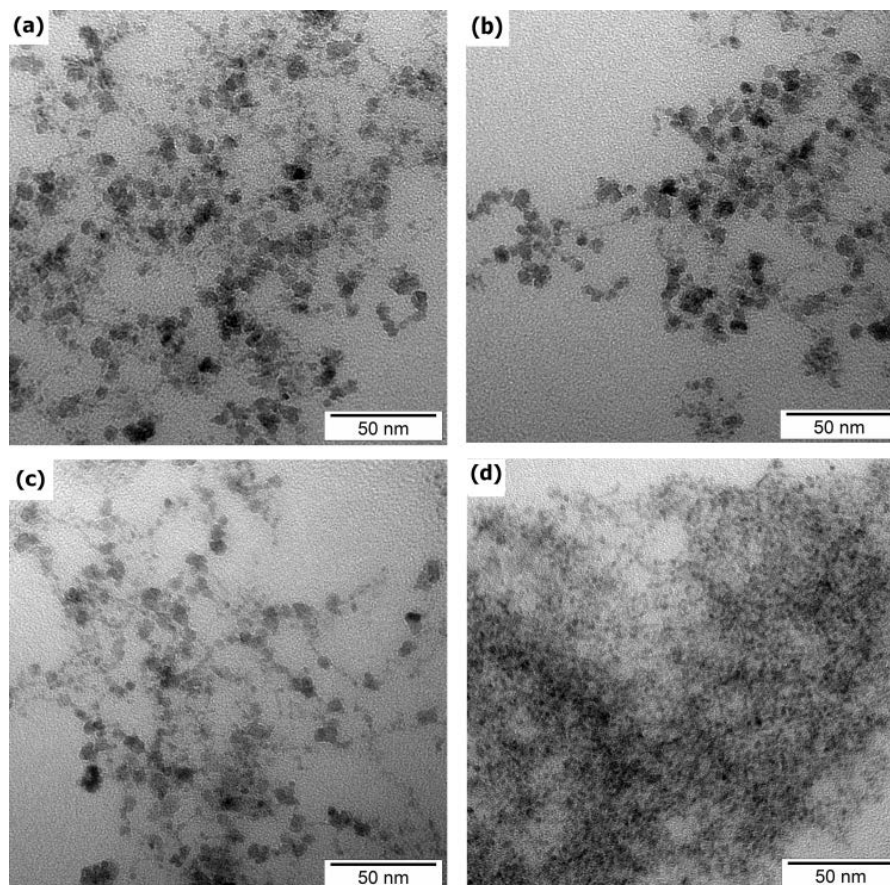


Figure 86: TEM micrographs of DEAE-Dextran coated SPIO-NPs (a) SPIO-NPs at 40 °C (b) SPIO-NPs at 1000 rpm (3.03 m/s stirrer tip speed) (c) SPIO-NPs at pH 8.49 (d) SPIO-NPs at Fe^{3+}/Fe^{2+} molar ratio = 2:1

TEM images of DEAE-Dextran coated SPIO-NPs are shown in the above figure 86. Average SPIO-NPs sizes are 50 nm with a little tendency to agglomerate. Morphology of the synthesized SPIO-NPs is nearly spherical at different reaction parameters. Primary particles having a size less than 40 nm can be considered as single domain particles with superparamagnetic properties.

*Table 20: Variations of the experiments (using kinematic viscosity $\nu = 6.10 \cdot 10^{-7} \text{ m}^2/\text{s}$)

RPM	Stirrer tip speed ' V_s ' in m/s	Stirrer tip speed ' V_s ' in rad/s	Turbulent energy dissipation rate ' ϵ ' in m^2/S^3	Reynold numbers ' Re '
400	1.21	41.88	1.55	37377
600	1.82	62.83	5.25	56066
800	2.42	83.77	12.44	74755
1000	3.03	104.71	24.30	93444

*Calculations are given in appendix

We synthesized SPIO-NPs coated with Tween 80, Dextran 70,000, and DEAE-Dextran. As an average, all nanoparticles are in the size range of 10~100 nm and have positive or negative zeta potentials. But the size distribution using Tween 80 as

the surface coating material is narrower and also has higher zeta potentials. The positive zeta potential on nanoparticles is due to the presence of OH^- group which is largely distributed on the synthesized iron oxide nanoparticles surface [285]. In all experiments, nanoparticle size is increasing with enhancing in a solution pH which is mainly to the nucleation of the SPIO-NPs. We got the best particle size distribution with best particle size at the optimum condition: at high pH (<11), higher stirring velocity (1000 rpm), the $\text{Fe}^{3+}/\text{Fe}^{2+}$ molar ratio (2:1), and at low temperature (40 °C). The effects of these reaction parameters already have been discussed in chapter 4 (section 4.3). Best particle size is expected with a $\text{Fe}^{3+}/\text{Fe}^{2+}$ molar ratio of 2:1. Our all experiments were performed in an air atmosphere and therefore, the oxidizing factor cannot be ignored. For Tween 80-SPIO-NPs, best size distribution was achieved at $\text{Fe}^{3+}/\text{Fe}^{2+}=1.25:1$ and for DEAE-Dextran-SPIO-NPs, best size distribution was obtained at 1.75:1. This can be explained by the fact that when we disturbed the normal $\text{Fe}^{3+}/\text{Fe}^{2+}=2:1$, Fe^{2+} oxidized to Fe^{3+} in the air – so, the general ratio of $\text{Fe}^{3+}/\text{Fe}^{2+}$ (2:1) is very difficult to be maintained during the precipitation reaction. The polydispersity index (PDI) of our superparamagnetic iron oxide nanoparticles is somehow in the range of 0.23 to 0.5 and this PDI range is also reported in the literature [91], [286]. High stirring velocity, the $\text{Fe}^{3+}/\text{Fe}^{2+}$ molar ratio of 2:1, low temperature, and 8-11 solution pH range lead the uniform SPIO-NPs synthesis. Particle size increased with the increase in the solution pH for the case of DEAE-Dextran coated nanoparticles synthesis which might be due to (1) early particles growth at pH 8.75 by coagulation and aggregation, (2) hydrolysis and precipitation of dissolved iron with the rise in solution pH, (3) or formation of a coating layer on the SPIO-NPs surface which therefore, shielding the charge in the case of DEAE-Dextran. It is also possible that DEAE-Dextran favor a greater discrimination between particles and for this reason, a surface layer sorbed onto the iron oxide aggregates.

Zeta potential depends mainly on the surface chemistry and associated solution chemistry. We had negative and positive zeta potentials in our results which were due to the change in a solution pH. At lower pH values, the zeta potential is more positive and when pH goes on increasing, normally negative zeta potential is achieved. So, a range of zeta potentials can be attained on a different pH profile. The between the point where zeta potential crosses the negative and positive values and have no electrical charge is called isoelectric point (IEP). For metallic nanoparticles, when going to decrease in pH values or changes in surface chemistry on changing the solution pH, might prohibit that change in zeta potential could be possible. For the case where IEP is at some extreme lower pH, it could be very difficult to have a positive zeta potential. At this point surface properties of nanoparticles play an important role.

6 Cytotoxicity and uptake studies of coated fluorescent SPIO-NPs

Cytotoxicity (*in vitro*), *in vivo*, and *ex vivo* uptake of the synthesized coated SPIO-NPs was a most important concern of our work. For *in vitro* toxic studies, the surface properties of SPIO-NPs are most important for cellular uptake. For evaluating the *in vivo* toxic studies as already discussed before in this dissertation, NPs size, shape, dose, and surface coating play a significant role. When SPIO-NPs are administered by an intravenous injection, they accumulate into liver and spleen. During the recent years, interest in *in vitro* studies over *in vivo* studies of SPIO-NPs is increased due to their easy manipulation; ease in their interpretation, and also of cost-effective methods. Although *in vivo* methods are expensive with the involvement of many ethical issues, but these are considered as an integral part of today's research for the better understanding of the SPIO-NPs in the body.

6.1 *In vitro* toxicity experiments

As discussed in chapter 4, fluorescent SPIO-NPs were prepared by labelling with propidium iodide and rhodamine 123. For this purpose, SPIO-NPs were dissolved with fluorescent dyes (propidium iodide (1.2 mg/ml) and rhodamine 123 (2 mg/ml)) solutions followed by the centrifugation separation and re-dispersed in DI water. This process was repeated to make sure the labelling of SPIO-NPs with fluorescent dyes. These fluorescent SPIO-NPs were then exposed to different concentrations (in µg/ml) with the C6 glioma cells at different incubation times.

6.1.1 Cytotoxicity of fluorescent Tween 80 coated SPIO-NPs

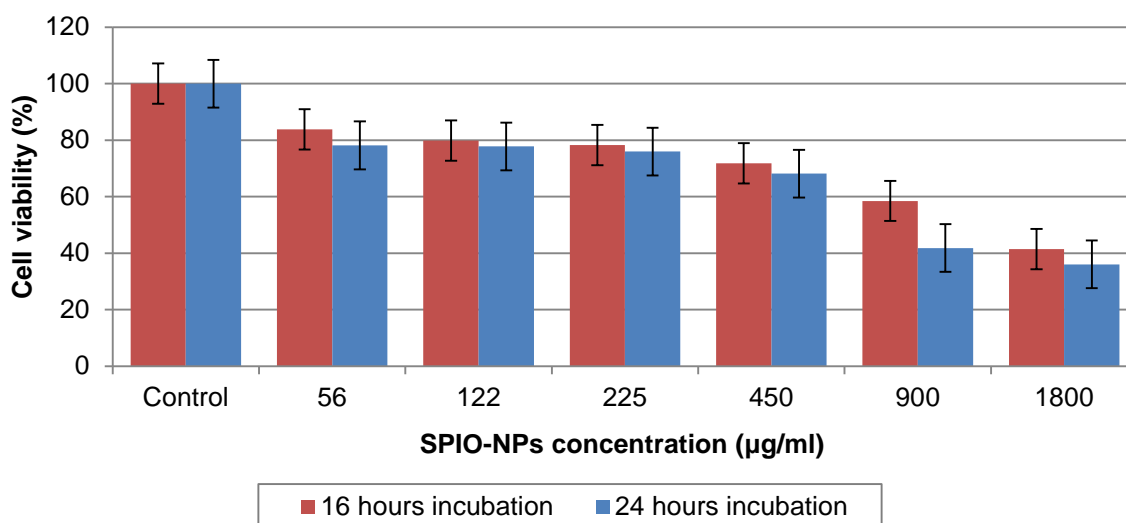


Figure 87: The effects of Tween 80-SPIO-NPs on the cell viability of C6 glioma cells determined by MTT assay

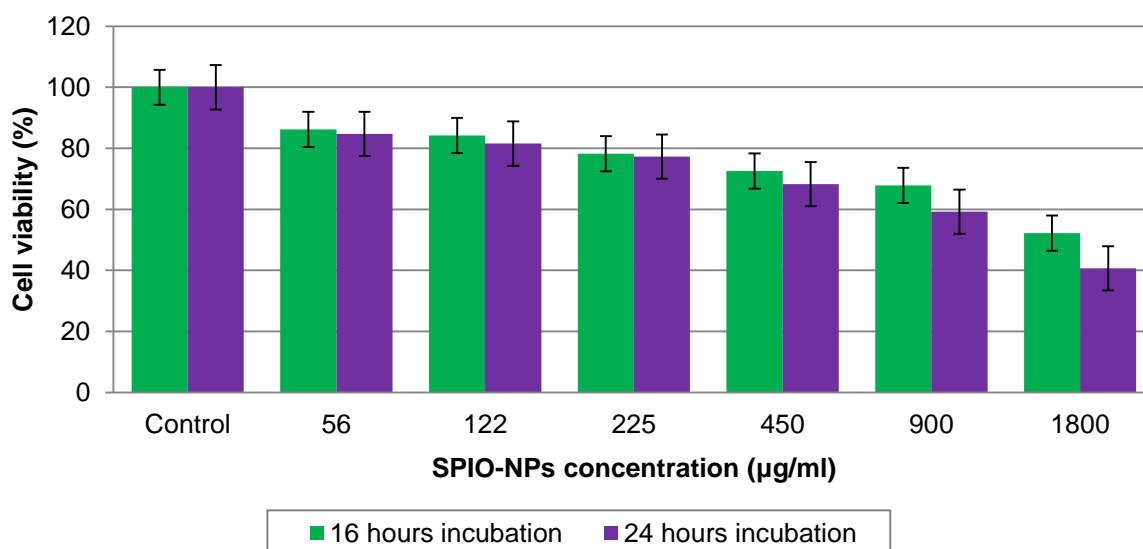


Figure 88: The effects of Tween 80-SPIO-NPs labelled with rhodamine 123 on the cell viability of C6 glioma cells determined by MTT assay

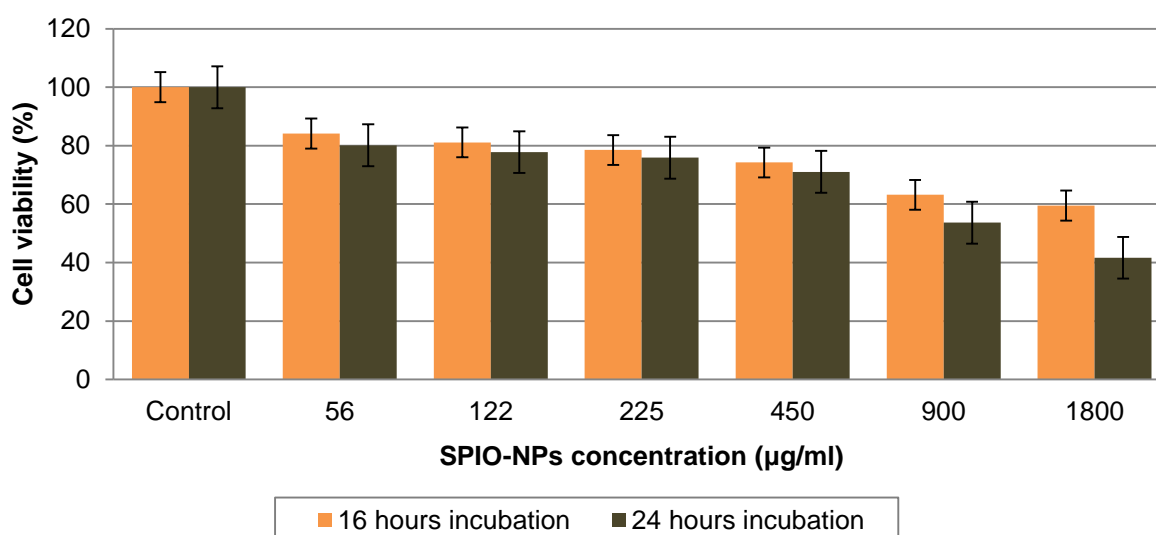


Figure 89: The effects of Tween 80-SPIO-NPs labelled with propidium iodide on the cell viability of C6 glioma cells determined by MTT assay

When C6 glioma cells were exposed to 56 µg/ml of Tween 80 coated SPIO-NPs without fluorescent dye (figure 87), the cell viability 83.79% was observed. There was no significant change observed in the cell viability up to 225 µg/ml dosage of SPIO-NPs and was recorded 78.23%. At higher dosage, the cell viability was going to decreasing to 41.46% at 1800 µg/ml for both 16 hours and 24 hours' incubation times. The cell viability was almost the same at 450 µg/ml and no any statistical difference was observed. Also, the cell viability at 16 hours' incubation was higher at a higher SPIO-NPs dosage as compared to 24 hours' incubation time.

When Tween 80 coated SPIO-NPs were labelled with rhodamine 123 and then exposed to C6 glioma cells, the cell viability remained almost the same 86.17% and

84.74% at both 16 hours and 24 hours' incubations at 56 $\mu\text{g/ml}$ dose respectively. At a higher dosage of 122 $\mu\text{g/ml}$, the cell viability slightly decreased for both incubation times as shown in figure 88. When SPIO-NPs dose was increased to 1800 $\mu\text{g/ml}$, the cell viability was also observed the further decreasing to 52.19%. When these results were compared with only Tween 80 coated SPIO-NPs, it revealed that up to the dosage of 225 $\mu\text{g/ml}$, the cells viability on C6 glioma cells was almost the same and these two results are consistent at the same SPIO-NPs concentration.

Tween coated SPIO-NPs were labelled with propidium iodide and were examined for their cytotoxicity (figure 89). The cell viability was higher 84.12% at 16 hours' incubation and 80.15% at 24 hours' incubation respectively at 56 $\mu\text{g/ml}$. Interestingly, for the SPIO-NPs concentration of 225 $\mu\text{g/ml}$, the cell viability was in consistent with the previous results i.e., without and with labelling with rhodamine 123 fluorescence dye. Maximum cell viability 59.49% was achieved in this case at higher concentration of 1800 $\mu\text{g/ml}$ at 16 hours' incubation and 41.66% cell viability was recorded after a longer incubation time of 24 hours.

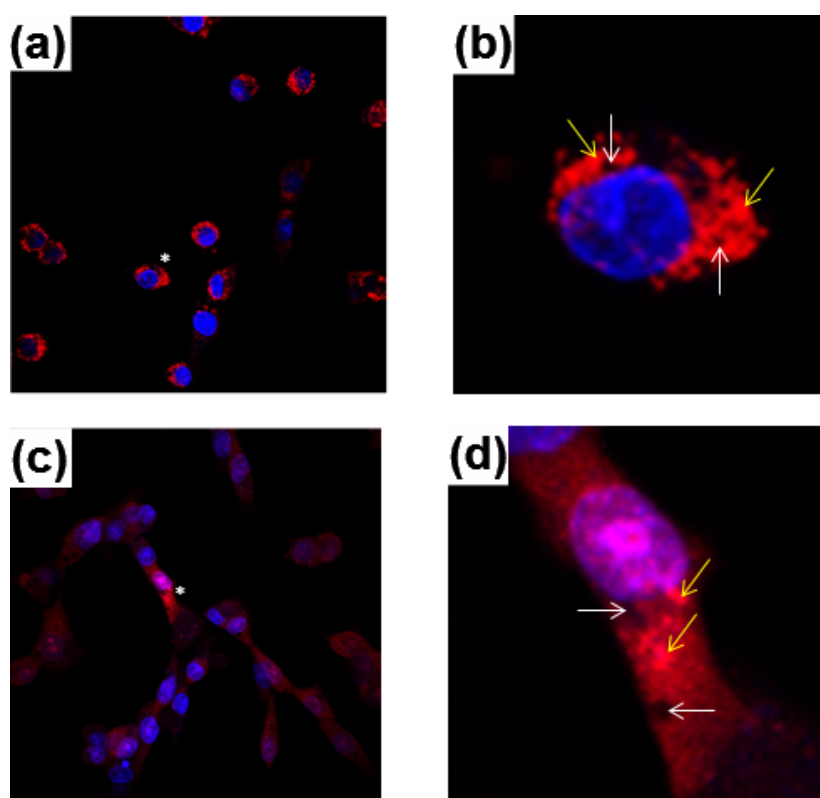


Figure 90: Intracellular localization of Tween 80 coated SPIO-NPs in C6 glioma cells is shown by confocal microscopic images after 24 hours of incubation (a) when SPIO-NPs were labelled with rhodamine 123, (c) when SPIO-NPs were labelled with propidium iodide, (b) and (d) zoom into cell labelled with an asterisk in (a) and (c) to illustrate the dotted labelling (yellow arrows) and gap (white arrows) for both rhodamine 123 and propidium iodide respectively

To find the fluorescent labelled Tween 80-SPIO-NPs bounded on the cells or an intracellular localization by nanoparticles in the cells, confocal images were taken

(figure 90). Confocal images show that SPIO-NPs were found inside the C6 glioma cells after 24 hours' incubation. Clearly, cell's nuclei are counterstained with Hoechst 33342.

For better pharmaceutical applications and especially for a targeted drug delivery, it is recommended that the concentration of 225 $\mu\text{g/ml}$ is safe to use in such applications. Our results are the concentration-dependent and time-dependent usage of coated and fluorescent SPIO-NPs. At higher concentration and longer incubation time, SPIO-NPs are cytotoxic to cells [245] so, for successful pharmaceutical applications, low dosage and low treatment with SPIO-NPs is suggested. It is considered that surface modified SPIO-NPs up to 100 $\mu\text{g/ml}$ dosage are safe enough to use in pharmaceutical implementations [248]. Our experimental data reveal that the concentration of 225 $\mu\text{g/ml}$ is non-toxic to the living cells. Our these findings are similar to the study that different surfactant modified SPIO-NPs are equally suitable for various pharmaceutical uses [287]. Our these results show that for a longer incubation time (24 hours) on C6 glioma cells for the concentration of 225 $\mu\text{g/ml}$, Tween 80 modified SPIO-NPs are equally suitable for a number of different pharmaceutical applications. When cytotoxicity of Tween 80-SPIO-NPs (without labelling) was quantified, the cytotoxic profile was almost in linear with the rhodamine 123 and propidium iodide labelled Tween 80-SPIO-NPs. It is therefore, suggested that both fluorescents labelled Tween 80-SPIO-NPs are equally safe to use on C6 glioma cells and in different biomedical uses. This study is also in linear with the different reports where Tween 80-SPIO-NPs with size 90 nm is non-toxic and successfully employed in the blood-brain barrier [288] and our average particle size is 50 nm.

6.1.2 Cytotoxicity of fluorescent Dextran 70,000 coated SPIO-NPs

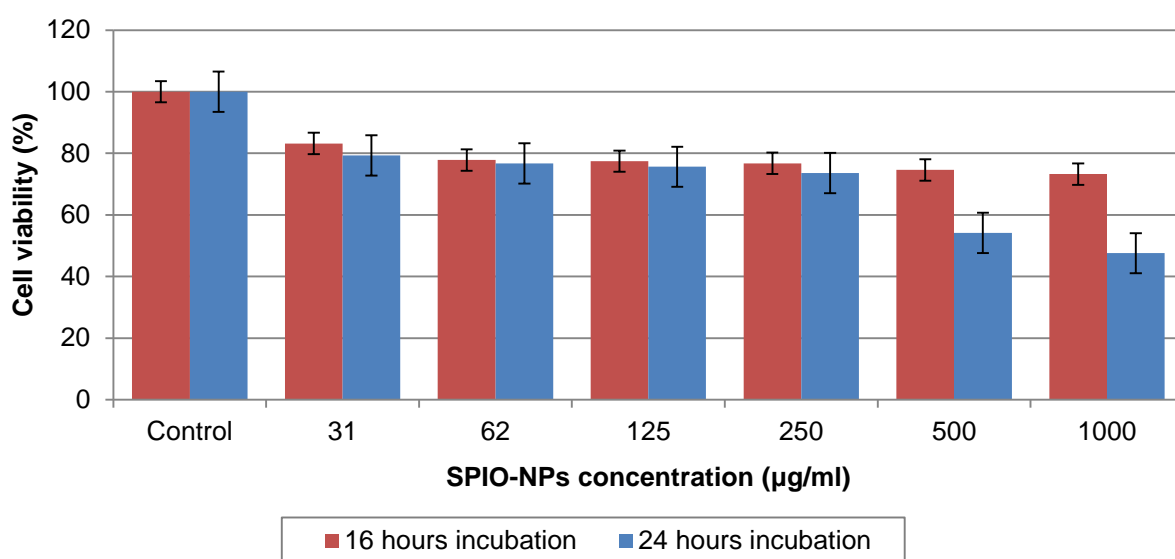


Figure 91: The effects of Dextran 70,000-SPIO-NPs on the cell viability of C6 glioma cells determined by MTT assay

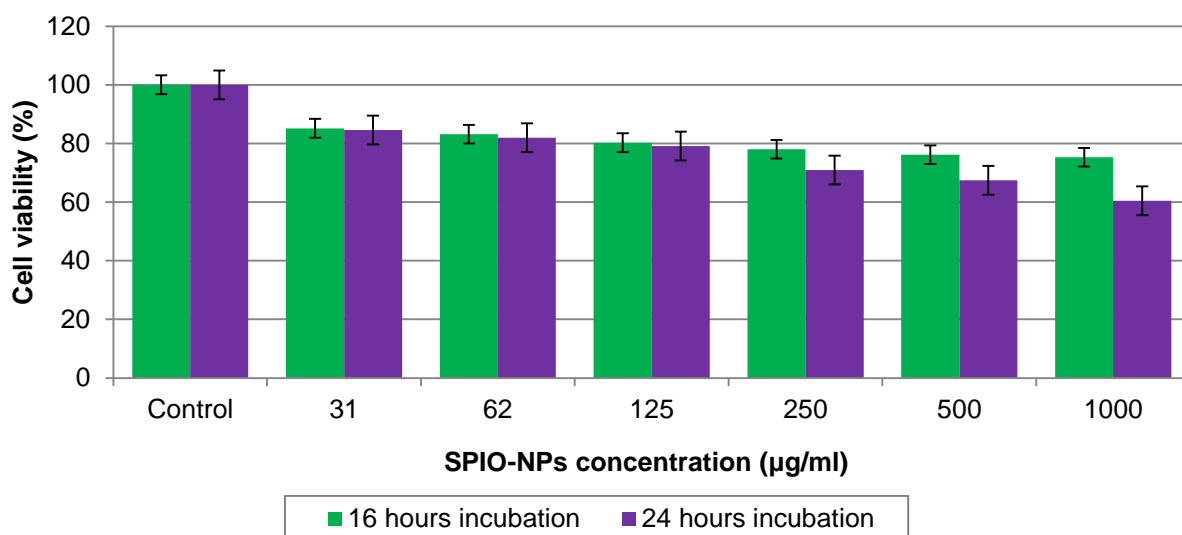


Figure 92: The effects of Dextran 70,000-SPIO-NPs labelled with rhodamine 123 on the cell viability of C6 glioma cells determined by MTT assay

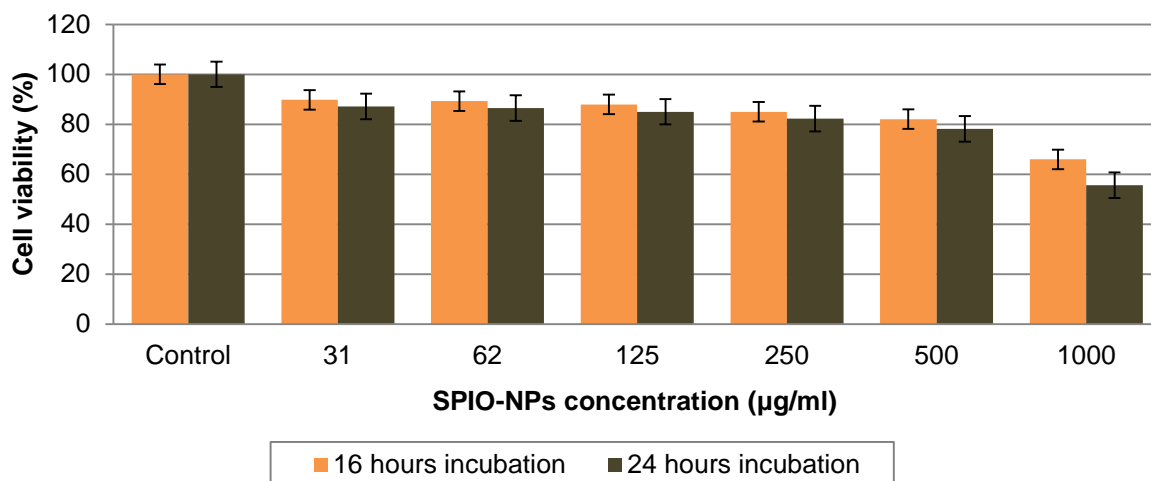


Figure 93: The effects of Dextran 70,000-SPIO-NPs labelled with propidium iodide on the cell viability of C6 glioma cells determined by MTT assay

Dextran 70,000 coated SPIO-NPs were exposed to C6 glioma cells (figure 91). At lower concentration of 31 µg/ml, the cell viability rate for both 16 hours and 24 hours' incubation was 83.19% and 79.30% respectively. At higher concentration of 250 µg/ml, the cell viability rate 76.76% was recorded at 16 hours' incubation. After 24 hours' incubation, the cell viability rate was 73.65% for the same SPIO-NPs concentration. Interestingly, at further higher concentrations of 500 µg/ml and 1000 µg/ml, the cell viability decreased after 16 hours' incubation to a much lower value measured at 24 hours' incubation. Prominently, at a higher concentration of 1000 µg/ml, the cell viability was 73.24% at 16 hours' incubation. A noticeable decrease in the cell viability rate 47.58% was observed at this highest concentration in the case of 24 hours' incubation.

When Dextran 70,000 coated SPIO-NPs were labelled with fluorescent dye rhodamine 123 (figure 92), the cell viability was also very high for both incubation times and for a broad range of NPs concentrations. At highest concentrations of 500 and 1000 $\mu\text{g/ml}$, we again detected a difference between 16 hours and 24 hours' incubation times, the cells being less viable after 24 hours. This trend was observed up to the dosage of 125 $\mu\text{g/ml}$. At the highest concentration of 1000 $\mu\text{g/ml}$, the cell viability of rhodamine 123 labelled Dextran 70,000-SPIO-NPs was very high i.e., 75.30% at 16 hours' incubation time. At 24 hours' incubation, the cell viability rate was only 60.47% at this concentration. From this finding, it can be concluded that rhodamine 123 is a non-toxic fluorescent dye and when attached to the Dextran 70,000 coated SPIO-NPs, does not increase the toxicity of the nano-systems.

In the next case, when Dextran 70,000 coated SPIO-NPs were labelled with the fluorescent dye propidium iodide (figure 93), the least concentration of 31 $\mu\text{g/ml}$ was highly suitable for the cell surviving or viability at both incubation times. For the 250 $\mu\text{g/ml}$ concentration, no big changes were observed for both 16 hours and 24 hours' incubation times with respect to the cell viability. At the highest SPIO-NPs concentration of 1000 $\mu\text{g/ml}$, 65.96% cell viability rate was recorded at 16 hours' incubation and 55.60% was recorded for 24 hours' incubation. This decrease in the cell viability was less (9.34% at 16 hours and 4.87% at 24 hours' incubations) when compared these findings of Dextran 70,000 coated SPIO-NPs labelled with the rhodamine 123 at the highest dosage to C6 glioma cells. It is therefore, suggested that rhodamine 123 is a comparatively less toxic fluorescent dye than the propidium iodide when the core is iron oxide.

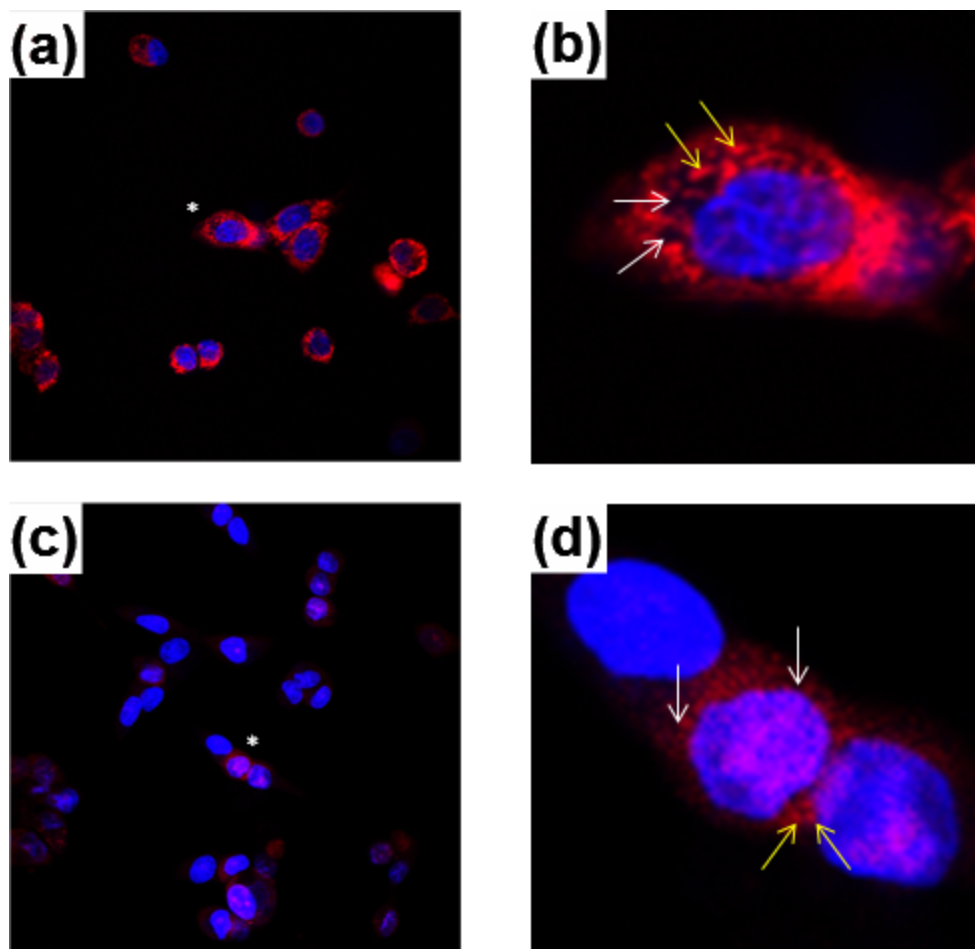


Figure 94: Intracellular localization of Dextran 70,000 coated SPIO-NPs in C6 glioma cells is shown by confocal microscopic images after 24 hours of incubation (a) when SPIO-NPs were labelled with rhodamine 123, (c) when SPIO-NPs were labelled with propidium iodide, (b) and (d) zoom into cell labelled with an asterisk in (a) and (c) to illustrate the dotted labelling (yellow arrows) and gap (white arrows) for both rhodamine 123 and propidium iodide respectively

Figure 94 confirmed the fluorescent staining of the cell nucleus for both rhodamine 123 and propidium iodide at 500 $\mu\text{g/ml}$ of SPIO-NPs concentration. Above figure also show the internalization of SPIO-NPs into the C6 glioma cells. Observations from figure 94 revealed that cells also became fluorescent with some dark shadow inside the nuclei location.

SPIO-NPs are considered biocompatible and effective for many important pharmaceutical applications; but for a properly designing these SPIO-NPs, many side effects must be considered for such uses. An important criterion that must be taken into account is the stability of the synthesized SPIO-NPs in biological fluids with their physiological pH. To solve this issue, SPIO-NPs must be coated with the biocompatible surfactants which not only prevent SPIO-NPs from agglomeration but also increase their biocompatibility [248]. Dextran coated SPIO-NPs also have higher cellular uptake [248]. During the MTT assay for *in vitro* cytotoxicity, the amount of formazan produced due to mitochondrial activity is directly proportional to the number of living or viable cells as read by a spectrophotometer with light absorption [289].

The SPIO-NPs are safe enough and also non-toxic when the exposed cells viability is approximately 80% or higher [289]. It already has been mentioned in the previous section that 1-100 $\mu\text{g/ml}$ of SPIO-NPs are quite safe to use in pharmaceutical applications. For our case (Dextran 70,000-SPIO-NPs), our cell viability is 83.19% at 16 hours' incubation time and 79.30% at 24 hours' incubation respectively at 31 $\mu\text{g/ml}$ when NPs were treated without a fluorescence labelling. After labelling with rhodamine 123, the cell viability is above 80% at the SPIO-NPs dosage of 125 $\mu\text{g/ml}$. So, for our case when labelled with the rhodamine 123, 125 $\mu\text{g/ml}$ is a threshold limit to use in pharmaceutical applications especially in the blood-brain barrier. This threshold limit tends to increase when SPIO-NPs labelled with the propidium iodide to 500 $\mu\text{g/ml}$ (16 hours' incubation) and 250 $\mu\text{g/ml}$ (24 hours' incubation). Our results are in agreement with the previous study presented by Prodan et al. [289]. In other words, the cells viability has an inverse relation with the concentration and incubation time. These results with Tween 80 and Dextran 70,000 coatings show that light is notably increased in both studies except when the concentration and incubation time were enhanced. So, for a low cell viability, it is suggested that absorbance of light is overestimated [290].

6.1.3 Cytotoxicity of fluorescent DEAE-Dextran coated SPIO-NPs

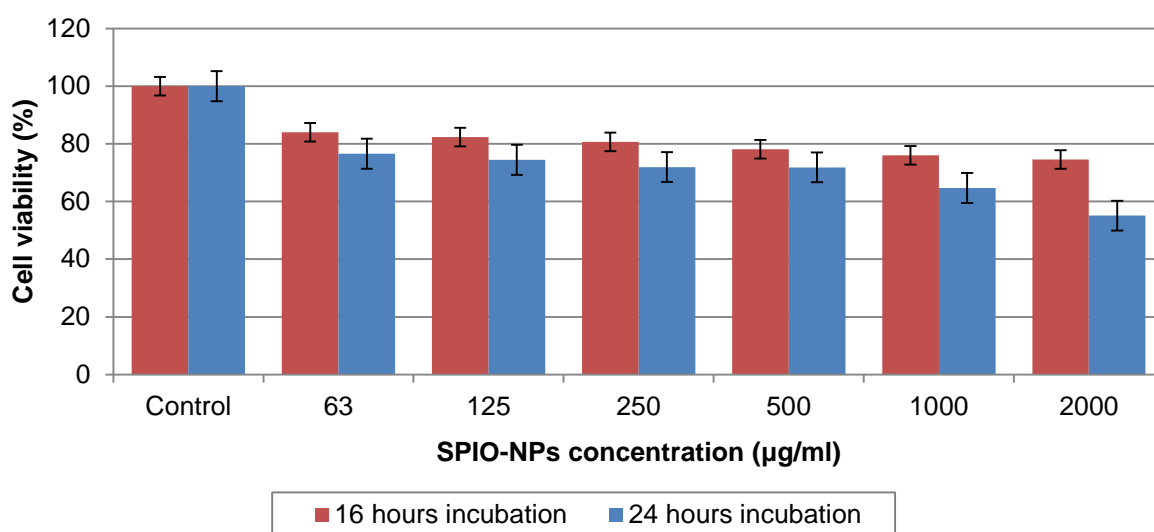


Figure 95: The effects of DEAE-Dextran-SPIO-NPs on the cell viability of C6 glioma cells determined by MTT assay

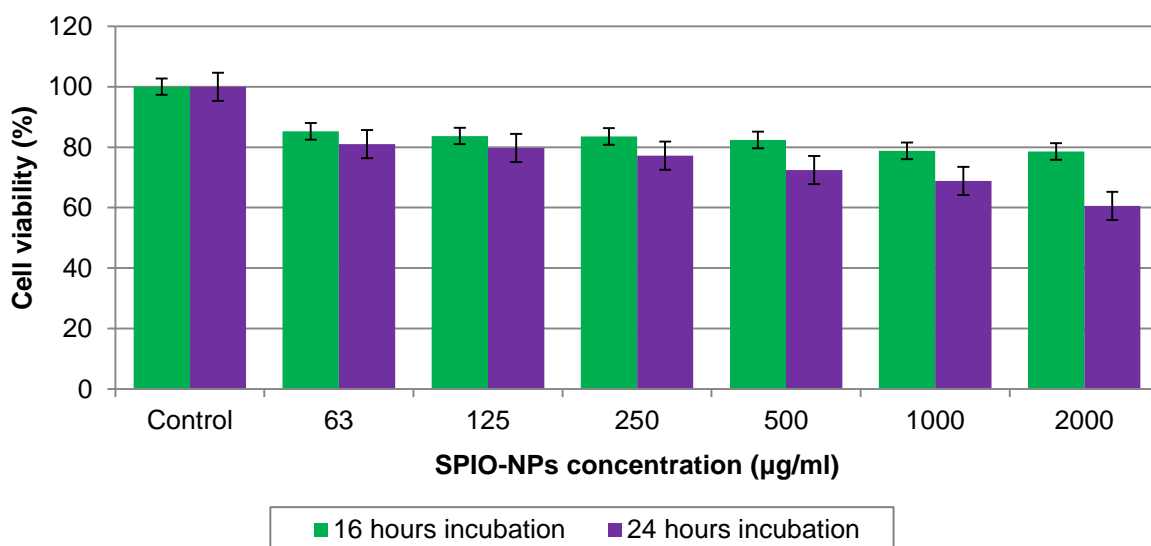


Figure 96: The effects of DEAE-Dextran-SPIO-NPs labelled with rhodamine 123 on the cell viability of C6 glioma cells determined by MTT assay

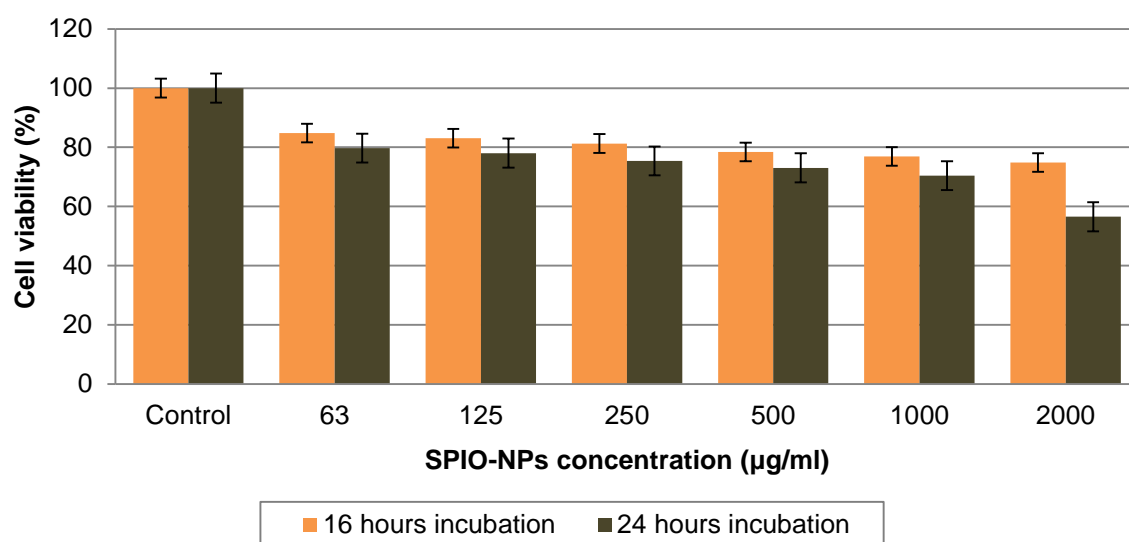


Figure 97: The effects of DEAE-Dextran-SPIO-NPs labelled with propidium iodide on the cell viability of C6 glioma cells determined by MTT assay

The cytotoxicity of fluorescent DEAE-Dextran-SPIO-NPs was assessed by the same manners as the previous two studies. When DEAE-Dextran-SPIO-NPs were exposed to C6 glioma cells for different incubation times, the increase in the cell viability was observed at 16 hours' incubation (figure 95). Maximum cell viability 84% was recorded at a lower concentration of 63 µg/ml after 16 hours' treatment with the C6 glioma cells. While at the same concentration, the cell viability 76.57% was recorded after 24 hours' incubation. Up to 250 µg/ml dosage, the cell viability rate was 80.65% at 16 hours and then it goes to decrease as the concentration further increased. After 24 hours' incubation, the cell viability was decreasing more rapidly and became 55.10% at 2000 µg/ml.

Cytotoxicity profile of rhodamine 123 labelled DEAE-Dextran-SPIO-NPs is shown in figure 96. At least SPIO-NPs dosage of 63 $\mu\text{g/ml}$, the maximum cell viability was 85.26% and at 500 $\mu\text{g/ml}$ dosage, the cell viability 82.35% was assessed after 16 hours' cells treatment. According to our previous results, it is suggested that 500 $\mu\text{g/ml}$ concentrations may be treated as a non-toxic because the cell viability is above 80%. For the case of 24 hours' incubation, maximum cell viability 80.96% was observed only at a low concentration of 63 $\mu\text{g/ml}$. As a comparison of both incubation times, the longer treatment time is not preferred and a shorter incubation of 16 hours has greater cell viability.

When propidium iodide labelled DEAE-Dextran-SPIO-NPs were treated with the C6 glioma cells, the obtained results were very similar to the bared DEAE-Dextran-SPIO-NPs and are depicted in figure 97. The cell viability of 84.81% was assessed at very low 63 $\mu\text{g/ml}$ concentrations and the cell viability 81.28% $\mu\text{g/ml}$ was observed at 250 $\mu\text{g/ml}$ at 16 hours' incubation time. Least cell viability 74.84% was recorded at 2000 $\mu\text{g/ml}$ at this incubation time. Maximum cell viability 79.93% was observed at 63 $\mu\text{g/ml}$ concentration for a longer incubation time of 24 hours and show toxic behavior at 2000 $\mu\text{g/ml}$ with the 56.56% cell viability. From these findings, it can be suggested that for propidium iodide, longer cells incubation is not preferable. We have shown here concentration and incubation (treatment) time-dependent cytotoxic behavior of our synthesized SPIO-NPs coated with the different surface masking agents and also attached with the fluorescent dyes.

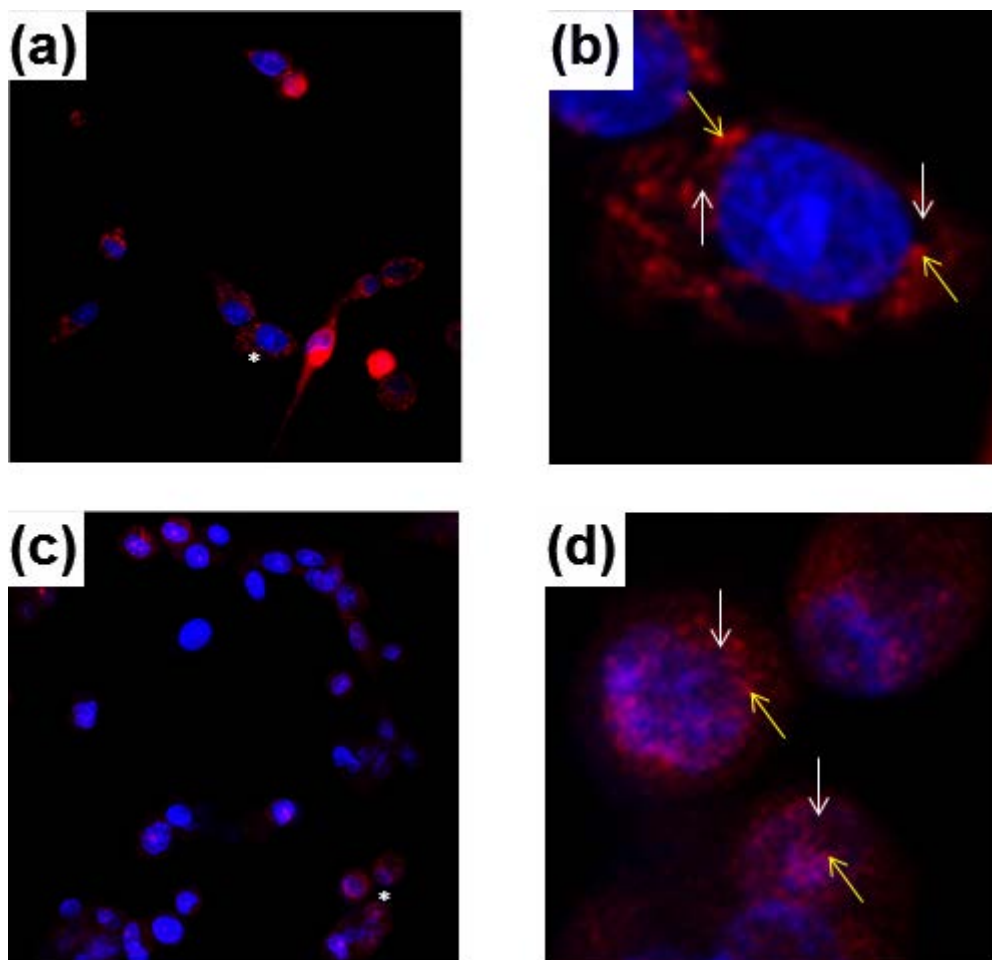


Figure 98: Intracellular localization of DEAE-Dextran coated SPIO-NPs in C6 glioma cells is shown by confocal microscopic images after 24 hours of incubation (a) when SPIO-NPs were labelled with rhodamine 123, (c) when SPIO-NPs were labelled with propidium iodide, (b) and (d) zoom into cell labelled with an asterisk in (a) and (c) to illustrate the dotted labelling (yellow arrows) and gap (white arrows) for both rhodamine 123 and propidium iodide respectively

Cellular uptake in C6 glioma cells of fluorescent DEAE-Dextran coated SPIO-NPs was confirmed by confocal imaging in figure 98. Fluorescent signals were strong enough after 24 hour's cell incubation. Intracellular fate of the fluorescence was also confirmed after internalization when SPIO-NPs were cultured with the C6 glioma cells.

Above obtained results suggest that our coated SPIO-NPs show virtually no toxic effect at a low concentration and also for a short treatment or incubation time. The coating on NPs also influences the toxicity; it already has been reported that surface modifications of different NPs with different masking agents have different and also significant chemical reactivity and therefore, possesses different and sometimes acute toxic effects [290]. Our synthesized SPIO-NPs are very small in size (~10-100 nm with an average size 50 nm) and due to this small size; nanoparticles interact with the cells and other subcellular structures. Information for this interaction mechanism is still lacking in the existing literature [291]. Cytotoxicity of different iron oxide nanoparticles has already been reported in various studies. One common

investigation in these studies is that the low concentration ($\sim 50 \mu\text{g/ml}$) produces minimum toxicity and sometimes they are non-toxic [291]. For our nanoparticles which are in the superparamagnetic regime, are also non-toxic at low concentration and we show that our synthesized SPIO-NPs are of low toxicity up to $250 \mu\text{g/ml}$ at short incubation time and also after a longer incubation of 24 hours. Our results are in streamline with the findings of Iacovita et al. [292]. Normally, small size nanoparticles show higher toxicity than the larger ones. In general, MNPs show toxicity due to the reactive oxygen species (ROS) production which is responsible for cell death. ROS have a short lifetime of an intermediate compound and the compounds have a free unpaired electron in their outer most shell; thus to have a stable structure, they obtain an electron from their adjacent molecule which themselves become unstable and this continues as a chain reaction [247]. Every cell and living system has its own mechanism to void or prevent themselves from the ROS, but the excessive ROS lead to different cytotoxicity and eventually cell death. In the case of SPIO-NPs where the size is very small (10-90 nm) and these small-sized SPIO-NPs have a larger surface area (because of the surface-to-volume ratio) when compared with the larger magnetic nanoparticles, are able to produce more ROS and eventually become more toxic [292].

ROS generation may be also a mechanism underlying the reduced cell viability after incubation with high doses of SPIO-NPs (500 and 2000 $\mu\text{g/ml}$). However, as we see only significantly impaired cell viability after long incubation of 24 hours, we certainly do not induce necrotic cell death with our NPs as this would be detectable after a few hours. So, in case of ROS-induced damage, it may be that only low amounts are generated which may accumulate or may activate pathways of delayed cell death like apoptosis, as suggested by Bae et al. [293] who showed that increased intracellular ROS levels are necessary for the apoptosis but not for the reversible reduction in the cell viability. This also suggests that the slight reduction of cell viability, which is seen already with lower doses of SPIO-NPs, is probably not due to the ROS induction. It has been shown that the reduced generation of formazan not necessarily equals cell death, but can be a reversible decrease in an enzymatic cell activity. Therefore, it is also possible that in our experiments especially with low concentrations of coated and labelled SPIO-NPs did not induce cell death at all, but only a reduction in the metabolic activity. Since in our *in vitro* experiments, the reduction in the cell viability is low at a lower concentration and for a short incubation period. So, our surface modified fluorescent SPIO-NPs are highly suitable for many pharmaceutical applications, especially in the targeted drug delivery application.

Surface coatings have a great influence on the cytotoxicity of the SPIO-NPs. Tween 80 and Dextran capping agents make them suitable for many pharmaceutical implementations.

All above *in vitro* results indicate that all variations of the SPIO-NPs are taken up by the cells in these C6 cell culture models after 16 hours and 24 hours of incubations in

a low concentration with a better cell viability after 16 hours' incubation. Strong fluorescent signals were especially detectable with the SPIO-NPs with rhodamine 123 as a marker. As there was a double-labelling performed using Hoechst 33342 which selectively stains the nucleus of cells - our images indicate that the SPIO-NPs are accumulating in the cell soma but do not enter the nucleus. As the cells incubated with Dextran coated SPIO-NPs reveal very bright signals - especially in comparison to Tween 80 coated SPIO-NPs. It can be assumed that the Dextran coatings allow a better uptake than the Tween 80 coating. The fluorescent signals and therefore, presumably the SPIO-NPs are evenly distributed throughout the cell soma but in a dotted pattern which indicates that the SPIO-NPs accumulate at certain intracellular structures. Further, SPIO-NPs are clearly staining for endosomal-lysosomal uptake in the cell organelles as shown by the confocal images. A more detailed investigation of the exact sub-cellular distribution awaits further investigations.

In general, all C6 cells in culture incubated with SPIO-NPs labelled with propidium iodide show clearly weaker signals than the rhodamine 123 SPIO-NPs. Binding of propidium iodide to DNA causes a two- to threefold increase in the fluorescence intensity. So, one possible underlying cause of the weak staining is that the propidium iodide bound to the SPIO-NPs cannot enter the nucleus, as a consequence cannot intercalate with the DNA and therefore, only rather weak fluorescent signals are detected.

6.1.4 Cytotoxicity of fluorescent dyes: rhodamine 123 and propidium iodide

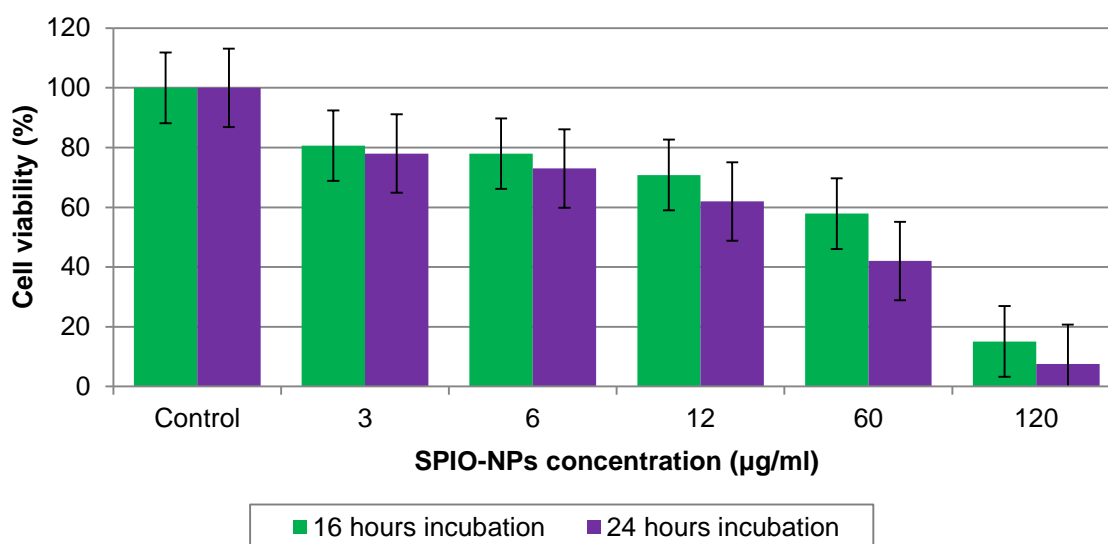


Figure 99: The effect of rhodamine 123 on the cell viability of C6 glioma cells determined by MTT assay

Cytotoxicity profile of rhodamine 123 is given in the above figure 99. The standard concentration of fluorescent rhodamine 123 used for labelling the SPIO-NPs is 2 mg/ml. The rhodamine 123 is itself a non-toxic with its low concentration. For our

case and C6 glioma cells, 6 $\mu\text{g/ml}$ is safe enough for the living cells with a short incubation time. High concentration is considered toxic. Noticeably, when rhodamine 123 is labelled on different coatings, then its toxicity profile is very good, but it is not recommended to use in its pure form.

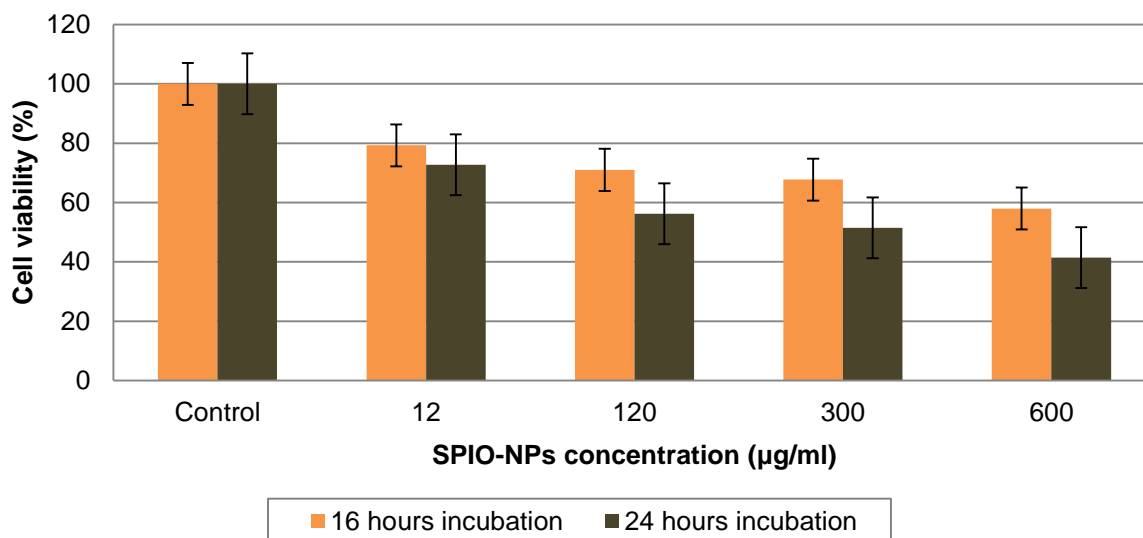


Figure 100: The effect of propidium iodide on the cell viability of C6 glioma cells determined by MTT assay

Cytotoxicity profile of propidium iodide is explained in the above figure 100. The standard concentration of fluorescent propidium iodide 1.2 mg/ml for labelling the SPIO-NPs is recommended for the experiments. At low dosage to the C6 glioma cells, the cytotoxicity is almost in linear with the rhodamine 123. For a higher dosage, short incubation (16 hours) is preferred. Higher SPIO-NPs dosage of 300 $\mu\text{g/ml}$ has high cell viability when propidium iodide was labelled on Dextran 70,000 at the concentration of 500 $\mu\text{g/ml}$; the cell viability rate was 82.04% at 16 hours and 78.18% after 24 hours' treatment time. So, it is suggested that propidium iodide increase the cell viability rate; not in alone but by the conjugation with the biocompatible surface coatings.

6.2 *In vivo* and *ex vivo* uptake experiments

Anaesthetized rats were fixed on a microscope stage and photomicrographs of the retina were taken using a confocal laser scanning microscope. Image of neurons was possible when the fluorescently labelled SPIO-NPs were injected into the retinal ganglion cells (RGCs) via a retrograde axonal transport from the superior colliculus (SC) of the midbrain. This whole procedure is explained with the help of the following figure 101.

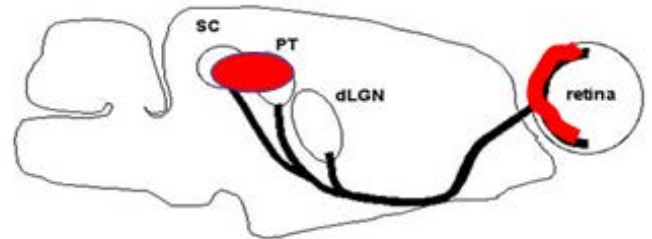


Figure 101: Retrograde labelling of retinal ganglion cells by injection of fluorescently labelled SPIO-NPs into the superior colliculus. The focused shows the position of a contact lens which is directly placed on the rat's eye (left). Internal structure of retinal is shown (right) [106], [294]

With the help of an *in vivo* confocal neuroimaging (ICON), it was possible to visualize invasively the single retinal ganglion cells and blood vessels. This process was repeatedly, in real-time, and also under natural conditions.

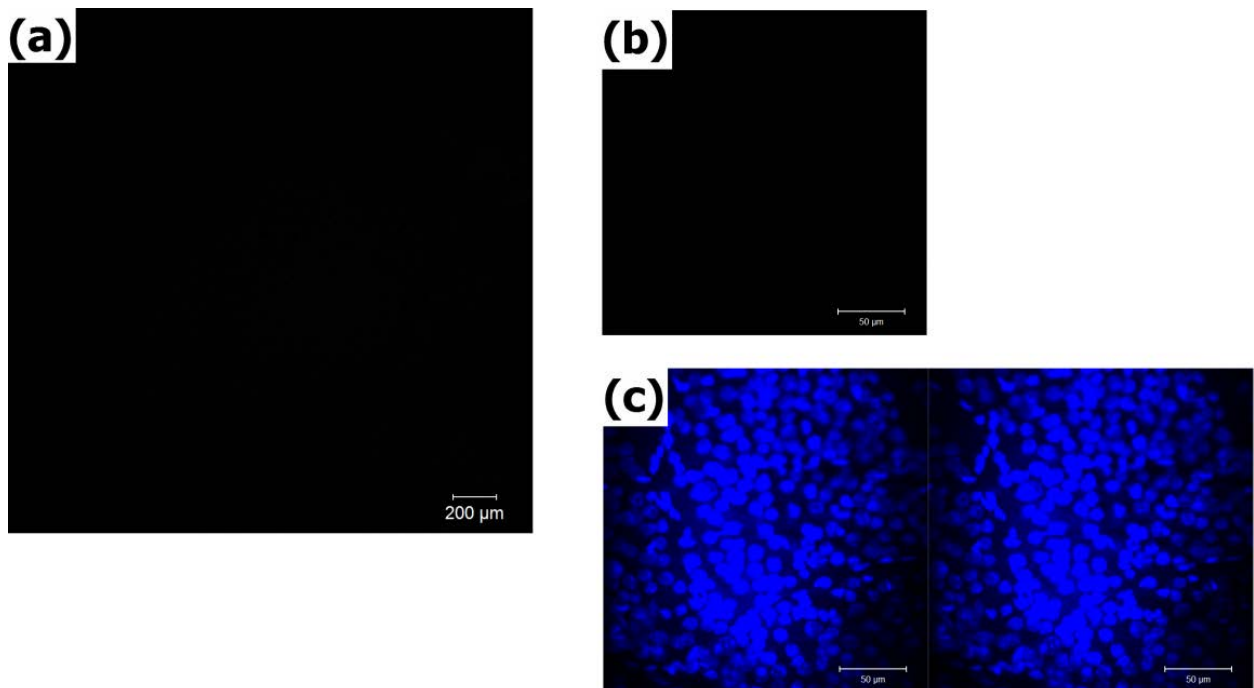


Figure 102: Photographs of control animal experiments where animals received the only phosphate buffered saline intravitreally: (a) it can be clearly seen that no fluorescence visibly *in vivo* cellular images appeared of the retina of animals, (b) no any signal in the *ex vivo* retina (whole mount), (c) the whole mount is imaged after incubation with Hoechst 33342, which is selective maker of nuclei

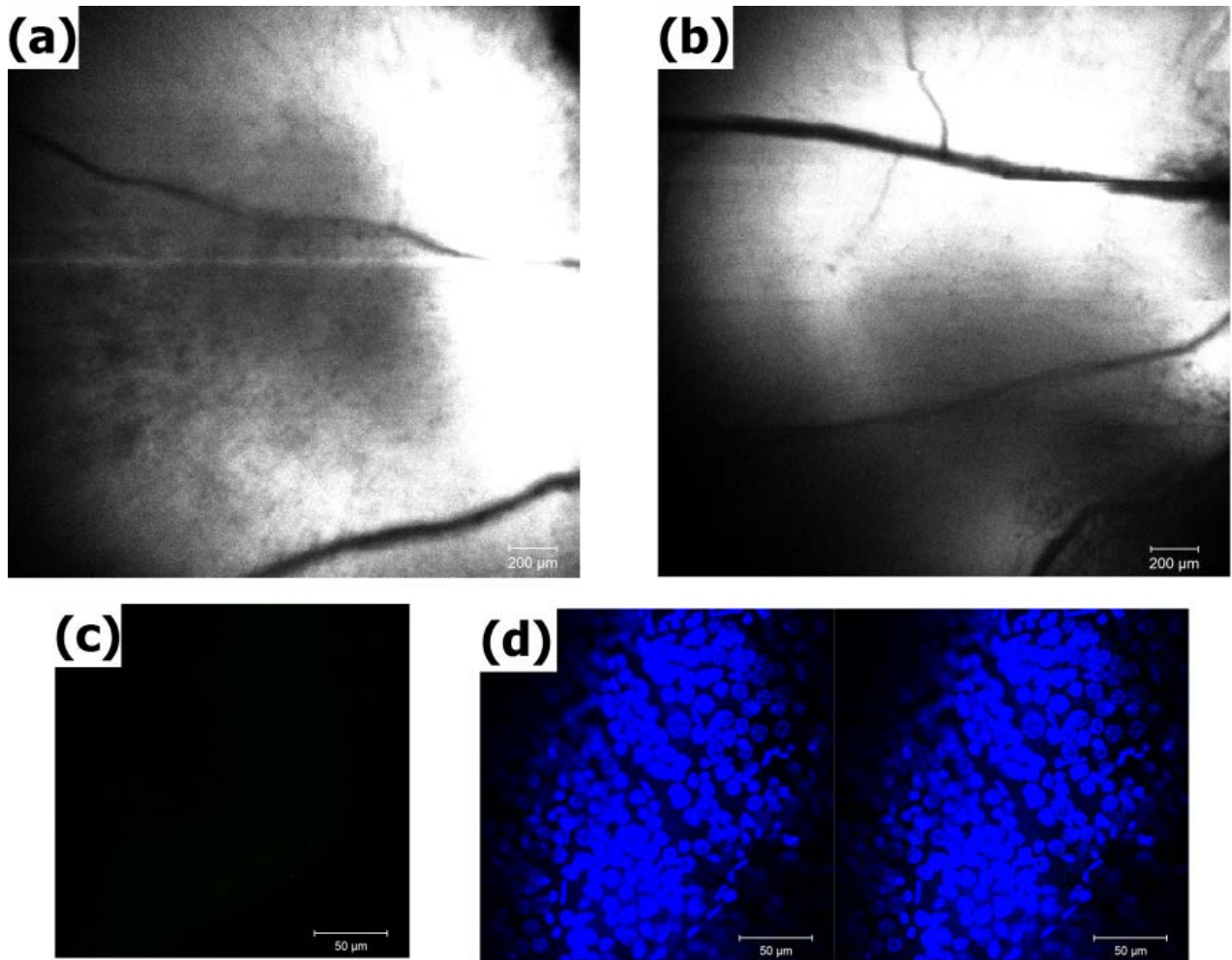


Figure 103: Repeated clear and bright imaging of the same fluorescent labelled ganglion cells when animals received 500 $\mu\text{g/ml}$ concentration dose intravitreally of Dextran coated SPIO-NPs labelled with rhodamine 123: (a) left eye image of animal, (b) right eye image of animal, (c) no any signal in the *ex vivo* retina (whole mount), (d) the whole mount is imaged after incubation with Hoechst 33342, which is selective maker of nuclei

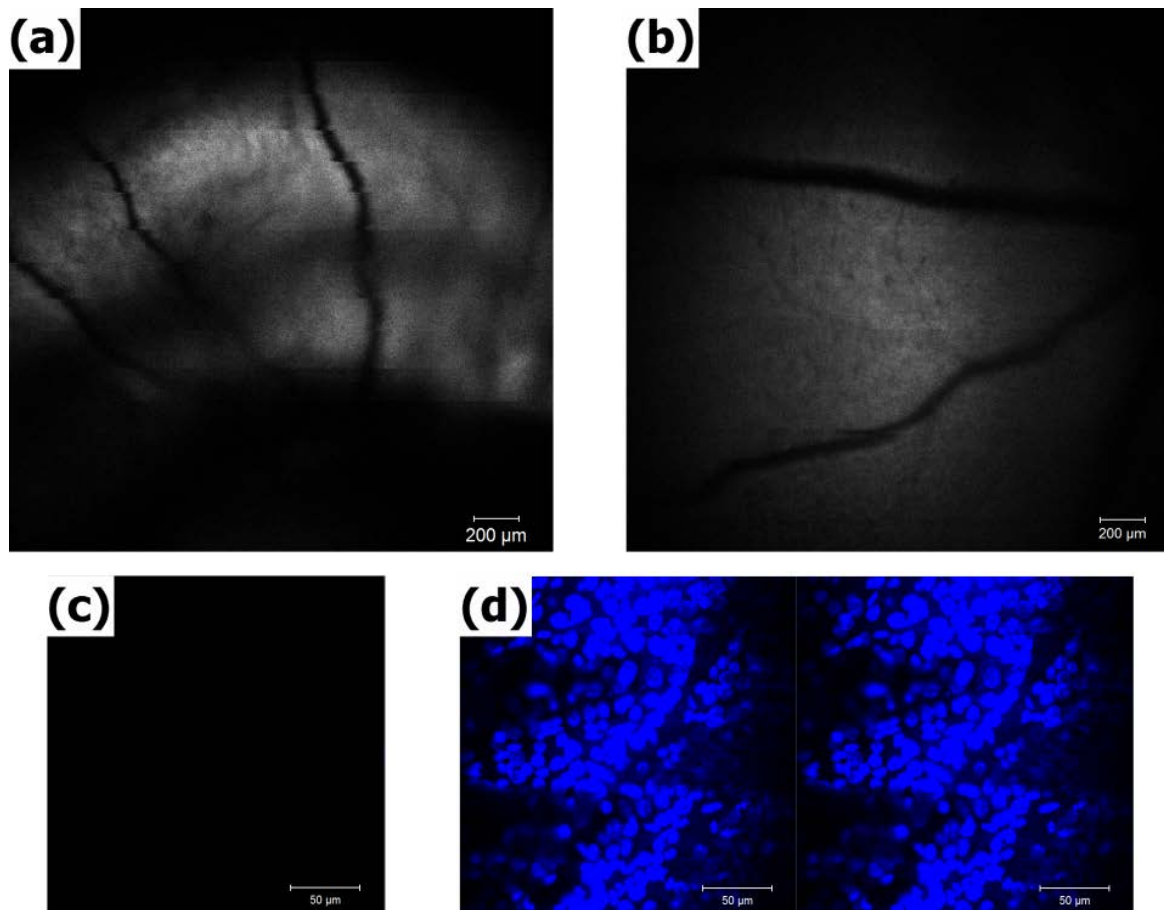


Figure 104: Repeated clear and bright imaging of the same fluorescent labelled ganglion cells when animals received 31 $\mu\text{g/ml}$ concentration dose intravitreally of Dextran coated SPIO-NPs labelled with rhodamine 123: (a) left eye image of animal, (b) right eye image of animal, (c) no any signal in the *ex vivo* retina (whole mount), (d) the whole mount is imaged after incubation with Hoechst 33342, which is selective maker of nuclei

Using dissociated C6 cell culture, the basic ability of SPIO-NPs to cross the cellular membrane and accumulate inside the cells was demonstrated. However, in an *in vivo* situation, additional factors can influence the uptake kinetics as compared to the situation of the cells in *in vitro*. Therefore, we injected SPIO-NPs into the eyes' vitreous body of live animals. The vitreous body and the retina can be seen as a natural *in vivo* "dish" of live and intact brain parenchyma which, most importantly, is accessible by *in vivo* confocal neuroimaging (ICON) the subsequent distribution and possible uptake of the SPIO-NPs into the retina tissue of living rats, which is a part of the central nervous system (CNS). Dextran coated SPIO-NPs labelled with rhodamine 123 were locally injected into the eyes' vitreous body of anaesthetized adult Wistar rats (concentration 31 $\mu\text{g/ml}$ and 500 $\mu\text{g/ml}$). After 2 days of injections, the ICON of the retina was performed. The images indicate a dose-dependent, diffuse distribution of the nanoparticles at the retina: when focusing at the upper level of the retina-layers (inner region) - with the major retinal arteries as landmarks - we revealed a strong fluorescent signal in rats injected with the high dose of SPIO-NPs (figures 103a and 103b), whereas in control animals which had received only vehicle injections, virtually no fluorescence was detected (figure 102a). In animals injected

with the low dose of labelled SPIO-NPs, we saw a weak, diffuse signal which was, however, unevenly distributed over the retina (figures 104a and 104b).

Interestingly, *ex vivo*, after preparation of the retina whole mount, we did not detect any fluorescent signal of rhodamine 123 anymore. Because the whole mount had been incubated with Hoechst 33342; therefore, as expected, the cellular nuclei showed up in bright blue (figures 102c, 103d, and 104d). These results indicate that after intravitreal injections, the SPIO-NPs attach to the retina surface as shown by ICON, however, probably not with the direct contact to the neuronal cells but only to the inner limiting membrane and the basal lamina which covers the retina tissue as a boundary to the vitreous humour. These results suggest that the particles are not taken up by the retinal parenchyma like cells or extracellular matrix after an intravitreal injection. When is only attached to the inner limiting membrane, the SPIO-NPs can be washed away during the preparation procedures of the retina whole mount and therefore, the nanoparticles with the rhodamine 123 signals have disappeared and are not detectable anymore during the subsequent imaging of the whole mount. In case of a cellular uptake, we would expect that rhodamine 123 labelling also in the whole mount preparation. These experiments confirm the assumption that the SPIO-NPs are incorporated into the cells through an active uptake mechanism and not by a passive diffusion which is unlike due to the size of SPIO-NPs. Therefore, it can be hypothesized that these uptake mechanisms of the cell membrane are not present at the inner limiting membrane; the SPIO-NPs do not enter into the retina tissue but stay attached to the upper surface of the retina and are washed away during the whole mount preparation.

This contrast between *in vivo* and *ex vivo* results leads to the assumption that the inner limiting boundary is not endowed with the same uptake mechanisms as the lipid bi-layer barrier around the cells. Our experiments are therefore also in line with the hypothesis that the SPIO-NPs are incorporated into the cells – as shown in the *in vitro* experiments - through an active uptake mechanism and not by a passive diffusion. Such an active uptake mechanism is also reasonable as it is known that only small non-polar molecules like O₂ can easily cross the cell membranes by a passive diffusion, but the barrier around the cells is virtually impermeable against the larger, uncharged polar molecules and all charged molecules including ions [295]. Although in comparison to other nano-formulations our SPIO-NPs are very small (40 nm), in comparison to the molecules which can easily diffuse through the cell membranes, SPIO-NPs are several orders of magnitude too large. Therefore, it requires active mechanisms for the cellular uptake, which we demonstrated for SPIO-NPs in the *in vitro* experiments, but which may be not present at the boundary between the retina and the vitreous body. As this may also apply to other biological boundaries and sheath, organs of mammals may have a natural safeguard against the unwanted uptake of superparamagnetic iron oxide nanoparticles.

7 Conclusions and future outlook

This final chapter summarizes the observations and conclusions drawn from this work. Superparamagnetic iron oxide nanoparticles were synthesized and investigated for their different biological and animal tests for use in pharmaceutical applications. Based on the evaluation of a series of experiments, following conclusions and future recommendations can be drawn.

7.1 Conclusions

In recent years, a significant progress has already been carried out for the synthesis and efficient use of the magnetic nanoparticles in biomedical applications. Apart from the various pros and cons regarding the toxicity, iron oxide nanoparticles (including SPIO-NPs) are the only and promising candidates among other magnetic nanoparticles which are in use for many pharmaceutical applications today. This study has shown the synthesis of SPIO-NPs successfully with a narrow size distribution by a co-precipitation method in a size range of 10-100 nm at different reaction parameters. Control over nanoparticle size is difficult in a co-precipitation method due to the occurrence of chaotic reactions within the semi-batch reactor during the course of the reaction. Synthesized SPIO-NPs were stabilized with different surface coating agents like Tween 80, Dextran 70,000, and DEAE-Dextran to use them in drug delivery to the brain by crossing the blood-brain barrier. We obtained the best size distribution using Tween 80 as the surface coating material with high zeta potentials. The positive zeta potential on nanoparticles was due to the presence of OH⁻ group which is largely distributed on the synthesized iron oxide nanoparticles surface. During a series of synthesis experiments, nanoparticle size was increasing with enhancing in the solution pH due to the nucleation of the NPs. Therefore, pH <11 was the most optimum condition for selecting a pH value. At higher stirring velocity (1000 rpm), we received the least-sized SPIO-NPs because, at higher stirring velocity, nanoparticles size was decreased due to the reason of irregular diffusion with impeded particles growth. At an elevated temperature, particle size was increased. This increase in size was due to the increase in particles mobility followed by the greater numbers of the collisions. It is a point of pondering that all experiments were performed in an air atmosphere and therefore, the oxidizing factor was impossible to ignore. For the case of Tween 80-SPIO-NPs, best size distribution was achieved at Fe³⁺/Fe²⁺=1.25:1 and for DEAE-Dextran-SPIO-NPs, best size distribution was obtained at 1.75:1. When the standard molar ratio was disturbed from 2:1, then Fe²⁺ oxidized to Fe³⁺ in the air, for this reason, the standard ratio of Fe³⁺/Fe²⁺ (2:1) is very difficult to be maintained during the precipitation reaction. The polydispersity index (PDI) of our superparamagnetic iron oxide nanoparticles was somehow in the range of 0.23 to 0.5 and this PDI range is also reported in the literature. Transmission electron microscopy also confirmed the size and morphology of our synthesized SPIO-NPs.

In vitro toxicity was assessed on C6 glioma cells which are widely used for brain glioma. Although, C6 glioma cells are under in an intensive research, as per our best knowledge, Tween 80 coated and DEAE-Dextran coated SPIO-NPs were not studied on C6 glioma cells for delivering the drug to the brain. Also, rhodamine 123 was not used as a fluorescent dye to label the SPIO-NPs and hence no any suitable data was available for SPIO-NPs with rhodamine 123 labelling with such fluorescent dye. Our suggested data reveal that 225 µg/ml is a threshold limit to use them in drug delivery application at lower incubation time. Confocal photographs with rhodamine 123 show strong and bright fluorescent signals. Double-labelling was performed by using Hoechst 33342 which selectively stained the cell's nucleus. Our confocal images confirmed the SPIO-NPs accumulation in the cell soma but did not enter the nucleus.

Information from our *in vitro* findings was the decisive aspect for our *in vivo* and *ex vivo* assessments and experiments. We first ever studied the SPIO-NPs in ICON as a model of BBB in the retinal ganglion cells. Fluorescent coated SPIO-NPs were injected intravitreally into the rat's eye. *In vivo* study of synthesized SPIO-NPs show that for a higher dosage of 500 µg/ml of SPIO-NPs, we received strong and brighter signals of fluorescent rhodamine 123 as compared to the control animals which only received vehicle injection no fluorescence was detected. In the case where low SPIO-NPs dosage was injected, we did not get bright but week signals which may be due to the uneven distribution of the fluorescent SPIO-NPs over the retina. The *in vitro*, *in vivo*, and *ex vivo* experimental results hypothesized that SPIO-NPs were incorporated into the cells through an active uptake mechanism and not by a passive diffusion.

Our coated and fluorescent SPIO-NPs did not show any toxic effect at low concentration and also for a short treatment or incubation period of 16 hours in *in vitro* studies. Toxicity of the SPIO-NPs also depends on the nature of the coating over the SPIO-NPs. Different coatings have different levels of toxicity and also significant chemical reactivity as shown by the different studies. Toxicity shown by such coated SPIO-NPs is very acute; therefore, it is primarily important to evaluate their toxicity before their biomedical applications. Usually, long-term treatment with any nano-system is not preferred due to the reason that we cannot get rid of the toxic effects although; we can minimize the toxic effects to the living organisms. We synthesized SPIO-NPs in a very small size (~10-100 nm with an average size 50 nm) and due to this small size; nanoparticles interact with the cells and other subcellular structures. Our produced and tested SPIO-NPs are non-toxic at low concentration and the present study show that synthesized SPIO-NPs are of low toxicity up to 250 µg/ml at short incubation time and also after longer incubation of 24 hours. Only significantly impaired cell viability was observed and we do not induce necrotic cell death after 24 hours' incubation period. Toxicity of nanoparticles is mainly due to the production of reactive oxygen species (ROS) and also a major factor is a threshold dose for the living organisms at a specified treatment time. Generation of ROS is acute at a higher dosage and also can be severe at longer incubation or treatment

time. The electron donor or acceptor sites on the nanoparticles react with molecular oxygen, resulting in the formation of superoxide anions or hydrogen peroxide, which subsequently oxidizes other molecules. By modifications of SPIO-NPs with a specific ligand, aptamer or antibody, it is possible to have optimal transport through the cell wall and in the blood-brain barrier. The ligands could bind to a receptor specifically and the receptor is a switch to control the pathway on the cell membrane and judge which molecule can go into the cells.

Overall on the basis of the correlation between *in vitro* toxicity and *in vivo* uptakes, it can be concluded that all synthesized and modified SPIO-NPs are safe enough, less toxic, and biocompatible 'nanocarriers' for successful therapeutic and drug delivery pharmaceutical applications at low concentrations and for a shorter incubation or treatment time.

7.2 Future outlook

Some future recommendations which can lead the further research in this emerging field of iron oxide nanoparticle technology are:

- At higher dosage, it is expected that SPIO-NPs may cause cellular stress and hence, a response may be altered. Therefore, a comprehensive study is required in this direction;
- Research is required to further study our synthesized fluorescent SPIO-NPs in other biomedical applications e.g., in hyperthermia for cancer treatment other than drug delivery. More research is also needed for the detection of our synthesized fluorescent SPIO-NPs in tissues;
- We used Dextran 70,000, DEAE-Dextran, and Tween 80 as capping and surface modifying agents. But in each and every case such coatings can produce genetic toxicity on C6 glioma cells. Therefore, understanding the mechanism of this genetic toxicity comparing with different surface masking substances is also demanding;
- Almost all studies describe the implementation of SPIO-NPs in various pharmaceutical applications. When SPIO-NPs are exposed for *in vitro* or after the *in vivo* administration of these nanoparticles, then only a few studies are available on the removal and final destination of treated SPIO-NPs from the body after successful pharmaceutical use; so it's primarily important to study and clarify the questions about such clearance of SPIO-NPs.

Bibliography:

- [1] S. P. Gubin, Y. A. Koksharov, G. B. Khomutov, and G. Y. Yurkov, "Magnetic nanoparticles: Preparation, structure and properties," *Russ. Chem. Rev.*, vol. 74, no. 6, pp. 489–520, 2005.
- [2] A. Akbarzadeh, M. Samiei, and S. Davaran, "Magnetic nanoparticles: Preparation, physical properties, and applications in biomedicine," *Nanoscale Res. Lett.*, vol. 7, no. 1, p. 144, 2012.
- [3] R. Konwar and A. B. Ahmed, "Nanoparticle: An overview of preparation, characterization and application," *Int. Res. J. Pharm.*, vol. 4, no. 4, pp. 47–57, 2013.
- [4] R. Raliya, T. S. Chadha, K. Haddad, and P. Biswas, "Perspective on nanoparticle technology for biomedical use," *Curr. Pharm. Des.*, vol. 22, pp. 2481–2490, 2016.
- [5] A. H. Lu, E. L. Salabas, and F. Schüth, "Magnetic nanoparticles: Synthesis, protection, functionalization, and application," *Angew. Chemie - Int. Ed.*, vol. 46, no. 8, pp. 1222–1244, 2007.
- [6] M. Mohapatra and S. Anand, "Synthesis and applications of nano-structured iron oxides / hydroxides – a review," *Int. J. Eng. Sci. Technol.*, vol. 2, no. 8, pp. 127–146, 2010.
- [7] R. M. Cornell and U. Schwertmann, *The Iron Oxides: Structure, Properties, Reactions, Occurances and Uses, second ed. Wiley-VCH Verlag GmbH & Co. KGaA, Weinheim, Germany. 2003.*
- [8] H. Guo and A. S. Barnard, "Naturally occurring iron oxide nanoparticles: Morphology, surface chemistry and environmental stability," *J. Mater. Chem. A*, vol. 1, no. 27, pp. 27–42, 2013.
- [9] Z. Karimi, L. Karimi, and H. Shokrollahi, "Nano-magnetic particles used in biomedicine: Core and coating materials," *Mater. Sci. Eng. C*, vol. 33, pp. 2465–2475, 2013.
- [10] S. K. Tripathi, R. Kaur, S. Bharti, I. Gawri, and J. Kaur, "Recent advances in synthesis, properties and applications of magnetic oxide nanomaterials," *Solid State Phenom.*, vol. 232, pp. 1–44, 2015.
- [11] Wahajuddin and Arora, "Superparamagnetic iron oxide nanoparticles: Magnetic nanoplatforms as drug carriers," *Int. J. Nanomedicine*, vol. 7, pp. 3445–3471, 2012.
- [12] A. Figuerola, R. Di Corato, L. Manna, and T. Pellegrino, "From iron oxide nanoparticles towards advanced iron-based inorganic materials designed for biomedical applications," *Pharmacol. Res.*, vol. 62, pp. 126–143, 2010.
- [13] S. F. Hasany, I. Ahmed, J. Rajan, and A. Rehman, "Systematic review of the preparation techniques of iron oxide magnetic nanoparticles," *Nanosci. Nanotechnol.*, vol. 2, no. 6, pp. 148–158, 2012.

- [14] A. G. Roca, R. Costo, A. F. Rebolledo, S. Veintemillas-Verdaguer, P. Tartaj, T. González-Carreño, M. P. Morales, and C. J. Serna, "Progress in the preparation of magnetic nanoparticles for applications in biomedicine," *J. Phys. D. Appl. Phys.*, vol. 42, pp. 1–11, 2009.
- [15] W. Wu, Z. Wu, T. Yu, C. Jiang, and W.-S. Kim, "Recent progress on magnetic iron oxide nanoparticles: Synthesis, surface functional strategies and biomedical applications," *Sci. Technol. Adv. Mater.*, vol. 16, 2015.
- [16] B. Vallina, J. D. Rodriguez-Blanco, A. P. Brown, L. G. Benning, and J. A. Blanco, "Enhanced magnetic coercivity of α -Fe₂O₃ obtained from carbonated 2-line ferrihydrite," *J. Nanoparticle Res.*, vol. 16, 2014.
- [17] Ö. Özdemir, D. J. Dunlop, and T. S. Berquó, "Morin transition in hematite: Size dependence and thermal hysteresis," *Geochemistry, Geophys. Geosystems*, vol. 9, no. 10, 2008.
- [18] Z. Zhang, C. Boxall, and G. H. Kelsall, "Photoelectrophoresis of colloidal iron oxides 1. Hematite (α -Fe₂O₃)," *Colloids Surfaces A Physicochem. Eng. Asp.*, vol. 73, pp. 145–163, 1993.
- [19] M. Tadic, L. Kopanja, M. Panjan, S. Kralj, J. Nikodinovic-Runic, and Z. Stojanovic, "Synthesis of core-shell hematite (α -Fe₂O₃) nanoplates: Quantitative analysis of the particle structure and shape, high coercivity and low cytotoxicity," *Appl. Surf. Sci.*, vol. 403, pp. 628–634, 2017.
- [20] E. Bykova, L. Dubrovinsky, N. Dubrovinskaia, M. Bykov, C. McCammon, S. V. Ovsyannikov, H.-P. Liermann, I. Kuppenko, A. I. Chumakov, R. Rüffer, M. Hanfland, and V. Prakapenka, "Structural complexity of simple Fe₂O₃ at high pressures and temperatures," *Nat. Commun.*, vol. 7, pp. 1–6, 2016.
- [21] R. U. Onyenwoke and J. Wiegel, "Magnetite: Structure, Properties and Applications," in *Structure, Properties, Microbiology and Applications of Magnetite*, Nova Science Publishers, Inc. USA, 2011, pp. 297–316.
- [22] C. DeArmitt, "Magnetite," *Encyclopedia of Polymers and Composites*, Springer-Verlag Berlin Heidelberg, Germany. pp. 1–11, 2014.
- [23] W. Wu, X. H. Xiao, S. F. Zhang, T. C. Peng, J. Zhou, F. Ren, and C. Z. Jiang, "Synthesis and magnetic properties of maghemite (γ -Fe₂O₃) short-nanotubes," *Nanoscale Res. Lett.*, vol. 5, pp. 1474–1479, 2010.
- [24] H. Shokrollahi, "A review of the magnetic properties, synthesis methods and applications of maghemite," *J. Magn. Magn. Mater.*, vol. 426, pp. 74–81, 2017.
- [25] R. Dronskowski, "The little maghemite story: A classic functional material," *Adv. Functional Mater.*, vol. 11, no. 1, pp. 27–29, 2001.
- [26] V. N. Nikiforov, A. E. Goldt, E. A. Gudilin, V. G. Sredin, and V. Y. Irhin, "Magnetic properties of maghemite nanoparticles," *Bull. Russ. Acad. Sci. Phys.*, vol. 78, no. 10, pp. 1075–1080, 2014.

- [27] A. Yan, X. Liu, G. Qiu, N. Zhang, R. Shi, R. Yi, M. Tang, and R. Che, "A simple solvothermal synthesis and characterization of round-biscuit-like Fe₃O₄ nanoparticles with adjustable sizes," *Solid State Commun.*, vol. 144, pp. 315–318, 2007.
- [28] Y. Zhu and Q. Wu, "Synthesis of magnetite nanoparticles by precipitation with forced mixing," *J. Nanoparticle Res.*, vol. 1, no. 3, pp. 393–396, 1999.
- [29] W. J. Stark, P. R. Stoessel, W. Wohlleben, and A. Hafner, "Industrial applications of nanoparticles," *Chem. Soc. Rev.*, vol. 44, pp. 5793–5805, 2015.
- [30] S. Si, A. Kotal, T. K. Mandal, S. Giri, H. Nakamura, and T. Kohara, "Size-controlled synthesis of magnetite nanoparticles in the presence of polyelectrolytes," *Chem. Mater.*, vol. 16, pp. 3489–3496, 2004.
- [31] Y. L. Pang, S. Lim, H. C. Ong, and W. T. Chong, "Research progress on iron oxide-based magnetic materials: Synthesis techniques and photocatalytic applications," *Ceram. Int.*, vol. 42, no. 1, pp. 9–34, 2016.
- [32] X. Liu, Z. Zhong, Y. Tang, and B. Liang, "Review on the synthesis and applications of Fe₃O₄ nanomaterials," *J. Nanomater.*, vol. 2013, pp. 1–7, 2013.
- [33] S. C. N. Tang and I. M. C. Lo, "Magnetic nanoparticles: Essential factors for sustainable environmental applications," *Water Res.*, vol. 47, pp. 2613–2632, 2013.
- [34] W. Liu, "Nanoparticles and their biological and environmental applications," *J. Biosci. Bioeng.*, vol. 102, no. 1, pp. 1–7, 2006.
- [35] A. F. Ngomsik, A. Bee, M. Draye, G. Cote, and V. Cabuil, "Magnetic nano- and microparticles for metal removal and environmental applications: A review," *Comptes Rendus Chim.*, vol. 8, pp. 963–970, 2005.
- [36] A. M. Gutierrez, T. D. Dziubla, and J. Z. Hilt, "Recent advances on iron oxide magnetic nanoparticles as sorbents of organic pollutants in water and wastewater treatment," *Rev. Environ. Health*, vol. 32, no. 1–2, pp. 111–117, 2017.
- [37] E. Blanco, H. Shen, and M. Ferrari, "Principles of nanoparticle design for overcoming biological barriers to drug delivery," *Nat. Biotechnol.*, vol. 33, no. 9, pp. 941–951, 2015.
- [38] R. Singh and J. W. L. Jr., "Nanoparticle-based targeted drug delivery," *Exp. Mol. Pathol.*, vol. 86, no. 3, pp. 215–223, 2009.
- [39] S. R. Mudshinge, A. B. Deore, S. Patil, and C. M. Bhalgat, "Nanoparticles: Emerging carriers for drug delivery," *Saudi Pharm. J.*, vol. 19, pp. 129–141, 2011.
- [40] P. Guardia, N. Pérez, A. Labarta, and X. Batlle, "Controlled synthesis of iron oxide nanoparticles over a wide size range," *Langmuir*, vol. 26, no. 8, pp. 5843–5847, 2009.

- [41] P. B. Santhosh and N. P. Ulrich, "Multifunctional superparamagnetic iron oxide nanoparticles: Promising tools in cancer theranostics," *Cancer Lett.*, vol. 336, no. 1, pp. 8–17, 2013.
- [42] H. Yan, J. Zhang, C. You, Z. Song, B. Yu, and Y. Shen, "Influences of different synthesis conditions on properties of Fe₃O₄ nanoparticles," *Mater. Chem. Phys.*, vol. 113, no. 1, pp. 46–52, 2009.
- [43] Y. K. Jeong, D. K. Shin, H. J. Lee, K. S. Oh, J. H. Lee, and D. H. Riu, "Nano magnetite particles prepared under the combined addition of urea and ammonia," *Key Eng. Mater.*, vol. 317–318, pp. 203–206, 2006.
- [44] N. Tran and T. J. Webster, "Magnetic nanoparticles: Biomedical applications and challenges," *J. Mater. Chem.*, vol. 20, pp. 8760–8767, 2010.
- [45] A. K. Gupta and M. Gupta, "Synthesis and surface engineering of iron oxide nanoparticles for biomedical applications," *Biomaterials*, vol. 26, pp. 3995–4021, 2005.
- [46] C. F. Jones and D. W. Grainger, "In vitro assessments of nanomaterial toxicity," *Adv. Drug Deliv. Rev.*, vol. 61, no. 6, pp. 438–456, 2009.
- [47] X. Tian, L. Zhang, M. Yang, L. Bai, Y. Dai, Z. Yu, and Y. Pan, "Functional magnetic hybrid nanomaterials for biomedical diagnosis and treatment," *Wiley Interdiscip. Rev. Nanomedicine Nanobiotechnology*, vol. 9, pp. 1–14, 2017.
- [48] S. Gyergyek, D. Makovec, M. Jagodič, M. Drofenik, K. Schenk, O. Jordan, J. Kovač, G. Dražič, and H. Hofmann, "Hydrothermal growth of iron oxide NPs with a uniform size distribution for magnetically induced hyperthermia: Structural, colloidal and magnetic properties," *J. Alloys Compd.*, vol. 694, pp. 261–271, 2017.
- [49] D. X. Chen, A. Sanchez, E. Taboada, A. Roig, N. Sun, and H. C. Gu, "Size determination of superparamagnetic nanoparticles from magnetization curve," *J. Appl. Phys.*, vol. 105, no. 8, 2009.
- [50] A. G. Kolhatkar, A. C. Jamison, D. Litvinov, R. C. Willson, and T. R. Lee, "Tuning the magnetic properties of nanoparticles," *Int. J. Mol. Sci.*, vol. 14, no. 8, pp. 15977–16009, 2013.
- [51] V. V. Mody, A. Singh, and B. Wesley, "Basics of magnetic nanoparticles for their application in the field of magnetic fluid hyperthermia," *Eur. J. Nanomedicine*, vol. 5, no. 1, pp. 11–21, 2013.
- [52] A. S. Teja and P.-Y. Koh, "Synthesis, properties, and applications of magnetic iron oxide nanoparticles," *Prog. Cryst. Growth Charact. Mater.*, vol. 55, pp. 22–45, 2009.
- [53] T. Indira, "Magnetic nanoparticles: A review," *Int. J. Pharm. Sci. Nanotechnol.*, vol. 3, no. 3, pp. 1035–1042, 2010.
- [54] D. Xiao, T. Lu, R. Zeng, and Y. Bi, "Preparation and highlighted applications of magnetic microparticles and nanoparticles: A review on recent advances," *Microchim. Acta*, vol. 183, pp. 2655–2675, 2016.

- [55] I. R. Harris and A. J. Williams, "Magnetic Materials," *Materials Science and Engineering-Encyclopedia of Life Support Systems (EOLSS)*, vol. II. pp. 49–83, 2009.
- [56] M. Arruebo, R. Fernández-pacheco, M. R. Ibarra, and J. Santamaría, "Magnetic nanoparticles for drug delivery," *Rev. Lit. Arts Am.*, vol. 2, no. 3, pp. 22–32, 2007.
- [57] S. Bedanta and W. Kleemann, "Supermagnetism," *J. Phys. D. Appl. Phys.*, vol. 42, pp. 1–28, 2009.
- [58] K. Ali, Y. Javed, and Y. Jamil, "Size and Shape Control Synthesis of Iron Oxide–Based Nanoparticles: Current Status and Future Possibility," in *Complex Magnetic Nanostructures*, Springer International Publishing AG, Switzerland, 2017, pp. 39–81.
- [59] J. Estelrich, E. Escribano, J. Queralt, and M. A. Busquets, "Iron oxide nanoparticles for magnetically-guided and magnetically-responsive drug delivery," *Int. J. Mol. Sci.*, vol. 16, no. 4, pp. 8070–8101, 2015.
- [60] B. Issa, I. M. Obaidat, B. A. Albiss, and Y. Haik, "Magnetic nanoparticles: Surface effects and properties related to biomedicine applications," *Int. J. Mol. Sci.*, vol. 14, no. 11, pp. 21266–21305, 2013.
- [61] U. Klekotka, D. Satuła, S. Spassov, and B. Kalska-Szostko, "Surfactant dependence on physicochemical properties of magnetite nanoparticles," *Colloids Surfaces A Physicochem. Eng. Asp.*, vol. 537, pp. 452–459, 2018.
- [62] W. Wu, C. Jiang, and V. A. L. Roy, "Designed synthesis and surface engineering strategies of magnetic iron oxide nanoparticles for biomedical application," *Nanoscale*, vol. 8, pp. 19421–19474, 2016.
- [63] B. Domènech, J. Bastos-Arrieta, A. Alonso, J. Macanás, M. Muñoz, and D. N. Muraviev, "Bifunctional Polymer-Metal Nanocomposite Ion Exchange Materials," in *Ion Exchange Technologies InTech*, Croatia, 2012, pp. 35–72.
- [64] J. Baumgartner, L. Bertinetti, M. Widdrat, A. M. Hirt, and D. Faivre, "Formation of magnetite nanoparticles at low temperature: From superparamagnetic to stable single domain particles," *PLoS One*, vol. 8, no. 3, pp. 1–6, 2013.
- [65] L. Gutiérrez, R. Costo, C. Grüttner, F. Westphal, N. Gehrke, D. Heinke, A. Fornara, Q. A. Pankhurst, C. Johansson, and M. P. Morales, "Synthesis methods to prepare single- and multi-core iron oxide nanoparticles for biomedical applications," *Dalt. Trans.*, vol. 44, pp. 2943–2952, 2015.
- [66] F. Assa, H. Jafarizadeh-Malmiri, H. Ajamein, N. Anarjan, H. Vaghari, Z. Sayyar, and A. Berenjian, "A biotechnological perspective on the application of iron oxide nanoparticles," *Nano Res.*, vol. 9, pp. 2203–2225, 2016.
- [67] I. Milosevic, L. Motte, B. Aoun, T. Li, Y. Ren, C. Sun, and M. L. Saboungi, "Effects of coating spherical iron oxide nanoparticles," *Biochim. Biophys. Acta - Gen. Subj.*, vol. 1861, no. 1, pp. 3621–3626, 2017.

- [68] P. Tartaj, M. del P. Morales, S. Veintemillas-Verdaguer, T. González-Carreño, and C. J. Serna, "The preparation of magnetic nanoparticles for applications in biomedicine," *J. Phys. D Appl. Phys.*, vol. 36, pp. R182–R197, 2003.
- [69] N. Löwa, M. Seidel, P. Radon, and F. Wiekhorst, "Magnetic nanoparticles in different biological environments analyzed by magnetic particle spectroscopy," *J. Magn. Magn. Mater.*, vol. 427, pp. 133–138, 2017.
- [70] C. C. Berry and A. S. G. Curtis, "Functionalization of magnetic nanoparticles for applications in biomedicine," *J. Phys. D. Appl. Phys.*, vol. 36, pp. R198–R206, 2003.
- [71] M. Ravichandran, S. Velumani, and J. T. Ramirez, "Water-dispersible magnetite nanoparticles as T2 MR imaging contrast agent," *Biomed. Phys. Eng. Express*, vol. 3, no. 1, pp. 1–9, 2017.
- [72] M. Palihawadana-Arachchige, V. M. Naik, P. P. Vaishnava, B. P. Jena, and R. Naik, "Gd-Doped Superparamagnetic Magnetite Nanoparticles for Potential Cancer Theranostics," in *Nanostructured Materials - Fabrication to Applications, InTech, Croatia*, 2017, pp. 79–109.
- [73] D. Couto, M. Freitas, F. Carvalho, and E. Fernandes, "Iron oxide nanoparticles: An insight into their biomedical applications," *Curr. Med. Chem.*, vol. 22, no. 15, pp. 1808–1828, 2015.
- [74] J. Chomoucka, J. Drbohlavova, D. Huska, V. Adam, R. Kizek, and J. Hubalek, "Magnetic nanoparticles and targeted drug delivering," *Pharmacol. Res.*, vol. 62, no. 1, pp. 144–149, 2010.
- [75] Y. Yun, B. K. Lee, and K. Park, "Controlled drug delivery systems: The next 30 years," *Front. Chem. Sci. Eng.*, vol. 8, pp. 276–279, 2014.
- [76] S. Laurent, A. A. Saei, S. Behzadi, A. Panahifar, and M. Mahmoudi, "Superparamagnetic iron oxide nanoparticles for delivery of therapeutic agents: Opportunities and challenges," *Expert Opin. Drug Deliv.*, vol. 11, no. 9, pp. 1449–1470, 2014.
- [77] K. McNamara and S. A. M. Tofail, "Nanoparticles in biomedical applications," *Adv. Phys. X*, vol. 2, no. 1, pp. 54–88, 2017.
- [78] M. Hofmann-Antenbrink, B. von Rechenberg, and H. Hofmann, "Superparamagnetic Nanoparticles for Biomedical Applications," in *Nanostructured Materials for Biomedical Applications, Transworld Research Network, Kerala, India*, 2009, pp. 119–149.
- [79] K. McNamara and S. A. M. Tofail, "Nanosystems: The use of nanoalloys, metallic, bimetallic, and magnetic nanoparticles in biomedical applications," *Phys. Chem. Chem. Phys.*, vol. 17, pp. 27981–27995, 2015.
- [80] S. Singh, V. K. Pandey, R. P. Tewari, and V. Agarwal, "Nanoparticle based drug delivery system: Advantages and applications," *Indian J. Sci. Technol.*, vol. 4, no. 3, pp. 177–180, 2011.

- [81] A. P. Nikam, M. P. Ratnaparkhiand, and S. P. Chaudhary, "Nanoparticles – an overview," *Int. J. Res. Dev. Pharm. L. Sci.*, vol. 3, no. 5, pp. 1121–1127, 2014.
- [82] G. S. Demirer, A. C. Okur, and S. Kizilel, "Synthesis and design of biologically inspired biocompatible iron oxide nanoparticles for biomedical applications," *J. Mater. Chem. B*, vol. 3, pp. 7831–7849, 2015.
- [83] M. Faraji, Y. Yamini, and M. Rezaee, "Magnetic nanoparticles: Synthesis, stabilization, functionalization, characterization, and applications," *J. Iran. Chem. Soc.*, vol. 7, no. 1, pp. 1–37, 2010.
- [84] B. Dutta, N. G. Shetake, B. K. Barick, K. C. Barick, B. N. Pandey, K. I. Priyadarsini, and P. A. Hassan, "pH sensitive surfactant-stabilized Fe₃O₄ magnetic nanocarriers for dual drug delivery," *Colloids Surfaces B Biointerfaces*, vol. 162, pp. 163–171, 2018.
- [85] O. Veisheh, J. W. Gunn, and M. Zhang, "Design and fabrication of magnetic nanoparticles for targeted drug delivery and imaging," *Adv. Drug Deliv. Rev.*, vol. 62, no. 3, pp. 284–304, 2010.
- [86] M. Gaumet, A. Vargas, R. Gurny, and F. Delie, "Nanoparticles for drug delivery: The need for precision in reporting particle size parameters," *Eur. J. Pharm. Biopharm.*, vol. 69, no. 1, pp. 1–9, 2008.
- [87] V. J. Mohanraj and Y. Chen, "Nanoparticles - a review," *Trop. J. Pharm. Res.*, vol. 5, no. 1, pp. 561–573, 2006.
- [88] W. H. De Jong and P. J. A. Borm, "Drug delivery and nanoparticles: Applications and hazards," *Int. J. Nanomedicine*, vol. 3, no. 2, pp. 133–149, 2008.
- [89] G. A. Silva, "Nanotechnology approaches to crossing the blood-brain barrier and drug delivery to the CNS," *BMC Neurosci.*, vol. 9, no. 3, pp. 1–4, 2008.
- [90] J. Kreuter, "Nanoparticulate systems for brain delivery of drugs," *Adv. Drug Deliv. Rev.*, vol. 47, pp. 65–81, 2001.
- [91] N. Voigt, P. Henrich-Noack, S. Kockentiedt, W. Hintz, J. Tomas, and B. A. Sabel, "Surfactants, not size or zeta-potential influence blood-brain barrier passage of polymeric nanoparticles," *Eur. J. Pharm. Biopharm.*, vol. 87, no. 1, pp. 19–29, 2014.
- [92] M. M. Patel and B. M. Patel, "Crossing the blood–brain barrier: Recent advances in drug delivery to the brain," *CNS Drugs*, vol. 31, no. 2, pp. 109–133, 2017.
- [93] B. Wilson, "Brain targeting PBCA nanoparticles and the blood-brain barrier," *Futur. Med.*, vol. 4, no. 5, pp. 499–502, 2009.
- [94] J. Kreuter, P. Ramge, V. Petrov, S. Hamm, S. E. Gelperina, B. Engelhardt, R. Alyautdin, H. Von Briesen, and D. J. Begley, "Direct evidence that polysorbate-80-coated poly(butylcyanoacrylate) nanoparticles deliver drugs to the CNS via specific mechanisms requiring prior binding of drug to the nanoparticles," *Pharm. Res.*, vol. 20, no. 3, pp. 409–416, 2003.

- [95] M. Kolter, M. Ott, C. Hauer, I. Reimold, and G. Fricker, "Nanotoxicity of poly(n-butylcyano-acrylate) nanoparticles at the blood–brain barrier, in human whole blood and in vivo," *J. Control. Release*, vol. 197, pp. 165–179, 2015.
- [96] M. Masserini, "Nanoparticles for brain drug delivery," *ISRN Biochem.*, vol. 2013, pp. 1–18, 2013.
- [97] M. Adabi, M. Naghibzadeh, M. Adabi, M. A. Zarrinfard, S. S. Esnaashari, A. M. Seifalian, R. Faridi-Majidi, H. T. Aiyelabegan, and H. Ghanbari, "Biocompatibility and nanostructured materials: Applications in nanomedicine," *Artif. Cells, Nanomedicine Biotechnol.*, vol. 45, no. 4, pp. 833–842, 2016.
- [98] "Health – Blood-Brain-Barrier." [Online]. Available: <https://www.emf.ethz.ch/en/knowledge/topics/health/blood-brain-barrier/>. [Accessed: 14-Dec-2017].
- [99] M. A. Busquets, A. Espargaró, R. Sabaté, and J. Estelrich, "Magnetic nanoparticles cross the blood-brain barrier: When physics rises to a challenge," *Nanomaterials*, vol. 5, no. 4, pp. 2231–2248, 2015.
- [100] C. Roney, P. Kulkarni, V. Arora, P. Antich, F. Bonte, A. Wu, N. N. Mallikarjuana, S. Manohar, H. F. Liang, A. R. Kulkarni, H. W. Sung, M. Sairam, and T. M. Aminabhavi, "Targeted nanoparticles for drug delivery through the blood-brain barrier for Alzheimer's disease," *J. Control. Release*, vol. 108, pp. 193–214, 2005.
- [101] E. Farkas and P. G. M. Luiten, "Cerebral microvascular pathology in aging and Alzheimer's disease," *Prog. Neurobiol.*, vol. 64, pp. 575–611, 2001.
- [102] G. N. Shah and A. D. Mooradian, "Age-related changes in the blood-brain barrier," *Exp. Gerontol.*, vol. 32, no. 4/5, pp. 501–519, 1997.
- [103] A. Reichel, "The role of blood-brain barrier studies in the pharmaceutical industry," *Curr. Drug Metab.*, vol. 7, pp. 183–203, 2006.
- [104] C. Dagenais, C. Rousselle, G. M. Pollack, and J. M. Scherrmann, "Development of an in situ mouse brain perfusion model and its application to mdr1a P-Glycoprotein-deficient mice," *J. Cereb. blood flow Metab.*, vol. 20, pp. 381–386, 1999.
- [105] S. Prilloff, M. I. Noblejas, V. Chedhomme, and B. A. Sabel, "Two faces of calcium activation after optic nerve trauma: Life or death of retinal ganglion cells in vivo depends on calcium dynamics," *Eur. J. Neurosci.*, vol. 25, pp. 3339–3346, 2007.
- [106] S. Prilloff, J. Fan, P. Henrich-Noack, and B. A. Sabel, "In vivo confocal neuroimaging (ICON): Non-invasive, functional imaging of the mammalian CNS with cellular resolution," *Eur. J. Neurosci.*, vol. 31, no. 3, pp. 521–528, 2010.
- [107] S. Prilloff, P. Henrich-Noack, and B. A. Sabel, "Recovery of axonal transport after partial optic nerve damage is associated with secondary retinal ganglion cell death in vivo," *Investig. Ophthalmol. Vis. Sci.*, vol. 53, no. 3, pp. 1460–1466, 2012.

- [108] P. Henrich-Noack, S. Prilloff, N. Voigt, J. Jin, W. Hintz, J. Tomas, and B. A. Sabel, "In vivo visualisation of nanoparticle entry into central nervous system tissue," *Arch. Toxicol.*, vol. 86, pp. 1099–1105, 2012.
- [109] J. Galvao, B. M. Davis, and M. F. Cordeiro, "In vivo imaging of retinal ganglion cell apoptosis," *Curr. Opin. Pharmacol.*, vol. 13, no. 1, pp. 123–127, 2013.
- [110] S. Liu, Z. W. Li, R. N. Weinreb, G. Xu, J. D. Lindsey, C. Ye, W. H. Yung, C. P. Pang, D. S. C. Lam, and C. K. S. Leung, "Tracking retinal microgliosis in models of retinal ganglion cell damage," *Investig. Ophthalmol. Vis. Sci.*, vol. 53, no. 10, pp. 6254–6262, 2012.
- [111] S. Angelow, P. Zeni, and H. Galla, "Usefulness and limitation of primary cultured porcine choroid plexus epithelial cells as an in vitro model to study drug transport at the blood – CSF barrier," *Adv. Drug Deliv. Rev.*, vol. 56, pp. 1859–1873, 2004.
- [112] W. M. Pardridge, "Blood-brain barrier biology and methodology," *J. Neurovirol.*, vol. 5, no. 6, pp. 556–569, 1999.
- [113] H. Steuer, A. Jaworski, B. Elger, M. Kausmann, H. Schneider, D. Stoll, and B. Schlosshauer, "Functional characterization and comparison of the outer blood–retina barrier and the blood–brain barrier," *Invest. Ophthalmol. Vis. Sci.*, vol. 46, no. 3, pp. 1047–1053, 2005.
- [114] H. Steuer, A. Jaworski, D. Stoll, and B. Schlosshauer, "In vitro model of the outer blood – retina barrier," *Brain Res. Protoc.*, vol. 13, pp. 26–36, 2004.
- [115] L. Zhang, W.-F. Dong, and H.-B. Sun, "Multifunctional superparamagnetic iron oxide nanoparticles: Design, synthesis and biomedical photonic applications," *Nanoscale*, vol. 5, pp. 7664–84, 2013.
- [116] D. Couto, M. Freitas, F. Carvalho, and E. Fernandes, "Iron oxide nanoparticles: An insight into their biomedical applications," *Curr. Med. Chem.*, vol. 22, no. 15, pp. 1808–1828, 2015.
- [117] C. Fu and N. M. Ravindra, "Magnetic iron oxide nanoparticles: Synthesis and applications," *Bioinspired, Biomim. Nanobiomaterials*, vol. 1, no. 4, pp. 229–244, 2012.
- [118] A. Ito, M. Shinkai, H. Honda, and T. Kobayashi, "Medical application of functionalized magnetic nanoparticles," *J. Biosci. Bioeng.*, vol. 100, no. 1, pp. 1–11, 2005.
- [119] A. Nochehdehi, S. Thomas, M. Sadri, S. Afghahi, and S. Mehdi Hadavi, "Iron oxide biomagnetic nanoparticles (IO-BMNPs); Synthesis, characterization and biomedical application—a review," *J. Nanomed. Nanotechnol.*, vol. 8, no. 1, pp. 1–9, 2017.
- [120] Z. Hedayatnasab, F. Abnisa, and W. M. A. W. Daud, "Review on magnetic nanoparticles for magnetic nanofluid hyperthermia application," *Mater. Des.*, vol. 123, pp. 174–196, 2017.

- [121] V. Patsula, M. Moskvin, S. Dutz, and D. Horák, "Size-dependent magnetic properties of iron oxide nanoparticles," *J. Phys. Chem. Solids*, vol. 88, pp. 24–30, 2016.
- [122] D. T. Nguyen and K.-S. Kim, "Functionalization of magnetic nanoparticles for biomedical applications," *Korean J. Chem. Eng.*, vol. 31, no. 8, pp. 1289–1305, 2014.
- [123] Z. Nemati, S. M. Salili, J. Alonso, A. Ataie, R. Das, M. H. Phan, and H. Srikanth, "Superparamagnetic iron oxide nanodiscs for hyperthermia therapy: Does size matter?," *J. Alloys Compd.*, vol. 714, pp. 709–714, 2017.
- [124] D. L. Huber, "Synthesis, properties, and applications of iron nanoparticles," *Small*, vol. 1, no. 5, pp. 482–501, 2005.
- [125] N. T. K. Thanh and L. A. W. Green, "Functionalisation of nanoparticles for biomedical applications," *Nano Today*, vol. 5, pp. 213–230, 2010.
- [126] Z. Shen, A. Wu, and X. Chen, "Iron oxide nanoparticle based contrast agents for magnetic resonance imaging," *Mol. Pharm.*, vol. 14, no. 5, pp. 1352–1364, 2017.
- [127] N. Lee, D. Yoo, D. Ling, M. H. Cho, T. Hyeon, and J. Cheon, "Iron oxide based nanoparticles for multimodal imaging and magnetoresponsive therapy," *Chem. Rev.*, vol. 115, no. 19, pp. 10637–10689, 2015.
- [128] D. Ková, A. Malá, J. Mlcochová, M. Kalina, Z. Fohlerová, A. Hlaválek, Z. Farka, P. Skládal, Z. S. Jr, R. Jirík, O. Slabý, and J. Hubálek, "Preparation and characterisation of highly stable iron oxide nanoparticles for magnetic resonance imaging," *J. Nanomater.*, vol. 2017, pp. 1–9, 2017.
- [129] T. D. Schladt, K. Schneider, H. Schild, and W. Tremel, "Synthesis and bio-functionalization of magnetic nanoparticles for medical diagnosis and treatment," *Dalt. Trans.*, vol. 40, pp. 6315–6343, 2011.
- [130] R. Qiao, C. Yang, and M. Gao, "Superparamagnetic iron oxide nanoparticles: From preparations to in vivo MRI applications," *J. Mater. Chem.*, vol. 19, pp. 6274–6293, 2009.
- [131] S. Laurent, D. Forge, M. Port, A. Roch, C. Robic, L. Vander Elst, and R. N. Muller, "Magnetic iron oxide nanoparticles: Synthesis, stabilization, vectorization, physicochemical characterizations and biological applications," *Chem. Rev.*, vol. 108, pp. 2064–2110, 2008.
- [132] H. Bin Na, I. C. Song, and T. Hyeon, "Inorganic nanoparticles for MRI contrast agents," *Adv. Mater.*, vol. 21, pp. 2133–2148, 2009.
- [133] H. Wei, O. T. Bruns, M. G. Kaul, E. C. Hansen, M. Barch, A. Wiśniowska, O. Chen, Y. Chen, N. Li, S. Okada, J. M. Cordero, M. Heine, C. T. Farrar, D. M. Montana, G. Adam, H. Itrich, A. Jasanoff, P. Nielsen, and M. G. Bawendi, "Exceedingly small iron oxide nanoparticles as positive MRI contrast agents," *Proc. Natl. Acad. Sci. U. S. A.*, vol. 114, no. 9, pp. 2325–2330, 2017.

- [134] P. Majewski and B. Thierry, "Functionalized magnetite nanoparticles-synthesis, properties, and bio-applications," *Crit. Rev. Solid State Mater. Sci.*, vol. 32, no. 3–4, pp. 203–215, 2007.
- [135] R. Hao, R. Xing, Z. Xu, Y. Hou, S. Goo, and S. Sun, "Synthesis, functionalization, and biomedical applications of multifunctional magnetic nanoparticles," *Adv. Mater.*, vol. 22, pp. 2729–2742, 2010.
- [136] M. Colombo, S. Carregal-Romero, M. F. Casula, L. Gutiérrez, M. P. Morales, I. B. Bohm, J. T. Heverhagen, D. Prospero, and W. J. Parak, "Biological applications of magnetic nanoparticles," *Chem. Soc. Rev.*, vol. 41, pp. 4306–4334, 2012.
- [137] A. Petrova, W. Hintz, and J. Tomas, "Investigation of the precipitation of barium sulfate nanoparticles," *Chem. Eng. Technol.*, vol. 31, no. 4, pp. 604–608, 2008.
- [138] W. Luther, "Industrial applications of nanomaterials-chances and risks," *Future Technology Division of VDI Technologiezentrum GmbH, Düsseldorf, Germany*, 2004.
- [139] B. Mishra, B. B. Patel, and S. Tiwari, "Colloidal nanocarriers: A review on formulation technology, types and applications toward targeted drug delivery," *Nanomedicine Nanotechnology, Biol. Med.*, vol. 6, no. 1, pp. 9–24, 2010.
- [140] M. Zahmakiran and S. Özkar, "Metal nanoparticles in liquid phase catalysis; From recent advances to future goals," *Nanoscale*, vol. 3, no. 9, p. 3462, 2011.
- [141] J. Xu, H. Yang, W. Fu, K. Du, Y. Sui, J. Chen, Y. Zeng, M. Li, and G. Zou, "Preparation and magnetic properties of magnetite nanoparticles by sol-gel method," *J. Magn. Mater.*, vol. 309, pp. 307–311, 2007.
- [142] D. Dozier, S. Palchoudhury, and Y. Bao, "Synthesis of iron oxide nanoparticles with biological coatings," *JOSHUA*, vol. 7, pp. 16–18, 2010.
- [143] E. M. Rajesh, K. Shamili, R. Rajendran, M. Elango, and S. R. M. Shankar, "Superparamagnetic nanoparticles of iron oxide: Synthesis and characterization," *Adv. Sci. Eng. Med.*, vol. 6, pp. 1–5, 2014.
- [144] M. Mahmoudi, A. Simchi, and M. Imani, "Recent advances in surface engineering of superparamagnetic iron oxide nanoparticles for biomedical applications," *J. Iran. Chem. Soc.*, vol. 7, pp. S1–S27, 2010.
- [145] A. Ali, H. Zafar, M. Zia, I. U. Haq, A. R. Phull, J. S. Ali, and A. Hussain, "Synthesis, characterisation, applications and challenges of iron oxide nanoparticles," *Nanotechnol. Sci. Appl.*, vol. 9, pp. 49–67, 2016.
- [146] A. Iqbal, K. Iqbal, B. Li, D. Gong, and W. Qin, "Recent advances in iron nanoparticles: Preparation, properties, biological and environmental application," *J. Nanosci. Nanotechnol.*, vol. 17, no. 7, pp. 4386–4409, 2017.
- [147] A. B. Seabra and N. Durán, "Nanotoxicology of metal oxide nanoparticles," *Metals (Basel)*, vol. 5, no. 2, pp. 934–975, 2015.
- [148] D. Ling and T. Hyeon, "Chemical design of biocompatible iron oxide nanoparticles for medical applications," *Small*, vol. 9, pp. 1450–1466, 2012.

- [149] M. Farahmandjou and F. Soflaee, "Synthesis and characterization of α -Fe₂O₃ nanoparticles by simple co-Precipitation method," *Phys. Chem. Res.*, vol. 3, no. 3, pp. 191–196, 2015.
- [150] G. Gnanaprakash, S. Mahadevan, T. Jayakumar, P. Kalyanasundaram, J. Philip, and B. Raj, "Effect of initial pH and temperature of iron salt solutions on formation of magnetite nanoparticles," *Mater. Chem. Phys.*, vol. 103, no. 1, pp. 168–175, 2007.
- [151] M. Pieper, S. Aman, W. Hintz, and J. Tomas, "Optimization of a continuous precipitation process to produce nanoscale BaSO₄," *Chem. Eng. Technol.*, vol. 34, no. 9, pp. 1567–1574, 2011.
- [152] R. Rahmawati, M. G. Permana, B. Harison, Nugraha, B. Yulianto, Suyatman, and D. Kurniadi, "Optimization of frequency and stirring rate for synthesis of magnetite (Fe₃O₄) nanoparticles by using coprecipitation-ultrasonic irradiation methods," *Procedia Eng.*, vol. 170, pp. 55–59, 2017.
- [153] C. Jiang, S. Yang, N. Gan, H. Pan, and H. Liu, "A method for determination of [Fe³⁺]/[Fe²⁺] ratio in superparamagnetic iron oxide," *J. Magn. Magn. Mater.*, vol. 439, pp. 126–134, 2017.
- [154] J. J. Ibarra-Sánchez, R. Fuentes-Ramírez, A. G. Roca, M. del P. Morales, and L. I. Cabrera-Lara, "Key parameters for scaling up the synthesis of magnetite nanoparticles in organic media: Stirring rate and growth kinetic," *Ind. Eng. Chem. Res.*, vol. 52, no. 50, pp. 17841–17847, 2013.
- [155] N. Saxena and M. Singh, "Efficient synthesis of superparamagnetic magnetite nanoparticles under air for biomedical applications," *J. Magn. Magn. Mater.*, vol. 429, pp. 166–176, 2017.
- [156] T. Sulistyaningsih, S. Juari Santosa, D. Siswanta, and B. Rusdiarso, "Synthesis and characterization of magnetites obtained from mechanically and sonochemically assisted co-precipitation and reverse co-precipitation methods," *Int. J. Mater. Mech. Manuf.*, vol. 5, no. 1, pp. 16–19, 2017.
- [157] R. Dinali, A. Ebrahiminezhad, M. Manley-Harris, Y. Ghasemi, and A. Berenjian, "Iron oxide nanoparticles in modern microbiology and biotechnology," *Crit. Rev. Microbiol.*, vol. 43, no. 4, pp. 4397–507, 2017.
- [158] S. Alibeigi and M. R. Vaezi, "Phase transformation of iron oxide nanoparticles by varying the molar ratio of Fe²⁺:Fe³⁺," *Chem. Eng. Technol.*, vol. 31, no. 11, pp. 1591–1596, 2008.
- [159] H. Aono, H. Hirazawa, T. Naohara, T. Maehara, H. Kikkawa, and Y. Watanabe, "Synthesis of fine magnetite powder using reverse coprecipitation method and its heating properties by applying AC magnetic field," *Mater. Res. Bull.*, vol. 40, pp. 1126–1135, 2005.
- [160] N. Mahmed, O. Heczko, O. Söderberg, and S.-P. Hannula, "Room temperature synthesis of magnetite (Fe_{3-δ}O₄) nanoparticles by a simple reverse co-precipitation method," in *IOP Conference Series: Materials Science and Engineering*, 2011, vol. 18, pp. 1–4.

- [161] B. Kowalczyk, I. Lagzi, and B. A. Grzybowski, "Nanoseparations: Strategies for size and/or shape-selective purification of nanoparticles," *Curr. Opin. Colloid Interface Sci.*, vol. 16, no. 2, pp. 135–148, 2011.
- [162] R. Massart, "Preparation of aqueous magnetic liquids in alkaline and acidic media," *IEEE Trans. Magn.*, vol. 17, no. 2, pp. 1247–1248, 1981.
- [163] S. Lefebure, E. Dubois, V. Cabuil, S. Neveu, and R. Massart, "Monodisperse magnetic nanoparticles: Preparation and dispersion in water and oils," *J. Mater. Res.*, vol. 13, no. 10, pp. 2975–2981, 1998.
- [164] S. Qu, H. Yang, D. Ren, S. Kan, G. Zou, D. Li, and M. Li, "Magnetite nanoparticles prepared by precipitation from partially reduced ferric chloride aqueous solutions," *J. Colloid Interface Sci.*, vol. 215, no. 1, pp. 190–192, 1999.
- [165] M. Mahdavi, M. Bin Ahmad, M. J. Haron, F. Namvar, B. Nadi, M. Z. A. Rahman, and J. Amin, "Synthesis, surface modification and characterisation of biocompatible magnetic iron oxide nanoparticles for biomedical applications," *Molecules*, vol. 18, no. 7, pp. 7533–7548, 2013.
- [166] U. S. Khan, N. S. Khattak, A. Manan, A. Rahman, F. Khan, and A. Rahim, "Some properties of magnetite nanoparticles produced under different conditions," *J. Electron. Mater.*, vol. 44, no. 1, pp. 303–312, 2015.
- [167] U. S. Khan, N. S. Khattak, A. Rahman, and F. Khan, "Optimal method for preparation of magnetite nanoparticles," *J. Chem. Soc. Pak.*, vol. 33, no. 5, pp. 628–633, 2011.
- [168] C. W. Lai, F. W. Low, M. F. Tai, and S. B. Abdul Hamid, "Iron oxide nanoparticles decorated oleic acid for high colloidal stability," *Adv. Polym. Technol.*, vol. 36, pp. 1–10, 2017.
- [169] N. Kandpal, N. Sah, R. Loshali, R. Joshi, and J. Prasad, "Co-precipitation method of synthesis and characterization of iron oxide nanoparticles," *J. Sci. Ind. Res.*, vol. 73, pp. 87–90, 2014.
- [170] A. P. A. Faiyas, E. M. Vinod, J. Joseph, R. Ganesan, and R. K. Pandey, "Dependence of pH and surfactant effect in the synthesis of magnetite (Fe_3O_4) nanoparticles and its properties," *J. Magn. Magn. Mater.*, vol. 322, pp. 400–404, 2010.
- [171] G. Rana and U. C. Johri, "Correlation between the pH value and properties of magnetite nanoparticles," *Adv. Mater. Lett.*, vol. 5, no. 5, pp. 280–286, 2014.
- [172] B. Wang, Q. Wei, and S. Qu, "Synthesis and characterization of uniform and crystalline magnetite nanoparticles via oxidation-precipitation and modified co-precipitation methods," *Int. J. Electrochem. Sci.*, vol. 8, pp. 3786–3793, 2013.
- [173] H. A. Eivari, A. Rahdar, and H. Arabi, "Preparation of super paramagnetic iron oxide nanoparticles and investigation their magnetic properties," *Int. J. Sci. Eng. Investig.*, vol. 1, no. 3, pp. 70–72, 2012.

- [174] H. A. Eivari and A. Rahdar, "Some properties of iron oxide nanoparticles synthesized in different conditions," *World Appl. Program.*, vol. 3, no. 2, pp. 52–55, 2013.
- [175] K. Petcharoen and A. Sirivat, "Synthesis and characterization of magnetite nanoparticles via the chemical co-precipitation method," *Mater. Sci. Eng. B*, vol. 177, pp. 421–427, 2012.
- [176] F. Yazdani and M. Edrissi, "Effect of pressure on the size of magnetite nanoparticles in the coprecipitation synthesis," *Mater. Sci. Eng. B*, vol. 171, pp. 86–89, 2010.
- [177] K. L. Palanisamy, N. M. Sundaram, V. Devabharathi, and P. Thangarasu, "Synthesis and characterization of olive oil mediated iron oxide nanoparticles," *Dig. J. Nanomater. Biostructures*, vol. 8, no. 2, pp. 607–612, 2013.
- [178] M. C. Mascolo, Y. Pei, and T. A. Ring, "Room temperature co-precipitation synthesis of magnetite nanoparticles in a large pH window with different bases," *Materials (Basel)*, vol. 6, no. 12, pp. 5549–5567, 2013.
- [179] M. Salavati-Niasari, T. Mahmoudi, and O. Amiri, "Easy synthesis of magnetite nanocrystals via coprecipitation method," *J. Clust. Sci.*, vol. 23, pp. 597–602, 2012.
- [180] M. I. Khalil, "Co-precipitation in aqueous solution synthesis of magnetite nanoparticles using iron (III) salts as precursors," *Arab. J. Chem.*, pp. 0–5, 2015.
- [181] R. Valenzuela, M. C. Fuentes, C. Parra, J. Baeza, N. Duran, S. K. Sharma, M. Knobel, and J. Freer, "Influence of stirring velocity on the synthesis of magnetite nanoparticles (Fe_3O_4) by the co-precipitation method," *J. Alloys Compd.*, vol. 488, no. 1, pp. 227–231, 2009.
- [182] S. Riaz, M. Bashir, and S. Naseem, "Iron oxide nanoparticles prepared by modified co-precipitation method," *IEEE Trans. Magn.*, vol. 50, no. 1, 2014.
- [183] X. Yang, Y. Shang, Y. Li, J. Zhai, N. R. Foster, Y. Li, D. Zou, and Y. Pu, "Synthesis of monodisperse iron oxide nanoparticles without surfactants," *J. Nanomater.*, vol. 2014, pp. 1–5, 2014.
- [184] W. Ramadan, M. Kareem, B. Hannyoy, and S. Saha, "Effect of pH on the structural and magnetic properties of magnetite nanoparticles synthesised by co-precipitation," *Adv. Mater. Res.*, vol. 324, pp. 129–132, 2011.
- [185] Z. L. Liu, Y. J. Liu, K. L. Yao, Z. H. Ding, J. Tao, and X. Wang, "Synthesis and magnetic properties of Fe_3O_4 nanoparticles," *J. Mater. Synth. Process.*, vol. 10, no. 2, pp. 83–87, 2002.
- [186] T. Ahn, J. H. Kim, H. M. Yang, J. W. Lee, and J. D. Kim, "Formation pathways of magnetite nanoparticles by coprecipitation method," *J. Phys. Chem. C*, vol. 116, pp. 6069–6076, 2012.

- [187] M. Mohapatra and S. Anand, "Synthesis and applications of nano-structured iron oxides / hydroxides – a review," *Int. J. Eng. Sci. Technol.*, vol. 2, no. 8, pp. 127–146, 2010.
- [188] Z. N. Kayani, S. Arshad, S. Riaz, and S. Naseem, "Synthesis of iron oxide nanoparticles by sol-gel technique and their characterization," *IEEE Trans. Magn.*, vol. 50, no. 8, pp. 1–4, 2014.
- [189] Y. Lu, Y. Yin, B. T. Mayers, and Y. Xia, "Modifying the surface properties of superparamagnetic iron oxide nanoparticles through a sol-gel approach," *Nano Lett.*, vol. 2, no. 3, pp. 183–186, 2002.
- [190] C. Okoli, M. Sanchez-Dominguez, M. Boutonnet, S. Järås, C. Civera, C. Solans, and G. R. Kuttuva, "Comparison and functionalization study of microemulsion-prepared magnetic iron oxide nanoparticles," *Langmuir*, vol. 28, no. 22, pp. 8479–8485, 2012.
- [191] M. A. Malik, M. Y. Wani, and M. A. Hashim, "Microemulsion method: A novel route to synthesize organic and inorganic nanomaterials," *Arab. J. Chem.*, vol. 5, no. 4, pp. 397–417, 2012.
- [192] J. Gautier, E. Allard-Vannier, K. Hervé-Aubert, M. Soucé, and I. Chourpa, "Design strategies of hybrid metallic nanoparticles for theragnostic applications," *Nanotechnology*, vol. 24, pp. 1–14, 2013.
- [193] H. K. Can, S. Kavlak, S. ParviziKhosroshahi, and A. Güner, "Preparation, characterization and dynamical mechanical properties of dextran-coated iron oxide nanoparticles (DIONPs)," *Artif. Cells Nanomedicine Biotechnol.*, vol. 45, pp. 1–11, 2017.
- [194] B. A. Kairdolf, X. Qian, and S. Nie, "Bioconjugated nanoparticles for biosensing, in vivo imaging, and medical diagnostics," *Anal. Chem.*, vol. 89, no. 2, pp. 1015–1031, 2017.
- [195] S. Mallakpour and M. Madani, "A review of current coupling agents for modification of metal oxide nanoparticles," *Prog. Org. Coatings*, vol. 86, pp. 194–207, 2015.
- [196] S. Sheng-Nan, W. Chao, Z. Zan-Zan, H. Yang-Long, S. S. Venkatram, and X. Zhi-Chuan, "Magnetic iron oxide nanoparticles : Synthesis and surface coating techniques for biomedical applications," *Chinese Phys. B*, vol. 23, no. 3, pp. 1–19, 2014.
- [197] S. Behrens, "Preparation of functional magnetic nanocomposites and hybrid materials: Recent progress and future directions," *Nanoscale*, vol. 3, pp. 877–892, 2011.
- [198] B. I. Kharisov, H. V. R. Dias, O. V. Kharissova, A. Vázquez, Y. Peña, and I. Gómez, "Solubilization, dispersion and stabilization of magnetic nanoparticles in water and non-aqueous solvents: Recent trends," *RSC Adv.*, vol. 4, pp. 45354–45381, 2014.

- [199] L. H. Reddy, J. L. Arias, J. Nicolas, and P. Couvreur, "Magnetic nanoparticles: Design and characterization, toxicity and biocompatibility, pharmaceutical and biomedical applications," *Chem. Rev.*, vol. 112, pp. 5818–5878, 2012.
- [200] M. Dadwal, "Polymeric nanoparticles as promising novel carriers for drug delivery: An overview," *J. Adv. Pharm. Educ. Res.*, vol. 4, no. 1, pp. 20–30, 2014.
- [201] C. E. Mora-Huertas, H. Fessi, and A. Elaissari, "Polymer-based nanocapsules for drug delivery," *Int. J. Pharm.*, vol. 385, pp. 113–142, 2010.
- [202] C. Vauthier and K. Bouchemal, "Methods for the preparation and manufacture of polymeric nanoparticles," *Pharm. Res.*, vol. 26, no. 5, pp. 1025–1058, 2009.
- [203] N. Jawahar and S. Meyyanathan, "Polymeric nanoparticles for drug delivery and targeting: A comprehensive review," *Int. J. Heal. Allied Sci.*, vol. 1, no. 4, pp. 217–223, 2012.
- [204] B. V. N. Nagavarma, H. K. S. Yadav, A. Ayaz, L. S. Vasudha, and H. G. Shivakumar, "Different techniques for preparation of polymeric nanoparticles- a review," *Asian J. Pharm. Clin. Res.*, vol. 5, no. 3, pp. 16–23, 2012.
- [205] S. Lahkar and M. K. Das, "Surface modified polymeric nanoparticles for brain targeted drug delivery," *Curr. Trends Biotechnol. Pharm.*, vol. 7, no. 4, pp. 914–931, 2013.
- [206] J. P. Rao and K. E. Geckeler, "Polymer nanoparticles: Preparation techniques and size-control parameters," *Prog. Polym. Sci.*, vol. 36, no. 7, pp. 887–913, 2011.
- [207] F. Bertorelle, C. Wilhelm, J. Roger, F. Gazeau, C. Ménager, and V. Cabuil, "Fluorescence-modified superparamagnetic nanoparticles: Intracellular uptake and use in cellular imaging," *Langmuir*, vol. 22, no. 12, pp. 5385–5391, 2006.
- [208] K. D. Mahajan, Q. Fan, J. Dorcéna, G. Ruan, and J. O. Winter, "Magnetic quantum dots in biotechnology-synthesis and applications," *Biotechnol. J.*, vol. 8, pp. 1424–34, 2013.
- [209] G. Ruan, D. Thakur, S. Deng, S. Hawkins, and J. O. Winter, "Fluorescent-magnetic nanoparticles for imaging and cell manipulation," *Proc. Inst. Mech. Eng. Part N J. Nanoeng. Nanosyst.*, vol. 223, pp. 81–86, 2010.
- [210] L. Lou, K. Yu, Z. Zhang, B. Li, J. Zhu, Y. Wang, R. Huang, and Z. Zhu, "Functionalized magnetic-fluorescent hybrid nanoparticles for cell labelling," *Nanoscale*, vol. 3, pp. 2315–2323, 2011.
- [211] M. P. Cabrera, P. E. C. Filho, C. M. C. M. Silva, R. M. Oliveira, C. F. G. C. Geraldés, M. M. C. A. Castro, B. F. O. Costa, M. S. C. Henriques, J. A. Paixão, L. B. Carvalho, B. S. Santos, F. Hallwass, A. Fontes, and G. A. L. Pereira, "Highly fluorescent and superparamagnetic nanosystem for biomedical applications," *Nanotechnology*, vol. 28, no. 28, pp. 1–17, 2017.

- [212] H. Xia, R. Tong, Y. Song, F. Xiong, J. Li, S. Wang, H. Fu, J. Wen, D. Li, Y. Zeng, Z. Zhao, and J. Wu, "Synthesis and bio-applications of targeted magnetic-fluorescent composite nanoparticles," *J. Nanoparticle Res.*, vol. 19, no. 4, p. 149, 2017.
- [213] W. Zhang, Y. Zhang, X. Shi, C. Liang, and Y. Xian, "Rhodamine-B decorated superparamagnetic iron oxide nanoparticles: preparation, characterization and their optical/magnetic properties," *J. Mater. Chem.*, vol. 21, p. 16177, 2011.
- [214] F. Yan, Y. Wang, S. He, S. Ku, W. Gu, and L. Ye, "Transferrin-conjugated, fluorescein-loaded magnetic nanoparticles for targeted delivery across the blood-brain barrier," *J. Mater. Sci. Mater. Med.*, vol. 24, no. 10, pp. 2371–2379, 2013.
- [215] A. Quarta, R. Di Corato, L. Manna, A. Ragusa, and T. Pellegrino, "Fluorescent-magnetic hybrid nanostructures: Preparation, properties, and applications in biology," *IEEE Trans. Nanobioscience*, vol. 6, no. 4, pp. 298–308, 2007.
- [216] S. A. Corr, Y. P. Rakovich, and Y. K. Gun'Ko, "Multifunctional magnetic-fluorescent nanocomposites for biomedical applications," *Nanoscale Res. Lett.*, vol. 3, no. 3, pp. 87–104, 2008.
- [217] N. Chekina, D. Horák, P. Jendelová, M. Trchová, M. J. Beneš, M. Hrubý, V. Herynek, K. Turnovcová, and E. Syková, "Fluorescent magnetic nanoparticles for biomedical applications," *J. Mater. Chem.*, vol. 21, p. 7630, 2011.
- [218] C. Kaewsaneha, P. Tangboriboonrat, D. Polpanich, and A. Elaissari, "Multifunctional fluorescent-magnetic polymeric colloidal particles: Preparations and bioanalytical applications," *ACS Appl. Mater. Interfaces*, vol. 7, no. 42, pp. 23373–23386, 2015.
- [219] H. Qu, D. Caruntu, H. Liu, and C. J. O'Connor, "Water-dispersible iron oxide magnetic nanoparticles with versatile surface functionalities," *Langmuir*, vol. 27, no. 6, pp. 2271–2278, 2011.
- [220] C. Wu, P. R. Chang, H. Ren, J. Li, J. Huang, and H. Yuan, "Fluorescent labelled iron oxide nanoparticles for tracing their uptake behavior by plant," *Nano Reports*, vol. 1, pp. 115–120, 2015.
- [221] T. Sarkar, S. Tiwari, K. Rawat, P. R. Solanki, and H. B. Bohidar, "Hydrophilic, fluorescent and superparamagnetic iron oxide-carbon composite nanoparticles," *Colloids Surfaces A Physicochem. Eng. Asp.*, vol. 514, pp. 218–225, 2017.
- [222] J. Erler, S. Machunsky, P. Grimm, H.-J. Schmid, and U. A. Peuker, "Liquid–liquid phase transfer of magnetite nanoparticles — evaluation of surfactants," *Powder Technol.*, vol. 247, pp. 265–269, 2013.
- [223] D. I. Gittins and F. Caruso, "Spontaneous phase transfer of nanoparticulate metals from organic to aqueous media," *Angew. Chemie - Int. Ed.*, vol. 40, no. 16, pp. 3001–3004, 2001.
- [224] J. Yang, J. Y. Lee, and J. Y. Ying, "Phase transfer and its applications in nanotechnology," *Chem. Soc. Rev.*, vol. 40, pp. 1672–1696, 2011.

- [225] S. Machunsky and U. A. Peuker, "Liquid-liquid interfacial transport of nanoparticles," *Phys. Sep. Sci. Eng.*, vol. 2007, pp. 1–7, 2007.
- [226] A. Kumar, H. Joshi, R. Pasricha, A. B. Mandale, and M. Sastry, "Phase transfer of silver nanoparticles from aqueous to organic solutions using fatty amine molecules," *J. Colloid Interface Sci.*, vol. 264, pp. 396–401, 2003.
- [227] M. Sastry, A. Kumar, and P. Mukherjee, "Phase transfer of aqueous colloidal gold particles into organic solutions containing fatty amine molecules," *Colloids Surfaces A Physicochem. Eng. Asp.*, vol. 181, pp. 255–259, 2001.
- [228] S. Y. Zhao, S. H. Chen, D. G. Li, and H. Y. Ma, "Phase transfer of Ag nanoparticles by help of centrifugation," *Colloids Surfaces A Physicochem. Eng. Asp.*, vol. 242, pp. 145–149, 2004.
- [229] S. Machunsky, P. Grimm, H.-J. Schmid, and U. A. Peuker, "Liquid-liquid phase transfer of magnetite nanoparticles," *Colloids Surfaces A Physicochem. Eng. Asp.*, vol. 348, no. 1–3, pp. 186–190, 2009.
- [230] M. Rudolph and U. A. Peuker, "Coagulation and stabilization of sterically functionalized magnetite nanoparticles in an organic solvent with different technical polymers," *J. Colloid Interface Sci.*, vol. 357, pp. 292–299, 2011.
- [231] G. Mériquet, E. Dubois, and R. Perzynski, "Liquid-liquid phase-transfer of magnetic nanoparticles in organic solvents," *J. Colloid Interface Sci.*, vol. 267, no. 1, pp. 78–85, 2003.
- [232] Y. Wang, J. F. Wong, X. Teng, and X. Z. Lin, "'Pulling' nanoparticles into water: Phase transfer of oleic acid stabilized monodisperse nanoparticles into aqueous solutions of α -cyclodextrin," *Nano Lett.*, vol. 3, no. 11, pp. 1555–1559, 2003.
- [233] U. S. Patil, S. Adireddy, A. Jaiswal, S. Mandava, B. R. Lee, and D. B. Chrisey, "In vitro/in vivo toxicity evaluation and quantification of iron oxide nanoparticles," *Int. J. Mol. Sci.*, vol. 16, pp. 24417–24450, 2015.
- [234] V. Zavisova, M. Koneracka, J. Kovac, M. Kubovcikova, I. Antal, P. Kopcansky, M. Bednarikova, and M. Muckova, "The cytotoxicity of iron oxide nanoparticles with different modifications evaluated in vitro," *J. Magn. Magn. Mater.*, vol. 380, pp. 85–89, 2015.
- [235] R. M. Patil, N. D. Thorat, P. B. Shete, P. A. Bedge, S. Gavde, M. G. Joshi, S. A. M. Tofail, and R. A. Bohara, "Comprehensive cytotoxicity studies of superparamagnetic iron oxide nanoparticles," *Biochem. Biophys. Reports*, vol. 13, pp. 63–72, 2018.
- [236] M. Mahmoudi, A. Simchi, A. S. Milani, and P. Stroeve, "Cell toxicity of superparamagnetic iron oxide nanoparticles," *J. Colloid Interface Sci.*, vol. 336, pp. 510–518, 2009.
- [237] C. Buzea, I. I. Blandino, and K. Robbie, "Nanomaterials and nanoparticles: Sources and toxicity," *Bointerphases*, vol. 2, no. 4, p. MR17-MR172, 2007.

- [238] L. Lei, J. Ling-Ling, Z. Yun, and L. Gang, "Toxicity of superparamagnetic iron oxide nanoparticles: Research strategies and implications for nanomedicine," *Chinese Phys. B*, vol. 22, no. 12, pp. 1–10, 2013.
- [239] G. Liu, J. Gao, H. Ai, and X. Chen, "Applications and potential toxicity of magnetic iron oxide nanoparticles," *Small*, vol. 9, no. 9–10, pp. 1533–1545, 2013.
- [240] H. Su, Y. Zheng, C. Chu, and G. Liu, "Magnetic Iron Oxide Nanoparticles: Bioapplications and Potential Toxicity," in *Biomedical Nanomaterials*, Wiley-VCH Verlag GmbH & Co. KGaA, Weinheim, Germany, 2016, pp. 361–385.
- [241] Y. Wang, L. Ding, C. Yao, C. Li, X. Xing, Y. Huang, T. Gu, and M. Wu, "Toxic effects of metal oxide nanoparticles and their underlying mechanisms," *Sci. China Mater.*, vol. 60, no. 2, pp. 93–108, 2017.
- [242] B. Kong, J. H. Seog, L. M. Graham, and S. B. Lee, "Experimental considerations on the cytotoxicity of nanoparticles," *Nanomedicine*, vol. 6, no. 5, pp. 929–941, 2011.
- [243] M. Mahmoudi, H. Hofmann, B. Rothen-Rutishauser, and A. Petri-Fink, "Assessing the in vitro and in vivo toxicity of superparamagnetic iron oxide nanoparticles," *Chem. Rev.*, vol. 112, no. 4, pp. 2323–2338, 2012.
- [244] I. Cicha, C. D. Garlich, and C. Alexiou, "Cardiovascular therapy through nanotechnology - how far are we still from bedside?," *Eur. J. Nanomedicine*, vol. 6, no. 2, pp. 63–87, 2014.
- [245] S. Naqvi, M. Samim, M. Z. Abidin, F. J. Ahmed, A. N. Maitra, C. K. Prashant, and A. K. Dinda, "Concentration-dependent toxicity of iron oxide nanoparticles mediated by increased oxidative stress," *Int. J. Nanomedicine*, vol. 5, no. 1, pp. 983–989, 2010.
- [246] N. S. Remya, S. Syama, A. Sabareeswaran, and P. V. Mohanan, "Toxicity, toxicokinetics and biodistribution of dextran stabilized iron oxide nanoparticles for biomedical applications," *Int. J. Pharm.*, vol. 511, pp. 586–598, 2016.
- [247] H. M. Kouchesfehiani, S. Kiani, A. A. Rostami, and R. Fakheri, "Cytotoxic effect of iron oxide nanoparticles on mouse embryonic stem cells by MTT assay," *Iran. J. Toxicol.*, vol. 7, no. 21, pp. 849–853, 2013.
- [248] M. Balas, C. S. Ciobanu, C. Burtea, M. S. Stan, E. Bezirtzoglou, D. Predoi, and A. Dinischiotu, "Synthesis, characterization, and toxicity evaluation of dextran-coated iron oxide nanoparticles," *Metals (Basel)*, vol. 7, no. 2, pp. 1–17, 2017.
- [249] R. P. Friedrich, C. Janko, M. Poettler, P. Tripal, J. Zaloga, I. Cicha, S. Dürr, J. Nowak, S. Odenbach, I. Slabu, M. Liebl, L. Trahms, M. Stapf, I. Hilger, S. Lyer, and C. Alexiou, "Flow cytometry for intracellular SPION quantification: Specificity and sensitivity in comparison with spectroscopic methods," *Int. J. Nanomedicine*, vol. 10, no. 1, pp. 4185–4201, 2015.
- [250] Y. Xu, J. A. Sherwood, K. H. Lackey, Y. Qin, and Y. Bao, "The responses of immune cells to iron oxide nanoparticles," *J. Appl. Toxicol.*, vol. 36, no. 4, pp. 543–553, 2016.

- [251] J. K. Fard, S. Jafari, and M. A. Eghbal, "A review of molecular mechanisms involved in toxicity of nanoparticles," *Adv. Pharm. Bull.*, vol. 5, no. 4, pp. 447–454, 2015.
- [252] A. Petri-Fink, B. Steitz, A. Finka, J. Salaklang, and H. Hofmann, "Effect of cell media on polymer coated superparamagnetic iron oxide nanoparticles (SPIONs): Colloidal stability, cytotoxicity, and cellular uptake studies," *Eur. J. Pharm. Biopharm.*, vol. 68, no. 1, pp. 129–137, 2008.
- [253] J. B. Mamani, J. M. Malheiros, E. F. Cardoso, A. Tannús, P. H. Silveira, and L. F. Gamarra, "In vivo magnetic resonance imaging tracking of C6 glioma cells labeled with superparamagnetic iron oxide nanoparticles," *Einstein*, vol. 10, no. 2, pp. 164–70, 2012.
- [254] W. Rastedt, K. Thiel, and R. Dringen, "Uptake of fluorescent iron oxide nanoparticles in C6 glioma cells," *Biomed. Phys. Eng. Express*, vol. 3, pp. 1–14, 2017.
- [255] A. Elsaesser and C. V. Howard, "Toxicology of nanoparticles," *Adv. Drug Deliv. Rev.*, vol. 64, pp. 129–137, 2012.
- [256] J. Ai, E. Biazar, M. Jafarpour, M. Montazeri, A. Majdi, S. Aminifard, M. Zafari, H. R. Akbari, and H. G. Rad, "Nanotoxicology and nanoparticle safety in biomedical designs," *Int. J. Nanomedicine*, vol. 6, pp. 1117–1127, 2011.
- [257] V. Valdiglesias, N. Fernández-Bertólez, G. Kiliç, C. Costa, S. Costa, S. Fraga, M. J. Bessa, E. Pásaro, J. P. Teixeira, and B. Laffon, "Are iron oxide nanoparticles safe? Current knowledge and future perspectives," *J. Trace Elem. Med. Biol.*, vol. 38, pp. 53–63, 2016.
- [258] L. Ramírez, "Magnetite (Fe₃O₄) nanoparticles: Are they really safe?," *La Granja*, vol. 21, no. 1, pp. 77–83, 2015.
- [259] T. D. Schladt, K. Schneider, H. Schild, and W. Tremel, "Synthesis and bio-functionalization of magnetic nanoparticles for medical diagnosis and treatment," *Dalt. Trans.*, vol. 40, pp. 6315–6343, 2011.
- [260] A. Baronov, K. Bufkin, D. W. Shaw, B. L. Johnson, and D. L. Patrick, "A simple model of burst nucleation," *Phys. Chem. Chem. Phys.*, vol. 17, no. 32, pp. 20846–20852, 2015.
- [261] R. Viswanatha and D. D. Sarma, "Growth of Nanocrystals in Solution," in *Nanomaterials Chemistry: Recent Developments and New Directions*, Wiley-VCH Verlag GMBH & Co. KGaA, Weinheim, Germany, 2007, pp. 139–170.
- [262] P. W. Dunne, A. S. Munn, C. L. Starkey, T. A. Huddle, and E. H. Lester, "Continuous-flow hydrothermal synthesis for the production of inorganic nanomaterials.," *Philos. Trans. A*, vol. 373, pp. 1–21, 2015.
- [263] S. Jana, "Advances in nanoscale alloys and intermetallics: Low temperature solution chemistry synthesis and application in catalysis," *Dalt. Trans.*, vol. 44, pp. 18692–18717, 2015.

- [264] E. C. Vreeland, J. Watt, G. B. Schober, B. G. Hance, M. J. Austin, A. D. Price, B. D. Fellows, T. C. Monson, N. S. Hudak, L. Maldonado-Camargo, A. C. Bohorquez, C. Rinaldi, and D. L. Huber, "Enhanced nanoparticle size control by extending LaMer's mechanism," *Chem. Mater.*, vol. 27, no. 17, pp. 6059–6066, 2015.
- [265] J. Polte, "Fundamental growth principles of colloidal metal nanoparticles - a new perspective," *CrystEngComm*, vol. 17, no. 5, pp. 6809–6830, 2015.
- [266] G. Trefalt and M. Borkovec, "Overview of DLVO Theory," in *Laboratory of Colloid and Surface Chemistry, University of Geneva, Switzerland*, 2014, pp. 1–10.
- [267] Â. Andrade, R. Ferreira, J. Fabris, and R. Domingues, "Coating Nanomagnetic Particles for Biomedical Applications," in *Biomedical Engineering - Frontiers and Challenges, InTech, Croatia*, 2011, pp. 157–176.
- [268] A. Ulrich, S. Losert, N. Bendixen, A. Al-Kattan, H. Hagendorfer, B. Nowack, C. Adlhart, J. Ebert, M. Lattuada, and K. Hungerbuhler, "Critical aspects of sample handling for direct nanoparticle analysis and analytical challenges using asymmetric field flow fractionation in a multi-detector approach," *J. Anal. At. Spectrom.*, vol. 27, no. 7, pp. 1120–1130, 2012.
- [269] J. A. A. Júnior and J. B. Baldo, "The behavior of zeta potential of silica suspensions," *New J. Glas. Ceram.*, vol. 4, pp. 29–37, 2014.
- [270] "Zeta Potential Measurements." [Online]. Available: <http://departments.agri.huji.ac.il/zabam/zetasizer.html>. [Accessed: 13-Feb-2017].
- [271] W. Hintz, S. Antonyuk, W. Schubert, B. Ebenau, A. Haack, and J. Tomas, "Determination of Physical Properties of Fine Particles, Nanoparticles and Particle Beds," in *Modern Drying Technology, Wiley-VCH Verlag GmbH & Co. KGaA, Weinheim, Germany*, vol. 2–4, 2014, pp. 1–96.
- [272] M. Joshi, A. Bhattacharyya, and S. W. Ali, "Characterization techniques for nanotechnology application in textiles," *Indian J. Fibre Text. Res.*, vol. 33, no. 3, pp. 304–317, 2008.
- [273] K. Takahashi, H. Kato, T. Saito, S. Matsuyama, and S. Kinugasa, "Precise measurement of the size of nanoparticles by dynamic light scattering with uncertainty analysis," *Part. Part. Syst. Charact.*, vol. 25, no. 1, pp. 31–38, 2008.
- [274] J. Lim, S. P. Yeap, H. X. Che, and S. C. Low, "Characterization of magnetic nanoparticle by dynamic light scattering," *Nanoscale Res. Lett.*, vol. 8, no. 1, pp. 381–394, 2013.
- [275] S. L. Pal, U. Jana, P. K. Manna, G. P. Mohanta, and R. Manavalan, "Nanoparticles: An overview of preparation and characterization," *J. Appl. Pharm. Sci.*, vol. 1, no. 6, pp. 228–234, 2011.
- [276] S. Charurvedi and P. N. Dave, "Microscopy in Nanotechnology," in *Current Microscopy Contributions to Advances in Science and Technology, Formatex (Microscopy Series N^o 5), Spain, Vol. 2*, 2012, pp. 946–952.

- [277] R. Srivastava, "Synthesis and characterization techniques of nanomaterials," *Int. J. Green Nanotechnol.*, vol. 4, no. 1, pp. 17–27, 2012.
- [278] S. A. Aseyev, P. M. Weber, and A. A. Ischenko, "Ultrafast electron microscopy for chemistry, biology and material science," *J. Anal. Sci. Methods Instrum.*, vol. 3, no. 1, pp. 30–53, 2013.
- [279] "Instruments of Microscopy." [Online]. Available: <https://courses.lumenlearning.com/microbiology/chapter/instruments-of-microscopy/>. [Accessed: 09-Oct-2017].
- [280] B. R. Kirupakar, B. A. Vishwanath, M. P. Sree, and Deenadayalan, "Vibrating sample magnetometer and its application in characterisation of magnetic property of the anti cancer drug magnetic microspheres," *Int. J. Pharm. Drug Anal.*, vol. 4, no. 5, pp. 227–233, 2016.
- [281] "Magnetometry - VSM." [Online]. Available: <http://www.nanophys.kth.se/nanophys/facilities/hf-lab/index-2.html>. [Accessed: 29-Jan-2018].
- [282] "Spectrophotometry." [Online]. Available: https://chem.libretexts.org/Core/Physical_and_Theoretical_Chemistry/Kinetics/Reaction_Rates/Experimental_Determination_of_Kinetics/Spectrophotometry. [Accessed: 29-Jan-2018].
- [283] M. Gaumet, A. Vargas, R. Gurny, and F. Delie, "Nanoparticles for drug delivery: The need for precision in reporting particle size parameters," *Eur. J. Pharm. Biopharm.*, vol. 69, no. 1, pp. 1–9, 2008.
- [284] M. Khalkhali, S. Sadighian, K. Rostamizadeh, F. Khoeini, M. Naghibi, N. Bayat, M. Habibzadeh, and M. Hamidi, "Synthesis and characterization of dextran coated magnetite nanoparticles for diagnostics and therapy," *BiolImpacts*, vol. 5, no. 3, pp. 141–150, 2015.
- [285] S. A. Jadhav and S. V. Patil, "Facile synthesis of magnetic iron oxide nanoparticles and their characterization," *Front. Mater. Sci.*, vol. 8, no. 2, pp. 193–198, 2014.
- [286] S. Beyaz, H. Kockar, and T. Tanrisever, "Simple synthesis of superparamagnetic magnetite nanoparticles and ion effect on magnetic fluids," *J. Optoelectron. Adv. Mater. - Symp.*, vol. 1, no. 3, pp. 447–450, 2009.
- [287] D. Y. Seo, M. Jin, J.-C. Ryu, and Y.-J. Kim, "Investigation of the genetic toxicity by dextran-coated superparamagnetic iron oxide nanoparticles (SPION) in HepG2 cells using the comet assay and cytokinesis-block micronucleus assay," *Toxicol. Environ. Health Sci.*, vol. 9, no. 1, pp. 23–29, 2017.
- [288] Y. Huang, B. Zhang, S. Xie, B. Yang, Q. Xu, and J. Tan, "Superparamagnetic iron oxide nanoparticles modified with Tween 80 pass through the intact blood-brain barrier in rats under magnetic field," *ACS Appl. Mater. Interfaces*, vol. 8, no. 18, pp. 11336–11341, 2016.

- [289] A. M. Prodan, S. L. Iconaru, C. S. Ciobanu, M. C. Chifiriuc, M. Stoicea, and D. Predoi, "Iron oxide magnetic nanoparticles: Characterization and toxicity evaluation by in vitro and in vivo assays," *J. Nanomater.*, vol. 2013, pp. 1–10, 2013.
- [290] C. Costa, F. Brandão, M. J. Bessa, S. Costa, V. Valdiglesias, G. Kiliç, N. Fernández-Bertólez, P. Quaresma, E. Pereira, E. Pásaro, B. Laffon, and J. P. Teixeira, "In vitro cytotoxicity of superparamagnetic iron oxide nanoparticles on neuronal and glial cells. Evaluation of nanoparticle interference with viability tests," *J. Appl. Toxicol.*, vol. 36, no. 3, pp. 361–372, 2016.
- [291] M. Rezaei, H. Mafakheri, K. Khoshgard, A. Montazerabadi, A. Mohammadbeigi, and F. Oubari, "The cytotoxicity of Dextran-coated iron oxide nanoparticles on Hela and MCF-7 cancerous cell lines," *Iran. J. Toxicol.*, vol. 11, no. 5, pp. 31–36, 2017.
- [292] C. Iacovita, A. Florea, R. Dudric, E. Pall, A. I. Moldovan, R. Tetean, R. Stiufiuc, and C. M. Lucaciu, "Small versus large iron oxide magnetic nanoparticles: Hyperthermia and cell uptake properties," *Molecules*, vol. 21, no. 10, pp. 1–21, 2016.
- [293] J. E. Bae, M. Huh, B. K. Ryu, J. Y. Do, S. U. Jin, M. J. Moon, J. C. Jung, Y. Chang, E. Kim, S. G. Chi, G. H. Lee, and K. S. Chae, "The effect of static magnetic fields on the aggregation and cytotoxicity of magnetic nanoparticles," *Biomaterials*, vol. 32, no. 35, pp. 9401–9414, 2011.
- [294] B. A. Sabel, R. Engelmann, and M. F. Humphrey, "In vivo confocal neuroimaging (ICON) of CNS neurons," *Nat. Med.*, vol. 3, no. 2, pp. 244–247, 1997.
- [295] N. J. Yang and M. J. Hinner, "Getting across the cell membrane: An Overview for small molecules, peptides, and proteins," *Methods Mol Biol.*, vol. 1266, pp. 29–53, 2015.

Appendix

Reaction conditions for the synthesis of superparamagnetic iron oxide nanoparticles (SPIO-NPs) are listed below:

Stirrer diameter (D_a)	0.058	m
Volume of the three-neck reactor (V)	2.5×10^{-4}	m^3
Power number (N_p)	2	-
Number of revolutions of stirrer (n)	400, 600, 800, 1000	min^{-1}
Water density (ρ)	988.037	Kg.m^{-3}
Water viscosity (η)	0.6×10^{-3}	$\text{Kg.m}^{-1}. \text{s}^{-1}$

Calculation of kinematic viscosity ν

Kinematic viscosity (ν) of solution (water in the present case) was calculated by using following mathematical relation:

$$\nu = \frac{\eta}{\rho} = \frac{0.6 \cdot 10^{-3} \text{ Kg/m.s}}{988.037 \text{ Kg/m}^3} = 6 \cdot 10^{-7} \text{ m}^2/\text{s}$$

* Calculation of turbulent energy dissipation rate ε

Turbulent energy dissipation rate (ε) for two blade stirrer or propeller can be calculated with the help of the following equation:

$$\varepsilon = \frac{N_p n^3 D_a^5}{V} = \frac{2 \cdot \left(\frac{400}{60} \text{ s}^{-1}\right)^3 \cdot (0.058\text{m})^5}{2.5 \cdot 10^{-4} \text{ m}^3} = 1.55 \text{ m}^2/\text{s}^3$$

Calculation of stirrer tip speed V_s

$$V_s = \pi \cdot n \cdot D_a = 3.14 \cdot \left(\frac{400}{60} \text{ s}^{-1}\right) \cdot (0.058\text{m}) = 1.21 \text{ m/s}$$

**** Calculation of Reynold number Re**

Reynold number (Re) can be calculated by using following equation:

$$\text{Re} = \left(\frac{D_a^2 \cdot n}{\nu} \right) = \left(\frac{(5.8 \cdot 10^{-2})^2 \cdot \left(\frac{400}{60} \right)}{6 \cdot 10^{-7}} \right) = 37377$$

*Gotoh, K., H. Masuda, and K. Higashitani, Powder Technology Handbook, 2nd edition Revised and Expanded. New York, Marcel Dekker Inc. 1997.

**Wang, P., A. Anderko, and R. D. Young, "Modeling viscosity of concentrated and mixed-solvent electrolyte systems," Fluid Phase Equilibria, vol. 226, pp.71-82, 2004.

Publications and master thesis supervised

Publication

Khalid, M. K.; Asad, M.; Henrich-Noack, P.; Sokolov, M.; Hintz, W.; Grigartzik, L.; Zhang, E.; Dityatev, A.; Wachem, B. van; Sabel, B. A. "Evaluation of Toxicity and Neural Uptake In Vitro and In Vivo of Superparamagnetic Iron Oxide Nanoparticles" *Int. J. Mol. Sci.* 2018, 19, 1–14, doi:10.3390/ijms19092613 (Impact factor 3.687)

Master thesis supervised (for the degree of M.Sc. Chemical and Energy Engineering)

1. Selokar, N.; (2016) *Synthesis and characterization of oleic acid coated iron oxide nanoparticles by co-precipitation method*, Otto-von-Guericke University (OvGU), Magdeburg, Germany
2. Hafeez, H.; (2016) *Effect of process parameters on inorganic surfactant modified iron oxide nanoparticles via co-precipitation method*, Otto-von-Guericke University, Magdeburg, Germany
3. Raza, M.; (2016) *Study of different synthesis parameters of dextran 70,000 coated iron oxide (Fe_3O_4) nanoparticles by modifying co-precipitation method for use in drug delivery applications*, Otto-von-Guericke University (OvGU), Magdeburg, Germany
4. Divanjee, S. V.; (2017) *Effect of pH on particle size, particle size distribution, and magnetic properties of organic coated magnetic core nanoparticles (iron oxide, Fe_3O_4) in a large pH window with different bases*, Otto-von-Guericke University (OvGU), Magdeburg, Germany
5. Khan, M. S.; (2017) *Designing and comparative study of DEAE-Dextran and Tween 80 stabilized iron oxide nanoparticles for use in pharmaceutical applications*, Otto-von-Guericke University (OvGU), Magdeburg, Germany
6. Zohaib, M.; (2017) *Designing and study the optimum conditions by comparing organic and inorganic coated superparamagnetic iron oxide (Fe_3O_4) nanoparticles with respect of their particle size distribution, stability, and morphology*, Otto-von-Guericke University (OvGU), Magdeburg, Germany
7. Chaudhary, M. Z.; (2017) *Particle size, particle size distribution and stability of iron oxide (Fe_3O_4) nanoparticles by varying the $Fe^{2+}:Fe^{3+}$ molar ratio via co-precipitation and reverse co-precipitation methods at different synthesis parameters*, Otto-von-Guericke University (OvGU), Magdeburg, Germany
8. Asad, M.; (2018) *Fluorescent dyes labelling of superparamagnetic iron oxide nanoparticles for biological and pharmaceutical applications*, Otto-von-Guericke University (OvGU), Magdeburg, Germany

Curriculum vitae

Muhammad Kamran Khalid

Experience

- 01/2015 – 12/2018 Otto-von-Guericke University (OvGU), Magdeburg, Germany
Ph.D. researcher at Institute of Process Engineering
- Teaching the following subject at master level*
- Storage and flow of particulate solids (SFPS): WS 2015,
WS 2016 and WS 2017
- Master's thesis supervised*
- Supervision of eight master theses for the program of Chemical
and Energy Engineering (CEE) at OvGU, Magdeburg, Germany
- 01/2009 – 06/2009 King Saud University, Riyadh, Kingdom of Saudi Arabia
- Department of Chemical Engineering
- Senior Researcher*
- Worked on the development and characterization of catalysts for
the synthesis of Sulphur funded by Saudi Basic Industries
Corporation (SABIC)
- 06/2008 – 09/2014 University of the Punjab, Lahore, Pakistan
- Institute of Quality and Technology Management (IQTM)
Faculty member and undergraduate program manager
- 07/2007 – 06/2008 University of Borås, Sweden
- Project Assistant*
- Project in collaboration with Novartis Foundation Sweden, during
the master studies
- 03/2005 – 12/2006 Chemicals and Plastics, Lahore, Pakistan
- Chemical Analyst*
- Responsible to communicate with overseas suppliers and also
to check technical specification of all products covering P.V.C.
Resins, D.O.P Plasticizer, EVA Compound, and Butyl Acetate to
be imported

Education

01/2015 – 12/2018	Otto-von-Guericke University (OvGU), Magdeburg, Germany Institute of Process Engineering Ph.D. Chemical and Process Engineering
07/2007 – 06/2008	University of Borås, Sweden M.Sc. Industrial Engineering with emphasis on Quality and Environmental Management
01/2000 – 01/2005	University of the Punjab, Lahore, Pakistan Institute of Chemical Engineering and Technology (ICET) B.Sc. Chemical Engineering
03/1998 – 04/2000	B.Sc. with Physics, Chemistry, and Mathematics University of the Punjab, Lahore, Pakistan

Courses / Training

- Faculty Development Orientation from University of the Punjab, Lahore, Pakistan
- Research Management from University of the Punjab, Lahore, Pakistan

Registration / Membership

- Pakistan Engineering Council's professional engineer
- Senior Member of Pakistan Institute of Chemical Engineers (PIChE)